Karlsruher Institut für Technologie

Laser post-processing of laser powder bed fusion Ti-6Al-4V parts

Juliana dos Santos Solheid

Institut für Angewandte Materialien – Angewandte Werkstoffphysik – IAM-AWP

KIT – Die Forschungsuniversität in der Helmholtz-Gemeinschaft

Laser post-processing of laser powder bed fusion Ti-6Al-4V parts

Zur Erlangung des akademischen Grades einer
DOKTORIN DER INGENIEURWISSENSCHAFTEN (Dr.-Ing.)

von der KIT-Fakultät für Maschinenbau des
Karlsruher Instituts für Technologie (KIT)
genehmigte

DISSERTATION

von

M.Sc. Juliana dos Santos Solheid

Hauptreferent:
Prof. Dr. rer. nat. habil. Hans Jürgen Seifert
Korreferenten:
Prof Dr. rer. nat. Wilhelm Pfleging
Prof. Dr.-Ing. Andreas Ostendorf

Tag der mündlichen Prüfung: 11.07.2025

Contents

List of Figures

List of Tables

Acknowledgements

This work was developed during my PhD studies in Karlsruhe Institute of Technology (KIT) at the Institute for Applied Materials – Applied Materials Physics (IAM-AWP) and it has received funding from the European Union's programme PAM^2 within Horizon 2020 under grant agreement No. 721383.

I would like to acknowledge and thank Prof. Dr. Hans Jürgen Seifert who contributed to this work with his valuable supervision and great opportunities of discussions and presentations within IAM-AWP.

I am truly thankful to Prof. Dr. Wilhelm Pfleging for giving me the opportunity of joining the Laser Materials Processing Group, and for the continuous support during the development of this research.

My sincere appreciation to Heino Besser for all the support during the fs laser processing, to Torsten Wunsch and Dr. Thomas Gietzelt from the Institute for Micro Process Engineering (IMVT) for all the assistance with laser polishing experiments, to Xuanqing Hong for the assistance with the samples metallographic analysis, to Dr. Mohamad Bayat and Dr. Sankhya Mohanty from Denmark Technical University (DTU) for all the discussion and support with COMSOL modelling, to Dr. Ahmed Elkaseer from the Institute for automation and Applied Informatics (IAI) for sharing with me his experience and knowledge about process development, to Dr. Peter Weidler from the Institute of Interfaces (IFG) for the specific support with XRD experiments, to Vanessa Trouillet from the Institute for Applied Materials – Energy Storage Systems (IAM-ESS) for the support with XPS analysis, and to Simone Weigel and Dr. Tim Scharnweber from the Institute for Biological Interfaces (IBG) for their support with biocompatibility experiments.

My special thanks to Alexandra Reif, not only for her endless support with experiments and fruitful discussions about metallographic results, but also for guiding and helping me in my initial years in Germany.

My deepest appreciation to my friends and colleagues from the PAM² project for all the knowledge, experiences, frustrations, and fun shared.

Finally, I would like to give my special thanks to my husband Rodolfo for supporting my pursuit of a doctoral degree with infinite patience and constant encouragement.

Abstract

Titanium alloy Ti-6Al-4V is one of the many materials used to produce components by laser powder bed fusion (LPBF), an additive manufacturing technique, especially in medical technology due to its excellent mechanical properties and high biocompatibility. However, the surface quality of additively manufactured components is often limited, and post-processing methods are essential to ensure that the manufactured components meet the design and functional requirements. To this end, surface post-processing with laser radiation is to be developed, either alone or as a supplement to the conventional post-processing methods established to date, which are primarily based on mechanical processes.

Laser polishing of Ti-6Al-4V samples with a continuous wave laser proved to be very advantageous in terms of increasing surface quality and reducing roughness values in a short time. In addition to the removal of unevenness, the samples exhibited hydrophilic surface properties after laser polishing. However, the process is also characterized by the immediate formation of heat-affected zones (HAZ) and the resulting microstructural changes that influence the mechanical properties of the components. In this work, laser polishing trials were executed according to a design of experiments. Apart from the experimental data used as input for surface roughness statistical models, simulations from a heat transfer model were used to obtain the input data for the HAZ depth statistical assessment. Both input data sets were processed by quadratic regression and artificial neural network algorithms. In this case, the artificial neural network models are the most suitable, as the regression models for surface roughness have significant accuracy limitations. A multi-objective genetic algorithm optimization (Pareto optimization) based on the artificial neural network models is used to define parameter combinations that allow the determination of an acceptable range of values for the given input parameters (laser power, focus offset, axial feed rate, number of repetitions and scan speed) that simultaneously produces satisfactory values for roughness values (Ra) and HAZ. In addition, the results obtained by the simulations are discussed and compared with the experimental data, demonstrating the validity of the process models. Finally, the experimental studies also include the evaluation of the resulting microstructural properties of the metallic components at different stages of the process chain and the associated hardness properties.

In addition to the thermal process of laser polishing, non-thermal laser processing, so-called "cold ablation" using ultrashort pulse laser radiation, can also be advantageous as a post-processing step for LPBF produced Ti-6Al-4V components, as ultrashort pulse laser radiation with pulse lengths of less than 10 ps leads to extremely high peak intensities and is therefore suitable for cutting, drilling and ablation. The choice of laser and process parameters for the ablation process not only influences the ablation rate but can also lead to different surface topographies. These are usually characterized by nano-ripple structures, also known as laser-induced periodic surface structures (LIPSS), or porous structures created by selective material ablation. Both types of structures can strongly influence the functionality of the resulting parts, as they can change their original wettability and/or biocompatibility. In contrast to laser polished surfaces, all surfaces functionalized by ultrashort pulse laser irradiation showed hydrophobic properties. The cell growth feasibility study revealed that the applied post-processing did not adversely affect the biocompatibility of the Ti-6Al-4V parts. The presented approach is considered a suitable post-processing option to adjust different functionalities on defined areas of the components, to replace certain steps of the process chain or to establish a combination of both. Each laser-assisted process, individually and in combination, was carried out after different stages of the process chain and the resulting microstructure was evaluated together with the resulting surface hardness.

Kurzfassung

Die Titanlegierung Ti-6Al-4V ist einer der zahlreichen Werkstoffe, die für die Herstellung von Komponenten durch das pulverbettbasierte Laserstrahlschmelzen (LPBF), einer additiven Fertigungstechnik, verwendet werden, insbesondere in der Medizintechnik, aufgrund seiner hervorragenden mechanischen Eigenschaften und seiner hohen Biokompatibilität. Die Oberflächenqualität der additiv hergestellten Bauteile ist jedoch derart eingeschränkt, dass Nachbearbeitungsmethoden unbedingt erforderlich sind, um sicherzustellen, dass die hergestellten Komponenten den Design- und Funktionsanforderungen entsprechen. Hierzu soll die Oberflächennachbearbeitung mit Laserstrahlung, alleinig oder als Ergänzung zu den bislang etablierten, vorwiegend auf mechanischen Prozessen basierenden konventionellen Nachbearbeitungsmethoden, entwickelt werden.

Das Laserpolieren von Ti-6Al-4V-Proben mit einem Dauerstrichlaser erweist sich als sehr vorteilhaft bzgl. der Steigerung der Oberflächenqualität bzw. zur Reduzierung der Rauheitswerte in kurzer Zeit. Neben der Entfernung von Unebenheiten wiesen die Proben nach dem Laserpolieren hydrophile Oberflächeneigenschaften auf. Der Prozess ist jedoch auch durch die sofortige Bildung von wärmebeeinflussten Zonen (WEZ) und die daraus resultierenden mikrostrukturellen Veränderungen gekennzeichnet, die die mechanischen Eigenschaften der Bauteile beeinflussen. In dieser Arbeit werden Experimente und Simulationen zum Laserpolieren auf der Grundlage von Versuchsplänen durchgeführt, um die Auswirkungen der parametrischen Eingaben im Hinblick auf die resultierende Oberflächenrauheit und die Tiefe der Wärmeeinflusszone zu bewerten. Die gewonnenen Daten werden verwendet, um sowohl lineare Regressions- als auch künstliche neuronale Netzmodelle für jede Variable zu erstellen. In diesem Fall sind die Modelle mit künstlichen neuronalen Netzen am leistungsfähigsten, da die Regressionsmodelle für die Oberflächenrauheit deutliche Genauigkeitseinschränkungen aufweisen. Eine auf den Modellen des künstlichen neuronalen Netzes basierende multikriterielle genetische Algorithmus-Optimierung (Pareto-Optimierung) wird verwendet, um Parameterkombinationen festzulegen, die die Ermittlung eines akzeptablen Wertebereichs für die gegebenen Eingangsparameter (Laserleistung, Fokusversatz, axiale Vorschubgeschwindigkeit, Anzahl der Wiederholungen und Scangeschwindigkeit) ermöglichen, der gleichzeitig zufriedenstellende Werte für Rauwerte (Ra) und WEZ erzeugt. Darüber hinaus werden die durch die Simulationen erzielten Ergebnisse diskutiert und mit den experimentellen Daten verglichen, wodurch die Gültigkeit der Prozessmodelle nachgewiesen wird. Schließlich umfassen die experimentellen Studien auch die Bewertung der sich einstellenden mikrostrukturellen Eigenschaften der metallischen Bauteile in verschiedenen Stadien der Prozesskette und der damit verbundenen Härteeigenschaften.

Neben dem Prozess des thermalen Laserpolierens kann die athermale Laserprozessierung, die sogenannte "kalte Ablation“ mittels Ultrakurzpulslaserstrahlung, auch als Nachbearbeitungsschritt von LPBF hergestellten Ti-6Al-4V-Bauteilen von Vorteil sein, da Ultrakurzpulslaserstrahlung mit Pulslängen von weniger als 10 ps zu extrem hohen Spitzenintensitäten führt und daher zum Schneiden, Bohren und Abtragen geeignet ist. Die Wahl der Laser- und Prozessparameter für den Abtragprozess beeinflusst nicht nur die Abtragrate, sondern kann auch zu unterschiedlichen Oberflächentopographien führen. Diese werden üblicherweise durch Nano-Rippel-Strukturen, auch bekannt als laserinduzierte periodische Oberflächenstrukturen (LIPSS), oder als durch selektiven Materialabtrag erzeugte poröse Strukturen charakterisiert. Beide Strukturtypen können die Funktionalität der entstehenden Teile stark beeinflussen, da sie deren ursprüngliche Benetzbarkeit und/oder Biokompatibilität verändern können. Im Gegensatz zu laserpolierten Oberflächen zeigten alle

mittels Ultrakurzpulslaserstrahlung funktionalisierten Oberflächen hydrophobe Eigenschaften. Die Studie zur Durchführbarkeit des Zellwachstums ergab, dass die angewandte Nachbearbeitung die Biokompatibilität der Ti-6Al-4V-Teile nicht nachteilig beeinflusste. Der vorgestellte Ansatz wird als geeignete Nachbearbeitungsoption angesehen, um unterschiedliche Funktionalitäten an definierten Bereichen der Bauteile einzustellen, bestimmte Schritte der Prozesskette zu ersetzen oder um eine Kombination aus beidem zu etablieren. Jeder lasergestützte Prozess, einzeln und in Kombination, wurde nach unterschiedlichen Stufen der Prozesskette durchgeführt und die sich einstellende Mikrostruktur zusammen mit der resultierenden Oberflächenhärte bewertet.

List of Abbreviations

3D	3-dimensional
3DP	Binder Jetting 3D Printing
ATP	Ambient Temperature and Pressure
AB	As Built
AM	Additive Manufacturing
ANN	Artificial Neural Network
ANOVA	Analysis of Variance
bcc	Body-Centered Cubic
BIS	Beam Interference Solidification
BPM	Ballistic Particle Manufacturing
CA	Contact Angle
CAD	Computer-Aided Design
CCD	Central Composite Design
CGHE	Carrier Gas Hot Extraction
CS	Cross-Section
cw	Continuous Wave
DMD	Direct Metal Deposition
DMLS	Direct Metal Laser Sintering
DoE	Design of Experiments
DoF	Degrees of Freedom
EBM	Electron Beam Melting
FDM	Fused Deposition Modeling
FEM	Finite Element Method
FOP	Focal Position
FWHM	Full Width at Half Maximum
GA	Genetic Algorithm
GR	Ground
HAZ	Heat Affected Zone
hcp	Hexagonal Close-Packet
HIS	Holographic Interference Solidification
HT	Heat Treated
ICP-OES	Inductively Coupled Plasma - Optical Emission Spectroscopy
IJP	Ink Jet Printing
LENS	Laser Engineered Net Shaping
LIPSS	Laser-Induced Periodic Surface Structures
LOM	Laminated Object Manufacturing
LP	Laser Polishing
LPBF	Laser Powder Bed Fusion
LPD	Laser Powder Deposition
LTP	Liquid Thermal Polymerization
MAM	Metal Additive Manufacturing
MJM	Multi Jet Modeling
ML	Machine Learning
MOOP	Multi Objective Optimization
MSE	Mean Squared Error

RMS	Root Mean Square
SB	Sandblasted
SEM	Scanning Electron Microscopy
SFP	Solid Foil Polymerization
SGC	Solid Ground Curing
SHG	Second Harmonic Generation
SLA	Stereolithography
SLC	Selective Laser Cladding
SLM	Selective Laser Melting
SLS	Selective Laser Sintering
STL	Standard Triangle Language
THG	Third Harmonic Generation
XPS	X-Ray Photoelectron Spectroscopy
XRD	X-Ray Diffraction

.

1. Introduction

Recent growth in ecological consciousness shaped greatly the manufacturing sector, with particular interest and investigations focusing on the usage of additive manufacturing (AM) as an alternative technique in the direction of a more effective and environmental-friendly process that has the potential to alleviate pollutant substances emission, and to result in competent ways of handling waste and using resources [1]. AM, or 3-dimensional (3D) printing, is a fabrication process based on the deposition of thin layers of materials, consecutively, to produce a part or device. Now an established technology, the first 3D printers date from the 1980's [2]. AM has the potential to simplify the process chain because of the possibility of creating near net shape designs independently from their intricacies. Besides that, AM techniques are capable of fabricating workpieces with unique inner attributes. Those facts combined are exactly the shortcomings of conventional manufacturing techniques. This extreme flexibility of AM technologies provides more control over aspects such as time and material consumption, which are directly correlated to overall manufacturing costs. Moreover, it is the essential feature that turns such a manufacturing approach into a solution for high-volume production of customized items. As diverse types of AM exist, a wide variety of materials can be used, considering that the feedstock is compatible with the technology adopted. The most common types of materials are plastics, metals, ceramics, and composites. AM technologies have been the focus of research throughout the world in the past decade, and several industries already take advantage of the high flexibility of AM processes [3, 4].

Given the widespread usage of metallic materials across all manufacturing sectors, laser powder bed fusion (LPBF) is a widely used technique within metal additive manufacturing (MAM), since it offers many advantages amidst other MAM approaches. Through the procedure, a laser beam is responsible for melting fine layers of metal particles that are deposited onto a building platform. The fused metal particles take the designed form when in solid state [5]. Although a great increase in the number of metals and their alloys that can be submitted to LPBF is observed, the range remains restricted to those that can be cast and welded [4]. The materials used in metal AM vary according to the application of the produced parts. Titanium and its alloys are the most used metals for medical applications due to their outstanding mechanical properties and elevated biocompatibility [6]. The microstructural and material properties of conventionally manufactured Ti-6Al-4V are well known, and this factor accounts for the wide adoption of this material in the medical industry. The LPBF manufactured Ti-6Al-4V, on the other hand, presents completely different characteristics in terms of resulting microstructure and, consequently, mechanical properties [7, 8].

The applications for parts produced via LPBF has increased with the development of the process, ranging from industrial (e.g., aerospace, energy, oil and gas, automotive, and tooling) to healthcare (e.g., medical and dental) [3, 9]. Even though LPBF has numerous benefits, not all fabricated workpieces are fully compliant to the design requirements. The most recurring limitation is suboptimal surface condition of some produced workpieces. The mentioned disadvantage might be either a consequence of the layer-by-layer concept of the manufacturing technique or an outcome of adjacent metal particles adhering to the workpiece's external areas during the solidification of the molten material [10]. To address such constraints and meet product specifications, post-processes can be adopted with the drawback of potentially causing a lengthy and intricate LPBF workflow (Figure 1-1). Previous study was conducted in order to pinpoint manufacturing shortcomings and boost overall effectiveness of such technique [11]. Although approaches focused on improving the production precision and

efficiency when adopting LPBF are often addressed in the literature [12, 13, 14], researches on post-processing development topics are still rather scarce. Employing adequate post-processes could enhance the overall quality of AM components, which would tackle not only the crucial concerns on surface roughness but also microstructure uniformity that can lead to better mechanical performance. Established post-processes to address the former include traditional machining, sandblasting, and mechanical polishing, whereas heat treatments are employed to enhance the latter (Figure 1-1) [15, 16, 17, 18]. Conversely, instead of the traditional methods already discussed, alternative approaches are often applied, namely: (electro-)chemical machining, ultrasonic cavitation abrasive finishing, laser material processing, and electrical discharge machining [19, 20, 21].

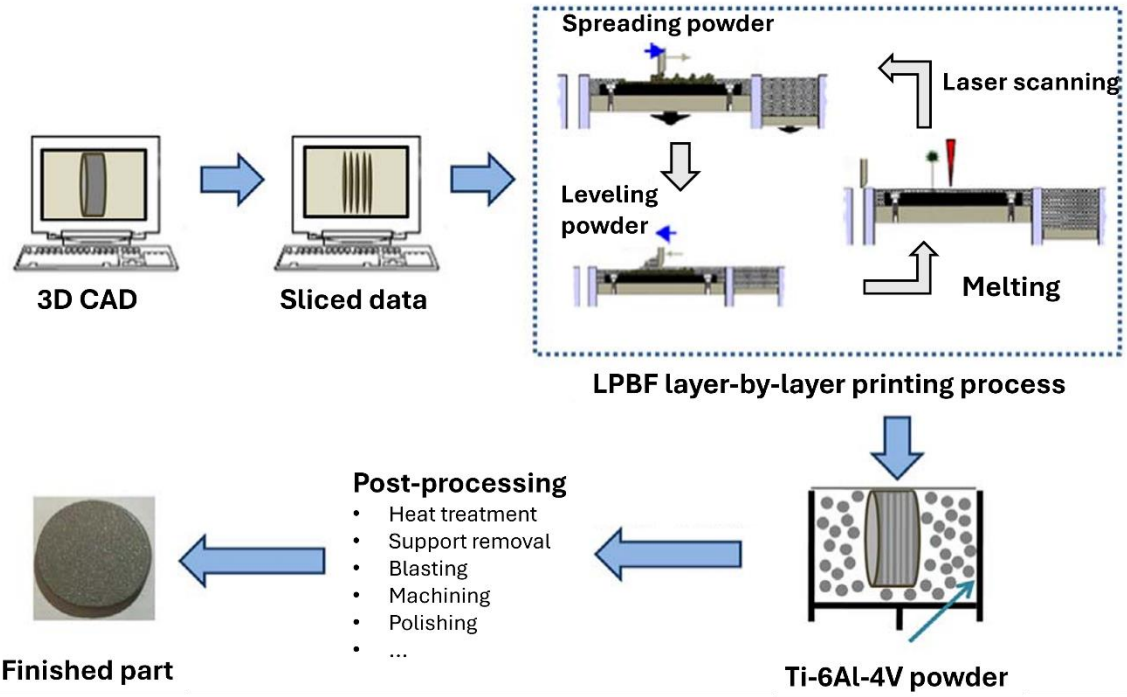

Figure 1-1: Process chain of LPBF starting at the design of the part to be manufactured followed by its slicing, manufacturing, and post-processing to achieve the final part. Adapted from [22].

One powerful non-conventional technique for surface smoothening is laser polishing (LP), in which the surface of the laser irradiated material is liquified, and this molten portion equally spreads across the uppermost layer of the workpiece. When the mentioned portion of material returns to solid state, the workpiece's surface roughness is potentially reduced. Taking into account all existing technology at one's disposal, the combination of AM and LP is an appealing solution. Furthermore, given that both processes are already individually highly flexible, their association increases the overall versatileness of the entire manufacturing workflow resulting in a more resourceful process. Its effectiveness and processing time, along with the absence of mechanical loads, consolidates the LP technique as an appropriate post-process of AM parts. Comparatively, this method is an apt alternative to mechanical polishing and/or grinding [23, 24, 25]. One obstacle of the LP is the possibility heat affected zones (HAZ) formations and, as a consequence, potential alterations in the microstructure and in the mechanical performance of the components [26, 27]. Therefore, the definition of parameters to be utilized in the process plays a crucial role in its outcome. Additionally, the HAZ can be mitigated or controlled when LP is combined within the AM workflow in an appropriate order. Nevertheless, it is vital to comprehend prospective material alterations and their inherent means. Pulsed

lasers can be as useful a post-processing step for LPBF Ti-6Al-4V parts as continuous wave (cw) laser polishing. The main difference between the mentioned techniques is that the laser energy reaches the part being processed continuously in the former, while the material is reached by timed pulses of energy in the latter.

The amount of energy in each pulse is a function of the average laser power and repetition rate, while the laser's peak power is a function of the pulse energy and duration. Small pulse duration causes higher peak power. Consequently, ultrafast laser radiation with pulse lengths shorter than 10 ps results in extremely high peak power and, therefore, is suitable for cutting, drilling, and ablation [28]. The short pulse duration limits the interaction time between laser and material, thus minimum thermally induced alterations or melting occur [29]. The choice of process parameters can lead to various surface topographies in addition to influencing the ablation rate. Two of the main topography types are nano-ripples, or laser-induced periodic surface structures (LIPSS), and porous structures caused by selective ablation, both of which allow potential modifications of wettability and/or biocompatibility [30, 31, 32, 33, 34].

The laser functionalization of Ti-6Al-4V for biological purposes has been the subject of extensive research, including teams dedicated to applying such method to LPBF Ti-6Al-4V parts [35, 36, 37]. The search of the relevant literature, however, returned no scientific investigation on the flexible manufacturing potential achieved when applying a combination of various laser post-processes and parameters that are capable of producing surfaces with polished aesthetic, systematic structure alterations or material removal.

2. Objectives and procedures

The aim of this research is to develop, evaluate and fundamentally assess laser-based methods to complement or replace conventional post-processing technologies for additive manufactured (AM) components made from the titanium alloy Ti-6Al-4V.For this purpose, advanced laser processing techniques based on laser polishing and ultrafast surface functionalization will be developed for customized and functionalized post-processing of Ti-6Al-4V AM parts. Hereby, the research is mainly driven by the following specific objectives:

- Understanding the governing physical phenomena involved in the technologies, such as laser-material interaction.
- Assessing the microstructural evolution of the processed parts.
- Evaluating the effects of the adopted post-processes on the resultant mechanical properties.
- Employ numerical tools for process development.
- Devise an approach for laser post-processes of metallic AM parts capable of providing different surface functionalization.

These specific objectives are fulfilled in two stages, which are initiated by the process development of laser polishing technology, followed by the investigation of laser surface functionalization approaches. The steps adopted for the first stage are described below:

(1) Laser polishing experiments according to a defined design of experiments (DoE) and surface texture measurements.
(2) Statistical analysis and modelling of the acquired data for evaluation of parameter interaction and surface texture prediction.
(3) Surface texture statistical model validation based on experimental data.
(4) Heat transfer model development to investigate the heat profiles depth during the process.
(5) Heat transfer model validation based on experimental data.
(6) Finite element simulations with parameter variation according to the defined DoE.
(7) Statistical analysis and modelling of the heat affected zone (HAZ) data for evaluation of parameter interaction and depth prediction.
(8) HAZ statistical model validation based on experimental data.
(9) Multi-objective optimization for obtaining the parameter set that would result in the minimum surface texture and minimum HAZ depth.
(10) Material characterization of the samples, before and after laser polishing.

The subsequent stage addresses the laser surface functionalization. A step-by-step procedure is depicted below:

(1) Laser processing of the samples for the generation of nano-ripples.
(2) Laser processing of the samples for the generation of surface pores.
(3) Material characterization of the samples after laser functionalization.
(4) Wettability tests for all reference and laser functionalized samples.
(5) Biocompatibility tests for all reference and laser functionalized samples.

The scientific output and contributions from this work cover the following subjects:

- A thermal model of the laser polishing process for the prediction of depth of the HAZ generated.
- A statistical model based on simulation data to assess how different parameter combinations affect the HAZ depth.
- A statistical model for the prediction of the surface texture after laser polishing based on experimental data.
- A multi-objective optimization to establish the laser polishing process parameters window that has potential to result simultaneously in lower roughness and heat affected zones.
- Laser processing approaches capable of generating different surface structures.
- The assessment of surface morphology, material hardness, microstructure evolution, and surface chemical composition of LPBF Ti-6Al-4V subjected to laser post-processing techniques within varied steps of the process chain.
- Evaluation of surface functions, such as wettability and biocompatibility, of different structures generated through laser post-processing.
- The combination of laser polishing and laser surface functionalization, which provides a novel, fast, and flexible technique for the post-processing of AM parts.

This chapter introduced the motivations and set of specific objectives defined to achieve the main goal of this research. Moreover, a brief overview of the chosen strategies is presented to elucidate how the objectives are accomplished throughout the research. The entire description of materials and methods adopted is exhibited in detail in Chapter 4.

3. Literature review

This chapter provides a detailed research background of additive manufacturing with a focus on the laser powder bed fusion process, the conventional post-processing steps of the process chain and alternative laser post-processes, in addition to the properties and characteristics of the Ti-6Al-4V alloy.

3.1. Additive manufacturing

Currently, several types of AM processes have been devised and are increasingly adopted in varied industry sectors. Alongside new and/or improved technologies, the AM processes allow the steady expansion of new suitable materials for use within their technologies, thus increasing the diversity of the conceivable fabricated components and, consequently, broadening the range of their applications [2]. The AM processes can be classified into distinct groups, according to their process characteristics, as shown in Figure 3-1. The meaning of each abbreviation can be found in the list of acronyms.

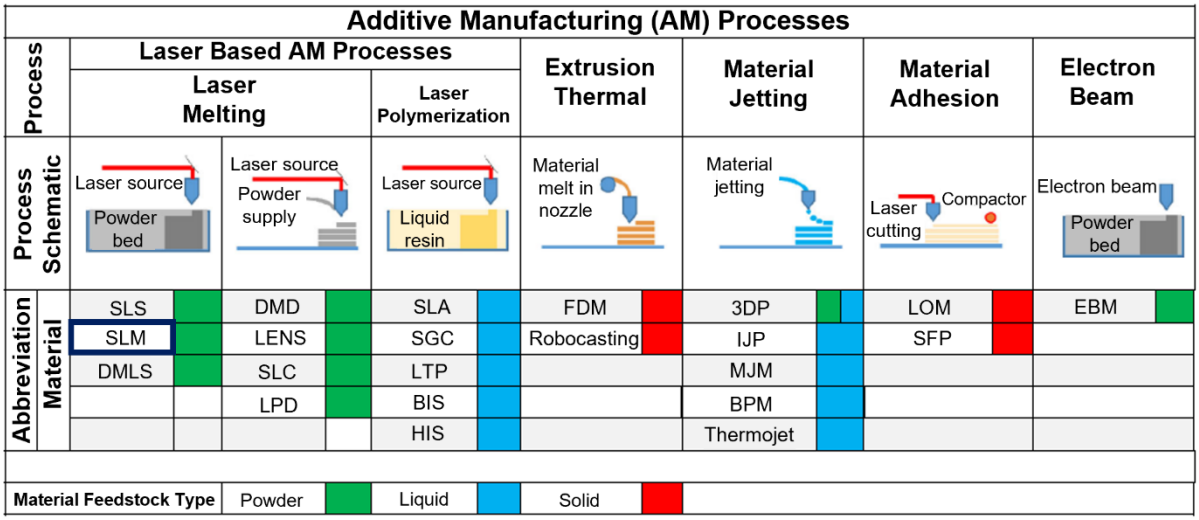

Figure 3-1. Categorization of distinct additive manufacturing processes according to material feedstock type. Adapted from [38].

Solid material feedstock can be used in processes such as materials adhesion and thermal extrusion, while liquids are employed in polymerization and jetting techniques. The adoption of powder feedstock is, currently, one of the most popular choices in industry and research. This work focuses on laser post-processing of LPBF parts, previously denoted as selective laser melting (SLM).

In general, the fabrication process using AM, from design to the final part, can be illustrated as in Figure 3-2. It starts with the creation and design of the geometry, which allows the generation of the standard triangle language (STL) file. This format is an input supported by many slicing software, also known as slicers, and describes the surface geometry of a 3D part as an approximation of the designed geometry composed of triangular shapes. With the slicer, a code to be used in the printer is generated based on the 3D model designed and process parameters pre-defined. If necessary, post-processes are applied to ensure the project requirements are met [39].

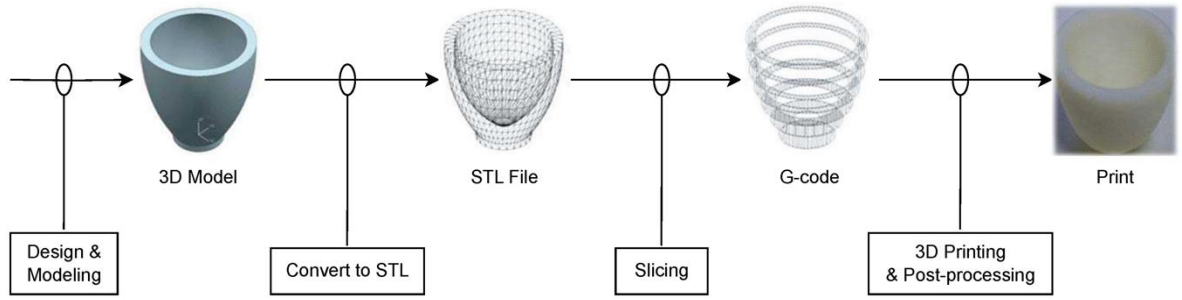

Figure 3-2. Stages of the additive manufacturing process. Adapted from [39].

3.1.1. Laser powder bed fusion

Generally, one LPBF apparatus is composed of at least one laser source and scanning mirror, powder supply, coating mechanism, the powder bed, and an excess powder repository as shown in Figure 3-3. Additionally, the process chamber provides an inert atmosphere [40].

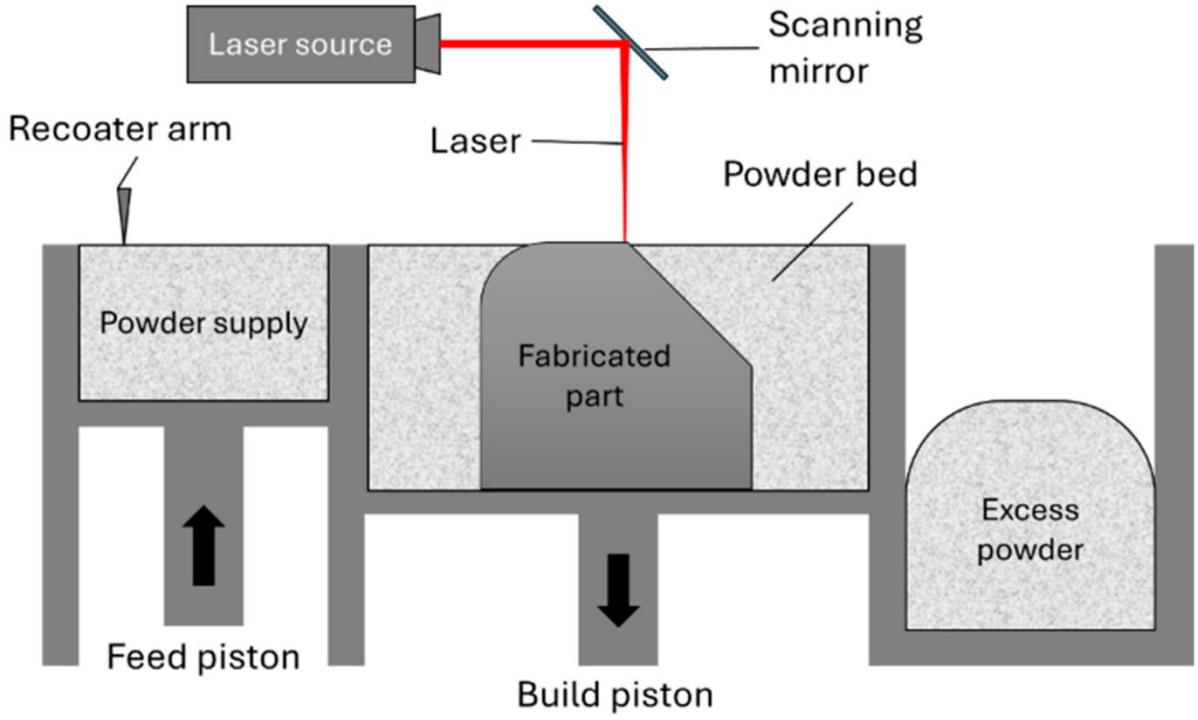

Figure 3-3. Schematic of a typical LPBF machine [41].

The recoater arm is responsible for pushing a certain amount of powdered material from the powder supply system to overlay the powder bed. The deposited material is selectively scanned by the laser beam with pre-established parameters and according to the programmed 3D design. As a consequence, the material becomes molten and, due to high cooling rates, quickly solidifies into the scanned shape. Between the laser scanning of each layer, the build piston is responsible for adjusting the height of the powder bed and, consequently, the thickness of the upcoming layer. The final workpiece is then obtained through the repetition of the described process. The powdered material that remains in the powder bed is removed from the surroundings of the part and reused after undergoing a recycling process [42, 43].

The proper selection of process parameters related to the laser scanning are of the utmost importance to the quality of the resulting parts as well as to the applicability of the LPBF process. Among the most relevant parameters, the scanning speed dictates the rapidity of the laser beam movement throughout its scanning track, which governs the time necessary to print the desired workpiece and the heat input onto the material. From a favorable perspective for the LPBF process, a balance must be found as the building time should be kept as low as possible and, concomitantly, the scanning speed should not be excessively hasty to guarantee the generation of a steady melt pool [44].

Besides the scanning speed, the laser power and spot size also have impact over the LPBF process outcome, since they are directly linked to the heat input employed onto the powdered material. Moreover, the required heat input and resultant printing duration are dependent on the thickness of each layer [45].

3.1.2. Challenges of the LPBF process

Even though the improvement of LPBF has been in evidence for several years now, the process still faces limitations and challenges often related to defects observed in the fabricated parts. Besides weakening the mechanical properties, these defects raise concerns about the precision and repeatability of the process, which are key factors for several industrial applications [46]. They can be classified into four groups according to the extension of the effects: (1) geometry and dimension, (2) surface quality, (3) microstructure, and (4) mechanical properties [47]. An overview of the specific defects influencing each particular group is gathered in Table 3-1.

Table 3-1. Classification of defects that are often observed in LPBF parts. Extracted data from [46] and [47].

Classification	Defects
(1) Geometry and dimension	• Geometry inaccuracy (form dimensional deviations) • Dimension inaccuracy (size dimensional deviations)
(2) Surface quality	• Surface roughness • Surface morphology • Surface deformation • Surface oxidation
(3) Microstructure	• Anisotropy • Heterogeneity
(4) Mechanical properties	• Fracture/cracks/holes • Bonding between layers • Porosity

One common factor for the occurrence of defects from both groups (1) and (2) is the layer-by-layer nature of the LPBF process. Geometry inaccuracies can be related to the finite dimension of the layer thickness, typically between 30 µm and 90 µm, especially in the case of geometries that are not exclusively vertical. A schematic of the issues caused by the "*stair-case effect*" in the geometry accuracy is presented in Figure 3-4, where a discrepancy is observed between the printed geometry represented by the gray blocks and the designed geometry represented by the dotted lines when the part is not vertically printed, while no discrepancy between design

and object is observed in the part printed in the vertical orientation. In addition, the surface roughness is not only affected by the so-called "*stair-case effect*", but it is also influenced by the amount of powder that is attached to the surface of parts at the end of the process. Both factors are closely related since in the presence of the "*stair-case effect*" more heat is transferred to the powder surrounding the part, thus facilitating the sintering to the surface [10].

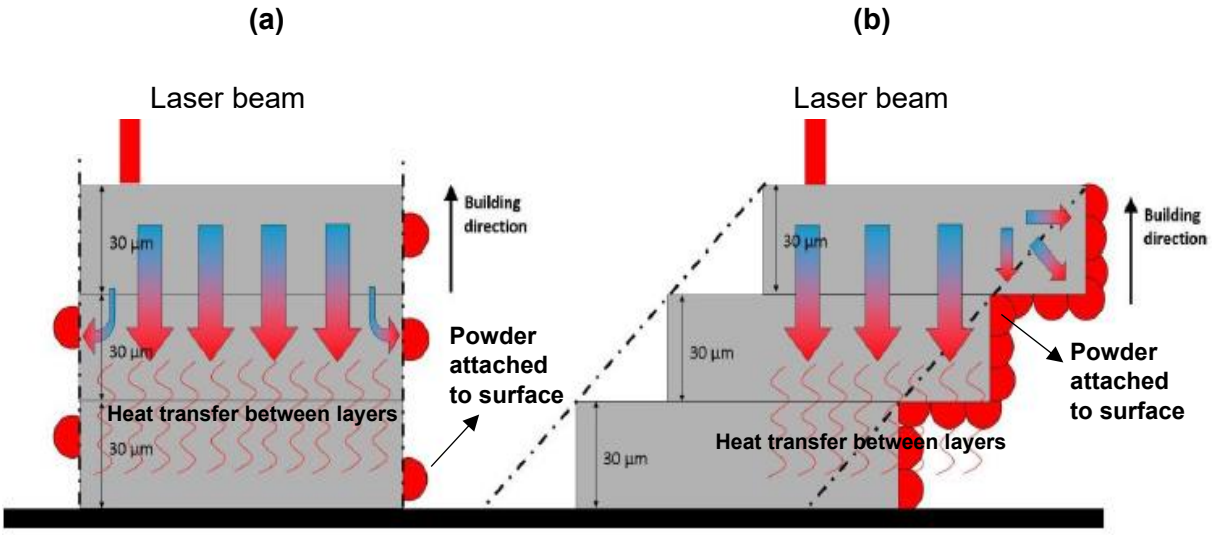

Figure 3-4. Schematic illustration of the "*stair-case effect*" influence on the powder adhesion to the surface of printed parts: (a) vertical building orientation and (b) inclined building orientation. Adapted from [10].

Design alone is not the only factor to contribute to the occurrence of defects from groups (1) and (2), since the selection of the process parameters plays a major role in the resulting parts. For example, when bulkier layers are selected (e.g., 90 µm), higher energy input is needed to completely melt the powdered material, which could cause melt pool instabilities. This unsteadiness often culminates in poor surface quality together with diminished dimensional accuracy. The hatch spacing, or the distance between two laser-scanning tracks, also dictates the amount of energy the material will eventually receive from the laser beam and is a factor of influence on all the mentioned challenges faced by the LPBF process usage [45].

Defects classified as belonging to groups (3) and (4) are more often related only to the selected process parameters. For example, the inverse relation between laser power and beam area results in the laser intensity parameter (W/cm²). Combined with the laser scanning speed, an insufficient low laser intensity could lead to a lack of fusion or pores, both defects are closely related to the part's density and the bonding between layers [48]. Such an issue could be mitigated by raising the laser intensity. Reducing layer thickness and/or hatch spacing would also elevate the temperatures endured by the affected material throughout the process.

In addition to the mentioned, further defects from groups (3) and (4) can be the results of the selected arrangement and size of the laser scanning pathway. The mentioned parameters are defined by the order and orientation in which the laser scanning will take place, and they are intimately related not only to potential shortcomings in the manufactured devices but also to the overall manufacturing process duration. During the AM process, distinct orientations and arrangements can be applied both within one layer and across subsequent layers [49]. Examples of commonly used arrangements are depicted in Figure 3-5.

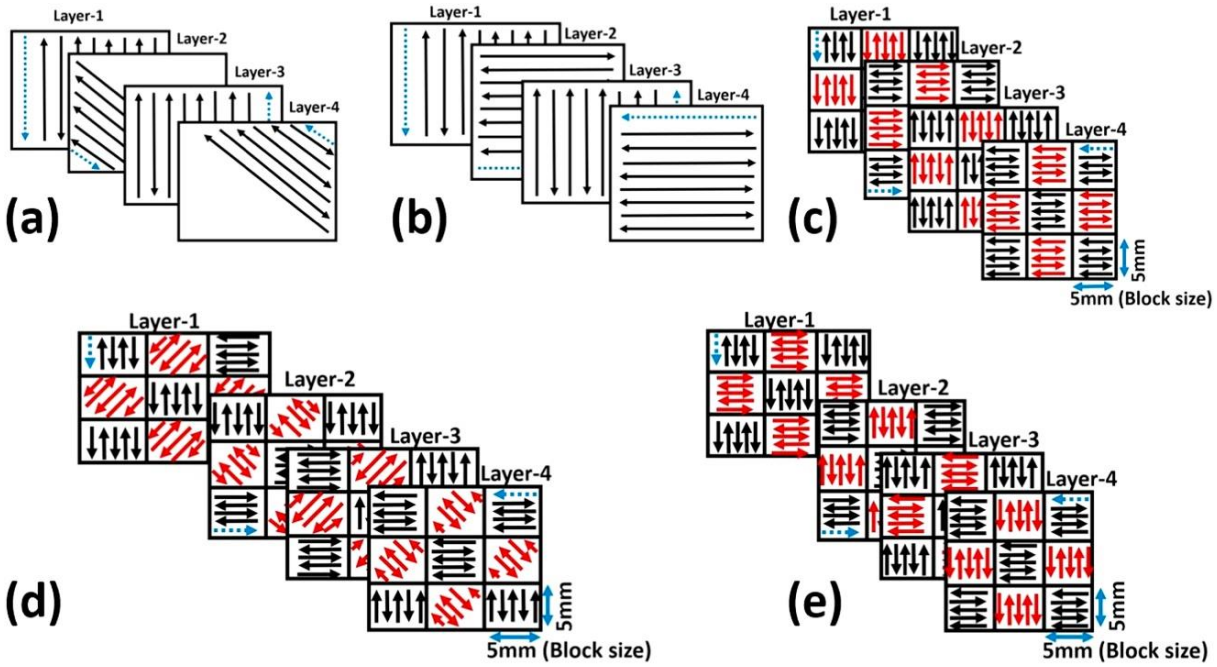

Figure 3-5. Schematics of laser scan strategies: (a) 45° alternating; (b) 90° alternating; (c) chessboard scanning; (d) chessboard scanning with consecutive chessboard block scanned in 45° rotated direction; (e) chessboard scanning with consecutive chessboard block scanned in 90° rotated direction [50].

By varying the laser scanning strategy between layers (Figure 3-5a, b), it is possible to avoid prospective defects during the LPBF process [50]. This approach can be even more efficient when using chessboard scanning strategies (Figure 3-5c, d, e), in which the cross-section to be scanned is segmented in order to have different scanning orientations for each portion. With the resulting smaller scanning lengths, the residual stresses caused during the LPBF process tend to be reduced, and with it defects related to mechanical properties classified as group (4). Although, the appropriate scanning length must be carefully chosen, since extremely short lengths could cause the opposite of the desired effect and increase residual stresses and thermal distortion [51, 52]. Overall, many efforts were deposited in post-processes to overcome the defects caused during the LPBF process.

3.1.3. Overview of LPBF post-processes

Among the defects presented, the inferior surface quality is the obvious and the most visible drawback in LPBF parts, and the focus of the current work. Although classified in different groups in the previous section, the surface roughness can also be linked to initiation of cracks and suboptimal mechanical behavior, more specifically fatigue. The propagation of the cracks, in its turn, is related to the porosity that some parts can present [53].

To some extent, the occurrence of a few defects cited can be reduced or extinguished when appropriate process parameters are adopted. However, even the frequent LPBF parameter optimization is not able to significantly reduce defects such as surface roughness, ductility, corrosion, and wear performance [54]. In response, the LPBF parts are subjected to a series of post-processes of thermal or mechanical nature [4]. Table 3-2 presents a summary of conventional and unconventional post-processes adopted to treat LPBF components, in general and without a particular material specification, with the potential resulting properties after the listed post-processes.

Table 3-2. Potential conventional and unconventional post-processes to treat LPBF components and their respective potential property modification. Extracted data from [54].

Properties → Modification	Potential post-processes
Residual stresses → Reduction	• Heat treatment
Surface roughness → Reduction	• Finish-machining • Barrel finishing • Sandblasting • Grinding • Laser polishing • Magnetic polishing
Surface microhardness → Increase	• Shot peening
Microstructure → Homogenization/Refinement	• Heat treatment
Surface porosity → Reduction	• Shot peening • Laser polishing
Wear depth → Reduction	• Shot peening

The most common post-process to which LPBF parts are submitted is the heat treatment [55, 56] and it can be used for microstructure refinement, reduction of residual stresses; and have a direct impact in properties such as substrate microhardness. The goal of the remaining listed post-processes is to reduce the surface roughness and porosity, increase surface microhardness, and decrease wear depth.

Table 3-3 contains a summary of scientific investigations including the material used, the adopted post-processes, the properties assessed, and the results achieved. The emphasis of most investigations about post-processing of AM parts is the reduction of surface roughness due to the layer-by-layer nature of the technique, which is successfully achieved by methods such as vibratory surface finish, magnetic polishing, plastic media blasting, sandblasting, mechanical polishing, and barrel finishing. It is worth mentioning that the non-conventional laser post-process has a dedicated section with its own literature review later in this chapter.

Table 3-3. Key publications on post-processing techniques of LPBF parts.

Material	Post-process investigated	Properties assessed	Results	Ref.
LPBF Ti64 and Inconel718	Barrel finishing	Surface roughness	Ti64: Ra from 14 µm to below 1 µm with 48 hours of treatment Inconel 718: Ra from 11 µm to 1 µm with 24 hours of treatment	[57]
LPBF AlSi10Mg	Shot Peening	Surface roughness, microhardness, and residual stresses	Surface roughness: Ra from 12 µm to 6 µm Residual stresses: from 7.7 ± 5 MPa to -155 ± 7 MPa Hardness: from 125 HV to 165 HV on the surface	[58]
LPBF Ti64	Heat treatment	Microstructure and tensile behavior	Phase transition from α' to α+β Elongation at break from 5%-10% (above 1100 MPa) to 15%-20% (above 900 MPa)	[56]

Table 3-3. Continued

Material	Post-process investigated	Properties assessed	Results	Ref.
LPBF Ti64	Heat treatment, sandblasting, and mechanical polishing	Microstructure and tensile properties	Phase transition from α' to α+β Elongation at break from 10% (below 1000 MPa) to 20% (above 800 MPa) for sandblasting and mechanical polishing	[59]
LPBF A357.0	Laser shock peening, plastic media blasting, sandblasting, ceramic shot peening, metal shot peening	Surface roughness and fatigue behavior	Surface roughness (Sa): 25.9 µm (as built); 6.1 µm (plastic media blasting); 14.0 µm (sandblasting); 12.8 µm (ceramic shot peening); 9.0 µm and 8.0 µm (metal shot peening S70 and S170); 14.9 µm (laser shock peening) Fatigue behavior (maximum stress level for 2 x 106 cycles): 50 MPa (as-built); 90 MPa (plastic media blasting); 90 MPa (sandblasting); 90 MPa (ceramic shot peening); 70 MPa and 90 MPa (metal shot peening S70 and S170); 70 MPa (laser shock peening)	[60]
LPBF Inconel718	Magnetic polishing	Surface roughness and microhardness	Surface roughness (Rt): from 27.8 µm to 15.5 µm Microhardness: from 32.2 HRC10 to 38.7 HRC10	[61]
LPBF AlSi10Mg	Vibratory surface finish	Surface roughness	Surface roughness (Sa): reduced from 16 µm to 10 µm with 3 hours of VSF	[62]

As established previously, the focus of the current work is the assessment of laser treatments as post-processes of LPBF Ti-6Al-4V parts. From the presented table such material has been heavily investigated due to the vast application possibilities it presents.

3.2. Titanium and its alloys

This section provides an overview of the titanium element covering its crystalline structures and phase transitions. A review of well-known titanium alloys is presented, while characteristics and properties are focused on the Ti-6Al-4V alloy.

3.2.1. Crystalline structures

Titanium is an element that possesses a hexagonal close-packet (hcp) crystal structure (α-phase) at ambient temperature and pressure (ATP). At temperatures of 882 °C the phase transformation to a body-centered cubic (bcc) (β-phase) occurs [63]. A schematic of both crystal structures is disclosed in Figure 3-6.

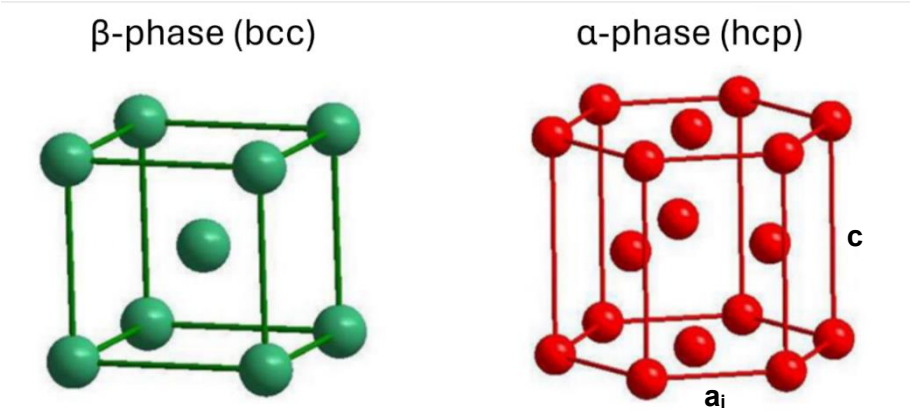

Figure 3-6. Schematic of unit cells related to the titanium α (hcp)-phase and β (bcc)-phase. Adapted from [64].

The α-phase possesses three hexagonal Bravais lattices, each with a two-atom motif. Their lattice parameter a_i has a dimension value of 0.295 nm, while c has a dimension value of 0.468 nm. Considering Figure 3-6, the mentioned hcp lattice parameters refer to the distance between adjacent atoms horizontally (a_i) and vertically (c). It is acknowledged that the optimal c/a ratio for an hcp crystal structure is 1.633, whilst the value obtained for the pure titanium element is 1.587. The β-phase possesses only one lattice parameter with a dimension of 0.332 nm. Finally, titanium is considered a light metal for holding a relative density of 4.51 g/cm^3 [63].

3.2.2. Titanium alloys

Superior mechanical and chemical properties are displayed by titanium parts when their base material is combined with other elements, forming the so-called titanium alloys. The parts resulting from such material present high performance with the shared advantage of reduced costs. Since titanium alloys were established, they have been widely used in several industry sectors such as chemical, medical, construction, energy, and automotive [65]. Different combinations of additional elements result in varied characteristics, which are governed by the content of α- and β-phases within the final material. Generally, the titanium alloys can be divided into 3 categories: (1) α-alloys, (2) (α+β)-alloys and (3) β-alloys. Several examples of titanium alloys and the categories to which they belong are exposed in Table 3-4.

Table 3-4. Titanium alloys and their categories. Extracted data from [66].

Category	Selected materials
α-alloys	Ti-5Al-2.5Sn Ti-3Al-2.5V Ti-2Cu Ti-0.3Mo-0.8Ni
(α+β)-alloys	Ti-6Al-4V Ti-6Al-4V ELI Ti-6Al-4V-2Sn Ti-6Al-2Sn-4Zr-6Mo
β-alloys	Ti-13V-11Cr-3Al Ti-11.5Mo-6Zr-4.5Sn Ti-13V-11Cr-3Al

The α-alloys consist of a single solid solution composed by α-phase, which cannot be modified by means of heat treatments. This implies that the properties displayed by components fabricated with this material can be hardly improved. Nonetheless, they are suitable for applications within the chemical and process engineering fields due to their outstanding corrosion resistance and deformability [66]. One classical example of industrial α-alloy is the Ti-5Al-2.5Sn, which utilizes the aluminum element as the α-phase stabilizer.

The (α+β)-alloys are composed of a solid solution and, differently from the group described before, contemplate the possibility of properties improvement with the adoption of heat treatments. They normally contain between 4 % and 16 % of β-stabilizers, which leads to the stabilization of the bcc crystal structure. These numbers signify a content between 10 % and 20 % of β-phase at room temperature [66]. Usually, transition metals such as vanadium, niobium, tantalum, and molybdenum are used as β-stabilizers once they are within the titanium structure. The manufacturing of such alloys is based on the ability of stabilizer elements to maintain the presence of the β-phase even below the mentioned phase transformation temperature. This means that, once in thermodynamic equilibrium, the presence of particles containing α-phase is observed around the retained β-phase grain boundaries and the final material composition includes both phases.

The most used alloy included in this category is the Ti-6Al-4V, which contains 6 wt. % aluminum (α-stabilizer), and 4 wt. % vanadium (β-stabilizer). The mixture of both phases in one material is a key factor for the wide application opportunities of such alloys, since it benefits from the conjunction of strength and ductility that are compelling characteristics of the α- and β-phases, respectively. Still, these alloys maintain the exceptional corrosion resistance and biocompatibility characteristics of titanium [67].

3.2.3. Phase transition and microstructure of the Ti-6Al-4V alloy

When compared to pure titanium, the phase transition temperatures for the Ti-6Al-4V alloy presents discrepancies due to the substitutional and interstitial elements incorporated into the material's lattice [63].

By means of a Thermo-Calc calculation, isothermal slice plots were generated across the Ti-6Al-4V (Ti64) phase diagrams from the region with lower ratio of aluminum and vanadium towards the area with higher proportion of both elements. Figure 3-7 depicts phase diagrams for two distinct temperatures, 1000 °C and 900 °C, obtained for the assessment of the phase transition in such material between said temperatures. When evaluating the phase of the material subjected to the former, it is possible to observe that the Ti64 positioning point lies within the β-phase region, indicating the sole existence of the mentioned phase at this temperature. By lowering the temperature to 900 °C, the Ti64 positioning point is moved within the (α+β)-phase enclosure. This is a confirmation that, for the Ti64, the transition from β to (α+β) occurs at the temperature within the range from 1000 °C to 900 °C (β-transus temperature), which is in accordance to the value of 995 °C ± 20 °C seen in the literature [68].

Different from pure titanium, when in thermodynamic equilibrium state and ATP, the Ti64 is composed of a combination of α- and β-phase. The type of microstructure observed in the material, though, is dependent on the cooling rates to which it was subjected. Overall, they are divided in grain boundary allotriomorph (α_{GB}), primary or globular (α_p), lamellar or secondary (α_{SEC}), and martensitic structure (α') [63].

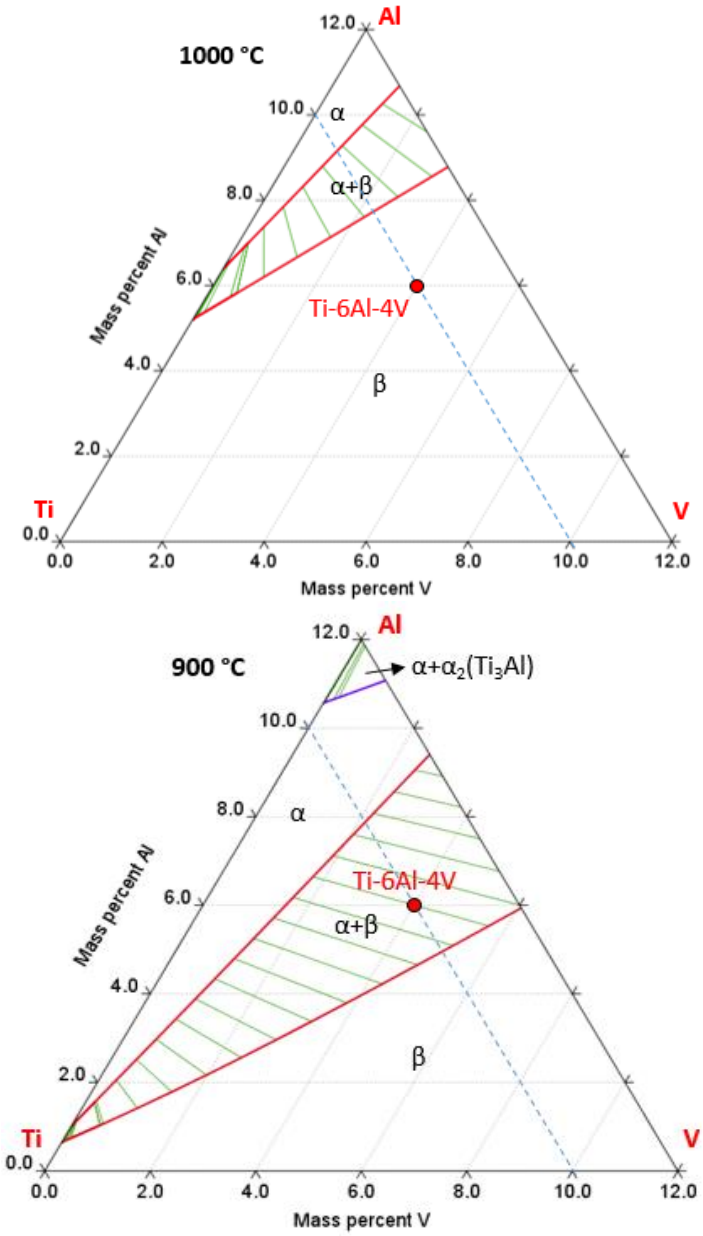

Figure 3-7. Isothermal sections of the ternary Ti-Al-V phase diagram at 1000 °C and 900 °C through the Ti-rich corner. Both plots were generated in Thermo-Calc Software with SSOL6: SGTE Alloy Solutions Database v6.0.

With steady and low cooling rates for the transition from β- to (α+β)-phase, α-layers are constantly developing adjacent to the β-grain boundaries. Moreover, parallel α-plates whose nucleation started in the same β-grain boundary compose an α-colony, and its propagation is interrupted when it encounters distinct α-colonies, i.e., colonies whose nucleation started in other β-grain boundaries. Cooling rates in the range of 10 °C/min are suitable for achieving fully equiaxed microstructures, with the presence of mainly α_p and small amounts of retained β-phase (Figure 3-8a). When higher cooling rates are applied, the α-phase nucleation around the grain boundaries of the retained β-phase increases but that reduces the time for diffusion, which reduces grain size development, thus different morphologies of the α-phase are formed. With 30 °C/min, the formation of the α_{GB} and α_p is clearer (Figure 3-8b). The presence of fine martensitic α' is also observed for the higher cooling rate of 300 °C/min (Figure 3-8c).

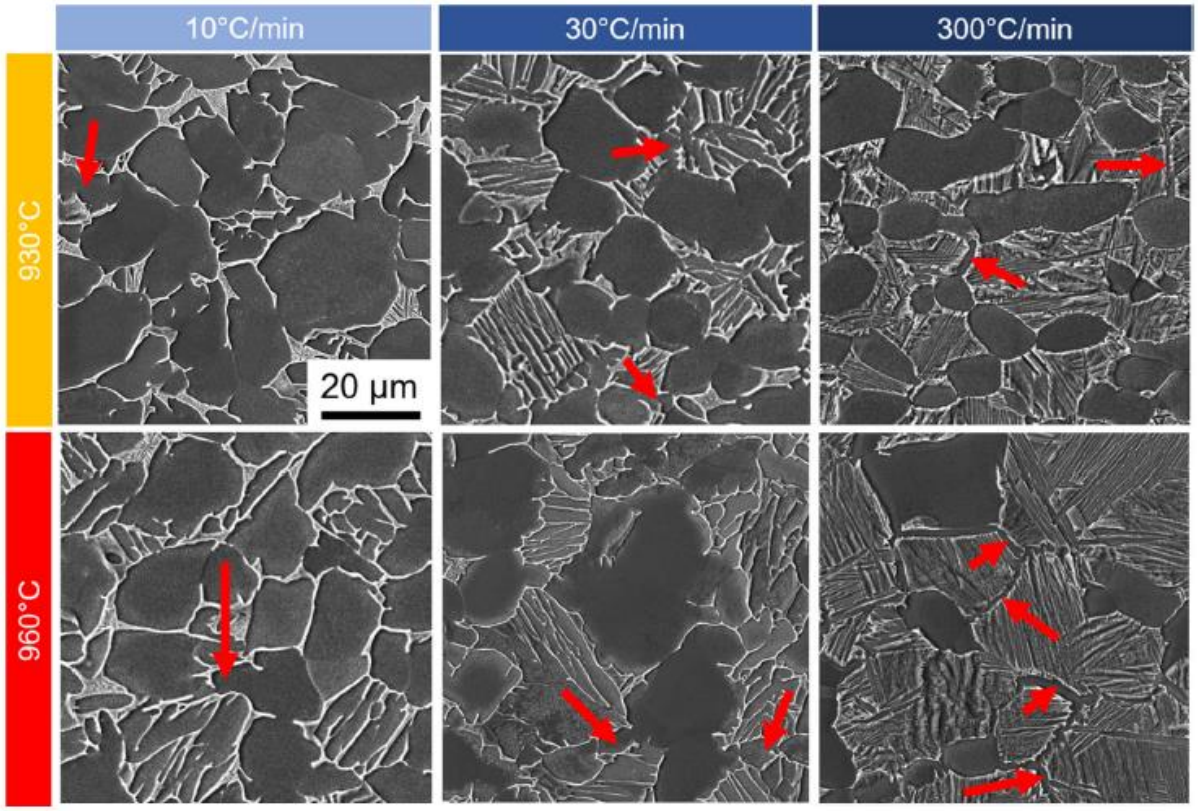

Figure 3-8. SEM images of Ti-6Al-4V after 1 hour at 930 °C and 960 °C and continuous cooling at: 10, 30 and 300 °C/min. The arrows are indicating the α_{GB} [69].

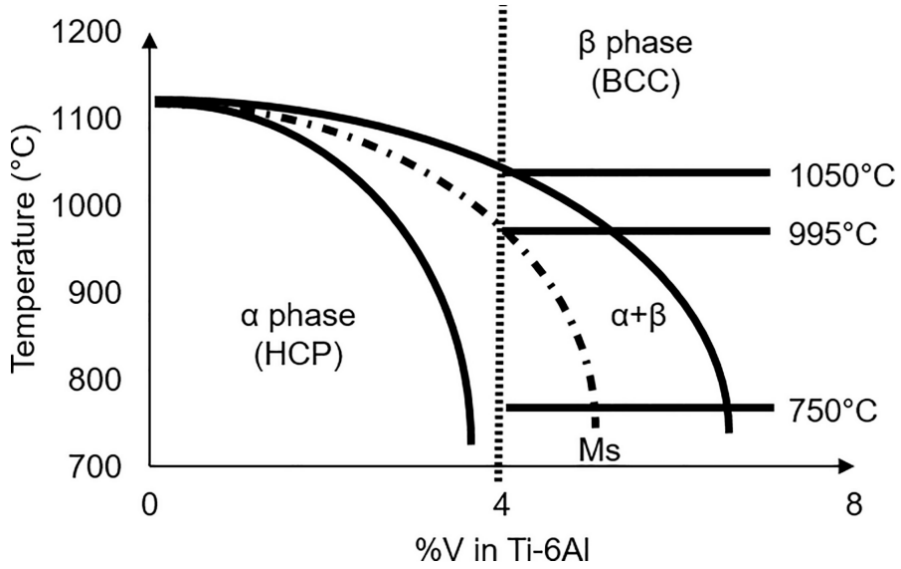

Figure 3-9. Schematic of the temperature composition section for Ti-6Al-4V (wt.%) [70].

Some manufacturing processes and post-processes induce extremely high cooling rates in Ti64 parts, which is the case of the LPBF and laser polishing with comparable cooling rates in the range between $1.2 \cdot 10^4$ K/s and $3 \cdot 10^5$ K/s [71, 72]. When that is the case, martensitic α'-phase develops, with a hexagonal crystal symmetry, comparable to the α-phase [73]. In Figure 3-9, the schematic of isopleth for Ti-6Al-V is presented. As displayed, the temperature to begin

the transition to martensite phase (Ms) drops with higher vanadium contents, which indicates that when subjected to the extremely high cooling rates mentioned above, the microstructure of the Ti64 material will show transition to the hexagonal α'-phase [63]. The deviation between the graphical data shown in Figure 3-7 and Figure 3-9 originates from the former being calculated in a software and the latter being a hand-drawn image with data from the literature. In Figure 3-10, the formation of α' martensite during the LPBF process is displayed. It confirms the effect of the scanning strategies on the microstructure evolution, the nucleation at the previous β-grain boundary and the fact that the mentioned extremely high cooling rates lead to reduced grain growth, resulting in needle-like microstructures.

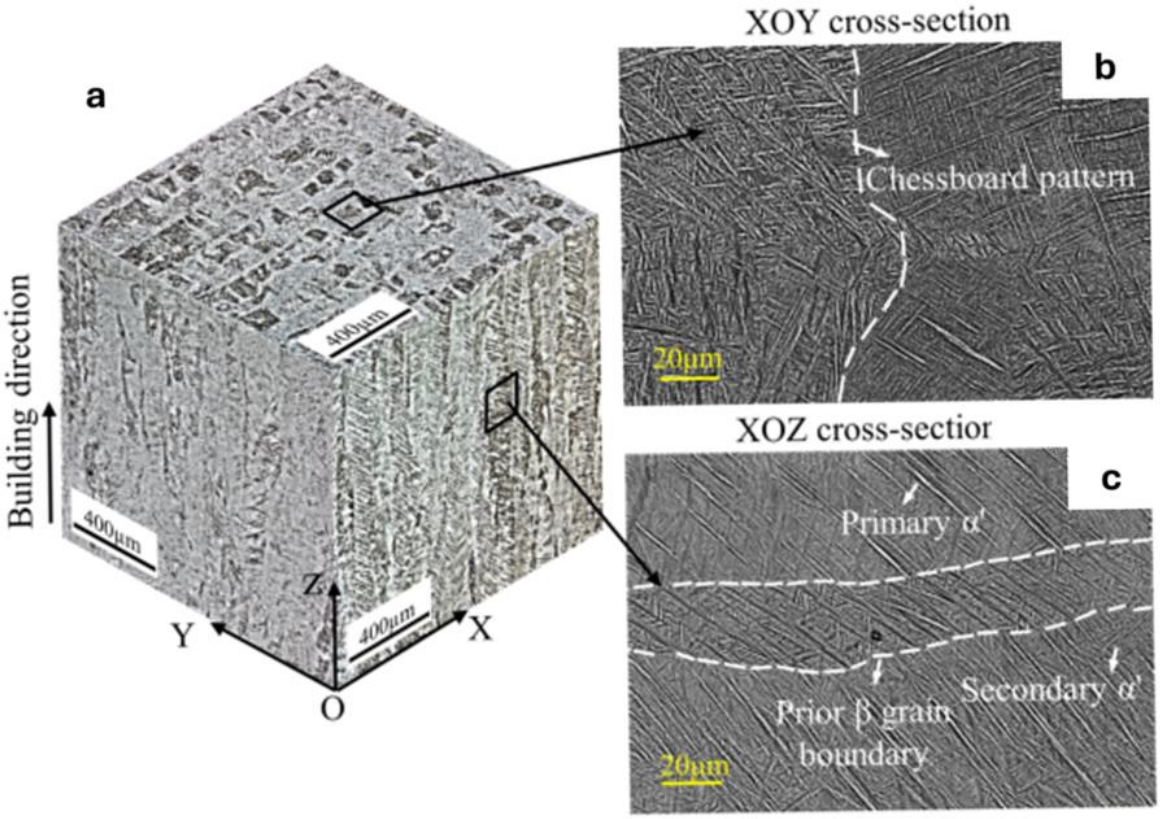

Figure 3-10. Microstructure formed on the top and side surfaces of LPBF Ti-6Al-4V parts. Adapted from [74].

As presented in the previous section, the microstructure and, consequently, the mechanical properties of LPBF parts can be altered considerably when post-processing methods such as heat treatment are applied. Traditionally, heat treatments for microstructural changes of LPBF Ti64 parts include increasing the workpiece temperature above the β-transus and cooling it down in a controlled rate to ensure the proper nucleation and propagation of α-grains, to replace the α' microstructure formed during the additive manufacturing process [75, 55]. With the increased adoption of the LPBF process in industrial applications, the need has arisen for the investigation of alternative heat treatments and their implications in the microstructure and mechanical properties [75]. Studies dedicated to this assessment were developed in the past, and a comparison of heat treatments with different temperatures, holding times, and cooling approaches are presented in Table 3-5.

Table 3-5. Resulting mechanical properties reached via heat treatments of LPBF Ti-6Al-4V parts. Extracted data from [76].

Heat treatment Nr.	Temperature (°C)	Time (h)	Cooling approach	E (GPa)	σ_y (MPa)	UTS (MPa)	$\varepsilon_{fracture}$ (%)
1	750	2	Air flux	113.7 ± 6.7	1060.5 ± 18.7	1121.9 ± 18.35	12.7 ± 3.8
2	800	2	Air flux	111.8 ± 2.1	1075.4 ± 8.2	1139.4 ± 6.7	16.8 ± 0.4
3	835	2	Air flux	110.8 ± 1.1	1025 ± 4.5	1107.5 ± 1.4	19.4 ± 1.8
4	870	2	Air flux	114.8 ± 2.3	1010.8 ± 7.6	1095.2 ± 12.7	16.6 ± 1.4
5	955 → 500	1.5 → 8	Water quenching → Air flux	116.5 ± 1.3	1067.3 ± 11.3	1195.9 ± 5.3	11.3 ± 0.9

The heat treatment 1, which uses temperatures below the β-transus showed a more brittle behavior, with extensional strain prior to fracture significantly lower when compared to other treatments. This characteristic resembles the properties in the presence of the α'-phase, thus these heat treatments must be carefully assessed according to the application considered. Differently, results comparable to the traditional processes can be obtained with heat treatments 2, 3, and 4, which apply temperatures close enough to the β-transus and holding times long enough to allow the amount of transition to the β-phase necessary to achieve the desired properties. The mechanical properties achieved with the 3 heat treatments mentioned presented similar characteristics of yield stress, σ, ultimate tensile strength (UTS), Young's modulus, E, and extensional strain, ε. Another important factor would be the selected cooling approach, which in its turn should ensure the nucleation of the α-phase within the β-phase grain boundaries. Despite using temperatures above β-transus, heat treatment 5 presented a brittle behavior similar to heat treatment 1 because water quenching cooling was adopted.

For all heat treatments discussed, what will dictate the parameters chosen for the microstructure modification and stress relief process of the LPBF Ti64 samples are the properties desired, according to the component's application.

3.3. Laser materials processing

Currently, the adoption of laser sources in the materials processing field, especially in the manufacturing sector, has played a significant role. Such technique provides extreme versatility, since the same laser can be used for different applications, which, combined with advantages in high productivity, automation suitability, contactless processing, improved product quality, and greater material utilization, represents a very cost-effective factor for any industry [77, 78].

In terms of metallurgical applications, laser materials processing can be divided according to their purposes: (1) plastic deformation of parts (forming), (2) joining parts and/or materials (welding, brazing, etc.), (3) removing material (cutting, drilling, etc.), and (4) surface modifications. As mentioned, one laser source can be used in varied applications, which is defined by the set of parameters used. The potential application as a function of power intensity and interaction time is shown in Table 3-6. The laser intensity is defined by laser power and

laser beam diameter, while the interaction time can be related to the pulse duration for pulsed lasers or a function of the processing time for continuous wave (cw) lasers [77].

Operations that require material removal are achieved with a combination of high intensity and short interaction time, while surface treatments require low intensity and long interaction time. Operations based on material melting are achieved in the intermediate zone of intensity and interaction time. The combination of intensity and interaction time is defined according to the degree of heating and phase transition required for the material adopted in each case.

Table 3-6. Different laser material processing for different laser intensity and pulse duration ranges. Extracted data from [77].

Power density range	Processing mechanism	Laser interaction time (s)			
		Up to 10^{-6}	$10^{-6} < t < 10^{-4}$	$10^{-4} < t < 10^{-2}$	$10^{-2} < t < 10^{0}$
Up to 10^4 (W/mm²)	Heating	-Paint stripping -Magnetic domain control -Bending	-Transformation hardening -Semiconductor annealing	-LCVD -Coloring	Stereolithography
	Melting			-Cladding -Melting -Welding	-Brazing -Reclamation
	Vaporization				-Cleaning -Engraving
Above 10^4 (W/mm²)	Heating				
	Melting	-Glazing -Surface amorphization	Alloying		
	Vaporization	-Drilling -Shock hardening	Cutting	Marking	

The focus of the present work is the group (4) in the classification of laser materials processing, which concerns surface modifications by means of laser irradiation. Investigations in this line are further classified as surface engineering, since it comprises the surface properties, such as composition, and/or characteristics, such as microstructure, of the region closest to the surface of a workpiece without affecting the bulk material [77]. Two classifications of different laser materials processes within the surface engineering field are presented in Table 3-7.

Table 3-7. General classification of laser surface engineering. Extracted data from [77].

Laser surface engineering	
Exclusively microstructural modification	**Microstructure and composition modifications**
• Hardening • Melting • Shocking • Texturing	• Alloying • Cladding • Remelting • Deposition

The first category includes processes that aim at modifying the topographies and/or surface microstructures, without any change in composition, while the second includes the modification of both microstructure and chemical compositional on the surface of the parts.

In this work, a cw laser was employed for the surface modification of LPBF Ti-6Al-4V parts by melting, while an ultrashort pulse laser was adopted for the surface texturing of the same material. The former process is defined as laser polishing, and the latter as laser surface functionalization. The following sections describe the basics of both processes, together with a review of the recent literature.

3.3.1. Principles of the laser polishing process

When compared to traditional surface quality improvement techniques, laser polishing has been under emphasis in the past years. The process consists of melting material on the outer regions of the workpiece, which are redistributed evenly due to capillary motion. The result is a part with reduced roughness without matter elimination [79]. Assessments of laser polishing in contrast to conventional processes have been addressed in the literature. Among the benefits reported are short operation time, treatment of localized regions, reduced residual stresses because of the contactless nature of the method, no material scraps and residues, and no adhesion of components from the grinding and polishing processes [23, 27, 80, 81, 82, 83]. For better illustrating the physics throughout the cw LP procedure, Figure 3-11 depicts a Ti64 workpiece whose surface is subjected to the mentioned process, in a simplified graphical representation.

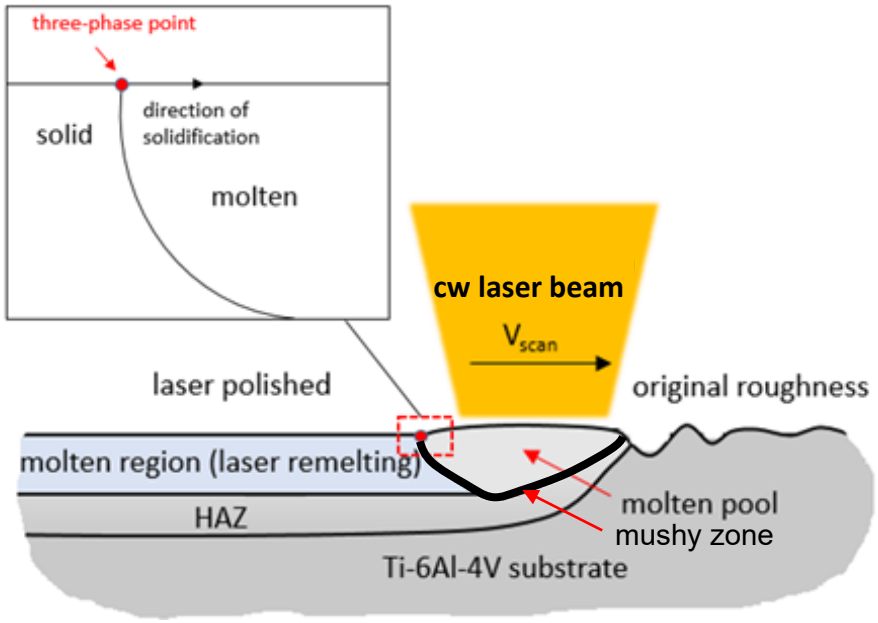

Figure 3-11. Schematic of the polishing process on the surface of the additively manufactured Ti-6Al-4V part using the cw laser beam. Adapted from [84].

The cw laser irradiation, besides melting the surface of the workpiece, generates a heat affected zone (HAZ) between the molten layer and the bulk material, and a mushy zone that represents mutual existence of the material in the liquid and solid states. The solidification occurs progressively, as the laser beam is moved away from the molten material in accordance with the adopted scanning speed (V_{scan}). In addition to the quantity of metal in the liquid phase during the laser scanning, the resulting topographies are highly affected by the motion of the

three-phase point, which represents the interface between solid and liquid phases of the Ti64, and the environment during the LP process. The dimension of the molten pool is highly linked to the laser power and spot size. Consequently, the HAZ depth is also governed by the association between the two mentioned and the additional LP process parameters [85].

Figure 3-12 depicts that the Gaussian laser beam waist, w_0, occurs in the focus position and the beam diameter increases until $\sqrt{2}w_0$ when it is defocused by using a focal position value that is the same as the Rayleigh length, z_R. The variable w_0 is a function of z_R and the laser wavelength, λ, and is calculated by the Equation (1) [86]:

$$w_0 = \sqrt{\frac{z_R \lambda}{\pi}} \tag{1}$$

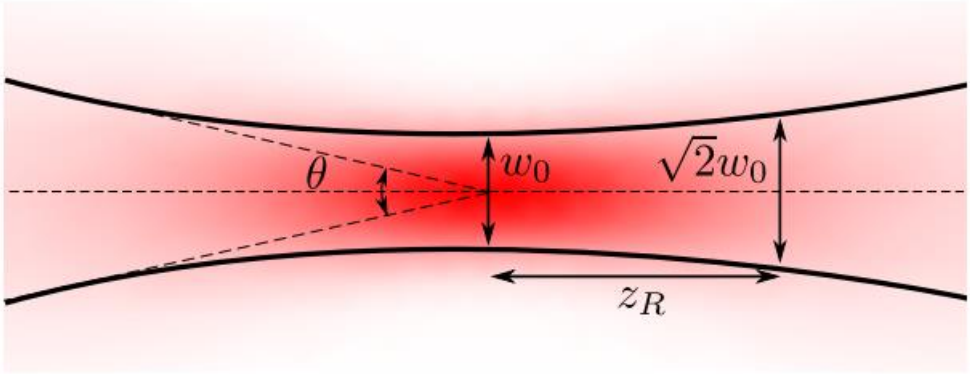

Figure 3-12. Schematic view of Gaussian laser beam radius variation [87].

Besides the governing parameters cited above, laser processing efficiency is highly dependable on material properties such as absorptivity, thermal conductivity, and specific heat. Among them, the absorptivity dictates the laser/material interaction by affecting the amount of energy absorbed by the workpiece [78]. The absorption itself depends on features such as, the temperature, laser wavelength, polarization, incident direction, and surface conditions [88, 89]. Amongst the surface conditions, the surface roughness plays a major role in the amount of absorbed laser energy, since different surface textures influence the material reflectivity [21, 90, 91, 92, 93, 94]. The properties of the material used in this work are presented and further discussed in Chapter 4.

In Table 3-8, relevant research on laser polishing of metallic materials is summarized. From it, it is evident that several metallic materials were the focus of laser polishing investigations throughout the years. The quantified results of surfaces roughness reduction show that different outcomes can be achieved with the laser polishing technique and confirm the need of combining its process parameters development with a thorough analysis of other features and properties affected by laser polishing. The most common assessment was the resulting surface morphology, present on 86% of the reviewed literature, followed by microstructural analysis present on 50% of them. Slightly less common but imperative from an application perspective, are the assessment of mechanical properties such as hardness, wettability, fatigue, tribology, and tensile strength, which are in most cases complementary to the assessment of features such as heat affected zones, porosity, surface chemical composition, biocompatibility, and corrosion resistance.

Table 3-8. Key publications on laser polishing of metals.

Material	Roughness pre/post	Properties investigated	Ref.
H13 steel	Sa 1.35/0.23	Single-track morphology	[95]
SKD61 tool steel	Sa 0.28/0.15	Morphology, strain, hardness, microstructure, tribology, and HAZ	[96]
Ti grade 2	Ra 0.58/0.42	Morphology	[23]
LMD 316L	Sa 14.0/5.39	Morphology, and surface chemical composition	[91]
LPBF CoCr	Sa 5.0/0.4	Only Sa was investigated	[97]
LPBF Ti64	Ra 10.2/2.1	Morphology, wettability, porosity, hardness, tensile properties, and cell growth	[98]
LPBF CoCr	Sa 5.0/0.45	Morphology, corrosion resistance, and microstructure	[26]
LPBF Ti64	Ra 10.2/2.45	Morphology, HAZ model, and hardness	[99]
LPBF Maraging steel	Ra 6.4/0.7	Morphology, oxidation, and wettability	[100]
LPBF Inconel 718	Ra 7.5/0.1	Morphology, microstructure, hardness, and tribology	[101]
LAM TC4	Sa 5.23/0.37	Morphology microstructure, and hardness	[27]
LAM TC11	Sa 7.21/0.73	Morphology microstructure, and hardness	[27]
LPBF Inconel 718	Sa 10.0/0.1	Porosity, and microstructure	[102]
LPBF Ti64	Ra 14.23/6.01	Morphology, fatigue behaviour, and microstructure	[103]

The laser polishing with cw laser is considered a process in the macro-scale, since it is not unusual that the effects of such treatment are observed in depths beyond 100 μm, while pulsed laser radiation is generally applied in micro-scale processes, since their effects rarely surpass 5 μm in depth [84].

3.3.2. Laser surface functionalization

As mentioned, a great diversity of energy sources and parameters are available to perform the laser materials processing technique. The nature of the resulting manufacturing method is linked to the laser intensity and laser/material interaction time. Pulsed lasers present smaller interaction times when compared to cw lasers, and they can vary from the milli- to the femtosecond range. This interaction time is known as pulse duration (τ). Another characteristic of the pulsed laser is the peak power achieved, being the highest values obtained with the smallest pulse duration [104]. The intense peak power makes the pulsed laser appropriate not only for processes that required material removal, such as drilling and cutting, but also for surface modification [30, 105, 106, 107]. Figure 3-13 shows a comparative schematic of the drilling process with a long pulse laser and an ultrafast laser, respectively. It is possible to observe that long pulses can generate micro cracks, surface debris, and recast layers, while

the ultrashort laser pulses remove material without passing through the liquid phase, thus no debris or recast layers are generated. Furthermore, the laser materials processing with ultrashort laser pulses is referred to as “cold ablation” process [108], thus it is less probable that the material surrounding the processed area will be affected by micro cracks or heat impact.

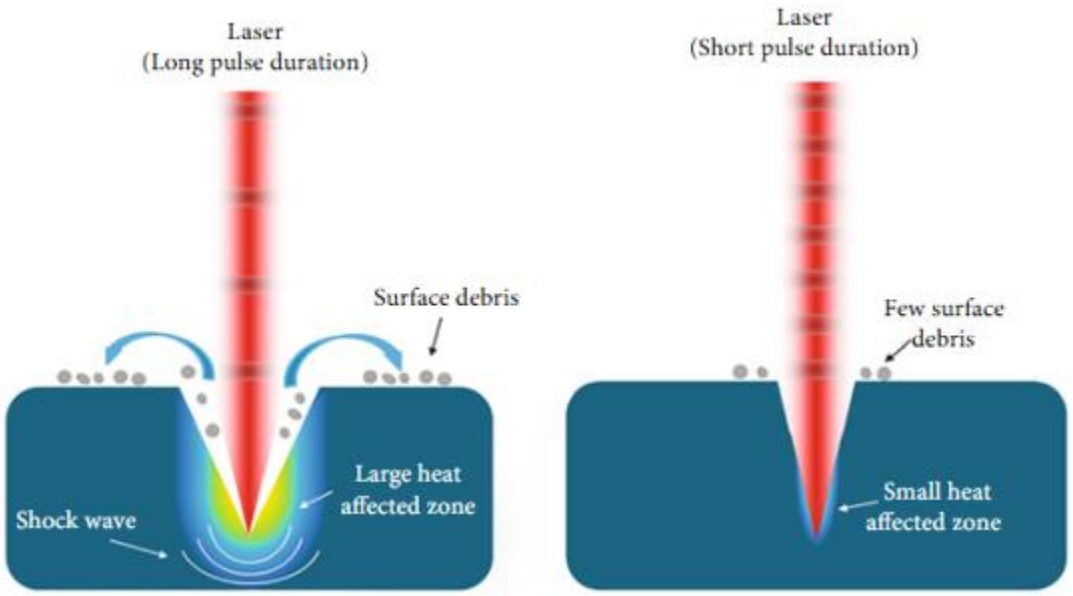

(a) (b)

Figure 3-13. Laser drilling schematic for: (a) long pulse laser beam; and (b) ultrashort laser pulses [109].

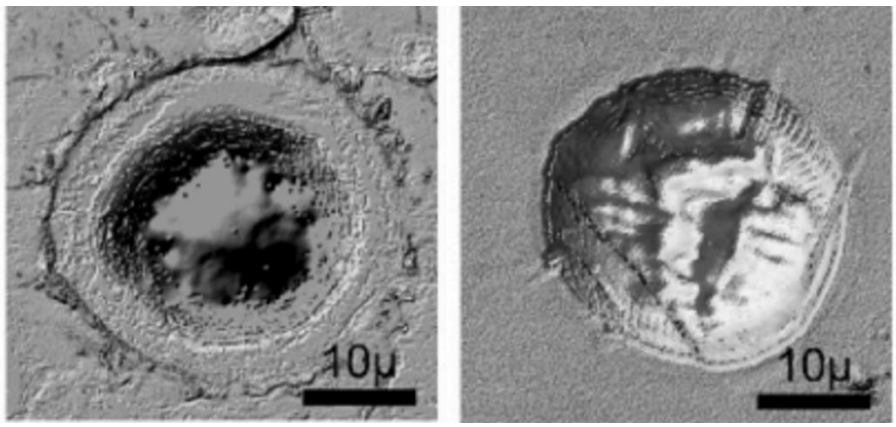

(a) (b)

Figure 3-14. Laser ablation performance with: (a) nanosecond laser; and (b) femtosecond laser [110].

Figure 3-14 shows the drilling performances using laser with different pulse durations. When comparing the hole obtained with nanosecond and femtosecond laser pulses, the former presents dimensional distortion, recast layers, and surface debris near the edges of the walls, while the former presents a much better surface quality, with sharp edges and no distortions. In the structuring, the presence of molten material, together with debris and recast on the surrounding surfaces, is evidenced with pulse lengths in the nanosecond regime, while almost pure sublimation occurs by using the femtosecond laser radiation. Even though the goal of the present research is not to perform machining operations with ultrafast laser radiation, the

selection of such approach for the investigation of the surface functionalization of LPBF Ti-6Al-4V parts are justified by the established superior performances in material removal process.

Previous works have established that by processing materials with an ultrafast laser, 3 types of structures can be achieved: (1) laser induced periodic surface structures (LIPSS), also known as nano-ripples, (2) nano pillars, and (3) columnar structures. Each of these structure types are presented in Figure 3-15.

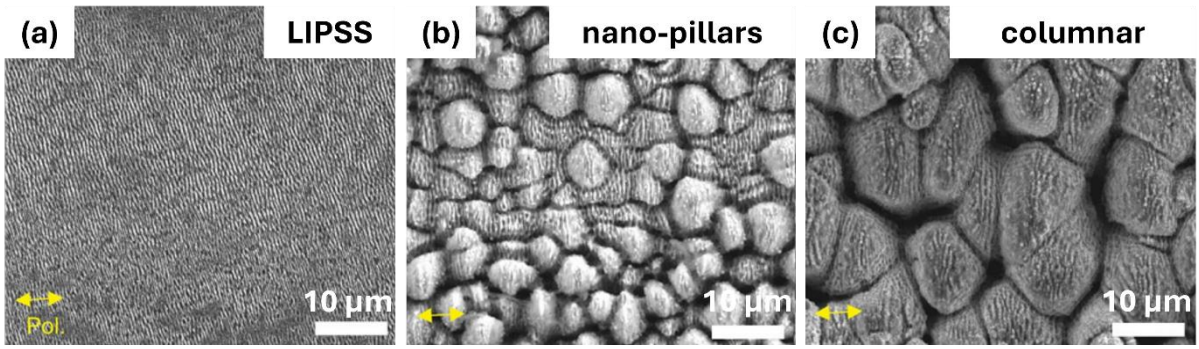

Figure 3-15. SEM micrographs of Ti-6Al-4V surface structures obtained by ultrafast laser processing: (a) nano-ripples; (b) nano-pillars; and (c) columnar structures. Adapted from [111].

Considering the same initial surface condition, the nano-ripples are formed when the material ablation threshold (around 0.1 J/cm^2 for Ti64) is slightly surpassed by the laser exposed to the workpiece, for that a fluence of 0.3 J/cm^2 and scanning speed of 0.2 mm/s were applied. The nano-pillars are obtained when applying the same parameters as for the LIPSS formation and increasing the number of repetitions, and the columnar structures are formed with higher laser energy density (0.6 J/cm^2) and low scanning speed (0.1 mm/s) [32].

The properties that the different structures obtained with femtosecond laser treatment display, in a variety of material types, have been intensively investigated in previous research. Table 3-9 presents relevant research on ultrafast laser structuring and functionalization of distinct metallic materials.

Table 3-9. Key publications on ultrafast laser structuring and functionalization of materials.

Material	Parameters investigated	Surface structure	Properties investigated	Ref.
Ti64	Scanning speed, number of repetitions, and polarization	Groove patterns with nano-ripples structures	Surface morphology, wettability, and cell culture	[31]
Titanium	Energy density, and number of pulses	Nano-ripples, nano-pillars, and columnar structures	Surface morphology	[112]
Stainless steel	Energy density, and number of pulses	Nano-ripples, and columnar structures	Surface morphology, and wettability	[113]
Grade 2 titanium alloy	Energy density, scanning speed, lateral displacement, linear polarization, and number of pulses	Nano-ripples and nano-pillars	Surface morphology, wettability, and bacterial adhesion	[114]

Table 3-9. Continued

Material	Parameters investigated	Surface structure	Properties investigated	Ref.
100Cr6 steel	Peak fluence and number of pulses	Nano-ripples, nano-pillars, and columnar structures	Surface morphology and tribological performance,	[115]
40CrMnMoS8-6 steel	Processing atmosphere	Nano-pillars	Surface morphology, wettability, and corrosion properties	[116]
304 stainless steel	Peak fluence and number of pulses	Nano-pillars and columnar structures	Surface morphology and wettability	[117]
Grade 2 titanium alloy	Peak fluence and number of pulses	Nano-pillars and columnar structures	Surface morphology and wettability	[117]
316L stainless steel	Fluence , scanning speed and number of pulses	Nano-pillars and columnar structures	Surface morphology and wettability	[118]
100Cr6 steel	Number of pulses	Nano-ripples, nano-pillars and columnar structures	Surface morphology and ablation volume	[119]
LPBF Ti64	Scanning speed	Nano-ripples and columnar structures	Surface morphology, chemical composition, and wettability	[120]

Similarly to the laser polishing technique, several metallic materials have been the focus of laser structuring and functionalization investigations throughout the years. In all cases in the literature reviewed, the focus was on the surface patterns and structures obtained, i.e., morphology was the main outcome to be evaluated qualitatively. Different surface structures result in different functionalities, for this reason, in addition to the surface morphology, investigations also include the assessment of surface properties such as wettability, toxicity, corrosion resistance, and tribological performance. Different combinations of process parameters result in varied surface structures, such as nano-ripples, nano-pillars, columnar structures, and groove patterns, which cause the modification of surface properties. This shows that different outcomes can be achieved with the laser structuring and functionalization technique and confirm the need of selecting the appropriate process parameters and combine them with a thorough analysis of other features and properties these altered structures affect.

Although the volume of research dedicated to the surface treatment with ultrafast laser is vast, little attention has been given to employing this approach in AM metallic surfaces. A combination of advanced manufacturing techniques, surface polishing with cw laser and functionalization with ultrafast laser, has been developed in this work as a novel two-step laser post-processing of AM Ti-6Al-4V parts. In Chapter 6, the content of the revised literature is addressed and compared with the results obtained in this research.

4. Samples and methods

This chapter provides a description of the samples used in the development of this research, as well as the laser post-processes to which they had been submitted, which include laser polishing and laser surface functionalization. It also provides an overview of the modelling and optimization techniques implemented together with a thorough report of the specific conditions and considerations for the development of this research. Finally, the analytical methods performed for the assessment of the surface morphology, topography, chemical composition, wettability, microstructural phases, mechanical properties, and surface toxicity are comprehensively presented.

4.1. Samples

All workpieces discussed in this work were produced through LPBF, with rectangular shape measuring 55 x 15 x 4 mm^3, using material Ti64 as material. The region of interest for the laser post-processing of the parts is the side surface, which presents the higher surface roughness due to its vertical orientation. Throughout all experiments, the workpieces were assessed under three different states: as-built, heat treated, and sandblasted. One part in each state mentioned is illustrated in Figure 4-1.

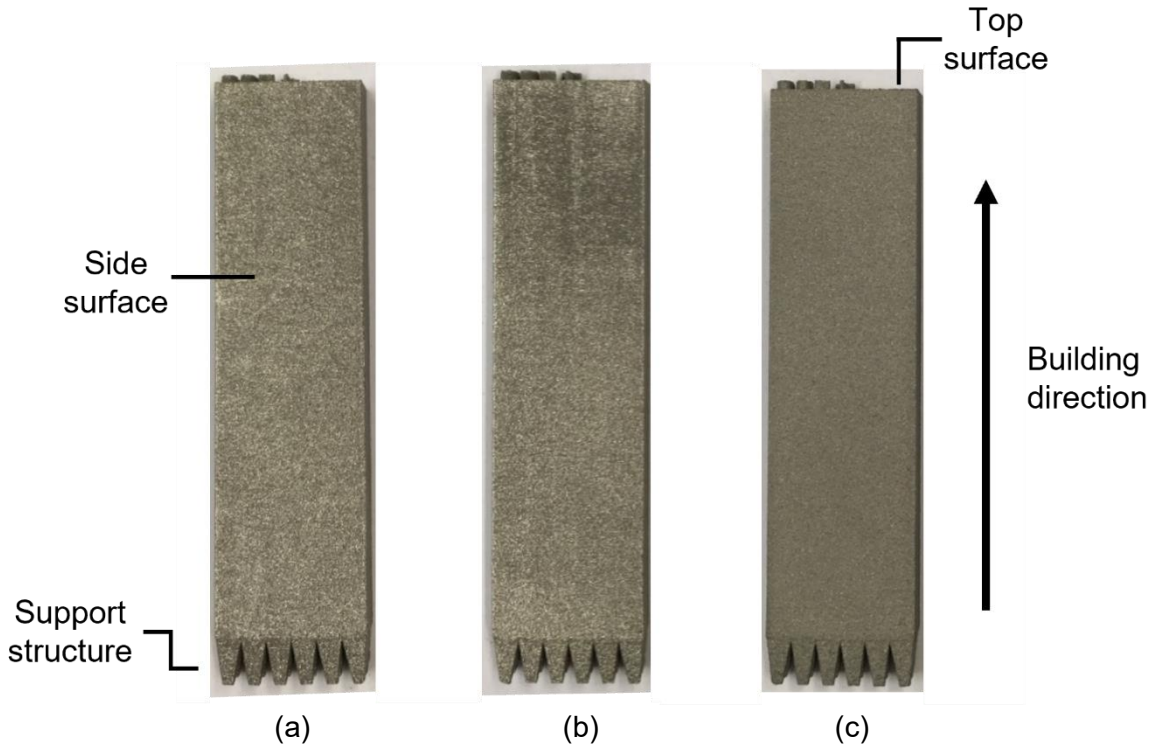

Figure 4-1. Ti-6Al-4V samples after: (a) additive manufacturing, (b) additive manufacturing and heat treatment, and (c) additive manufacturing, heat treatment, and sand blasting. Adapted from [121].

4.1.1. Additive manufacturing

The manufacturing of the test samples was performed at 3D Systems Leuven (Belgium), in a DMP Flex 350 machine, which is equipped with a cw fiber laser that achieves maximum power

of 450 W. It provides high repeatability and maintains the quality of the powder by means of a building chamber with O_2 level ≤ 25 ppm. In the 3DXpert software, developed by 3D Systems, it is possible to position the sample in the building plate as desired, taking into consideration information regarding the recoater movement and gas flow direction (Figure 4-2). With a build volume of 275 x 275 x 420 mm^3, several of the samples used in this work can be produced in a single batch, which minimizes the number of printing jobs required.

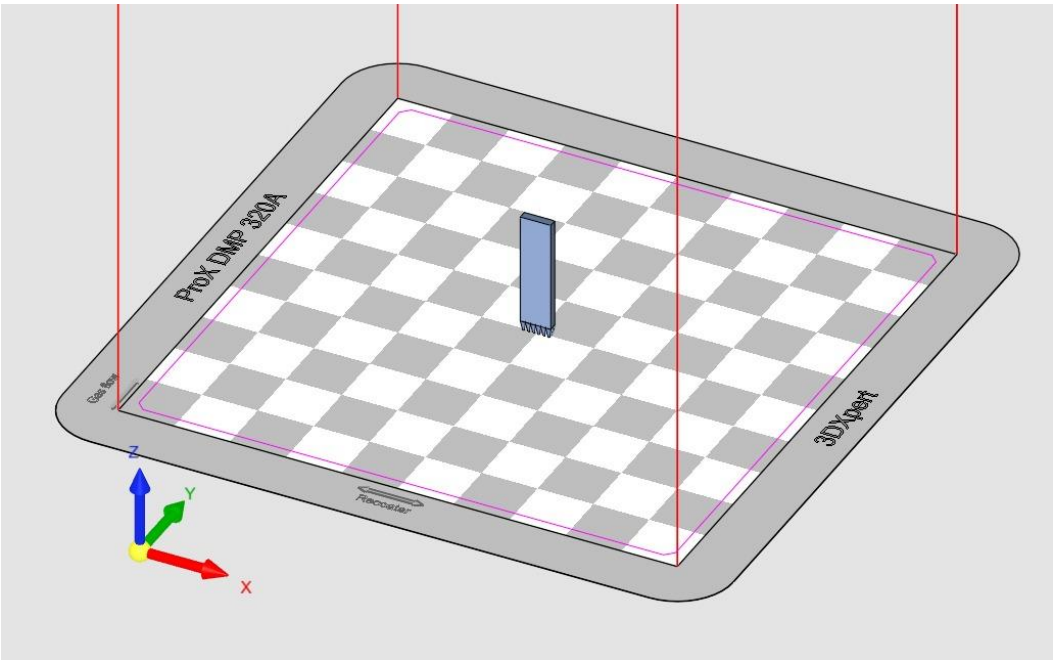

Figure 4-2. Building plate and sample schematic from 3DXpert software.

All samples were built with a layer thickness of 60 µm. The remaining governing parameters such as laser power, scanning speed, and hatching distance were also kept constant for the printing of all samples. Their specific values cannot be disclosed since they are commercial process parameters and propriety of 3D Systems. Following the manufacturing process, several samples were submitted to heat treatment for microstructure refinement and stress relief.

4.1.2. Chemical composition

The chemical composition analysis consisted of digesting the samples with acid in an ultrasonic bath. The element contents were determined with inductively coupled plasma – optical emission spectroscopy (ICP-OES). The carbon content was obtained by using a carbon and sulfur analyzer, while the presence of oxygen and nitrogen was quantified via carrier gas hot extraction (CGHE). The resultant ratio in wt.% per type of chemical element that composes the workpiece is summarized in Table 4-1.

Table 4-1. Chemical composition (wt.%) of the Ti-6Al-4V blocks produced by L-PBF. Adapted from [122] with the permission of the Laser Institute of America.

	Ti	Al	V	C	N	O
wt.%	87.57	6.42	3.972	0.0145	0.001	0.101
Standard deviation	0.08	0.04	0.004	0.0004	0.0001	0.002

4.1.3. Heat treatment

Some samples have undergone the standard stress release heat treatment provided by 3D Systems. Like the LPBF process, the specific parameters cannot be disclosed, although the temperatures and times of standard heat treatments for Ti-6Al-4V samples are extensively presented in section 3.2.3. Following the heat treatment process, some samples were submitted to sandblasting for surface quality improvement.

4.1.4. Sandblasting

Following the heat treatment, several samples were submitted to sandblasting. The sandblasting was performed manually in the material supplier facilities by trained personnel, in a Peenmatic micro 750 S machine. The adopted pressure for Ti-6Al-4V was kept constant at 5 bars, while the blasting medium was spherical ceramic beads based on zirconium dioxide (ZrO_2) with diameter below 1.2 mm.

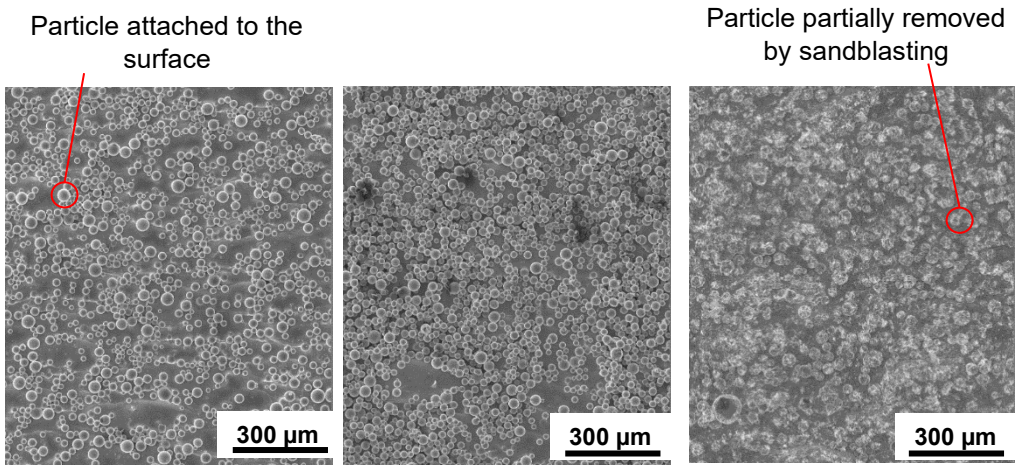

Figure 4-3. SEM image of the side surface of the samples after: (a) additive manufacturing (adapted from [122] with the permission of the Laser Institute of America), (b) heat treatment, and (c) sandblasting.

The surfaces of the samples in the three initial conditions are presented in Figure 4-3. The AM surface reveals a high number of particles attached to the part. The same is true for the heat-treated parts, while the samples submitted to sand blasting expose an overall successful removal of the powder particles from the part's surface.

4.2. Laser systems

In this work, the Ti-6Al-4V samples were submitted to two types of laser post-processing in different steps of the manufacturing workflow (Figure 4-4). The laser polishing with cw laser had the goal to increase the surface quality of the AM parts by reducing their initial roughness, while the surface functionalization with fs-laser aimed in providing the surfaces with different capabilities. A combination of laser polishing and functionalization was investigated during this work as a novel two-step laser post-processing of AM metallic parts for increased possibilities of functional properties, surface design, and production efficiency.

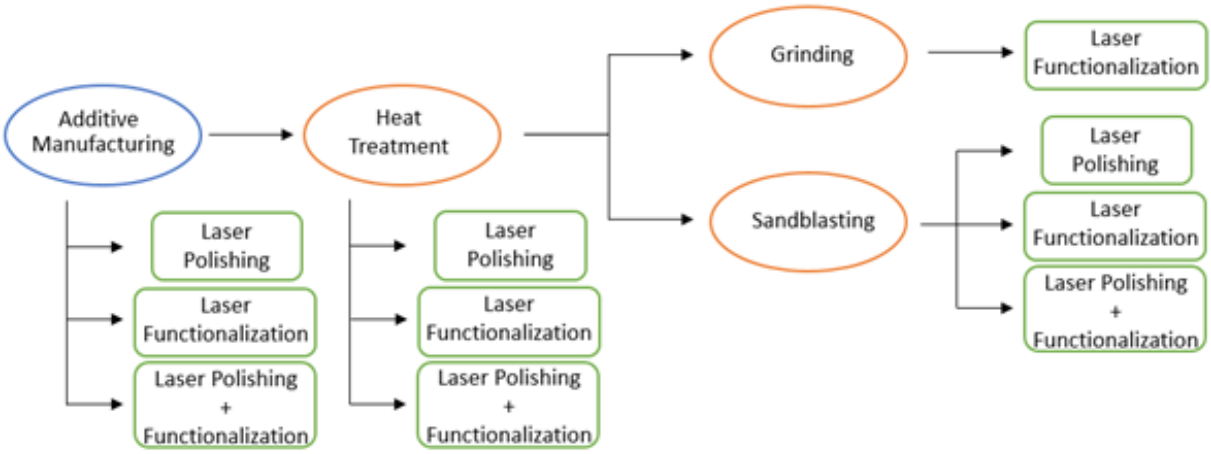

Figure 4-4. Schematic view of the different post-processing steps assessed during this work [123].

4.2.1. Laser polishing

The present investigation utilized the 5-axis TruLaser Cell 3010 hardware. The machine is equipped with a TruDisk 3001 laser system from TRUMPF GmbH with a set wavelength of 1064 nm, and BEO D70 lenses that possess 150 mm of focal length. The laser active medium was a Yb:YAG crystal disk. After collimation the diameter of the laser beam (d_{fc}) is 33 mm [124].

Based on the focal length f and the beam diameter d_{fc} after the collimation it is possible to calculate the beam divergence ϑ using Equation (2):

$$tan\frac{\vartheta}{2} = \frac{d_{fc}}{2f} \tag{2}$$

The value obtained for $\frac{\vartheta}{2}$ was 6.277 degrees. The "FOP" represents the focal position of the laser beam, when in focus the diameter d_0 is 0.1 mm [124]. A schematic image of the relation between the focal position and the beam diameter is presented in Figure 4-5a. The features and values described allow the calculation of the laser beam diameter as a function of the focal position FOP_i using Equation (3). The values obtained for different focal positions and adopted in this work are presented in Table 4-2.

$$d_i = d_0 + 2FOP_i\, tan\frac{\vartheta}{2} \tag{3}$$

Table 4-2. Laser beam diameter as a function of the focal position.

Focal position (mm)	0	+1	+2	+3	+4
Laser beam diameter (µm)	100	320	540	760	980

The laser scanning functions with a back and forth swinging motion. Figure 4-5b depicts a schematic of the swinging behavior, with the laser path in the 'x' axis and the laser feed rate in the 'y' axis. In this work, the sinusoidal laser beam oscillation ran at frequencies of 50 Hz and 100 Hz.

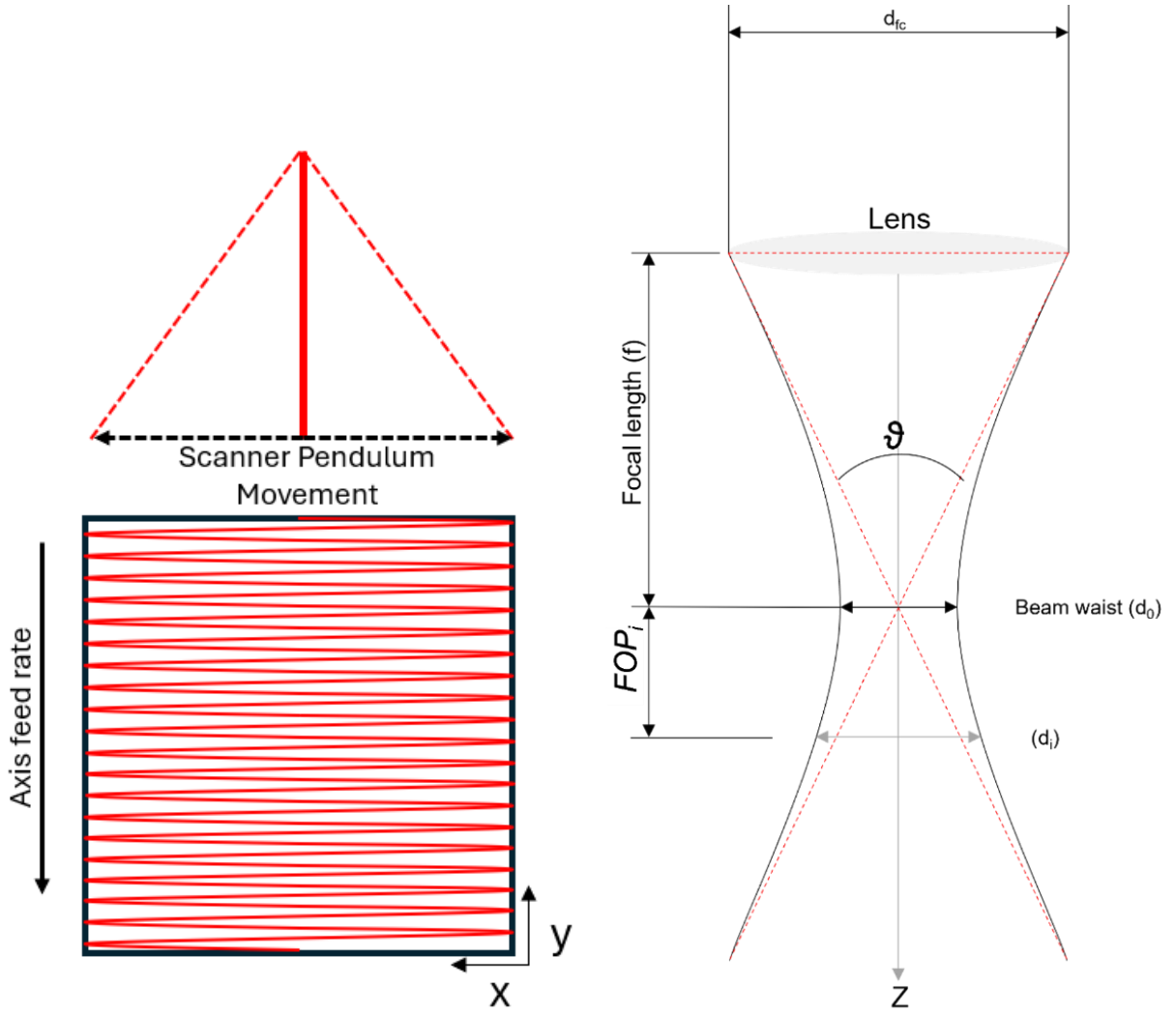

Figure 4-5. Laser polishing setup: (a) schematic view of the laser scanning strategy applied for laser polishing, and (b) schematic of the focal position FOP_i of the respective beam diameter. Adapted from [121].

Throughout the procedure, whenever a change in the trajectory of the laser beam is necessary, the mirror's motion shall be slowed down while still in the path being scanned and then hastened into the opposite direction. For this reason, the laser irradiates certain points of the workpiece for a longer time, specifically the points that are within the region where it is changing its scanning direction [125].

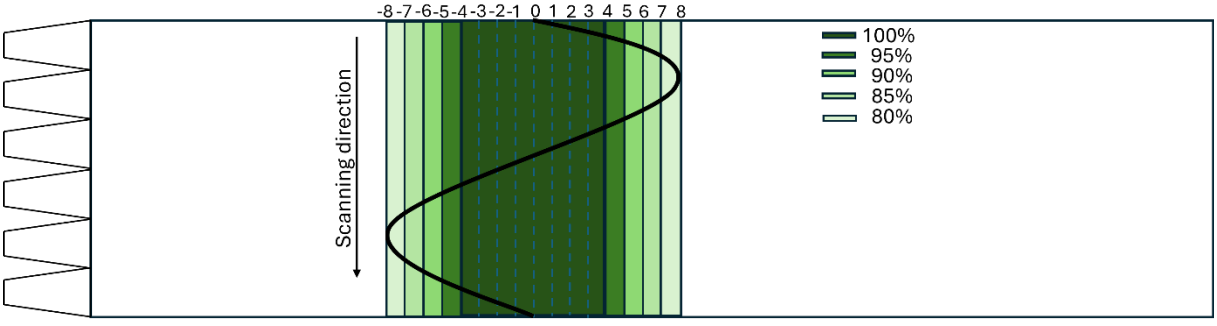

Figure 4-6. Power adjustment sections on the scan track.

Therefore, the energy input in those regions is higher, which might provoke low surface quality due to the disproportionate increase of the molten pool. To avoid the shortcoming mentioned, the laser power was controlled by a DC scanner, with different values being set for different positions of the laser path. Figure 4-6 depicts the areas in which the laser power was regulated and how the different values were distributed (shades of green). The values regulated as a percentage of the nominal laser power at different regions of the scanning amplitude are shown in Table 4-3. To keep a minimum width for surface roughness measurements in the sample's middle area, the nominal laser power was used on points located between lines "-3" and "+3". To avoid an abrupt reduction, the laser power was decreased continuously by 5% of the nominal value per line with the approximation of the turning points and increased at the same rate as the laser moved away from the turning points towards the sample's middle part, i.e., the nominal laser power oscillated between 80% and 100% during the process.

Table 4-3. Laser power adjustment at different points of the scanning amplitude.

Laser Power (%)	Line number
100	0 to ±3
95	±4
90	±5
85	±6
80	±7 and ±8

Table 4-4. Configuration data at low frequencies (5 Hz - 100 Hz) for controller.

Current		Frequency (Hz)					
(%)	(A)	100	77	50	20	10	5
		Scanning amplitude (mm)					
1	**0.06**	0.4	1.5				
2	**0.12**	0.8	4.0				
3	**0.18**	1.3	6.3				
4	**0.24**	1.5	8.3				
5	**0.3**	2.1	10.7	1.8	1.4	1.2	1.1
10	**0.6**	4.1		4.0	2.8	2.7	2.7
15	**0.9**	6.0		5.8	4.1	4.2	4.2
20	**1.2**	8.1		8.1	5.7	5.4	5.6
25	**1.5**	10.1		9.7	6.8	5.8	7.0
30	**1.8**			11.7	8.1	8.2	8.4
35	**2.1**			13.7	9.5	9.8	9.7
40	**2.4**				10.8	11	11.3
45	**2.7**				12.2	12.4	12.6
50	**3.0**						13.9

Table 4-4 gathers frequency and current values, along with the current's correspondent percentage, used as input to the controller in order to obtain the desired scanning amplitude. With different frequencies f and amplitudes a, it is possible to obtain different laser scanning speeds v_y. These values are estimated for the middle areas of the samples (away from the turning points) and the calculation consists in multiplying the pendulum frequency by two times the scanning amplitude (Equation (4)).

$$v_y = f2a \quad (4)$$

In contrast, another common laser processing parameter, the hatch distance, cannot be properly estimated when using the specified scanning system since the distance between two laser tracks increases slightly along the scanning amplitude.

Using the laser machine described above, the set of parameters chosen as the controllable variables for the distinct experiments are laser power, scanning speed, focal position, axial feed rate, and number of times the process is repeated on the same surface area. These parameters were adjusted systematically to control the energy input on the sample surface, with the goal of obtaining the combination of parameters that would result in the optimal surface quality. As a measure to keep the material from oxidizing, the superficial layer of the workpiece is blasted by an argon gas flux of 10 l/min throughout the polishing procedure.

4.2.2. Laser functionalization

For the laser functionalization of the LPBF Ti-6Al-4V samples, the laser workstation PS450-TO (Optec, Belgium) was used (Figure 4-7). The laser source (Tangerine, Amplitude Systèmes, France) consists of a fiber laser with a fundamental wavelength of 1030 nm, which is used to generate ultra-short laser pulses with duration between 10 ps and 390 fs. Through frequency conversion using a second harmonic generation (SHG) and a third harmonic generation (THG) crystal, wavelengths of 515 nm and 343 nm can be generated. The pulse frequency can be set between 200 kHz and 2 MHz using a pulse picker.

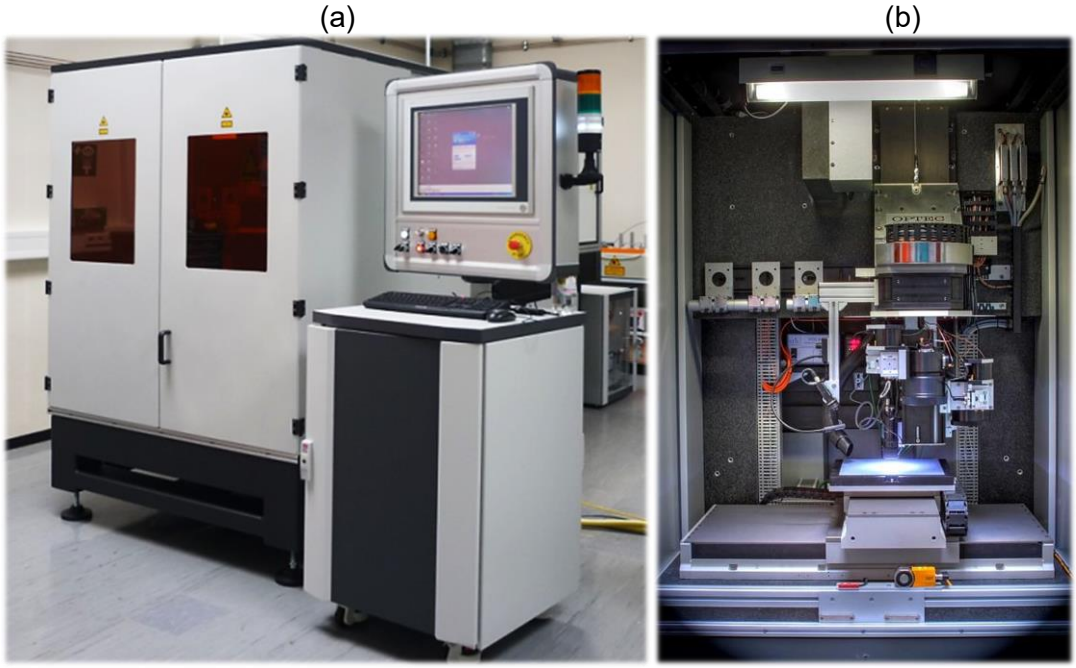

Figure 4-7. PS450-TO laser workstation in (a) overview and view of (b) laser processing chamber. Adapted from [126].

The scanner head (RhothorTM Laser Deflection System, Newson Engineering BV, USA), objective lenses (Sill Optics GmbH, Germany) for the respective wavelengths, and the camera system for positioning are mounted on a turret optic (Figure 4-7b). On the processing table, a porous ceramic plate acts as a motionless vacuum plate for fixing the samples. The laser

processing can be done either by laser scanning, by the movement of the processing table in the x and y directions or by a synchronized movement of both.

Throughout the development of this work, the influence of different ultrafast laser parameters on the surface of metallic AM parts was investigated. The core observation was that the outcome achieved was mainly material ablation with the formation of specific surface structures. Material melting, when reached, was in the form of spatters, often in combination with other surface structures and material ablation. With a controlled set of parameters, two main types of structures could be obtained homogeneously distributed on the sample's surface, nano-ripples, or so-called laser-induced periodic surfaces structures (LIPSS), and porous surface. Both types of structures were chosen to be the aim of the study functionalization of Ti-6Al-4V AM samples.

Table 4-5. Ultrafast laser process parameters to obtain micro-pores and/or nano-ripple structures (LIPSS) for surface functionalization. Adapted from [123].

Parameters	Value for pore structure	Value for nano-ripples structures
Laser power (W)	4	4
Scanning speed (mm/s)	400	400
Repetition rate (kHz)	1000	1000
Pulse duration (fs)	450	450
No. of repetitions	5	1

In the case of the laser functionalization process, the experiments were performed always with the near infrared fundamental wavelength of 1030 nm and without shielding gas. The governing parameters are the laser power, scanning speed, repetition rate, pulse duration, and number of repetitions. The respective values input to the laser system described to achieve the structures discussed are shown in Table 4-5. Low laser power is essential to keep material removal to a minimum, thus guaranteeing potential dimensional tolerances requests for specific applications. In this work, the value established for both structures was 4 W. When processing the workpiece once with the presented parameters, nano-ripples structures are expected to be obtained, as the same process is repeated five times, enough energy input should be achieved for the generation of porous structures. The ultrashort pulse duration of 450 fs was applied during the processing to obtain both structures, along with the same repetition rate of 1000 kHz and scanning speed of 400 mm/s.

4.3. Analytical methods

In this section, the methods adopted for the material and surface analysis of the samples processed with the laser systems previously described are detailed.

4.3.1. Texture measurements

The texture measurements were compliant with the standard (DIN EN ISO 4287), as described in our previous publications [121, 127], using a tactile surface measuring unit MarSurf XR 1 with a drive unit MarSurf GD 26 and a probe arm BFW A 10-45-2/90°. The measurements consisted of a stylus travel of 15 mm; 12.5 mm evaluation length, 2.5 mm of sampling length,

with a cut-off of 2.5 mm. The stylus used has a diamond tip with radius of 2 µm, and an opening angle of 90°.

The surface texture, Ra, was one indicator selected to evaluate the performance of the LP process considered in the current investigation. Figure 4-8 presents a qualitative schematic for the definition of Ra, which is the average of all individual measurements of a surface's peaks and valleys, i.e., surface height deviations from the mean line across the entire profile (DIN EN ISO 4287, DIN EN ISO 11562).

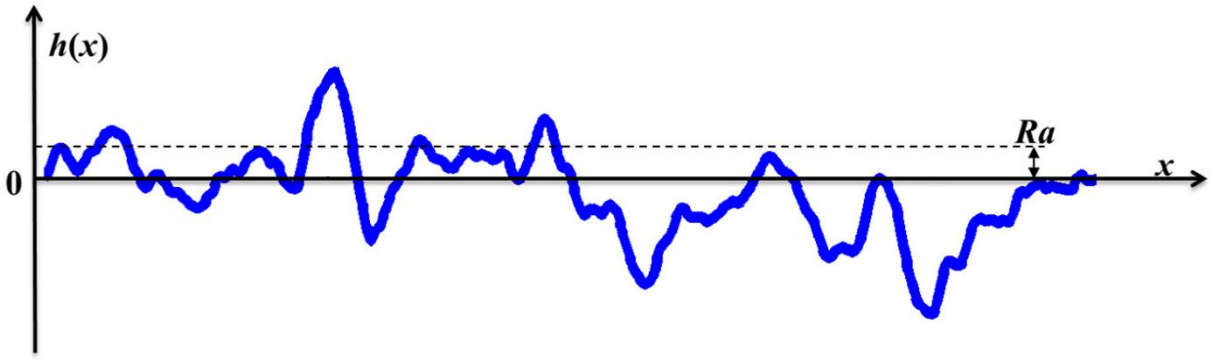

Figure 4-8. R-profile of 2D texture measurement. Adapted from [128].

The Ra values are obtained using Equation (5),

$$R_a = \frac{1}{l}\int_0^l |Z(x)|\, dx \tag{5}$$

with *l* representing the sampling length, and Z(x) representing the height deviations across the profile (DIN 4768:1990).

4.3.2. Optical and scanning electron microscopy

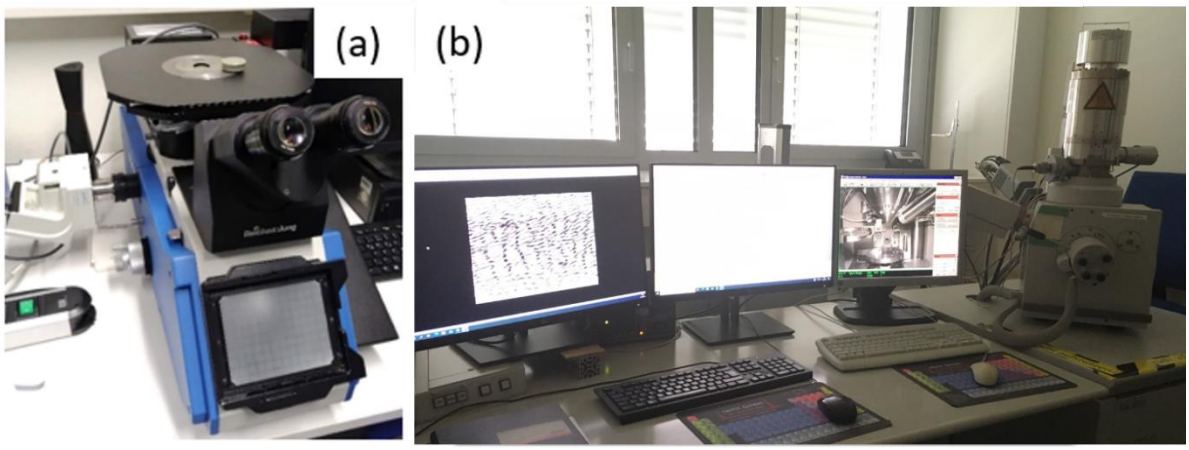

Figure 4-9. Microscopy analysis setup: (a) optical microscope and (b) scanning electron microscopy (SEM).

A Reichert-Jung MeF3 microscope was employed for the assessment of the structures in the workpieces' surfaces in the micro- and macro-scale. The microscope is equipped with a Jenoptik ProgRes C14 CCD camera and WPK 10x ocular lenses that possess objective lenses whose magnifications were varied between 2x to 100x. Additionally, the Olympus Stream

Enterprise software allowed the acquisition of interactive measurements, and its advanced image processing ability provided adequate images that are disclosed and discussed in Chapter 5. The optical microscope setup is illustrated in Figure 4-9a.

Considering that a higher level of magnification and resolution were necessary to assess some microstructures and topographies, in addition to the optical microscope, a scanning electron microscopy (SEM) was also employed. Figure 4-9b depicts the setup of the XL30S-FEG from Philips GmbH.

4.3.3. X-ray diffraction

Information about the phases present in the Ti-6Al-4V samples in different steps of the LPBF process chain, before and after the described laser treatments was obtained by X-ray diffraction (XRD).

The equipment used for this purpose was an X-ray diffractometer Bruker D8 Advance (Bruker AXS, Karlsruhe, Germany, Cu Kα1.2 radiation, Theta-theta arrangement, PSD Lynxeye detector with 89 active strips, variable divergence aperture V6). In this work, the 2θ angle range was varied from 10° to 90° and the analysis of the resultant spectra was performed with the DIFFRAC.SUITE EVA software (Bruker, Germany).

4.3.4. X-ray photoelectron spectroscopy

The following section contains text first presented in *Materials* (MDPI), referenced as [123], and is reproduced here for completeness:

> *For the surface chemical composition analysis, X-ray photoelectron spectroscopy (XPS) measurements were performed using a K-Alpha+ XPS spectrometer (ThermoFisher Scientific, East Grinstead, UK). The Thermo Avantage software was used for data acquisition and processing. All samples were analyzed using a microfocused, monochromated Al Kα X-ray source (400 µm spot size). The K-Alpha+ charge compensation system was employed during analysis using electrons of 8 eV energy and low-energy argon ions to prevent any localized charge build-up. The spectra were fitted with one or more Voigt profiles (BE uncertainty: ± 0.2 eV) and Scofield sensitivity factors were applied for quantification* [129]*. All spectra were referenced to the C1s peak (C–C, C–H) at a 285.0 eV binding energy controlled by means of the well-known photoelectron peaks of metallic Cu, Ag, and Au, respectively. (Solheid et al.* [123]*)*

4.3.5. Hardness measurements

In this work two hardness measurement systems were used, a Vickers micro hardness tester and a nanoindentation tester. Since laser polishing is a process that can cause HAZ in the micrometer range, both systems were used for the measurement of the samples submitted to such process and their reference materials. Differently, samples submitted to ultrafast laser processing, which leads to shallower zones affected by the laser (in the nanometer range), alongside their reference materials were measured only with nanoindentation.

The micro hardness assessment using an electronic Vickers tester (CMT) fabricated by Clemex Technologies Inc. (Figure 4-10a) consisted of the indentation of the workpiece with a

pyramidal diamond using a compression force of 98.07mN, which was held for 10 seconds. The angle between opposite faces of the pyramid is 136º (Figure 4-10b).

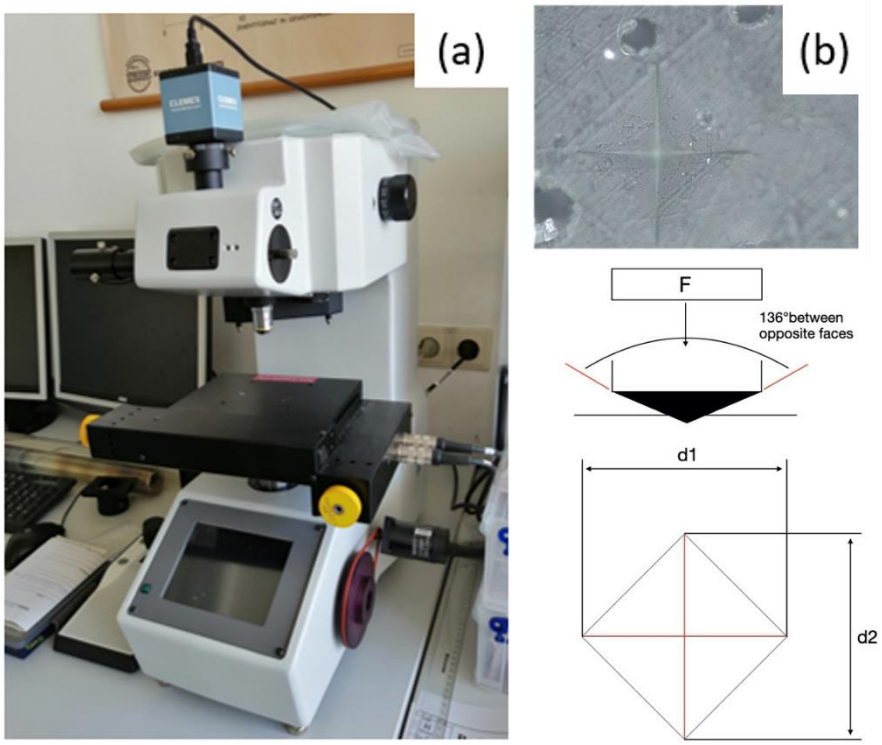

Figure 4-10. Microhardness measurement setup: (a) Automated Vickers micro hardness tester, and (b) schematic of the principle of Vickers hardness measurement with indenter and test indentation. Adapted from [130].

By means of the Olympus Stream Enterprise software, the assessment of the indentation marks took place, the values of the distance between each pyramid's opposite vertices (d1 and d2) were extracted, and their average value was obtained [131]. The Vickers micro hardness values were calculated by employing Equation (6)

$$HV = \frac{F}{A} = \frac{F}{d^2}\left(2sin(136^{\circ}/2)\right) = 0.1891\frac{F}{d^2} \ [N/mm^2] \quad (6)$$

with F representing the compression force (N), A representing indented area (mm²), and d representing the average value of the distance between the indented pyramid's opposite vertices (mm). The micro-hardness assessment is compliant with ASTM E 384 and DIN/ISO 6507, and the results are classified and displayed as HV0.01. In total, nine indentations were performed per workpiece, starting at 20 μm from the surface and distanced 20 μm from each other.

The nanoindentation was executed with an Anton Paar automated tester (Figure 4-11). This system is equipped with two distinct nanoindenters and, although the micro- and nano-hardness indentation measurements are not comparable, the diamond nanoindenter in the shape of a pyramid with an angle of 136º between opposite faces used for Vickers hardness was adopted for this analysis. The compression force was set to be 50 mN. Similarly to micro indentation, the procedure for the measurement of laser polished and their reference samples consisted of nine test points for each sample starting at 20 μm from the surface and distanced 20 μm from each other (Figure 4-12a). To detect the effects of the ultrafast laser

functionalization on the material hardness, the indents for the laser structured samples consisted of nine points cascading from the treated surface until a total length of 50 μm, with an offset between indents of 6.25 μm (Figure 4-12b). The values of the Vickers hardness are calculated automatically with the Anton Paar Software.

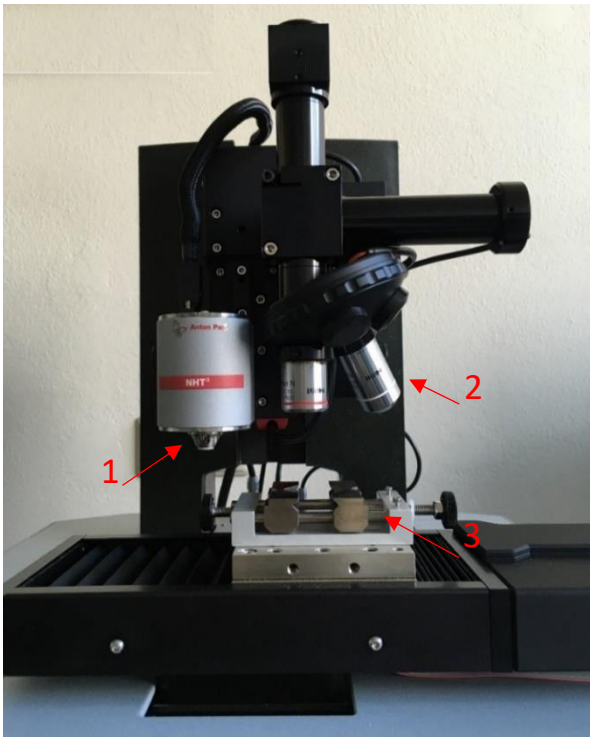

Main components description:

1. Indenter
2. Optical microscope
3. Sample clamp

Figure 4-11. Anton Paar nanoindentation system NHT3.

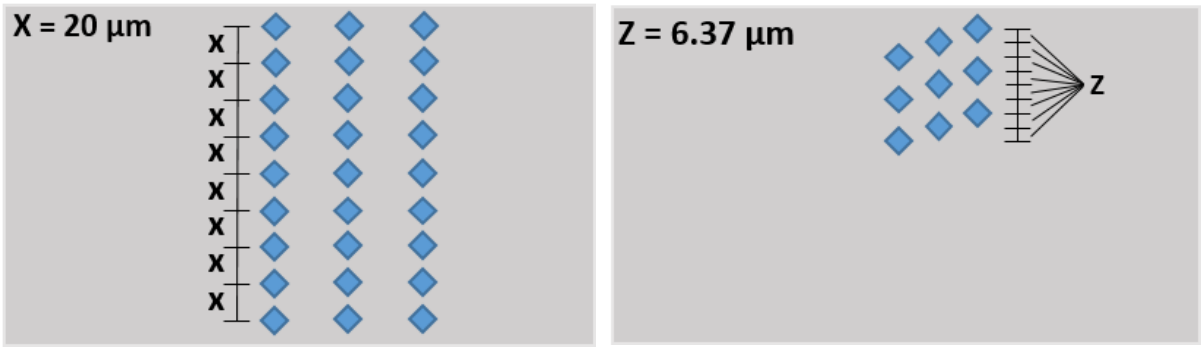

(a) (b)

Figure 4-12. Schematic of the nano indents position for: (a) laser polished and base materials, (b) ultrafast laser functionalization parts.

4.3.6. Wettability

The wettability properties of parts subjected to the laser post-processing approaches adopted in this work were assessed via an automated contact angle analysis system (Dataphysics, OCA 40Mirco) based on video image recording (Figure 4-13). The system is composed of cameras oriented towards the needle responsible for the distilled water dispensation onto the part's surface. The needle receives the liquid from the syringe-resembling recipient when it is pressed by the disposal platform. A single measurement consists of 0.7 μl/s of distilled water being released until the volume of 1 μl is reached, followed by the cameras capturing the

change in the contact angle over a ten-second period from beginning to end. As represented in Figure 4-14, surfaces with contact angles above and below 90° are considered hydrophobic and hydrophilic, respectively.

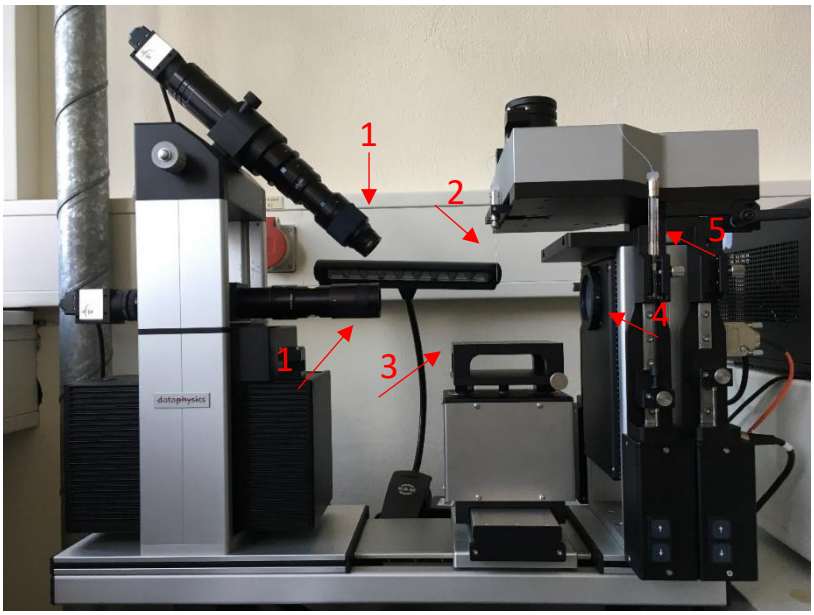

Main components description:

1. Cameras
2. Syringe
3. Sample stage
4. Light source
5. Syringe pump

Figure 4-13. Automatic video-based contact angle analysis system (Dataphysics, OCA 40Mirco).

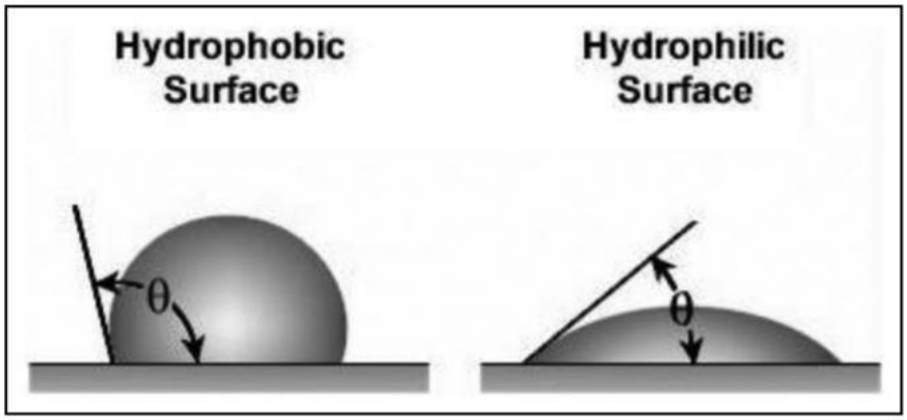

Figure 4-14. Contact angle schematic of droplets on hydrophobic and hydrophilic surfaces [132].

4.3.7. Biocompatibility

The following section contains text first presented in *Materials* (MDPI), referenced as [123], and is reproduced here for completeness:

> *The influence of the different post-processes on the part's biocompatibility was assessed by analyzing the viability of MC3T3-E1 cells (DSMZ ACC 210). This murine pre-osteoblast cell line is widely used as a model system in bone research. As implants for hard tissue is a potential application for the Ti-6Al-4V parts this cell line was chosen for the biocompatibility tests in this study. MC3T3-E1 cells were cultivated in alpha-MEM (minimal essential medium) supplemented with ribonucleosides, deoxyribonucleosides, 2 mM L- glutamine, 1 mM pyruvate, 10% (v/v) fetal calf serum and 1% penicillin/streptomycin (all Gibco, Invitrogen, Karlsruhe, Germany) in an atmosphere of 5% CO_2.*

To find a cytotoxic effect, an MTT assay was performed. The assay uses the ability of metabolically active cells to reduce the water-soluble tetrazolium salt MTT (3-(4,5-dimethylthiazol-2-yl)-2,5-diphenyltetrazolium bromide, Sigma-Aldrich, Taufkirchen, Germany) to a purple-colored formazan. The intensity of the dye is proportional to the number of metabolically active cells. For this assay, MC3T3-E1 cells growing in a microwell plate were exposed to extracts of the samples. In case of the release of toxic substances from the samples, the cells would be harmed, and their metabolic activity reduced.

In this study, $7.5x10^3$ MC3T3-E1 were seeded into each well of a 96-well plate and incubated for 24 hours. The samples were extracted by immersing them in complete cell culture medium for 24 h under cell culture conditions (37 °C, 5% CO_2, approx. 100% humidity). The extracts were tested in 2 concentrations: pure (100%) and diluted (10%, the extracts were diluted 1:10 with fresh cell culture medium). The positive controls were applied in 3 concentrations (100, 10 and 1%). As a negative control, cell culture medium was used, treated as the samples (24 h cell culture conditions). As a positive control, copper discs were used and extracted as samples. In all cases the cell culture medium was carefully removed and replaced by 100 µl of the extracts or controls. All samples were evaluated in quadruplicates. The cells were incubated for another 24 h. Afterwards, 50 µl of the MTT solution (1 mg/ml in MEM) was added and incubated for 4 h. Finally, the cell culture medium was removed, and the water insoluble formazan dissolved by adding 100 µl 2-propanol. The absorbance was measured using a spectro-photometer (Synergy H1, BioTek, USA) at 570 nm with a reference wavelength at 650 nm.

In a second series of tests, MC3T3-E1 cells were cultured on top of the Ti-6Al-4V parts, and their viability and morphology assessed with a fluorescence microscope. For cleaning and sterilization, the laser textured samples were sonicated in ethanol in an ultrasound bath and afterwards placed inside a 24 well culture plate. Cells were seeded onto the samples by adding 1.5 mL of cell suspension with a cell concentration of $6.5x10^6$/ml into the well. After incubation for 24 h, cell culture medium was removed, the cells were washed with PBS and fixed by incubating the cells for 30 min with 2% glutaraldehyde (Sigma-Aldrich, Taufkirchen, Germany) in PBS. Fixation with glutaraldehyde induces an autofluorescence in the cells, allowing observation of the cells in a fluorescence microscope without further staining [133]*. Additionally, the cell nuclei were stained using Hoechst 33342 (Invitrogen, Karlsruhe, Germany). Cell images were obtained using a fluorescence microscope (Axiovert 200M, Zeiss, Germany). (Solheid et al.* [123]*)*

4.4. Heat transfer model

An approach to predict the modifications inflicted to materials subjected to post-processes such as LP is the usage of computational simulations of practical procedures, in contrast to processing and assessing an extremely large number of workpieces. This alternative comprises the formulation of trustworthy numerical representations based on an inferior number of trials, and its greatest assets are the efficiency in terms of resource savings and shortened length of operation, particularly whilst inspecting the behavior and effects of plenty variables with values varying within broad bounds. Amid numerous possibilities, the finite element method (FEM) is widely adopted because it is capable of giving a fine comprehension over the assessed procedure's comportment.

The finite element method is a numerical technique for solving problems which are described by partial differential equations. It consists of dividing continuum domains, often represented by computer-aided design (CAD) models, into a mesh of finite elements. To each node that delimitates a finite element an approximating function is attributed (Figure 4-15). A continuous physical problem is then transformed into a discretized finite element problem.

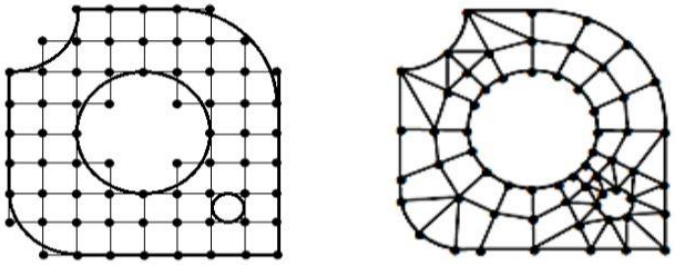

(a) (b)

Figure 4-15. Finite element method: (a) discretization; and (b) final mesh [134].

The illustration of how the main steps of the finite element solution procedure works is presented in Figure 4-16.

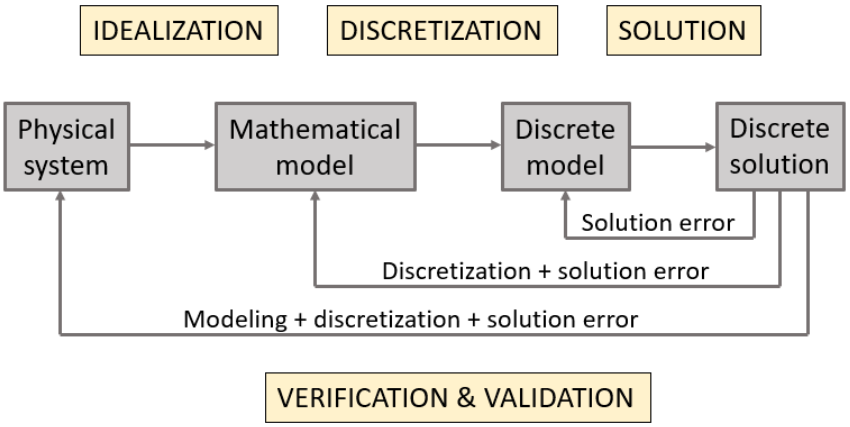

Figure 4-16. Main steps of the FEM simulation procedure [134].

The first step is the establishment of the physical system and of the governing mathematical equations for the system in question. This step is considered idealization. The next step is the discretization, which consists of dividing the solution region of the system into finite elements. The outcome of this step is a finite element mesh. Finally, the solution step involves solving the global equation system. After obtaining the solution for the model-based simulation, it is possible to use the output to improve the model even further by refining the mesh, reassessing the mathematical assumptions and/or adjusting the physical properties of the system. These stages are part of the verification and validation of the proposed model [135].

Using FEM, a mathematical representation is established, and traits that occur during processing are realistically depicted through simulation. Investigations aimed at improving the effectiveness of laser polishing modelling with strategies ranging from coupling of thermal energy exchange and molten material circulation to texture forecasting based on the starting condition of the sample's exterior and the surface tension-driven fluid dispersion [99, 136, 90]. Despite the fact that this approach could demand long processing intervals for highly elaborated numerical representations [137], it is still an advantageous methodology for the analysis of different technologies. Additionally, the outcome of FEM simulations can be easily

applied as input to diverse optimization algorithms, similarly to input obtained from experiments [138].

The following description is published *Materials* (MDPI), referenced as [121]. It is known that material processing with a cw laser can cause deep heat affected zones (HAZ), which can affect the performance of the parts during application. To have a rapid overview of the HAZ deepness as the aftermath of samples submitted to LP within the wide range of parameter variation tested, a heat transfer model was applied.

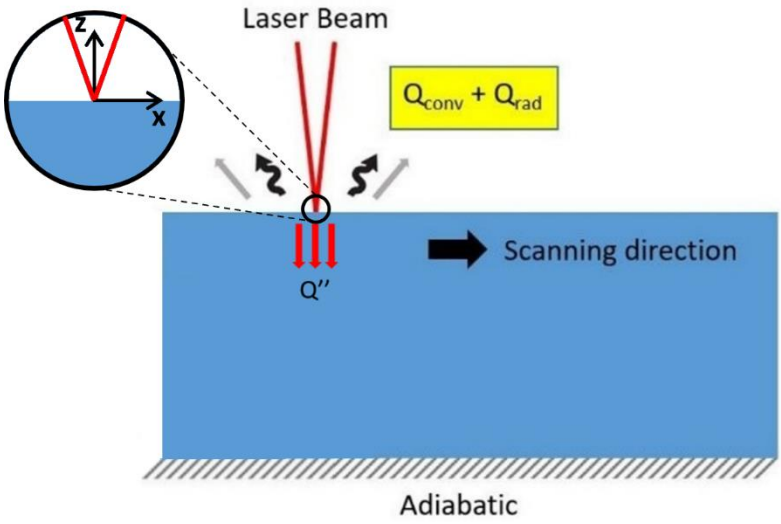

Figure 4-17. Schematic drawing of the thermal conditions for the applied heat transfer model. Reproduced and adapted from [122] with the permission of the Laser Institute of America.

Figure 4-17 offers a simple visualization of the assumptions considered to obtain the heat transfer mathematical representation. Initially, the workpiece is at room temperature, in this case 25 °C. A laser heat source focused onto the material's surface moves in a determined direction, with a pre-established speed, whilst processing a superficial layer of the material. The base of the sample is presumed to be adiabatic, whilst the remaining sides dissipate heat via radiation (Q_{rad}) and convection (Q_{conv}). Both conditions are illustrated in Figure 4-17, with former being represented by the curved arrow whereas the latter is depicted as straight grey arrow.

The surface heat source generated by the laser beam and transferred into the material by heat conduction (Q'') can be explained by a Gaussian distribution. Therefore, it can be mathematically represented, in W/m^3, by Equation (7),

$$Q'' = \frac{2AP_w}{\delta_{opt}\pi R_w^2} e^{\frac{-2(x^2+y^2)}{R_w^2}} \quad (7)$$

Where A is the laser absorptivity, P_w is the laser power in W, R_w is the heat source radial point distance in µm, and δ_{opt} is the optical penetration depth in m. The very small optical penetration depth, inherent to metallic materials, allows the assumption of the laser being a surface heat source (z = 0), as mentioned above.

The three-dimensional heat transfer considering the before mentioned thermal conditions is expressed in Equation (8),

$$\rho C_p \frac{\partial T}{\partial t} = k\nabla^2 T + Q'' - Q_{conv} - Q_{rad} \quad (8)$$

Where ρ is the specific heat density of the material in kg/m^3, C_p is the specific heat capacity of the material in J/kg K, and k is the thermal conductivity of the material in W/mK.

The remaining terms of Equation (8) represent heat exchanges with the environment through convection and radiation, since not all the surface heat generated is dissipated across the part. These heat dissipations, in W/m^3, are expressed by Equation (9) and (10), respectively,

$$Q_{conv} = h(T_{amb} - T) \quad (9)$$

$$Q_{rad} = \varepsilon\sigma(T_{amb}^4 - T^4) \quad (10)$$

with $h = 100$ [W/m^2 K] the convective heat transfer coefficient, $\varepsilon = 0.31$ and $\sigma = 5.67\ 10^{-8}$ [W/m^2 K^4] the surface emissivity and the Stefan-Boltzmann constant, respectively.

Table 4-6. Thermo-physical properties of Ti-6Al-4V and simulated process parameters [139, 140, 141]. Reproduced from [122] with the permission of the Laser Institute of America.

Property	Value
Density (ρ)	4000 kg/m^3
Solidus temperature (T_s)	1878 K
Liquidus temperature (T_l)	1928 K
Specific heat capacity, solid phase (C_{ps})	543 J/(kg K)
Specific heat capacity, liquid phase (C_{pl})	770 J/(kg K)
Thermal conductivity, solid phase (k_s)	13 W/(m K)
Thermal conductivity, liquid phase (k_l)	80 W/(m K)
Laser absorptivity (A)	0.3

Thermal simulations based on the presented heat transfer model were conducted with COMSOL Multiphysics 5.5. Moreover, material properties employed in the simulation are summarized in Table 4-6. The movement of molten material affects significantly the highest temperatures reached throughout LP because of its implications in the heat transfer physics [142]. Nevertheless, in this study, a compromise was made in this regard, and this movement is not simulated in order to preserve a reasonable computing time. Alternatively, the thermal conductivity in liquid phase (k_l) is adjusted to indirectly consider the impact of the fluid flow in a way that the model is capable of accurately depicting the HAZ deepness obtained experimentally, as disclosed in section 5.2.1.

The shape and mesh distribution designed for the current simulation is presented in Figure 4-18. The whole workpiece is 12 x 4 x 2 mm³ in size, but the surface area where the laser tracks occur during the LP process is 6 x 1 x 1 mm³ in size. Within this zone, the biggest mesh piece is 10^{-4} m in size. The maximum element size of the laser scanned area was selected after an extensive analysis of the influence of its size and distribution in the quality of the results, taking into consideration not only the output of the simulation but also the effect of the different meshes in the computational time. Examples of the results for one single track, when using the exact same processing parameters and areas, are presented in Table 4-7.

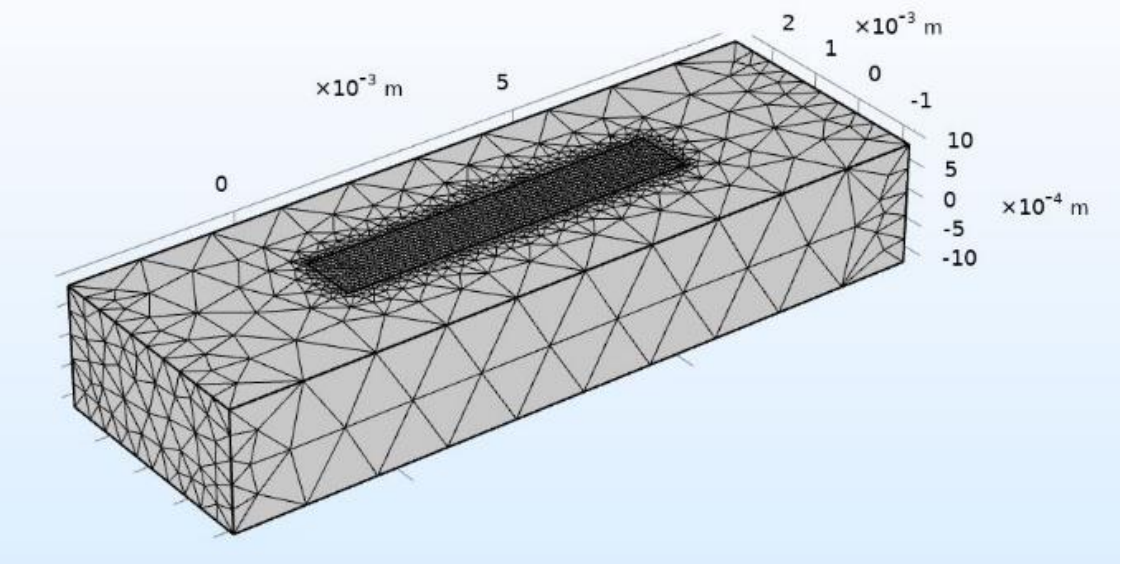

Figure 4-18. Geometry and mesh distribution of the presented model. Reproduced from [122] with the permission of the Laser Institute of America.

Table 4-7. Computational costs of distinct mesh element sizes and distribution.

Maximum element size (m)	Element distribution	Computational time
$0.7 \cdot 10^{-4}$	-	7m8s
$1 \cdot 10^{-4}$	12	21m15s
$0.7 \cdot 10^{-4}$	12	1h48m21s
$1 \cdot 10^{-4}$	20	22m45s
$0.4 \cdot 10^{-4}$	-	2h14m20s
$1 \cdot 10^{-4}$	-	5m7s

Compared to the selected maximum element size of 10^{-4} m, finer meshes, even when not distributed in the entire laser affected domain, were not able to significantly improve the simulation results, although the computational time increased considerably. A similar behavior was noticed when using the same mesh size with different distributions, where no major effect happened to the quality of the simulation output, while the simulation times did not present a reduction.

The different laser beam diameters, obtained when varying the focal position, were calculated previously (Table 4-2) and are implemented in the computational simulation directly in Equation (7). Moreover, the experimental hatch distance is difficult to estimate due to the scanning system characteristics. For this reason, the heat transfer model is developed to simulate the laser scanning movement in a single axis and is validated with single-track experiments.

4.5. Statistical model

The content in this section is published in Materials (MDPI), referenced as [121]. Statistical models consist of fitting into an equation that properly describes the behavior of the data distribution. The association of design of experiments (DoE) with numerical models is a resourceful approach to retrieve the utmost insights from a single dataset, and it facilitates the identification of how the controllable variables affect the dependent variable, both individually

and interactively, supporting the decision making and the definition of parameters to be adopted. Furthermore, with the equations that result from statistical models, it is possible to perform mathematical optimizations. In this context, the goal for using statistical models, in the current work, is to model the behavior of the surface roughness Ra and the depth of the HAZ as functions of the governing parameters for the laser polishing and use the resultant equations to find the optimal set of parameters for minimum Ra and HAZ.

Considering the adoption of a central composite design (CCD), five LP input parameters were chosen as factors. Namely, the laser power (W), focal position (mm), number of repetitions, axial feed rate (m/min), and scanning speed (mm/s). The DoE for surface texture contained 43 combinations of the five parameters within a total of 52 experimental runs. Five variation levels per factor were used. The distinct levels and overall range of each input parameter is disclosed in Table 4-8.

Table 4-8. DoE parameter values for the laser polishing test [121].

Laser power (W)	Focal position (mm)	No. repetitions	Axial feed rate (m/min)	Scanning speed (mm/s)
100	0	1	0.3	400
200	1	2	0.45	800
300	2	3	0.6	1200
400	3	4	0.75	1600
500	4	5	0.9	2000

A similar DoE was utilized for the HAZ deepness. In this case, the data was acquired through FEM simulations previously detailed in section 4.4. A difference from the DoE employed for the surface texture, is that for HAZ depth it has only four of the CCD factors. The axial feed rate was disregarded because the simulations that generated the database considered the laser scanning path on a single axis. Consequently, it comprised 25 distinct sets of parameters within a total of 34 computational simulations. Identical variation levels were considered for each one of the four factors (laser power, focal position, number of repetitions, and scanning speed), thus their values are the same found in Table 4-8.

4.5.1. Linear regression

In possession of information acquired either through experiments or simulation, there are many proven paths that would lead to the definition of an adequate set of parameters to be employed in the LP process. Perhaps one of the most explored methods is the “trial and error” strategy. However, such an approach significantly depends on the knowledge and experience of the person executing the experiments, in addition to the implication of considerable time and money spent [143]. Conversely, a vastly used technique to countermeasure the disadvantages of the mentioned approach is the usage of results based on a design of experiments (DoE) as input to a statistical method capable of generating a mathematical model that characterizes the behavior of the parameters, their interaction, and their impact in the final output. In contrast to “trial and error”, the combination of DoE and mathematical optimization requires a lower amount of experiments and/or simulations to comprehend comportments of a manufacturing approach. The outcome of this process is a numerical model that can forecast the impact of different set of parameters (independent variables) on the chosen dependent variables. Due to its versatility, this method is often adopted in different disciplines. Considering the scope of this work, applications that come to attention are the ones that utilized it to model and enhance laser-based processes, e.g., laser cladding, welding and surface hardening [144, 145, 146].

The first statistical method evaluated in this work is quadratic regression. The generic second order polynomial expression that is used to fit each case of acquired data is depicted by Equation (11),

$$y = b_0 + \sum_{i=1}^{n} b_i x_i + \sum_{i=1}^{n} b_{ii} x_i^2 + \sum_{i=1}^{n-1} \sum_{j=i+1}^{n} b_{ij} x_i x_j \quad (11)$$

where 'y' represents the dependent variable, 'b_0', 'b_i', 'b_{ii}' and 'b_{ij}' are predictors, or coefficients, 'x_i' are the values of the i^{th} independent variables, and 'n' is the number of distinct parameters.

The predictors were determined via MATLAB (R2018b, MathWorks) utilizing the least-square method as it is considered a resilient technique with good resistance against outliers. The technique consists of reassigning different weights to each term throughout the iterations. The starting point is predicting the coefficients considering the same weight to each term. After that, the weights are reassessed in every iteration according to their influence on the dependent variable. The last iteration is achieved when the values calculated for the predictors fulfil the pre-established convergence criteria.

The analysis of variance (ANOVA) with 95% confidence was utilized for the performance assessment of the resultant models.

4.5.2. Artificial neural networks

An alternative to regression models is to use machine learning (ML) approaches to attain different statistical models. Among several ML methods, artificial neural networks (ANN) are often employed for its proven learning and modelling results for a wide array of input datasets. For this reason, it is also being used for process development of distinct categories of manufacturing with relevant outcomes as presented in recent investigations [147, 148, 149]. The procedure emulates how a human being handles and assesses the information received, thus the technique's title. When using the ANN method, the data is moved from the input layer to the output layer, passing through one or more hidden layers. All mentioned layers are connected through neurons and each neuron has an associated bias used to offset the results. Besides that, the interaction between neurons (synapses) has a synaptic weight bound to each connection. A schematic image of an ANN neuron is depicted in (Figure 4-19).

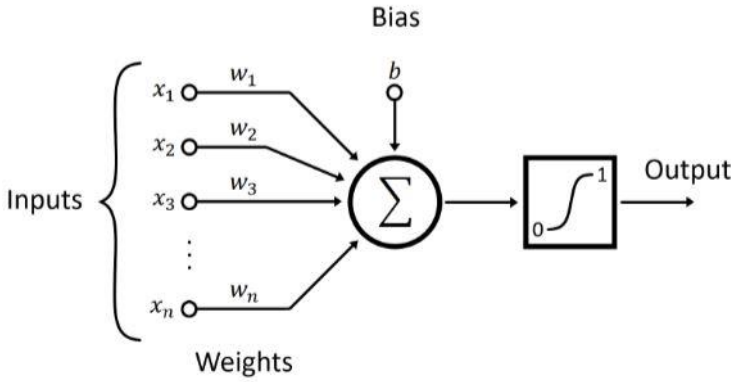

Figure 4-19. Schematic of one ANN neuron [150].

Similarly to the bias, the synaptic weights are also used to offset the results and to identify the strongest effects between input and output. This adaptability allows ANN to learn from the input dataset and through an iterative process, the bias and weights are adjusted until the statistical

model achieves an adequate representation of the data. In addition to the advantages already listed, another convenient leverage in comparison to other methods is the straightforward option to continue feeding new input data that will be processed and learned to enhance the accuracy of the model [151].

Considering all the advantages detailed above, the ANN technique was chosen to utilize the same input datasets as the linear regression method described previously. Two numerical models, one for surface texture and one for HAZ depth were attained via the Neural Network toolbox in MATLAB, which trains the network until a threshold based in the minimum least mean squared error (MSE) across epochs is reached. Since each output (Ra and HAZ depth) has a different set of input data, distinct architectures were tested for both models and the most suitable for each one of them was selected for this study. Considering that the input data for Ra contains more outliers, the most appropriate architecture for it was a cascade-forward network that contains two hidden layers between the input and output, being four neurons in the first hidden layer and two neurons in the second one. Conversely, the input data for Haz depth was more accurate as they were acquired through numerical simulations. Therefore, a simple feedforward network with a single hidden layer and one neuron was adopted for the HAZ depth predictor. A fundamental difference between the architectures is that the cascade-forward network associates all layers amidst them in the forward direction, i.e. the input layer is not only associated with the first hidden layer but also with the second hidden layer and the output layer, and the first hidden layer is also associated with the output layer not only to the input and second hidden layers. On the other hand, the simple feedforward network connects the layers with regular synapses between one layer and the next. To contribute to the visualization of each architecture, Figure 4-20 illustrates each of them.

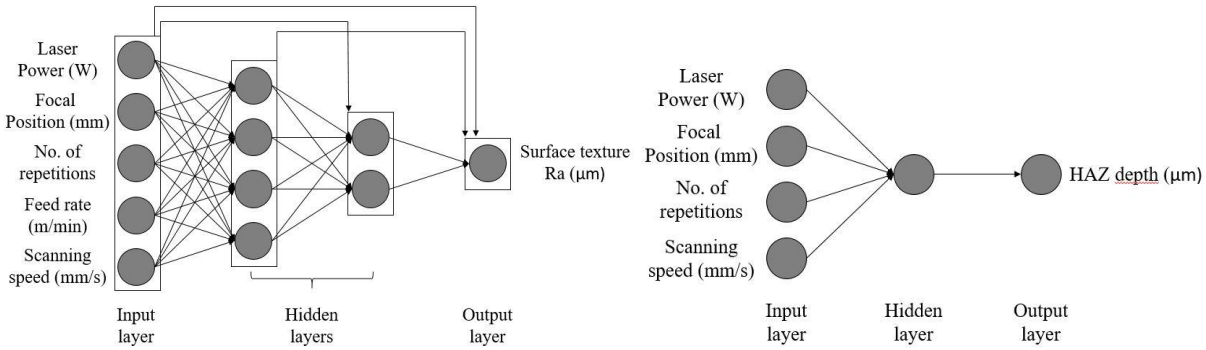

Figure 4-20. ANN architecture for: (a) surface texture, and (b) HAZ depth [121].

Both models utilize a hyperbolic tangent sigmoid as an activation function of hidden layers to reflect the nonlinearity of the model. Additionally, given that the aim of the models is to predict a numerical value, a linear activation function is used for the output layer. Another aspect in common between the models is the algorithm employed to train both networks. The Levenberg-Marquardt backpropagation method combines the advantages of gradient descent and Gauss-Newton algorithms, leading to a fast and stable convergence that reaches adequate MSE numbers [152]. The last common configuration is the percentage implemented to randomly split the input data. For both cases the fitting procedure described uses 70% of the input dataset for training, while the remaining 30% is split equally for testing (15%) and validation (15%).

A schematic for an entire ANN modelling is presented in Figure 4-21. The diagram includes a generic multilayer neuron network and the neuron output that will shape the final ANN model,

which is a standard formulation based on the chosen architecture (number of layers and number of neurons). New bias and weights are iteratively calculated by the chosen training methodology until the established threshold or cycle limits are reached.

In summary, the learning capability of such approach makes the technique stand out as a significant tool for accurately modelling small and medium input datasets for a broad range of applications, including the prediction of Ra and HAZ depth of laser polished AM workpieces.

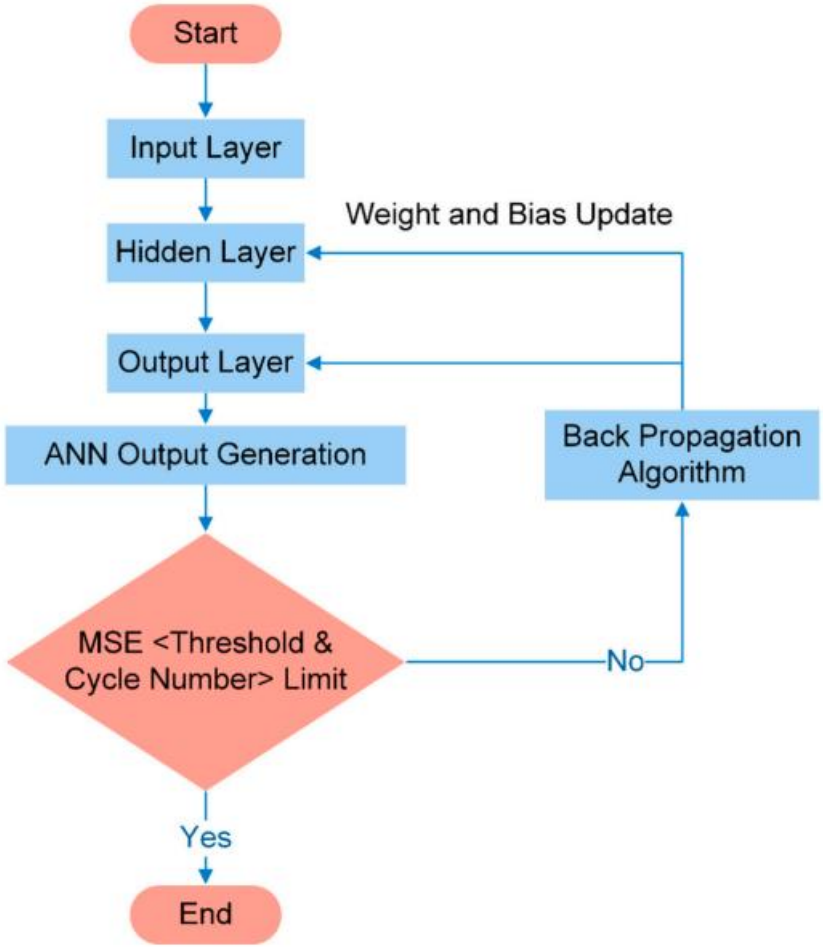

Figure 4-21. Flowchart of ANN modelling [153].

4.6. Genetic algorithm optimization

As the aftermath of the numerical modelling, the equations that represent the dependent variables' behavior can be used as the objective function of optimization methods to find optimal values of the independent variables according to individual needs. Therefore, this approach can be used in this work to attain suitable LP parameters for the post-processing LPBF metallic parts.

Bearing in mind that surface texture and HAZ depth are inversely proportional quantities, and that one target of the current work is to appoint a variety of values for the LP parameters that will lead to appropriate Ra and HAZ depth numbers, it is essential that both objective functions are concurrently optimized via multi-objective optimization problem (MOOP) methods.

Amongst all options, Genetic Algorithms (GA) emulates elements of biological evolution to solve MOOPs. The concepts of mutation, crossover, and selection are iteratively applied to the general data pool, which guarantees that its most befitting solutions are the selected ones to be combined and/or mutated and passed on to the next iteration. The most befitting solutions are characterized both by their calculated accuracy and by their ability to maintain or enhance the variability of the optimization results. The outcome of the iterative process is a set of solutions that fulfills a preestablished accuracy threshold, and that can be translated into a Pareto front similarly to the one depicted in Figure 4-22. Therefore, the multi-objective genetic algorithm toolbox in MATLAB uses a variant of the NSGA-II, which favors solutions with the characteristics described above (accuracy and variability) [154, 155, 156].

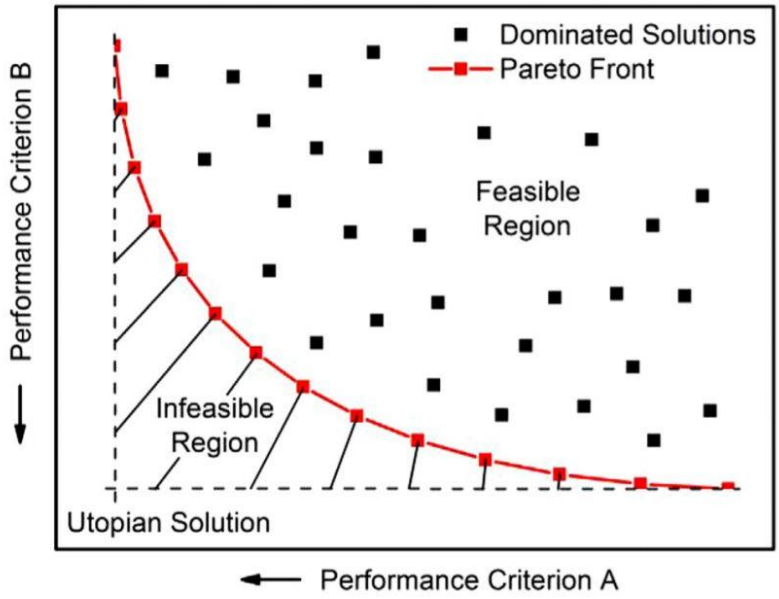

Figure 4-22. Pareto front schematic [157].

As observed in Figure 4-22, the Pareto front is formed by a collection of nondominated solutions of the MOOP. Any point on the front is considered one Pareto optimal, and by moving towards the edges of the curve you can reach a better solution for one of the objectives, however due to the essence of the problem it means that the other objective will be compromised. Despite the fact that the Pareto front is not capable of finding the global or utopian solution, it provides a collection of possible outcomes in a fast and visual way that will culminate in shaping the Pareto front. Consequently, it is a remarkable tool to identify the solutions with a convenient outcome for both Ra and HAZ depth, together with the adequate range for the input parameters that will lead to the expected values. The number of solution points that will be considered within a desired region is dependent on the design specifications. A flowchart representing the optimization procedure described is shown in Figure 4-23.

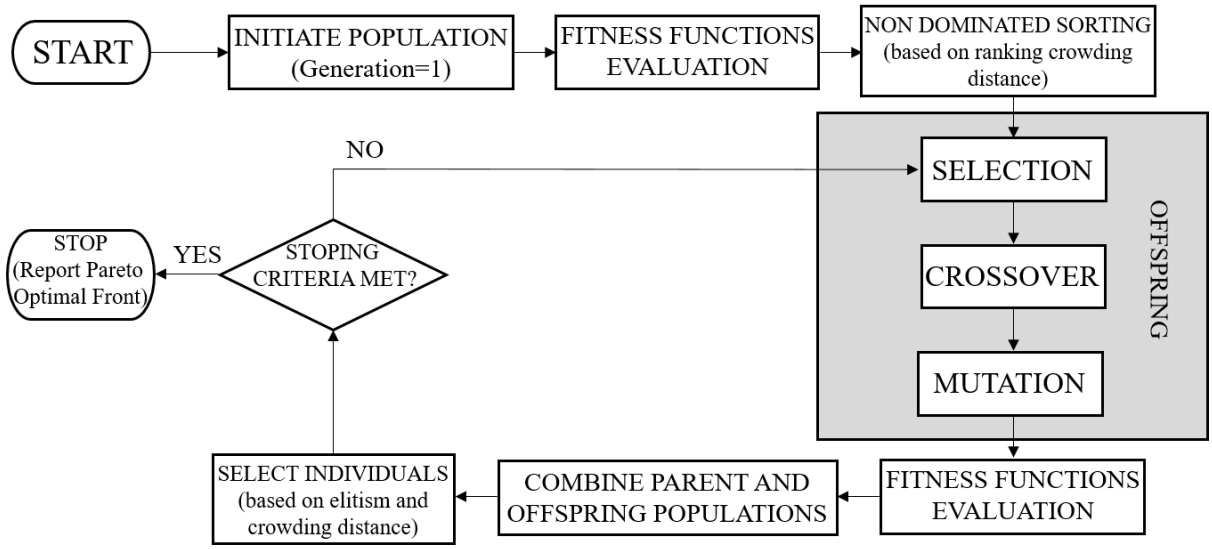

Figure 4-23. Flowchart of NSGA-II optimization method [158].

5. Results and discussion

This chapter presents the results and discussions regarding the laser post-processing of AM metal parts. The modification of the surface of Ti-6Al-4V samples subjected to laser polishing is presented, the goal is to overcome surface defects commonly present on LPBF parts, thus improving their quality, while assessing the effects on their properties and characteristics considering different steps of the LPBF process chain. The laser polishing process development and parameter selection, performed to obtain a significant reduction in the surface roughness, are aided by design of experiments techniques, statistical models, and numerical optimization. Furthermore, the use of ultrafast laser for the modification and functionalization of the surfaces of the Ti-6Al-4V, individually and combined with laser polishing, is used in samples from different steps of the process chain. The samples are assessed for resulting topography, microstructure, and nano hardness, in addition to the functionality analysis via wettability, surface chemical composition, cell growth, and surface toxicity.

5.1. Characterization and properties after laser polishing

In this section, the evaluation of the resultant characteristics and material properties of LPBF Ti-6Al-4V submitted to laser polishing is presented. The main reason to use such analysis in different steps of the process chain is obtaining a thorough understanding of the laser polishing effects for different starting conditions and suitability within the process chain. Some of the content in this section is published in Materials (MDPI), referenced as [121].

5.1.1. Morphology

The morphology analysis was carried out for LPBF Ti-6Al-4V samples in the three initial conditions prior to the laser polishing, as-built (AB), heat treated (HT), and sandblasted (SB). At first, 24 experiments were performed for HT samples. An overview of the results is presented in Figure 5-1.

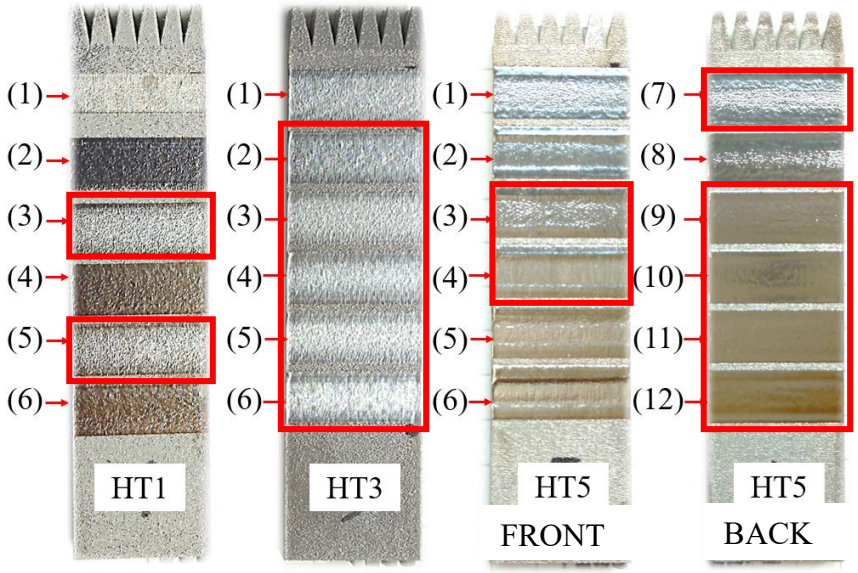

Figure 5-1. Overview of laser polished HT samples. Marked areas were selected for further analysis of AB and SB samples.

The parameter set for the processed areas that presented the less pertinent results are found in Table 5-1. The 14 marked areas represent the surfaces with the most relevant structures to be explored in terms of sampling the variety of results obtained, and the corresponding set of parameters were applied on AB and SB samples as well. An overview of the AB and SB resulting surfaces are displayed in Figure 5-2, whereas Table 5-2 describes the set of parameters adopted to achieve such structures in the AB, SB, and HT (marked areas).

Table 5-1. Scanning parameters for laser polishing of the less relevant areas from the HT samples

Sample No.	Laser power (W)	Feed rate (m/min)	No. repetitions	Focal position (mm)	Laser intensity (MW/cm²)
HT-(1-1)	100	0.8	1	0	1.27
HT-(1-2)	100	0.8	3	0	1.27
HT-(1-4)	100	0.6	3	0	1.27
HT-(1-6)	100	0.4	3	0	1.27
HT-(3-1)	200	0.8	1	0	2.54
HT-(5-1)	300	0.8	1	0	3.81
HT-(5-2)	300	0.8	3	0	3.81
HT-(5-5)	300	0.4	1	0	3.81
HT-(5-6)	300	0.4	3	0	3.81
HT-(5-8)	300	0.8	3	3	0.07

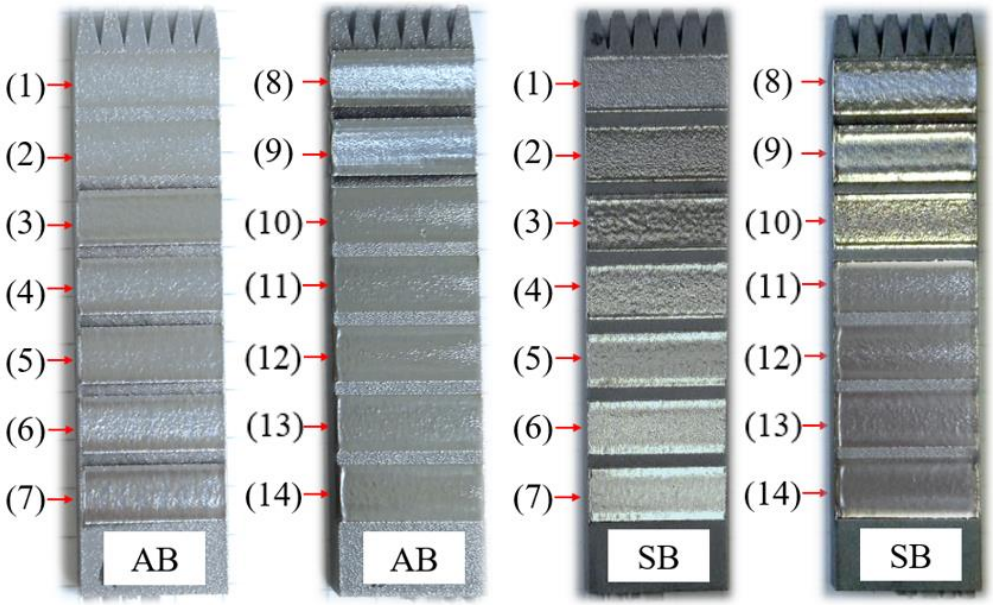

Figure 5-2. Overview of AB and SB samples with selected laser polishing parameters displayed on Table 5-2.

Comparing Figure 5-1 and Figure 5-2, it is noticeable that two input parameters of the LP have a significant repercussion on flattening the surface of the workpieces, since subjecting them to higher temperatures throughout the process by combining higher laser power and number of repetitions generates smoother surfaces. Conversely, the samples subjected to lesser temperatures during the LP process due to the application of low laser power, e.g., 100 W, presented inferior quality as a result of unsatisfactory re-melting. By increasing the power to 200 W, a shinier surface is observed, although the polished effect is not yet achieved. With the

highest power of 300 W, a combination of positive achievements of re-melting with undesired pits and humps were detected. Finally, the LP parameter set of the workpieces HT5-(9) to HT5-(12) consisted of a laser power of 300 W, along with +3 mm defocus, scanning with axial feed rates of 0.4 or 0.6 m/min. This combination resulted in no undesired effects on the processed surfaces. Furthermore, the macrostructures on the surfaces of the AB and SB samples after laser polishing are fairly similar to the laser polished HT samples.

Table 5-2. Scanning parameters of the laser polishing process for AB, HT, and SB Ti-6AL-4V AM samples.

Sample No.	Laser power (W)	Feed rate (m/min)	No. repetitions	Focal position (mm)	Laser intensity (W/cm²)
AB/SB-(1), HT-(1-3)	100	0.6	1	0	1.27
AB/SB -(2), HT-(1-5)	100	0.4	1	0	1.27
AB/SB -(3), HT-(3-2)	200	0.8	3	0	3.54
AB/SB -(4), HT-(3-3)	200	0.6	1	0	3.54
AB/SB -(5), HT-(3-4)	200	0.6	3	0	3.54
AB/SB -(6), HT-(3-5)	200	0.4	1	0	3.54
AB/SB -(7), HT-(3-6)	200	0.4	3	0	3.54
AB/SB -(8), HT-(5-3)	300	0.6	1	0	3.81
AB/SB -(9), HT-(5-4)	300	0.6	3	0	3.81
AB/SB -(10), HT-(5-7)	300	0.8	1	3	0.07
AB/SB -(11), HT-(5-9)	300	0.6	1	3	0.07
AB/SB -(12), HT-(5-10)	300	0.6	3	3	0.07
AB/SB -(13), HT-(5-11)	300	0.4	1	3	0.07
AB/SB -(14), HT-(5-12)	300	0.4	3	3	0.07

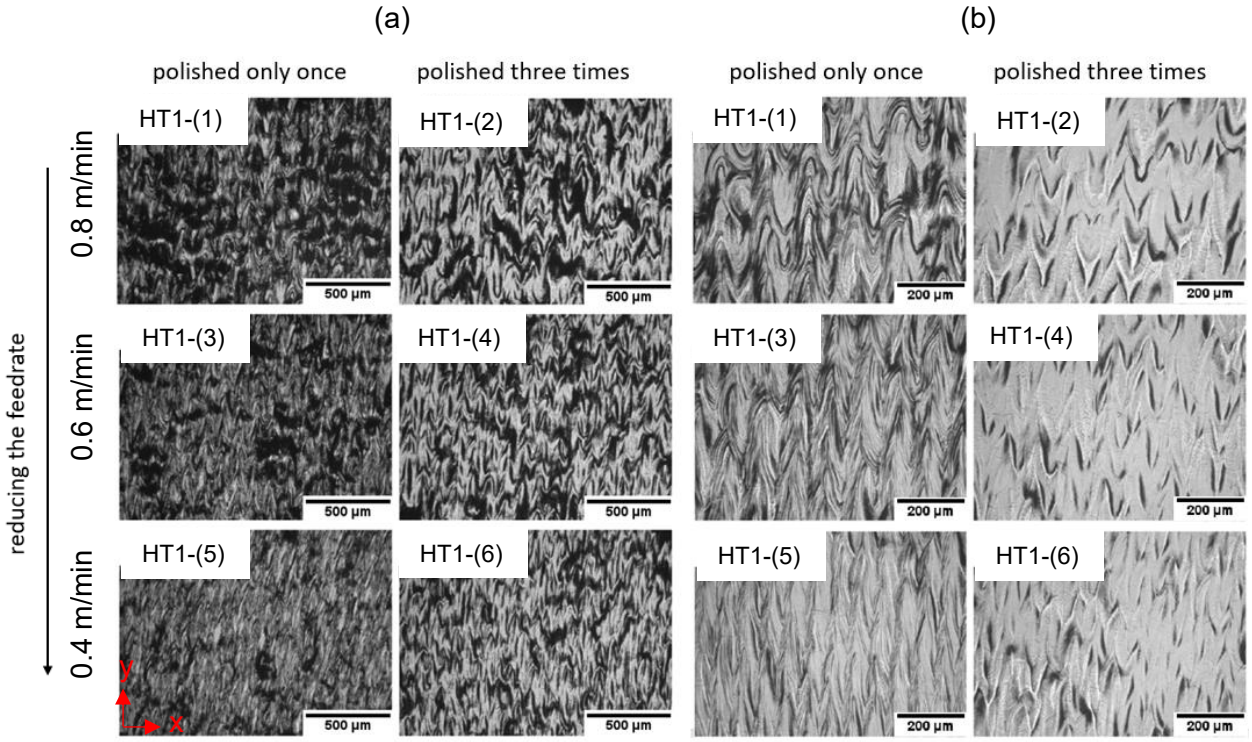

Figure 5-3. Optical microscopic images for the surface morphological analysis of sample HT1-(1) to HT1-(6) [121].

A surface morphology assessment was carried out for the first six HT1 workpieces. For such an evaluation, the parameters feed rate and the number of repetitions were diversified. From the micrographs Figure 5-3, it is evident that lower feed rate led to more efficient material melting, which is represented by the expanded surface homogenization. Ripples were the morphology observed in all cases. Their creation mechanism is addressed in 3.2.3 and is linked to the fast solidification intrinsic to the laser polishing process, in combination with the direction of movement of the heat source. Meaning that a portion of the liquid material tends to move to the edge of the melt pool, where the heat exchange with the environment is higher, and solidifies earlier than the center of the melt pool. The middle portion of the melt pool exchange heat with the environment at a lower rate than the edges and is maintained in the liquid phase for a slightly longer time, which influences the material movement to be parallel to the scanning direction. Even though slower than the edges, the center of the melt pool solidifies fast and takes the discussed ripple form towards the material flow. When conducting the exact same process thrice for the same workpiece, the resulting morphology was more homogeneous due to the additional melting of the same portion of the workpiece during the supplementary process repetitions, which lead to the scanning paths to become unclear (Figure 5-3b). As described in section 4.2.1, assessments of scanning speed and hatch distances must be performed in the middle section of the processed regions, since the occurrence of turning points during the scanning leads to reduced speeds and hatch distances in the extremities of the processed areas. Considering the aforementioned, it is observable that the general distance between the laser tracks is directly proportional to the feed rate, meaning that higher values of the latter result in higher values of the former as well.

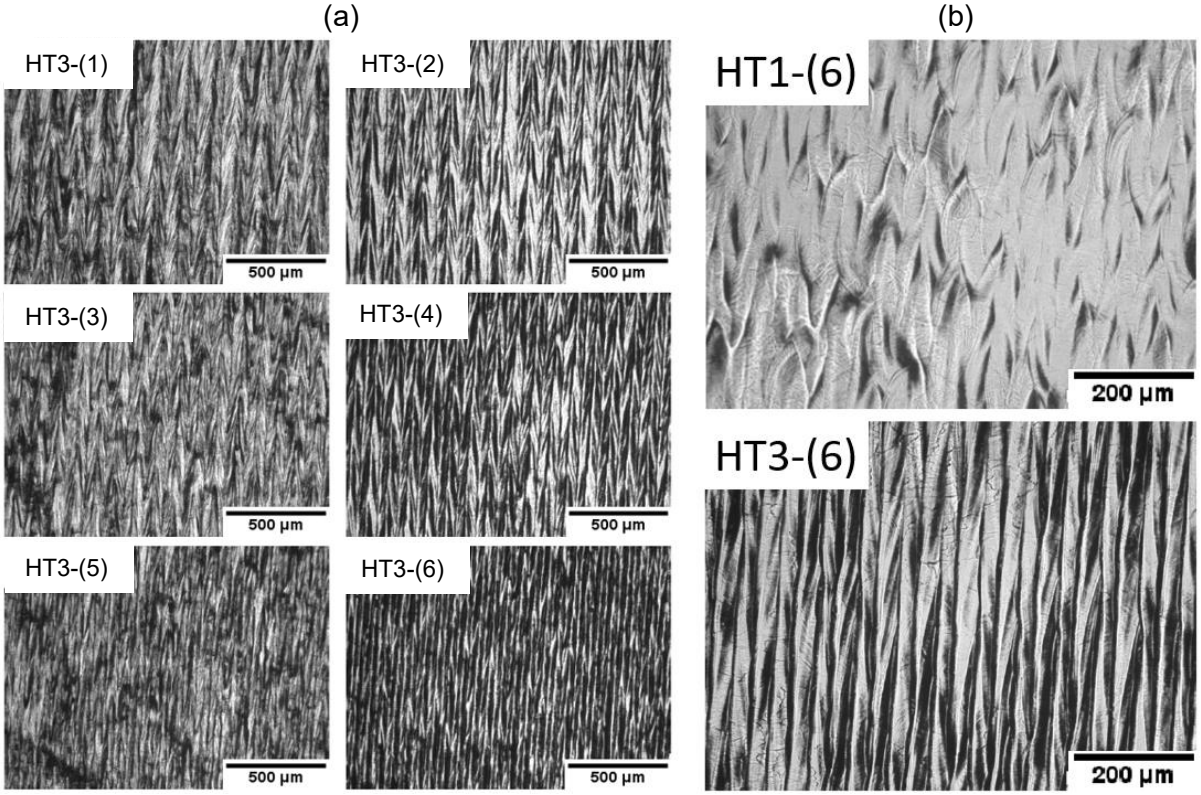

Figure 5-4. Optical microscopic images of: (a) the surface morphological analysis of the sample HT3, and (b) comparison between the samples of HT1-6 and HT3-6 [121].

Similarly to what was conducted for the HT1 workpiece, HT3 and HT5 were also morphologically assessed via micrographs. When altering the number of repetitions and feed rate, comparable effects were observed in the morphology of workpieces HT3 and HT1 (Figure

5-4a). Workpieces HT1-6 and HT3-6 are processed with the same parameters apart from laser power, with the former being subjected to 100 W, and the latter to 200 W. The outcome was an increased homogenization of the resulting morphology in the workpiece HT3-6 (Figure 5-4b). The better merging of neighboring tracks is observed for all 200 W processed HT3 workpieces, when compared to their corresponding 100 W processed HT1 parts.

The final HT sample to be analyzed is HT5, whose optical microscopic images for the morphological analysis can be seen in Figure 5-5. This workpiece was subjected to a laser power of 300 W, different numbers of repetitions, and different focal positions. Without defocus, i.e. focal position = 0 mm, groove forms with their characteristic linear edges between scanning paths were observed on the parts (Figure 5-5a). In combination with a lowered intensity caused by the defocus of +3 mm, low feed rates led to less noticeable groove forms, which nevertheless maintained their characteristic linear edges (Figure 5-5b). While the same defocus combined with high feed rates created a defect on workpieces HT5-7 and HT5-8, which is a consequence of deficient material melting in the presence of powder particles.

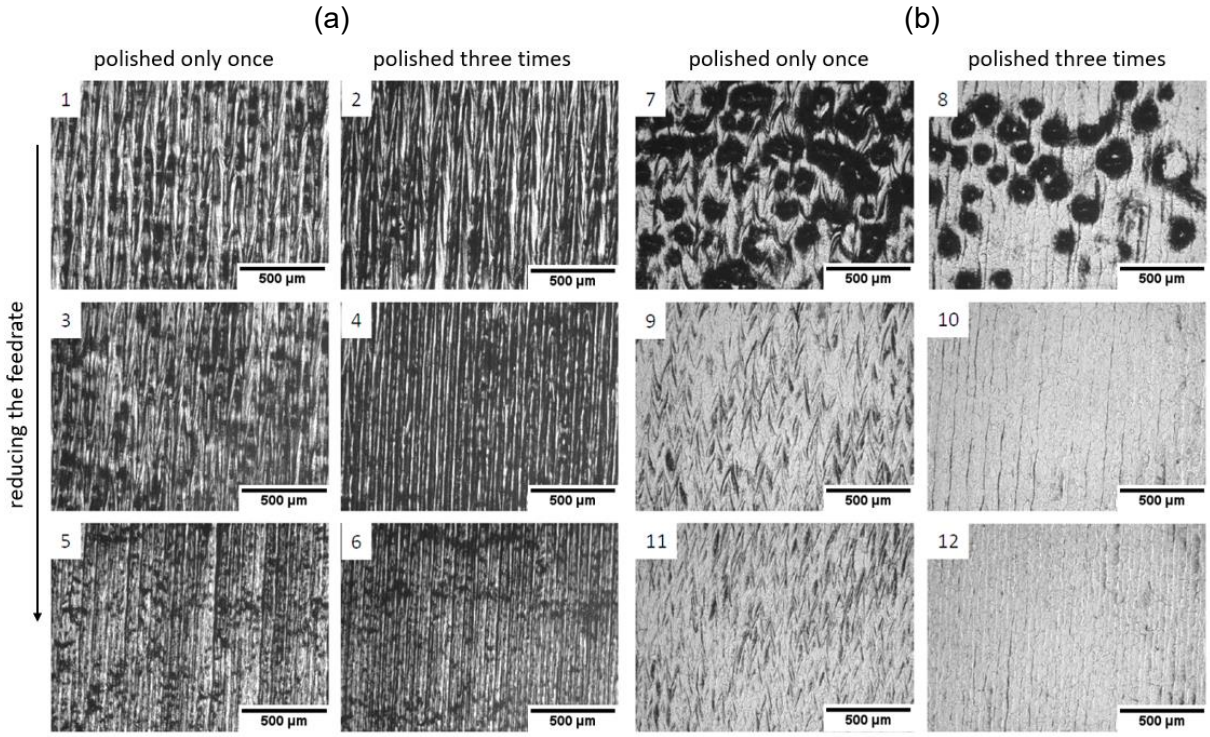

Figure 5-5. Optical microscopic images for the surface morphological analysis of: (a) sample HT5 (1–6), FOP = 0 mm, and (b) HT5 (7–12), FOP = +3 mm) [121].

On the surface of samples HT5-10 and HT5-12, the occurrence of the step structure could be observed (Figure 5-6). Different from the ripples and grooves, with the manifestation of the step structure the tracking boundaries become almost undistinguishable, making it hard to identify the residual signs of scanning overlap. With the specific parameters of the workpieces mentioned, an effective elimination of ripples and grooves was achieved. Although, the presence of step structures may hinder further surface flattening.

Step structures are generated because the grains within the material microstructure possess varied planar orientations, thus their deformation direction also varies when the material is subjected to heating and cooling rounds. The so-called steps on the material's surface represent the grains whose dislocation happened perpendicularly to the surface in question. Moreover, the texture inputted onto the workpiece's surface by the step structures generated

during cw LP is amplified as a function of the laser power and the hatch distance. The more the scan tracks overlap, the more heating and cooling rounds applied to the material, hence the elevated presence of this type of material deformation [159, 160]. Nevertheless, since these are microstructural deformations affecting the surface of the workpieces, the effect of step structures on the surface texture in a macro-scale is inconsequential when compared to ripples and grooves. Figure 5-7 presents SEM images of 3 structures formed, for comparison.

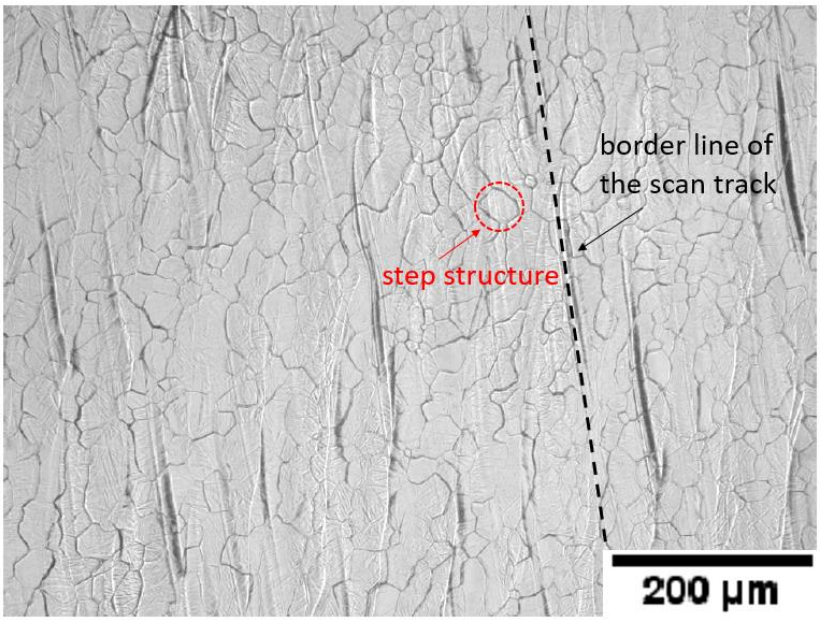

Figure 5-6. Step structures on the surface of the sample HT5-12.

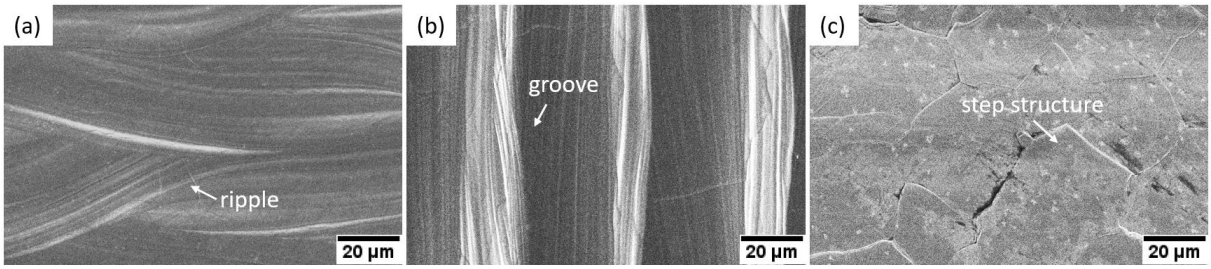

Figure 5-7. SEM images of the types of surface structures formed during laser polishing: (a) ripples, (b) grooves, and (c) step structure.

As mentioned, the laser polishing was also applied to AB samples, meaning that the surface was not submitted to any post-process following the LPBF manufacturing. Similarly to the HT samples, the surrounding powder was still attached to the part's surface. In contrast, following the heat treatment, a few samples had their surfaces sandblasted (SB), resulting in an alteration of surface morphology. With the attached powder roughly removed, the resultant surface presented uneven protuberances where there once were powder particles. Considering that a material's laser absorptivity is highly influenced by its surface topography, a smoother surface tends to sustain a higher reflectivity and, therefore, lower absorptivity. When that is the case during LP, the size of the melting region achieved is reduced and, potentially, the resultant smoothening effect is undesirably influenced.

A surface morphology assessment was carried out for the SB and AB workpieces and their respective micrographs are depicted in Figure 5-8 and Figure 5-9. The structures obtained on the surface of the distinct workpieces when the same parameter set is used are analogous,

although the results for the AB sample are overall more homogenous when compared to the SB sample's results. One justification for this observation can be the potentially higher laser absorptivity presented by the AB workpiece, discussed earlier, that leads to higher melt volume on the surface of the parts and, therefore, more material homogeneously distributed.

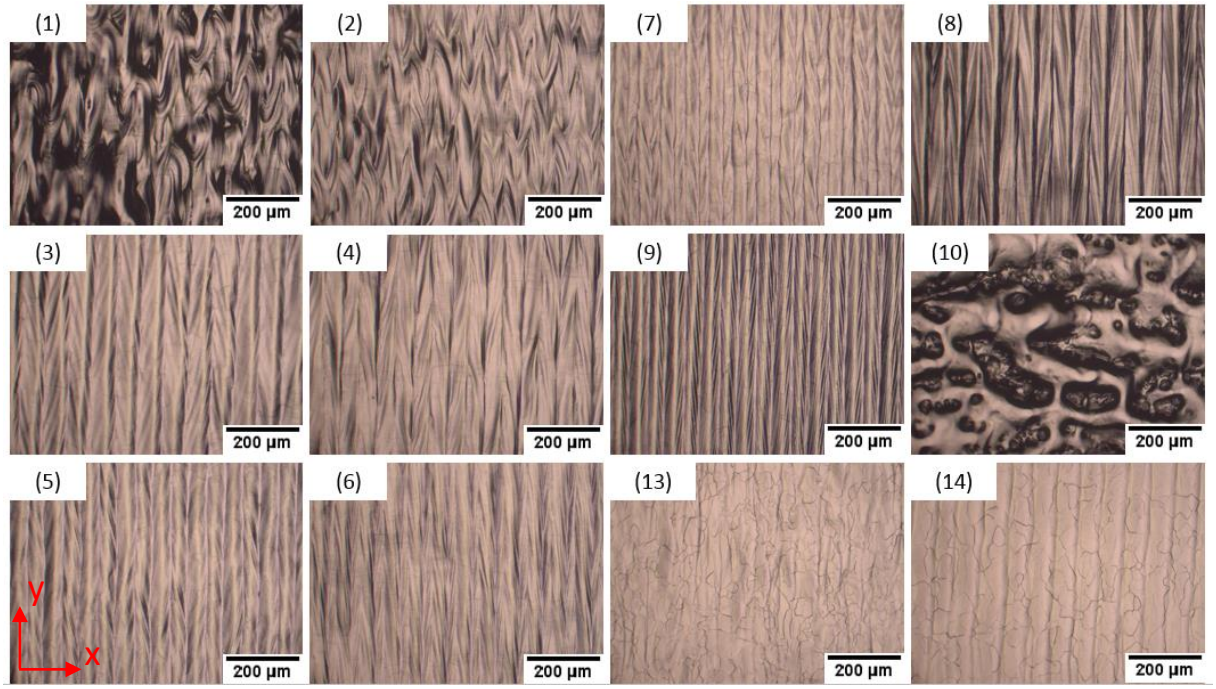

Figure 5-8. Optical microscopic images for the surface morphological analysis of the samples: SB (1–7): FOP = 0 and SB (10–14): FOP = +3 mm.

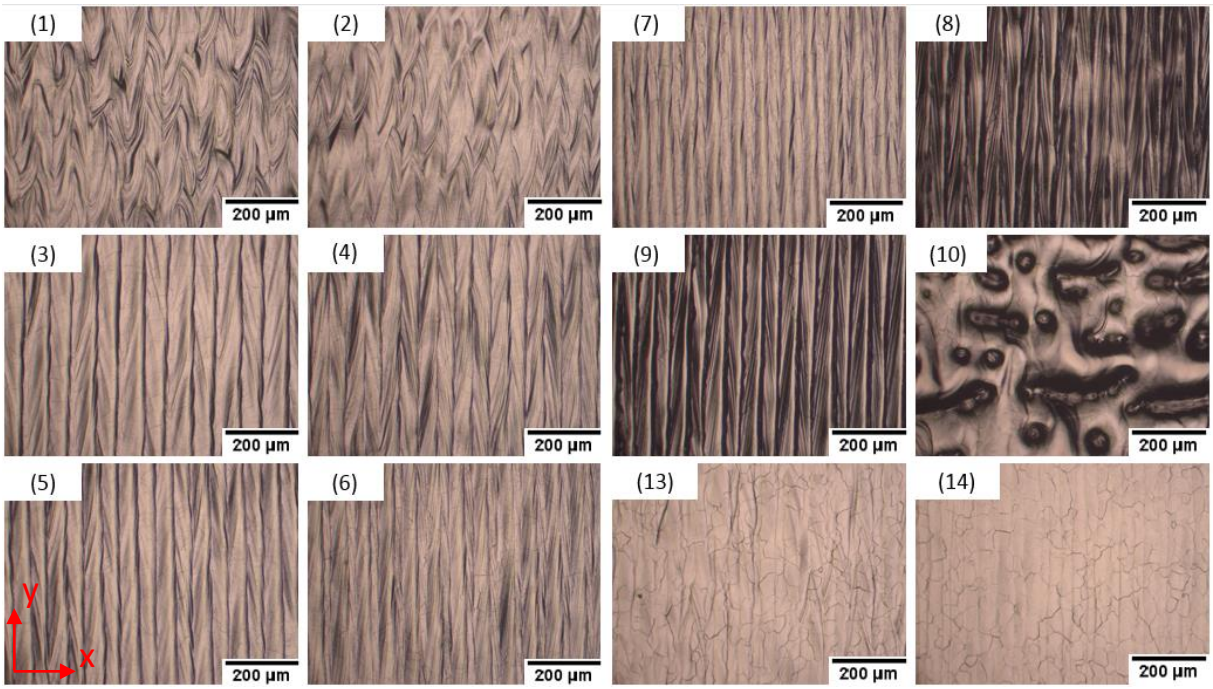

Figure 5-9. Optical microscopic images for the surface morphological analysis of the samples: AB (1–7): FOP = 0, and AB (10–14): FOP = +3 mm.

Throughout the LP procedure, the distance between two adjacent scanned paths, also known as hatch distance, dictates the axial dimension of the grooves. Illustrations of different distances obtained by adopting varying feed rates are displayed in Figure 5-10. Differently than expected, more than one groove dimension (d_1 and d_2) was observed on the illustrated workpieces AB3, AB5, and AB7, which have values for feed rate of 0.8, 0.6, and 0.4 m/min, respectively. As expected, the width of the grooves is reduced with the decreasing of the feed rate, which indicates that the laser tracks have a higher overlap and that, at a given point, the material is exposed to the laser beam for a longer period.

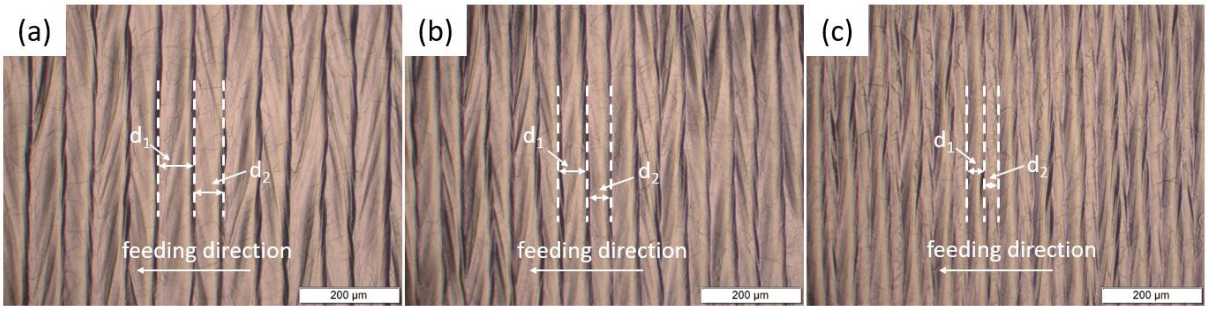

Figure 5-10. Optical microscopic images illustrating the widths of the grooves on the samples with feed rate of: (a) 0.8, (b) 0.6, and (c) 0.4 m/min.

Figure 5-11 depicts the interdependence of the feed rate and the two observed groove dimensions d_1 and d_2, together with an outlined linear fit for each dimension. Both mentioned dimensions tend to present higher values when the feed rate is elevated, which parallels to smaller laser track overlap.

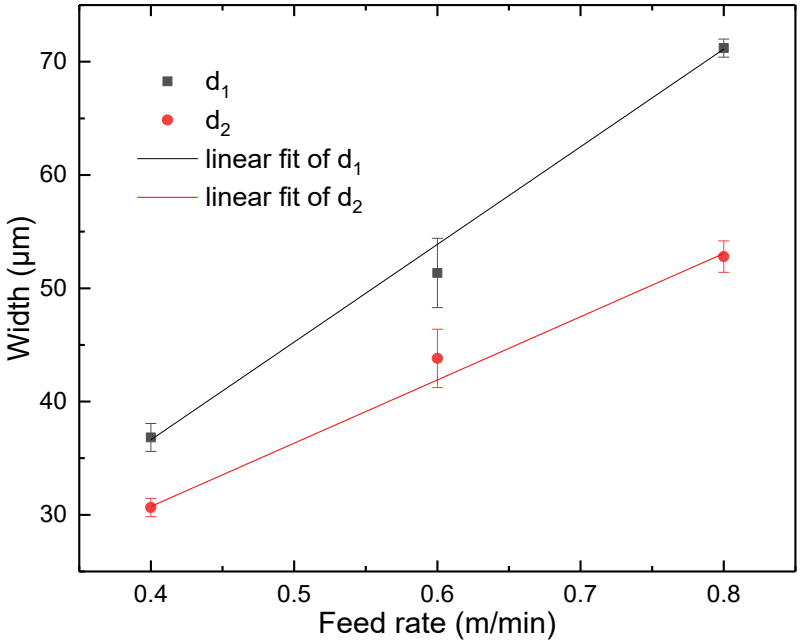

Figure 5-11. Widths of the grooves as a function of the feed rate.

The deficient melting efficiency observed on a couple of HT workpieces were detected on AB and SB samples as well, although for a different set of parameters (Figure 5-12). Its presence is slightly wider on the SB sample because its topography diverges from those of the AB and HT samples, leading to reduced laser absorptivity in comparison. This surface defect is called balling and as discussed, occurs due to insufficient intensity throughout a laser surface treatment [161, 162]. Figure 5-13 illustrates the balling formation principle, in which the liquid

material initially bounds the unmelted cores and can be solidified in that way, or it eventually flows though the solid pieces and is sintered together with the liquid material bounding and flowing through further unmelted cores.

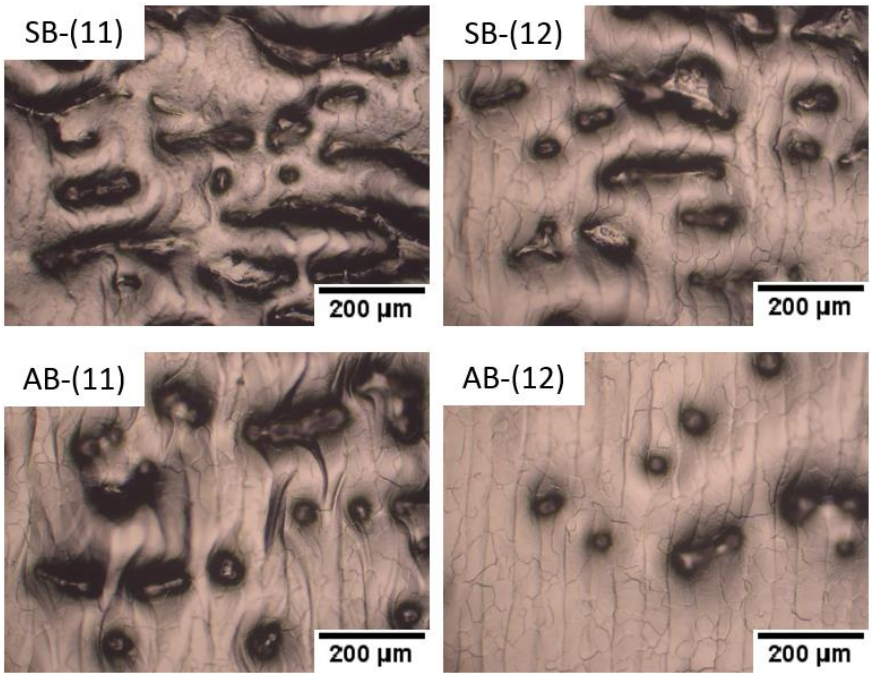

Figure 5-12. Optical microscopic images for the surface morphological analysis of the samples: SB11, SB12, AB11, and AB12 (FOP = +3 mm).

In addition to the low intensity of 0.07 MW/cm², another contributing factor for the balling formation is the capillarity driven distortion that elevated feed rates of 0.6 mm/min can create in the melt pool. Although the SB sample does not present attached powder on its surface, the humps resultant from the process, combined with the lower absorption of the laser energy by the material, are enough to sustain the balling effect mechanism.

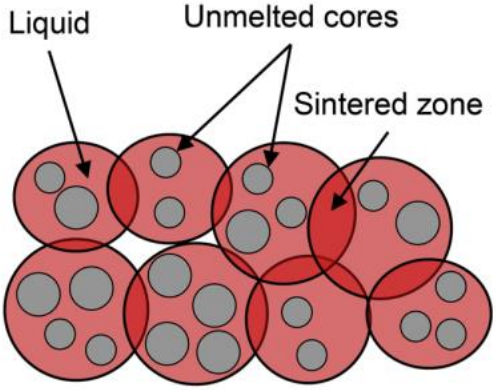

Figure 5-13. Schematic of the balling mechanisms [163].

5.1.2. Topography and heat affected zones.

For the assessment of microstructural changes within the heat affected zone (HAZ), caused during the laser polishing process, and the resultant topography of the samples, a cross-sectional analysis of the LPBF Ti64 samples subjected to the mentioned process was

performed in eight treated workpieces from each starting condition within the process chain, namely, AB, HT, and SB (Table 5-3).

Table 5-3. Scanning parameters of the laser polishing process for cross-sectional analysis of AB, HT, and SB Ti-6AL-4V AM samples.

Sample No.	Laser power (W)	Feed rate (m/min)	No. repetitions	Focal position (mm)	Intensity (MW/cm²)
CS1	100	0.6	1	0	1.27
CS2	100	0.4	1	0	1.27
CS3	200	0.6	1	0	2.54
CS4	200	0.4	1	0	2.54
CS5	300	0.6	1	0	3.81
CS6	300	0.6	3	0	3.81
CS7	300	0.8	1	3	0.07
CS8	300	0.6	3	3	0.07

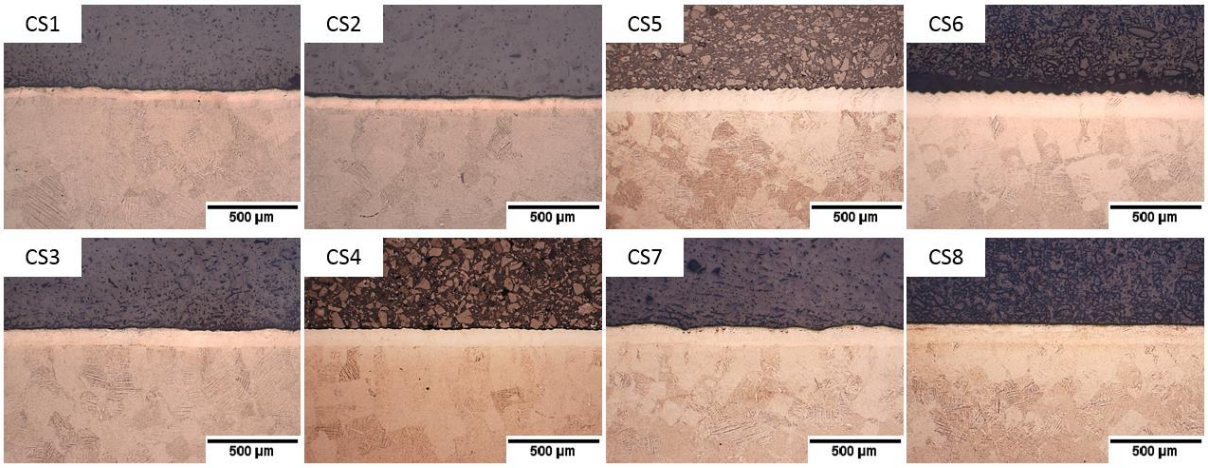

Figure 5-14. Optical microscopic images of the cross-sections of the laser polished HT samples.

The workpieces that allow the identification of both HAZ and melting regions are the HT and the SB, which are depicted in Figure 5-14 and Figure 5-15, respectively. The reason for it is that both mentioned workpieces were submitted to heat treatment following LPBF, which ensured the presence of (α+β)-phase in their microstructure. Under the microscope, such microstructures are clearly distinct from the α'-phase in the microstructure of the HAZ and melting regions. Differently, Figure 5-16 depicts the lack of demarcation between the bulk material of the AB workpiece and its HAZ and melting regions, which signify that only α'-phase is present in such workpiece both after LPBF and after LP due to their equivalent heating and cooling behaviors. Furthermore, when a particular surface of the workpiece is submitted to the LP process repeatedly, the boundary between the melted region and the HAZ becomes undistinguishable.

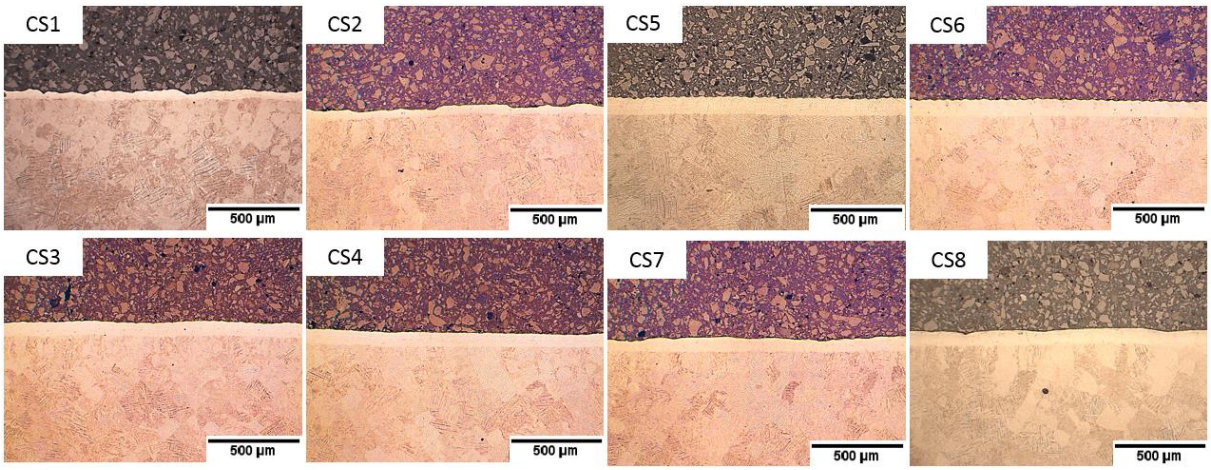

Figure 5-15. Optical microscopic images of the cross-sections of the laser polished SB samples.

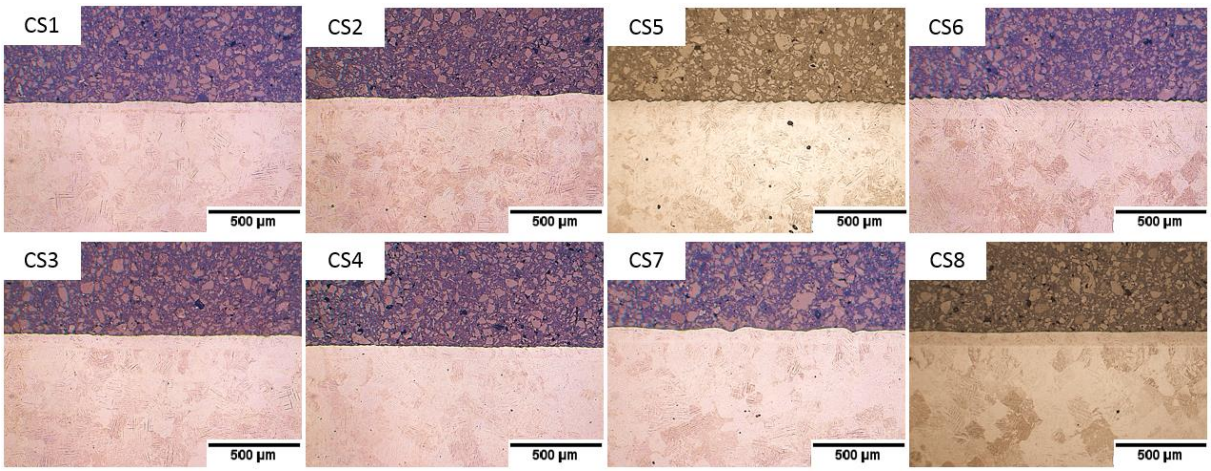

Figure 5-16. Optical microscopic images of the cross-sections of the laser polished AB samples.

Table 5-4. Depth of the HAZ on the cross-sections of HT, SB, and AB samples (unit: µm)

	CS1	CS2	CS3	CS4	CS5	CS6	CS7	CS8
HT	52.5 ± 4.3	55.8 ± 1.3	93.7 ± 1.8	94.1 ± 4.9	124.8 ± 5.5	134.9 ± 3.1	96.5 ± 13.3	103.4 ± 1.8
SB	46.9 ± 5.1	45.7 ± 7.4	76.8 ± 4.3	76.8 ± 1.9	99 ± 3.1	92.5 ± 3.1	79.6 ± 6.2	85.2 ± 2.5
AB	57.4 ± 1.8	64.2 ± 2.5	76.4 ± 1.3	69.5 ± 3.9	99.4 ± 2.4	108.7 ± 3.9	69.9 ± 9.2	75.5 ± 3.1

Table 5-4 gathers the measured values of HAZ depth for all assessed workpieces, while Figure 5-17 is a graphic comparison of these values. No major effects are observed on the HAZ depth values when the feed rate is altered, independently if the laser power adopted is 100 W (workpieces CS1 and CS2) or 200 W (workpieces CS3 and CS4). To assess the effect of the number of repetitions on the depth of the HAZ, samples CS5 and CS7 were compared to CS6 and CS8, respectively. With a minor discrepancy of around 10 µm between HAZ depth values when the assessed workpieces are compared as described previously, the assumption that the melted material has enough time to solidify prior to the initiation of the next repetition, because of extreme cooling rates involved in the laser polishing process, is confirmed. Therefore, the number of repetitions did not generate significant increase on the HAZ depth dimension. Finally, the shifting of the focal position from 0 to +3 mm was applied for the CS7

and CS8 workpieces, which resulted in a significant decrease of the HAZ depth values when they are compared to the values obtained for the CS5 and CS6 workpieces, respectively, which can be explained by the increased laser beam diameter from 100 to 760 µm and, consequently, extreme decrease of the intensity from 3.81 to 0.07 MW/cm². The discrepancy observed for the HAZ values indicated in Table 5-4 are mainly attributed to the thermal conductivity of the materials and to their levels of laser absorption. In this comparison, it is evident that, in most cases, the HT samples exhibited the highest HAZ values, which indicates a potentially greater thermal conductivity and/or laser absorption for such part.

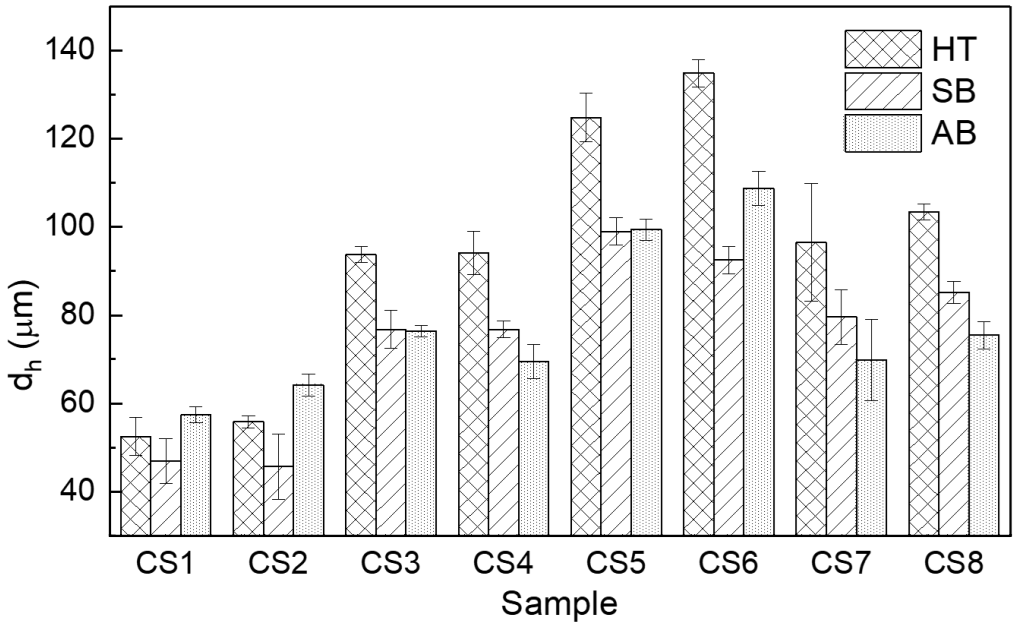

Figure 5-17. Comparison of the depths of the HAZ (d_h) of HT, SB, and AB samples.

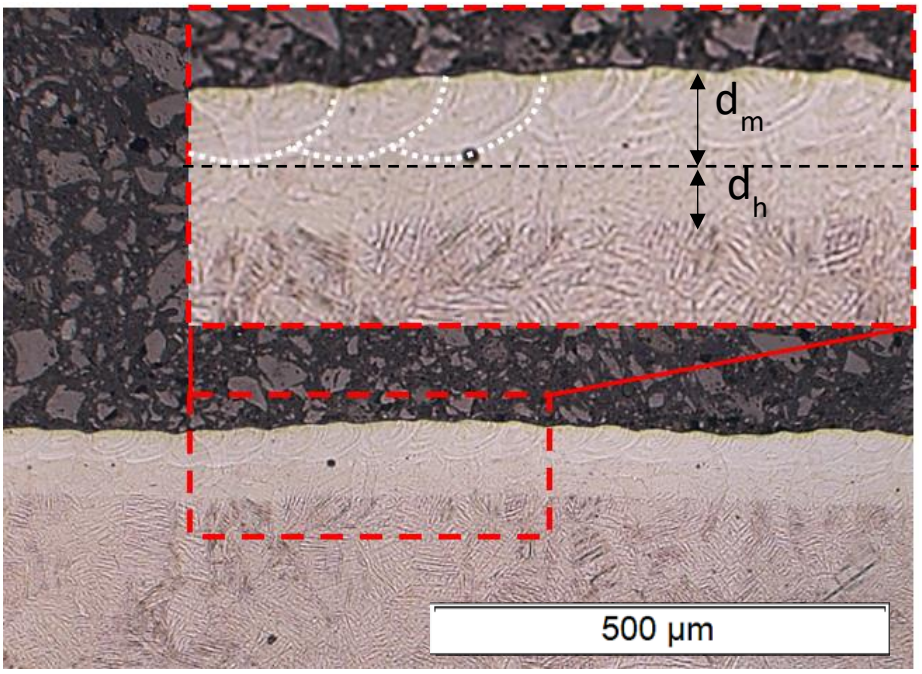

Figure 5-18. Optical microscopic cross-section image illustrating the molten pools (MP) of the sample SB-CS3.

The melted and HAZ regions presented by the CS3 workpiece from the sample that had SB as its starting condition is depicted in Figure 5-18, along with a zoomed image (red dashed box) of such regions for a better visualization of the melt pools' sizes and dispositions (white dashed lines), and the boundary between the melted region and the HAZ (black dashed line). The melted region dimension (d_m) is considered the distance from the workpiece's surface to the bottom of the identified melt pools, while the HAZ dimension (d_h) is the distance between the bottom of the identified melt pools to the end of the region with distinguishable microstructure modification. As displayed in Table 5-5, both mentioned dimensions tend to present higher values when the intensity is elevated. Nevertheless, the proportion between d_m and d_h in all cases is around 2, which signifies that, independently of the intensity applied, the melted region dimension has double the size of the HAZ dimension.

Table 5-5. Depth of the HAZ (d_h) and molten pools (d_m) of SB samples.

Sample No.	Intensity (MW/cm²)	d_h (µm)	d_m (µm)	Ratio (d_m/d_h)
CS1	1.273	22.5±3.3	46.9±5.1	2.08
CS2	1.273	23.4±4.9	45.7±7.4	1.95
CS3	2.547	38.0±1.8	76.8±4.3	2.02
CS4	2.547	35.5±1.9	76.8±1.9	2.16
CS5	3.820	47.3±1.2	99.4±1.2	2.10

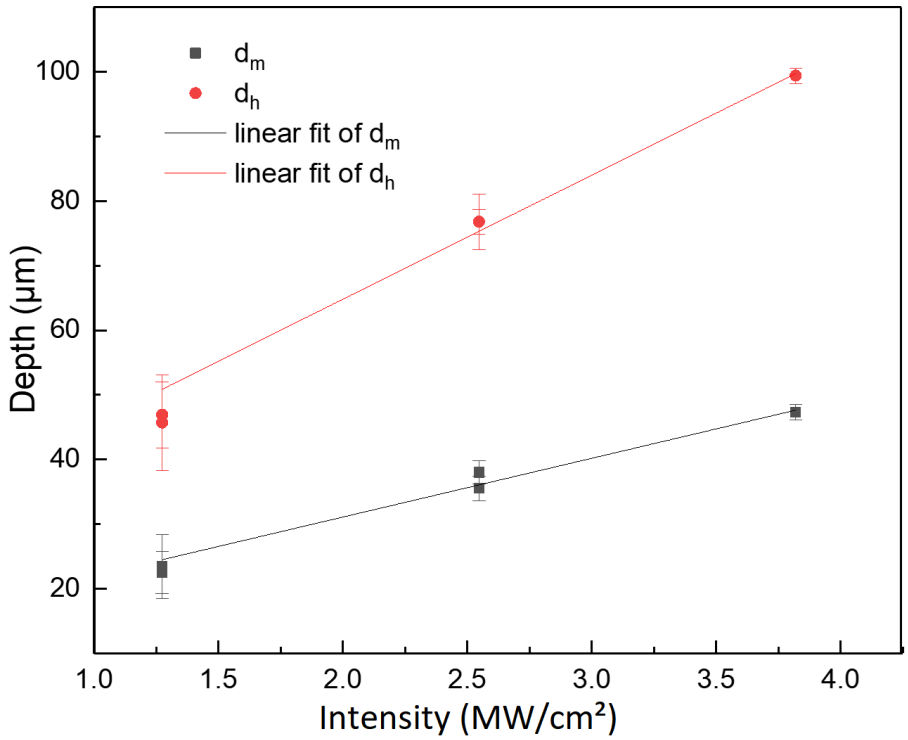

Figure 5-19. Depths of the HAZ and MP as a function of intensity.

Figure 5-19 depicts the interdependence of the intensity applied and the dimensions d_m and d_h, together with an outlined linear fit for each dimension. As presented in Table 5-5 and previously discussed, both mentioned dimensions tend to present higher values when the intensity is elevated. Additionally, the gradient of the d_h curve is nearly double the gradient of

the d_m curve (19.20 against 9.09), which is comparable to the proportion between the assessed dimensions themselves.

In terms of surface topography, Figure 5-20 presents a comparison of the LPBF parts before any type of post-processing, and the samples AB, HT, and SB after laser polishing. These cross-section images confirm what was already stated in the surface morphology analysis, the laser polishing successfully removed the attached powder from the surface of the samples. Furthermore, despite the dissimilar initial condition of the SB surface, after the laser polishing the resultant topography is analogous to the other samples.

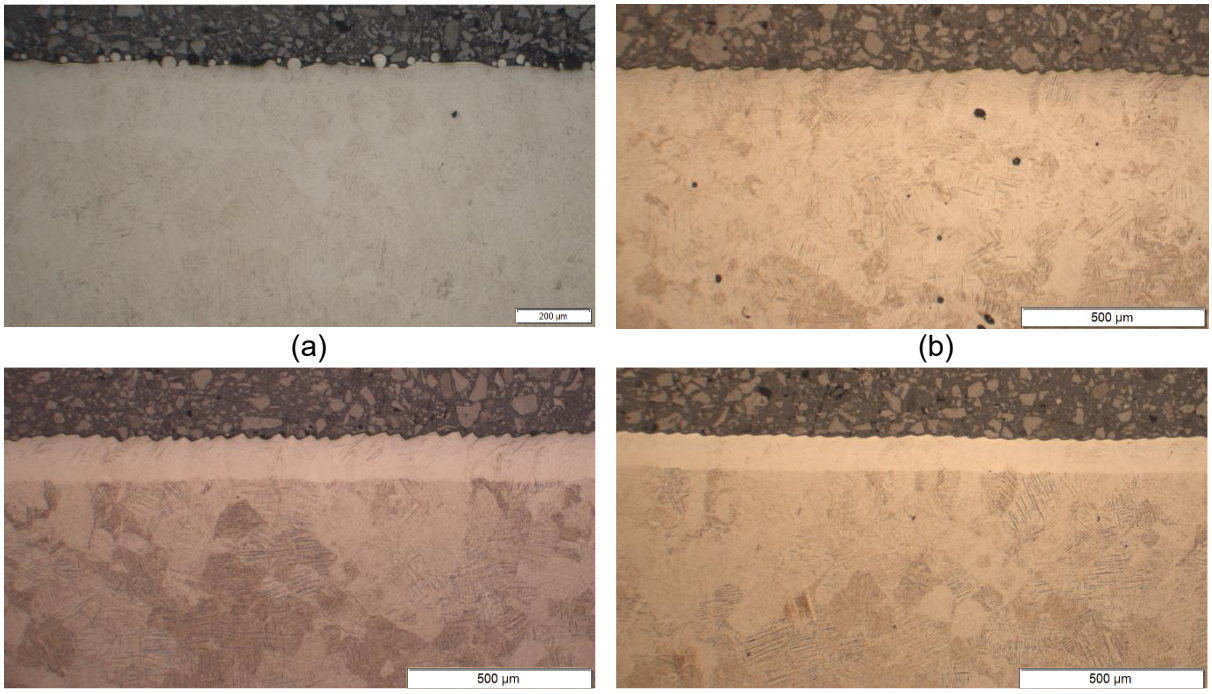

Figure 5-20. Comparison of the surface topography of: (a) AB sample before laser polishing, (b) AB sample after laser polishing, (c) HT sample after laser polishing, and (d) SB sample after laser polishing. Reproduced from [122] with the permission of the Laser Institute of America.

5.1.3. Microstructure evolution

The microstructure within the cross-section of the AB sample without any laser treatment is revealed in Figure 5-21b, d and Figure 5-22b, which confirm the presence of equiaxed grains where acicular α'-phase occurs. The α'-phase preferential growth in the axial orientation, with almost no growth in the radial orientation, suggests significant anisotropy [164]. When adopting LPBF to build parts in Ti64, a substantial amount of very thin acicular α'-phase oriented towards a particular direction is formed since the mentioned manufacturing approach involves extremely high cooling rates thoroughly discussed in section 3.2.3. Ti64 parts produced via LPBF were previously reported to have complete absence of β-phase [55]. Nevertheless, the occurrence of β-phase following the LPBF has also been reported [165], and it seems to be linked to the α'-phase decomposition that can occur inside the machine if the cooling rates decrease drastically in specific points of the material when the part being build is massive in volume and is completely surrounded by a great volume of metallic powder. Common parameters of the LPBF process, such as layer thickness and dwelling time, could affect greatly this potential β-phase occurrence [43]. When the material is being scanned by the laser beam, the temperatures to which it is subjected surpass the β-transus, which is the

temperature threshold for the exclusive presence of β-phase (995 ± 20 °C). The cooling rates of the material throughout the LPBF can reach values between $1.2 \cdot 10^4$ K/s and $3 \cdot 10^5$ K/s, which are greater than the value of 410 K/s that is linked to the occurrence of α'-phase.

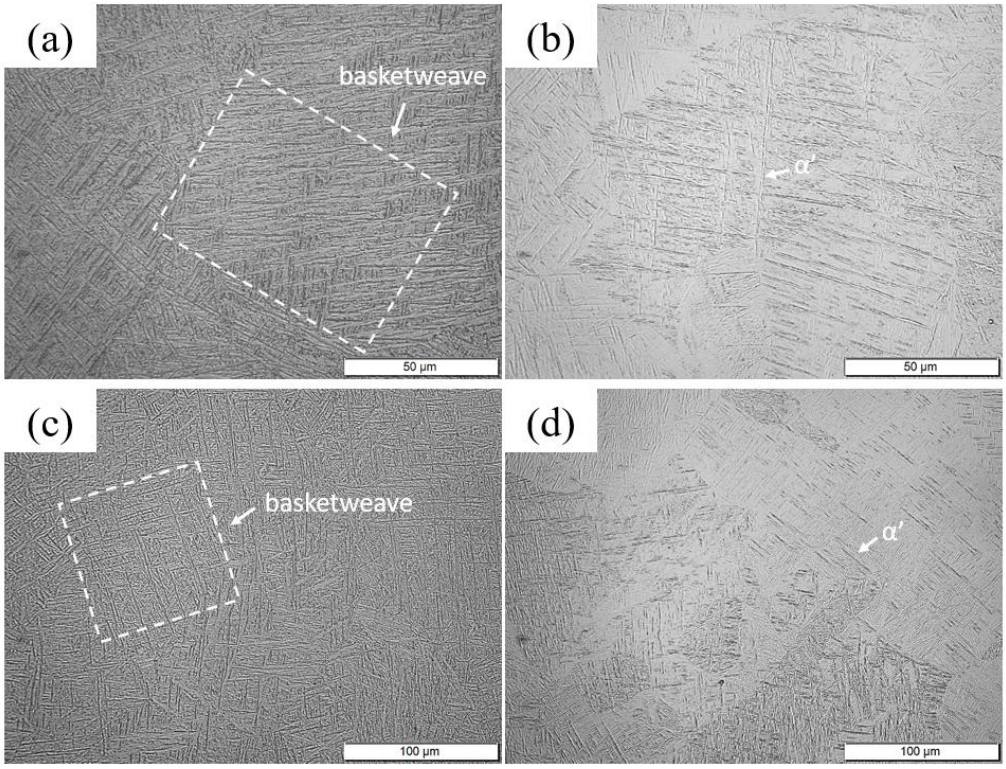

Figure 5-21. Optical microscopic images of the cross-sections of the base material: (a,c) basketweave (α+β)-structure (HT and SB samples), and (b,d) α'-phase structure (AB).

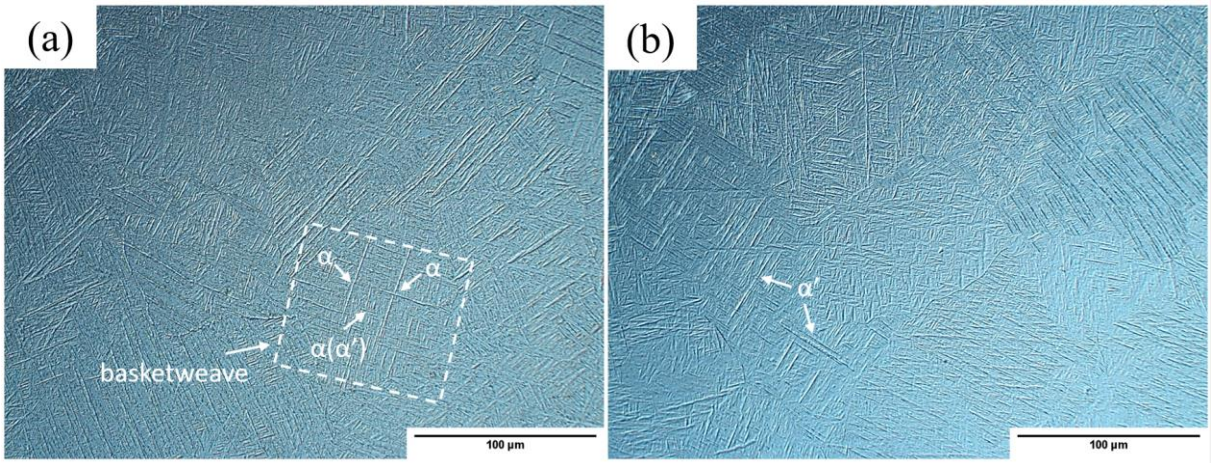

Figure 5-22. Polarized image of the cross-sections of the base material: (a) basketweave (α+β)-structure (HT and SB samples), and (b) α'-phase structure (AB).

The microstructure within the cross-section of the HT and SB samples without any laser treatment is revealed in Figure 5-21a,c and Figure 5-22a, which confirm the similarity between them, as they were submitted to heat treatment at the same time. This means that there are no divergences in the mentioned parts thermal record. Correspondingly, the basketweave structure is present, in both cases, when assessing the mentioned samples, since its occurrence is credited to the mechanism that allows the formation (α+β)-phase that happened

when the parts were subjected to the heat treatment. Briefly, the mentioned mechanism involves using temperatures above 705 °C, which is the α-dissolution temperature (T_{diss}), to guarantee that the thin acicular α'-phase will decompose and that the (α+β)-phase will be obtained once in the material is in thermal equilibrium [165]. Figure 5-22a depicts how the threadlike α-phase propagated inside the retained β-phase grain boundary. In case the β-transus temperature is not surpassed during the heat treatment, the amount of β-phase in the final (α+β)-structure can be impaired, which can affect the mechanical performance of the printed component [166].

The assessment of the laser polishing process effects on the microstructure of the Ti-6Al-4V parts for different steps of the post-processing chain was performed following the assessment of the microstructural conditions for the reference samples. Figure 5-23 depicts the molten regions of CS5 from the different samples assessed (HT, AB, and SB) following laser polishing. Within the melting zone, i.e., the upper most portion of the treated workpieces, the thin acicular α'-phase is seen. The α'-phase formation mechanism is the same for laser polishing and LPBF and is related to the high cooling rates values that can reach between $1.2x10^4$ K/s and $3x10^5$ K/s.

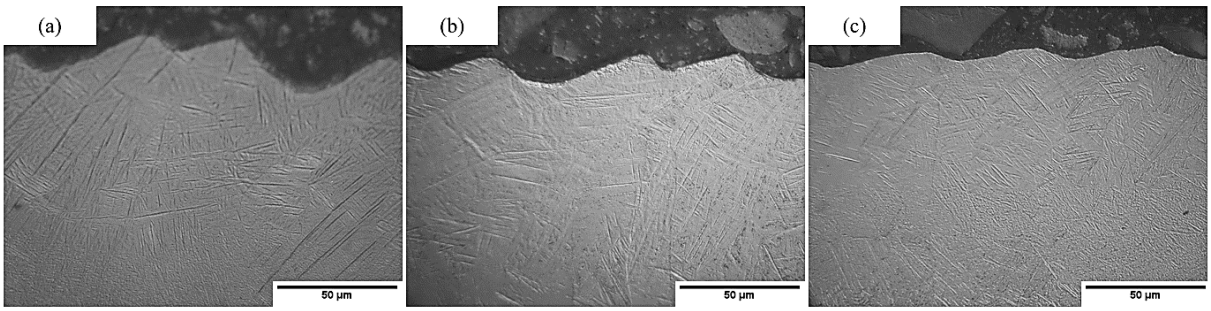

Figure 5-23. Optical microscopic cross-section images of the re-melted zones of the CS5 on samples: (a) HT, (b) AB, and (c) SB.

Figure 5-24 and Figure 5-25 exhibit the SEM micrographs of the molten regions and substrates of the samples HT, SB, and AB, respectively. This approach is adopted to corroborate the findings reached using the optical microscope by employing a technique that allows a similar investigation with considerably higher magnification and resolution. Similarly to the conclusions drew in the course of the optical microscopy assessment, α'-phase is present in the molten regions of the AB, HT, and SB samples subjected to laser polishing, while (α+β)-structures are only present in the substrate of the HT and SB samples. Still in Figure 5-25, the bcc β-phase and the hcp α-phase of the HT and SB samples can be identified by the light and dark colored portions of the image, respectively [167]. The (α+β)-structure occurs because of the decomposition of the α'-phase throughout the heat treatment process, such mechanism was discussed in detail in section 3.2.3. In contrast, α'-structure is present in the substrate of the AB sample. Figure 5-26 shows a comparison, on the same sample, of the microstructural aspects before and after laser polishing. It is possible to observe that three zones with different microstructures become present after the laser polishing of a sample submitted to heat treatment. The upper surface of the processed workpiece is composed of threadlike α'-phase, the middle area is the transition zone affected by the laser heat, and finally, the zone at the bottom characterizes the lamellar (α+β)-phase at the core of the heat-treated workpiece.

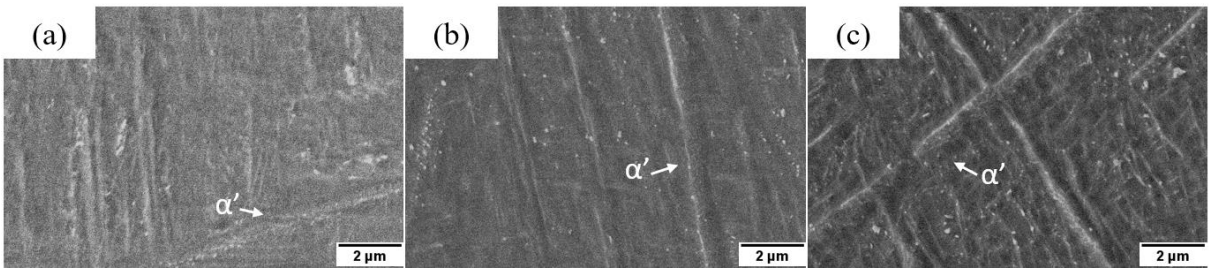

Figure 5-24. Scanning electron microscopic images of the molten regions of the CS8 on samples: (a) HT, (b) SB, and (c) AB.

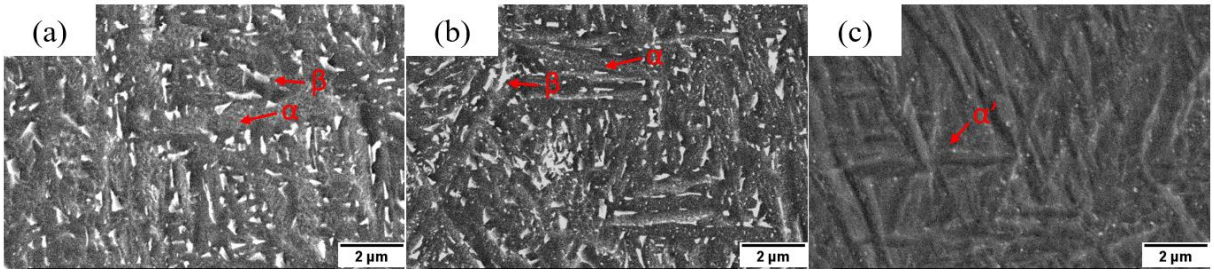

Figure 5-25. Scanning electron microscopic images of the base material cross-sections of the CS8 on the samples: (a) HT, (b) SB, and (c) AB.

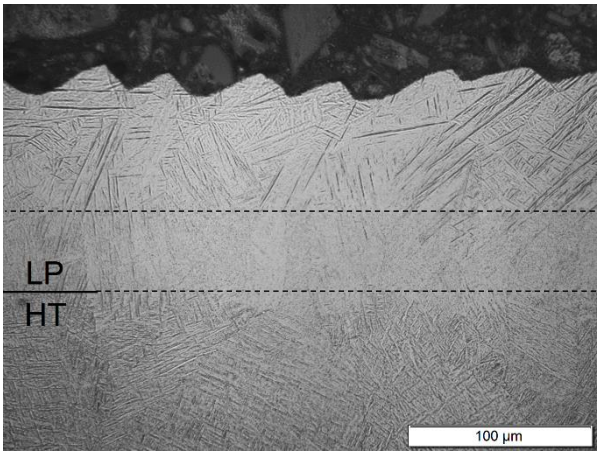

Figure 5-26. Cross section analysis: optical image of Ti-6Al-4V microstructure after LP (upper region) and HT (bottom region). Adapted from [122] with the permission of the Laser Institute of America.

XRD examination is an additional approach that can be used to assess the microstructure phases within the workpieces in their starting state and following laser polishing. The hcp lattice is present in α- and α'-phases, as mentioned in section 3.2.3, and in principle they cannot be differentiated between them in XRD results. Divergences in their XRD patterns can be identified with widening of the reflexes and minor changes on the 2θ angle, which are correlated to the higher residual stress condition of the α'-phase.

In Figure 5-27 the reflexes of the α-, α'-, and β-phases are detailed with their respective lattice planes identification. The α-, and α'-phases are present in the samples in all initial conditions, while β-plane (200) is identified in the XRD results of the reference HT and SB samples without any laser treatment. The difference between them being that the intensity of the mentioned reflex seems significantly reduced for the former, particularly when contrasted with the main α/α'-plane (101) reflex present in the HT workpiece without any laser treatment.

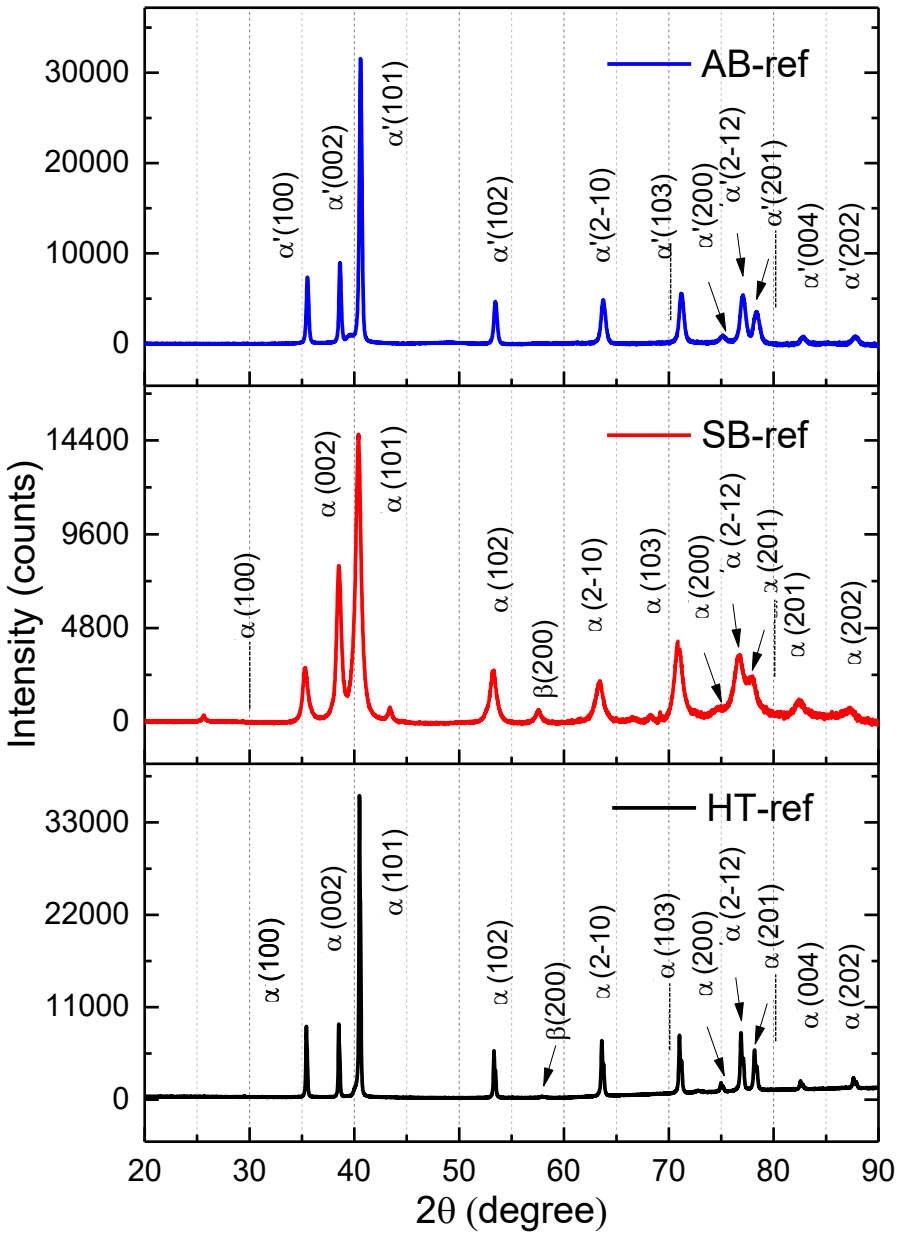

Figure 5-27. X-ray diffraction diagrams of the reference samples AB, SB, and SB before the laser polishing.

For the proper recognition of the main β-plane (110) reflex, the XRD results were investigated with higher focus for the Bragg angles (2θ) between 34° and 44° (Figure 5-28). It is possible to observe in Figure 5-28 that the α/α'-reflex (101) of the reference SB workpiece possesses an augmented full width at half maximum (FWHM) because it is combined with the reflex of the β-plane (110). Moreover, an elevation adjacent to the reflex of α/α' (101) at around 40° makes it more prominent than the opposite side of the reflex. Comparable in terms of behavior but reduced in size, such elevation is spotted in the HT workpiece without any laser treatment as well. The presence of the β-phase in the SB and HT workpieces not subjected to laser polishing causes the location of the α/α'-reflex (101) to change. The shifting of the Bragg angle because of the presence of the β-phase, seen from the detailed images of the XRD patterns, can also confirm the assumption that the broadening of all other reflexes width represents a different stress condition and probably different microstructure. Based on the XRD assessment, the HT

and SB workpieces in their starting conditions contain exclusively (α+β)-phase, while the AB workpiece in its starting condition is predominantly composed of the martensitic α'-phase.

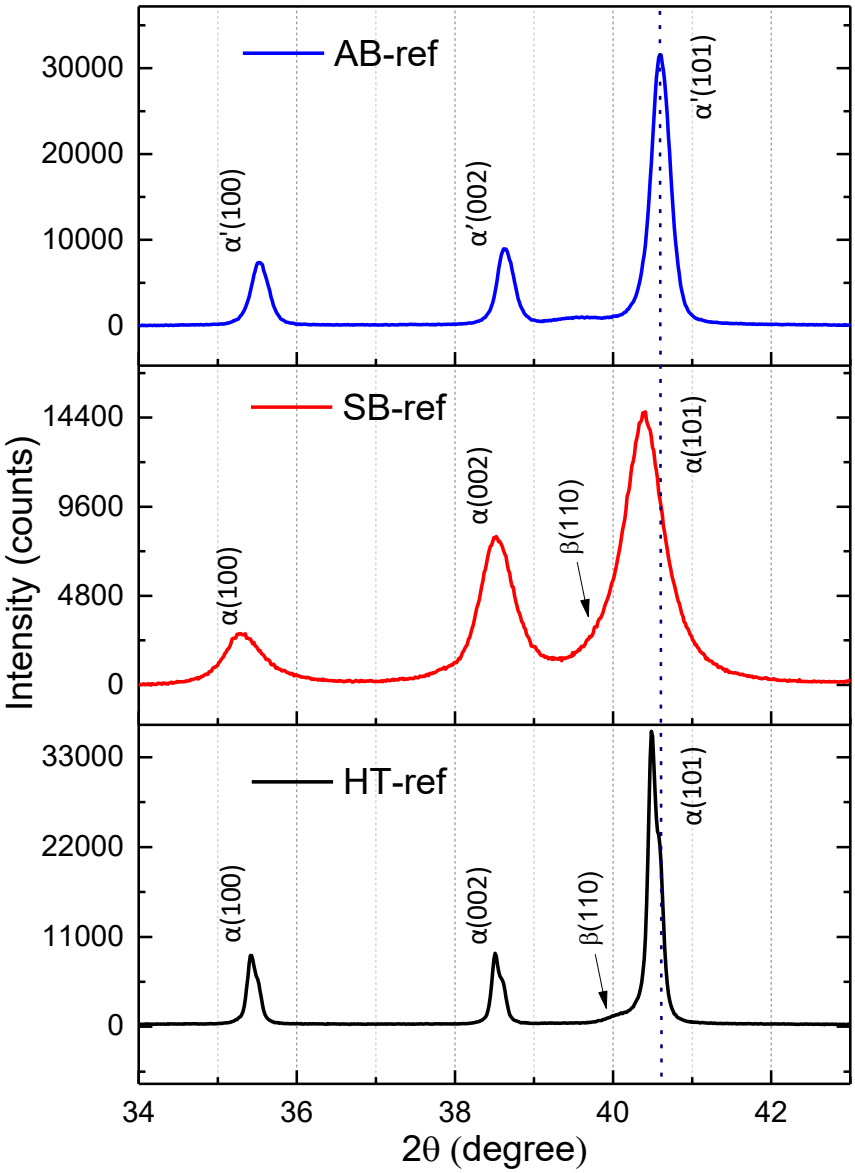

Figure 5-28. Detailed X-ray diffraction patterns, in the range of 34 to 44 degrees of the samples AB, SB, and HT before laser polishing.

Figure 5-29 depicts the XRD diagrams of the CS4 on HT, SB and AB workpieces subjected to laser polishing, and the results obtained display undistinguishable behavior in every instance. Similarly, such results correspond to the AB workpiece without any laser treatment, which indicates the matches of only martensite following laser polishing. This conclusion is based on the previously mentioned peak positions and widening. Since no β-phase peaks were identified, Figure 5-29, such as the image for the reference samples, describes the peaks of the α- and α'-phases with the corresponding lattice planes. Knowing the chemical composition of the parts used in this study, and that the vanadium element is used as a β-phase stabilizer if the material is submitted to the propitious cooling rates, the absence of the peaks of β-phase in the HT and SB samples after laser polishing confirm that the microstructure obtained consisted only of martensite α'.

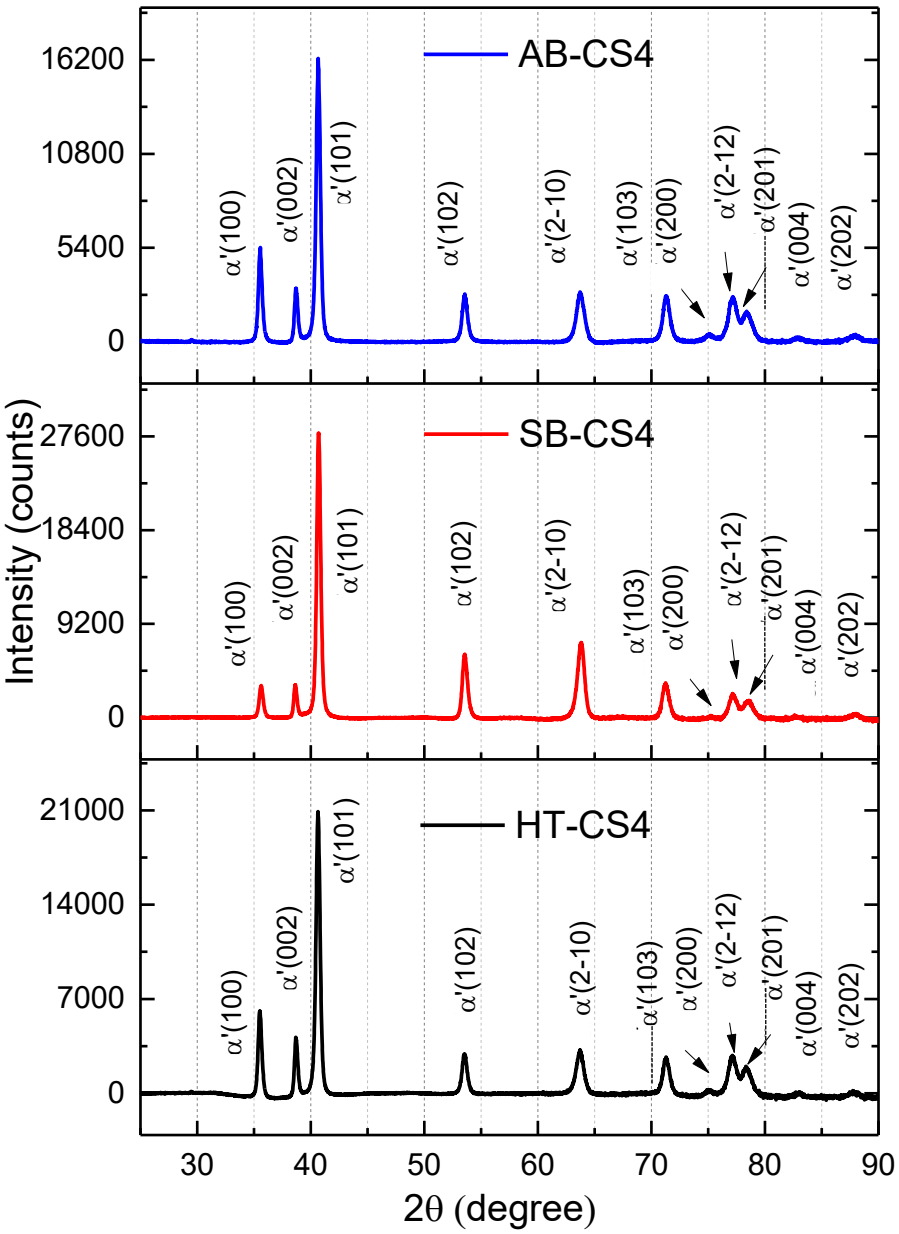

Figure 5-29. X-ray diffraction diagrams of the CS4 surfaces after the laser polishing for samples AB, SB, and HT).

Corroborating the microscopic images, the XRD analysis showed that the predominant microstructure following the laser polishing process is martensitic α'-phase. Confirming also that the modification from (α+β)-phase to α'-phase occurred throughout the mentioned post-process step. Additionally, any microstructural divergences present in the substrate of the workpieces in their starting conditions (AB, SB, HT) no longer exist in the superficial region that are directly affected by the laser polishing.

5.1.4. Hardness

The hardness of the workpieces CS1 to CS8 are assessed for the materials in all three initial conditions, namely, AB, HT, and SB. One example of how the measurements were performed is depicted in Figure 5-30. In it, the indentation marks, together with different regions of the LP workpiece (molten pool, HAZ, and substrate) in which they are contained, can be seen on a

micrograph of the SB-CS4 workpiece. The indentation started near the upper surface of the samples and continued going deeper towards the bulk material with a fixed distance between each indent. The same approach was followed for the analysis of all the samples.

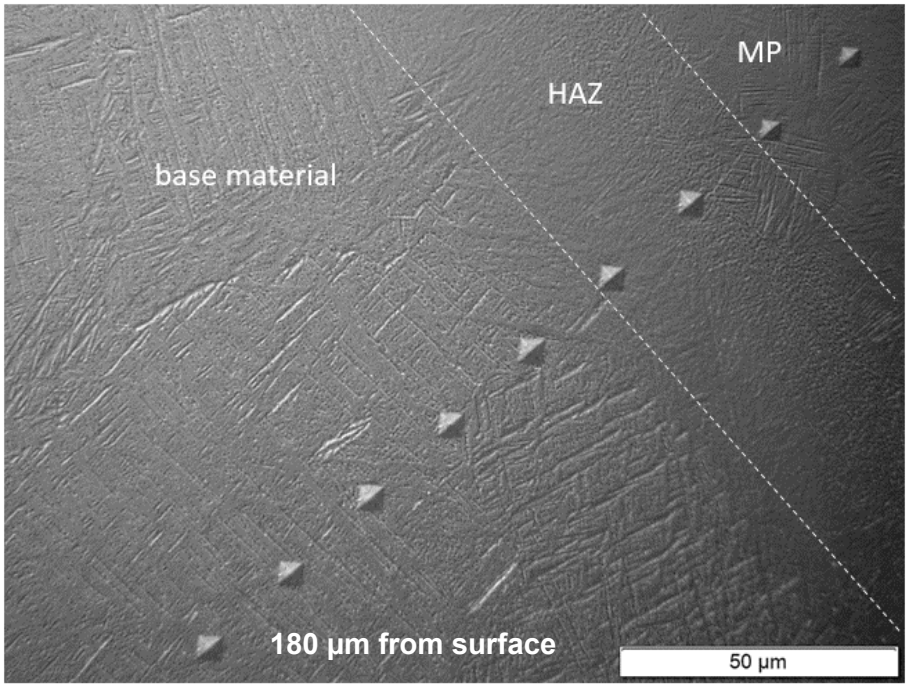

Figure 5-30. Optical microscopic cross-section image of the sample SB-CS4 with the indentations conducted during the Vickers hardness measurement.

The two indentation marks observed closer to the surface are clearly reduced in size when compared to the following marks. This indicates that α' microstructure is present in the molten pool (MP) of the SB-CS4 workpiece, hence the potential higher hardness when compared to the substrate and HAZ regions.

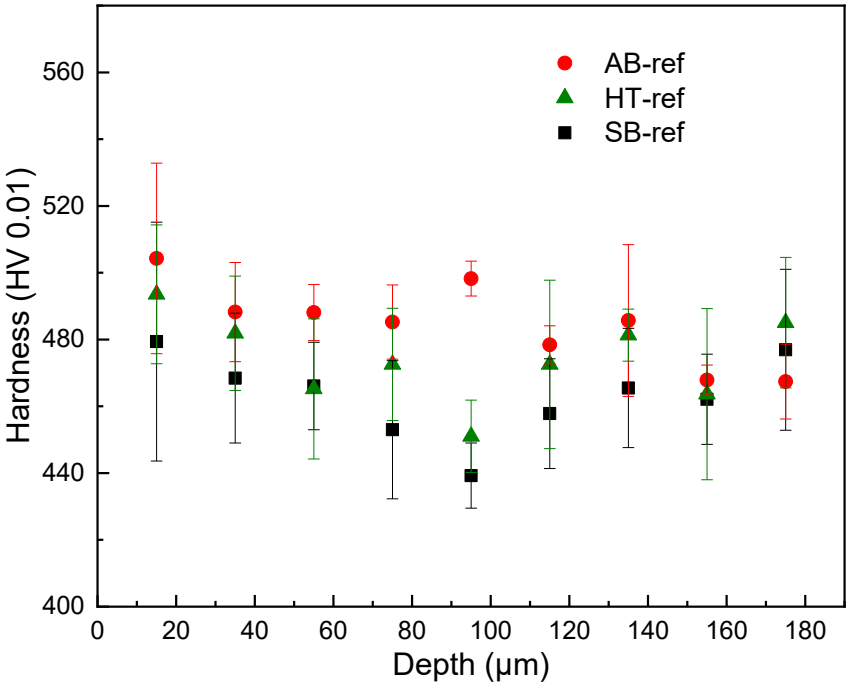

Figure 5-31. Vickers hardness values of the initial workpieces SB, AB, and HT.

The hardness of the samples in their starting conditions, i.e., not yet subjected to LP, are depicted in Figure 5-31. It states that no meaningful difference is observed in the hardness results of LPBF Ti64 when subjected to heat treatment and/or sandblasting. The difference is even less significant when the indentation reaches a depth from the surface of around 110 µm, which can implicate that the LPBF process itself affects the microstructure and stress conditions of AB samples.

As the molten pools and HAZ could be better identified in the SB samples, these will be presented first in this section. The measurement outputs, starting at 20 µm from the top of the SB workpieces and moving downwards in 20 µm steps, are shown in Figure 5-32 and Figure 5-33. The molten pool (d_m) and HAZ (d_h) deepness values were obtained from the topography and cross-sectional assessment, and they separate the three potential regions of a workpiece subjected to LP, namely MP, HAZ, and substrate.

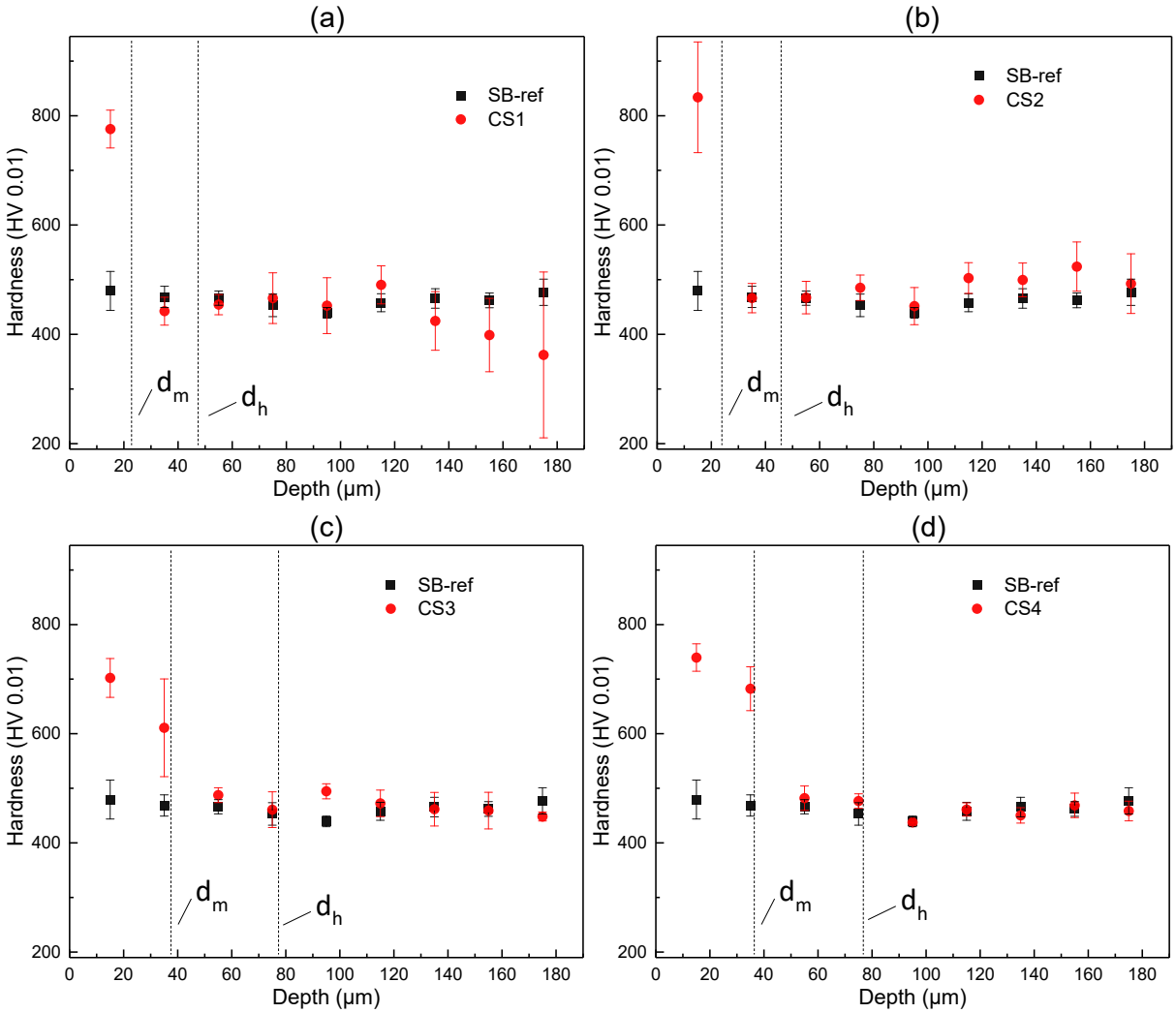

Figure 5-32. Vickers hardness values at various depths from the surface of the SB samples: (a) CS1, (b) CS2, (c) CS3, and (d) CS4. The melting and HAZ depths of each sample is determined by the boundaries d_m and d_h, respectively.

As exposed in Figure 5-32a, the average hardness of workpiece SB-CS1, measured 15 µm from the surface shows a significant increase when compared to value obtained SB samples not subjected to LP, with the former presenting 775.6 HV0.01 against 479.4 HV0.01 from the latter. For the same sample, deeper measurement points, within the HAZ and in the substrate

regions, didn't present the same noteworthy hardening effect. A similar behavior is observed for the samples SB-CS2, SB-CS3, and SB-CS4 in Figure 5-32b, c, and d, respectively, where the hardness values within the MP section are in the range of 800 HV0.01, which is significantly higher than the same region for the reference sample (around 500 HV0.01), even when the MP depth is large enough for two measurement indents to be obtained within the assumed area. The average hardness of the molten region of workpiece SB-CS2, measured 15 µm from the surface is 834 HV0.01, which is a significant increase when compared to value obtained SB samples not subjected to LP. On the other hand, deeper measurement points didn't present the same noteworthy hardening effect if compared to SB workpieces not subjected to LP. Because of the deeper molten region, that occurs with an association of parameters that resulted in a higher laser intensity, two measurement points could be obtained in the MP of workpieces SB-CS3 and SB-CS4. The results obtained showed hardness values of around 700 and 600 HV0.01 for measurement depths of 15 and 35 µm, respectively, on sample SB-CS3. Similarly, the values obtained for the sample SB-CS4 for depths of 15 and 35 µm are even higher, but also in the 700 HV0.01 range. This suggests that the molten regions of the SB-CS3 and SB-CS4 workpieces present a higher hardness than their counterpart not subjected to LP, while in the HAZ and bulk material there is no evident difference, which can confirm the previous analysis of a potential microstructural change from the heat treated (α+β) to the laser treated (α') microstructure.

The results described above are comparable to the works of Liang (2020) [98] and Marimuthu (2015) [99], summarized in Table 3-8, which observed the same behavior in Ti64 parts submitted to laser polishing, i.e., increased hardness within the HAZ depths and equivalent results between the reference and laser treated materials within depths beyond the HAZ. Although, the values of HAZ depth and micro hardness are not comparable because different laser sources, intensities and overall parameters were adopted among the studies.

Hardness measurements with high error at certain depths could have been affected by imperfections generated throughout the LPBF process, such as pores. Assumed defects were identified in the substrate in the cross-sectional assessment and, although these defects can also be caused during laser post-processing, the same analysis showed not to be the case for the parameter sets adopted in this work. The origin of such uncertainties can also be linked to the measurement procedure and human error.

Figure 5-33a to d depicts the outcomes of the hardness measurements of samples SB-CS5 to CS8, in which a reduction of around 50 HV0.01 in the discrepancy between the hardness within the molten region and the substrate not subjected to LP is observed. Regarding the differences in the parameter set of all samples, the intensity values from highest to lowest were presented in the following order, CS5 and 6, CS3 and 4, CS1 and 2, and CS 7 and 8. The assessment of the SB samples hardness showed that the ideal intensities for achieving a hardening effect on the surface of heat-treated Ti-6Al-4V samples with laser polishing were 1.273 (samples CS1 and CS2) and 2.547 (samples CS 3 and CS4) MW/cm^2. In contrast, the hardening effect was reduced on SB samples when using the intensity of 0.066 (CS 7 and CS8) and 3.820 (CS5 and CS6) MW/cm^2. The number of repetitions hardly had any effects on the hardening of the Ti-6Al-4V samples. Just as stated in the HAZ analysis, the melted material is capable of solidifying before the next repetition starts. Consequently, there is no heat accumulation between repetitions and the material is simply submitted to the same heating/cooling cycle several times, always forming the same microstructure, hence the similar hardness values. Furthermore, the factor in common amongst the samples with the diminished hardening effect is the laser power of 300 W, although with different intensities due to the laser beam defocus.

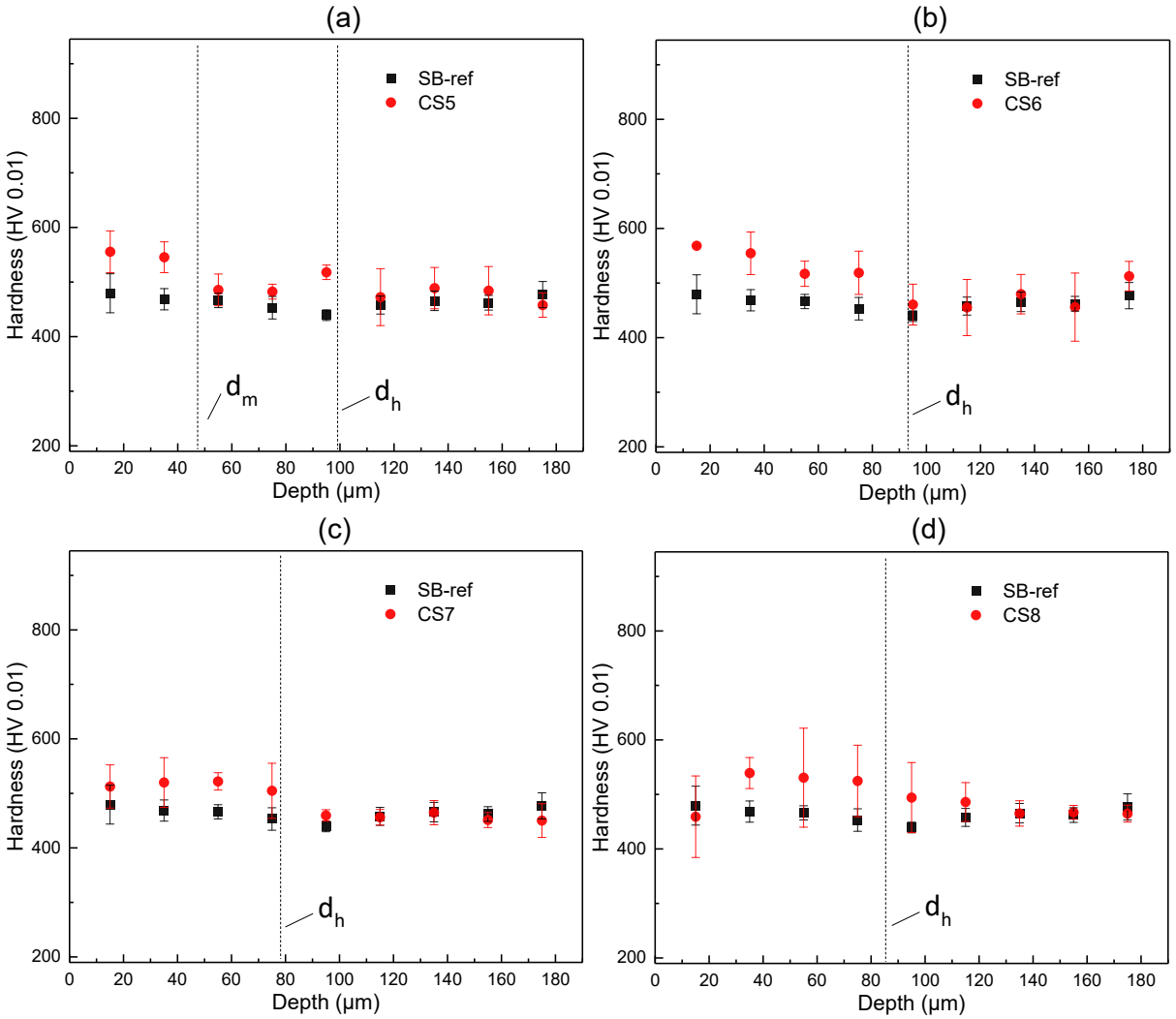

Figure 5-33. Vickers hardness values at various depths from the surface of the SB samples: (a) CS5, (b) CS6, (c) CS7, and (d) CS8. The melting and HAZ depths of each sample is determined by the boundaries d_m and d_h, respectively.

In the AB samples, neither the molten pools nor the HAZ could be properly identified, although the latter could be estimated by the contour of the transition zones. The results of the Vickers hardness measurement from the surface of the AB samples downwards are shown in Figure 5-34 and Figure 5-35. The laser absorption of the AB samples is assumed to be higher than for the SB samples, implicating in a profounder HAZ frontier (d_h) when each cross-section is compared. The outcomes imply that the assessed post-process has barely any effect on the hardness values of the AB samples, for all cases, when compared to the values obtained for the AB Ti-6Al-4V reference sample. These results sustain the microstructural evolution formulation described in the previous section, which admitted the major prevalence of α'-phase in the AB and in all samples submitted to laser polishing. With the presence of the same microstructure, similar values of hardness are expected. The results also indicate that there are no differences in the processing parameter sets, or combination of power densities, number of repetitions, and axial feed rates, within the ranges adopted in this research, that can cause the laser polishing to locally modify the hardness of the material. From the first to the ninth measurement points, the hardness of the samples AB-CS1 to 8 presented values that varied slightly but were always around the range of 500 HV0.01. The exact same variation is observed for the AB reference sample.

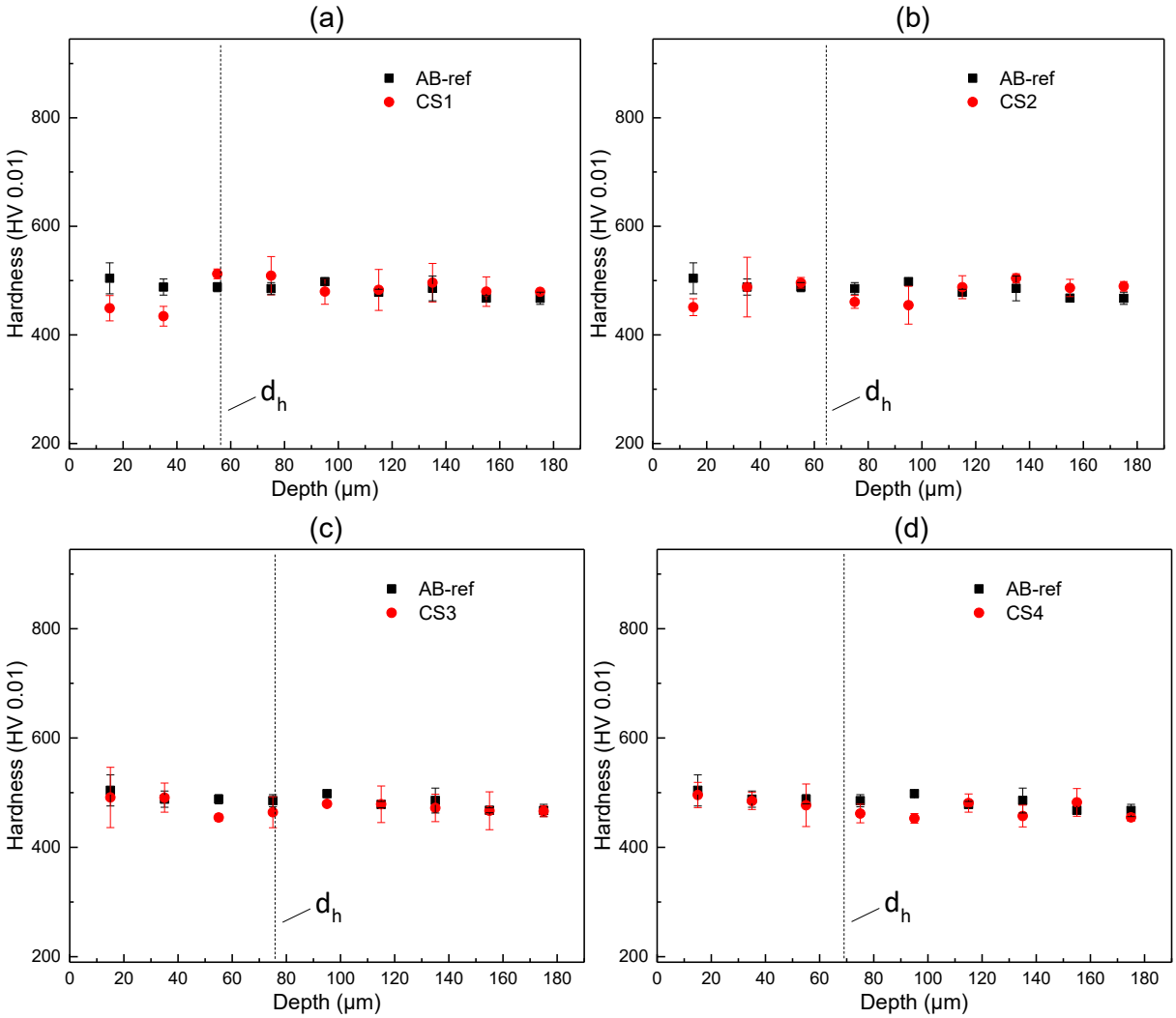

Figure 5-34. Vickers hardness values at various depths from the surface of the AB samples: (a) CS1, (b) CS2, (c) CS3, and (d) CS4. The HAZ depth of each sample is determined by the boundary d_h.

The HT samples were expected to present a behavior equivalent to the ones that had the sandblasted surface as the initial condition, due to the similar microstructure obtained during the heat treatment for stress relief, to which both types of samples were submitted. Despite the initial microstructural condition, the HT samples' behavior is much more alike to the AB. Likewise, the molten pools could not be properly identified both in the AB and HT samples, although for the latter the HAZ is easily identified due to the contrast between the (α+β)-phase and the α'-phase obtained through chemical etching. Another resemblance between the HT and AB samples is the initial surface having attached powder particles to it with a similar distribution. This alike surface results in a similar laser absorption, which is assumed to be higher than for the SB samples.

The results of the Vickers hardness measurement from the surface of the HT samples downwards are shown in Figure 5-36 and Figure 5-37. As expected, the HT samples also present deep HAZ borderline (d_h). When compared to the equivalent AB samples, the HT-CS3 to 8 present even deeper d_h between 90 and 130 μm, while samples CS1 and 2 have the HAZ borderline in the same range of 50 μm for both initial conditions.

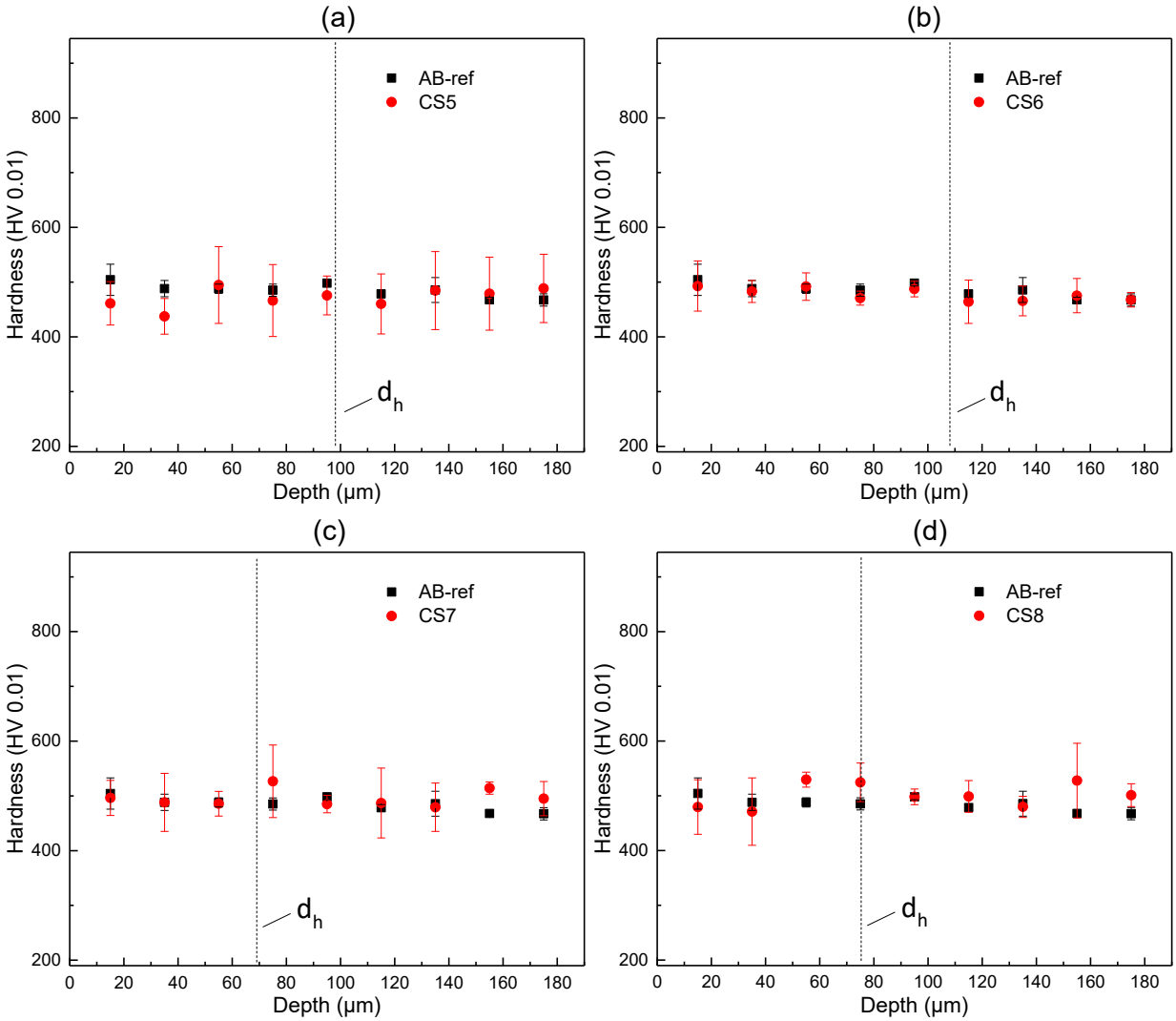

Figure 5-35. Vickers hardness values at various depths from the surface of the AB samples: (a) CS5, (b) CS6, (c) CS7, and (d) CS8. The HAZ depth of each sample is determined by the boundary d_h.

Although, independent of the depth of the HAZ, the hardness values obtained for the HT samples, as for the AB, always vary within the 500 HV0.01 range. Both AB and HT reference samples vary within the same range. Therefore, a couple of conclusions for the hardness analysis of the HT samples remains the same as for the AB ones. Meaning that, in all cases, the assessed post-process has barely any effect on the hardness values of the HT samples and there are no differences in the processing parameter sets, or combination of laser intensity, number of repetitions, and axial feed rates, within the ranges adopted in this research, that can cause the laser polishing to modify the hardness of the material. But in contrast, the results disagree with the microstructural evolution formulation described in the previous section, for AB and HT samples should have different behaviors, while SB and HT samples should behave similarly as with the presence of the same microstructure, similar values of hardness are expected.

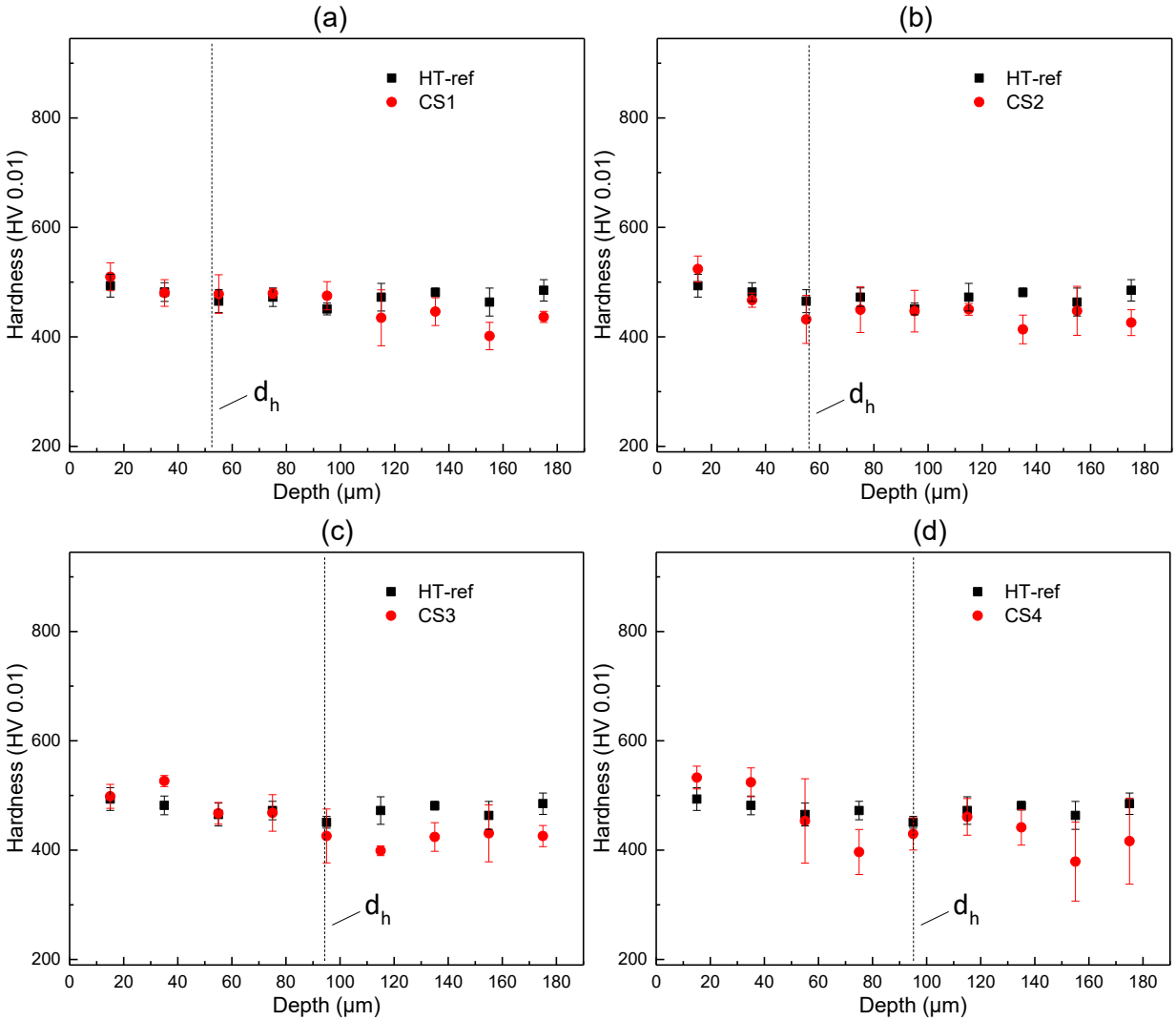

Figure 5-36. Vickers hardness values at various depths from the surface of the HT samples: (a) CS1, (b) CS2, (c) CS3, and (d) CS4. The HAZ depth of each sample is determined by the boundary d_h.

The fact that it is possible to observe the molten pools in the SB samples and not in the HT can be related to their different surface absorption values. With the disparity between absorptions, the temperature and thermal gradients achieved during the laser polishing process can differ, hence the different values of hardness. This implies that the same microstructure can be obtained with different thermal gradients but, when that is the case, the resultant mechanical properties can vary accordingly. Using a similar concept, the AB and HT samples have an almost identical initial surface and, accordingly, an almost identical absorption. This means that the thermal gradients consequential from the laser polishing process are similar, which can justify the comparable hardness values. In this case, the implication is that the same microstructure was obtained with a comparable thermal gradient and, as a result, the values of hardness attained are within an equivalent range.

In conclusion, the change in microstructure and the different stress conditions have their implications on the mechanical properties of the parts, as expected. Despite HT and AB workpieces' inconsistent behaviors, it is well known that a material with exclusively martensitic microstructure (α') exhibits higher hardness values than a material whose microstructure consists of α- and β-phases combined.

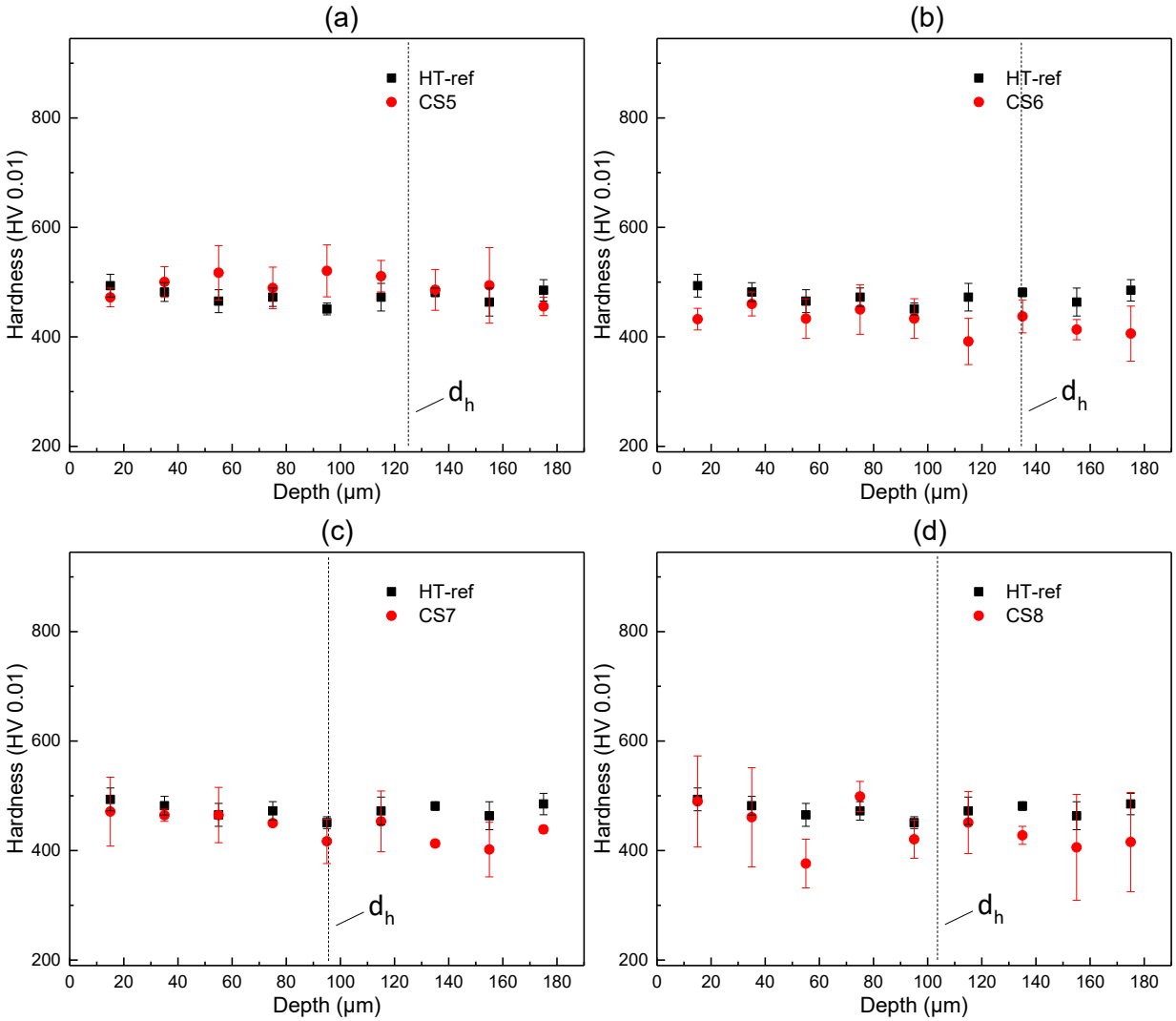

Figure 5-37. Vickers hardness values at various depths from the surface of the HT samples: (a) CS5, (b) CS6, (c) CS7, and (d) CS8. The HAZ depth of each sample is determined by the boundary d_h.

5.2. Numerical tools for laser polishing process development

In this section, different modelling approaches for the laser polishing process development are presented. A finite element method (FEM) simulation was employed for the fast prediction of the HAZ depths, while statistical models were developed to investigate the process parameters interaction, to predict the surface texture Ra and HAZ depths, and to be applied in a genetic algorithm multi-objective optimization with focus on achieving parameter sets that would result in suitable values of Ra and HAZ depth simultaneously. This study was focused on the HT samples because they allow the practical assessment of the HAZ depths for the heat transfer model validation, and they represent one of the earlier process chain steps with critical surface quality. Most of the content in this section is published in *Materials* (MDPI), referenced as [121], with complementary content published in the Journal of Laser Applications (AIP Publishing), referred as [122].

5.2.1. Heat transfer model

In order to supply relevant data in a fast and reliable manner for this study, a heat transfer model that was previously described in section 4.4 was devised using COMSOL Multiphysics software. The numerical simulation was validated with a simplified experimental approach that consists of processing single lines on the surface of the samples, each experiment was repeated three times. For this work, the two sets of parameters adopted are shown in Table 5-6.

Table 5-6. Parameter sets for single track validation experiments of the HAZ depth prediction heat transfer model.

Parameter set	Laser power (W)	Scanning speed (mm/s)	Focal position (mm)	Repetitions	Intensity (MW/cm²)
1	300 W	1200	0	1	3.82
2	300 W	800	0	1	3.82

The experimental validations exhibited that the forecasted HAZ contours and deepness were quite similar to the three practical outcomes of each set of parameters (Figure 5-38 and Figure 5-39). The contours represent the boundaries where phase changes were achieved within the material during the laser polishing process, being liquid within the melted zone and α' in the HAZ. From the images, it is noticeable that the numerical simulation tends to accomplish superior results if the process involves smaller amount of heat. This is the scenario observed for the first set of parameters from Table 5-6, as the 50% higher speed leads to overall reduced heat on the surface of the parts. Furthermore, some acute responses seen for the heat transfer model contours are due to the coarseness of the selected mesh. As discussed in section 4.4, considering that the relevant conclusions can be drawn from the obtained results, a compromise was made between a more refined mesh and the computational efficiency when choosing the size of the mesh. The compatible outcomes revealed that the heat transfer model simulated a maximum temperature of approximately 3500 K for the first set of parameters whilst with the second set of parameters the maximum temperature simulated was around 4500 K. This means that the melting and boiling points of Ti-6Al-4V, which are 1659.85 °C and 2862 °C [168], respectively, were certainly surpassed in both cases. It is important to highlight that the vaporization phase change was not considered in the present heat transfer model. For a better visualization of the simulation, the Figure 5-40 depicts the heat dissipation onto the surface of the material in the course of the assessed process.

Once the heat transfer model was successfully validated through experimental results, simulations were made using the DoE parameter sets, which comprised 34 different runs and were previously showed in Table 4-8 of the section 4.5. Part of the outcomes acquired through the numerical simulation are depicted in Figure 5-41 and Figure 5-42 to demonstrate the influence of the scanning speed, laser power, and focal position in the depth of the HAZ. The same behavior observed in the validation step was confirmed in the additional simulation results. A closer look into Figure 5-41 indicates the better performance of the model for a power of 200 W when compared to 400 W. An extra relevant characteristic that was properly reflected in the forecasts of the HAZ deepness is the contact zone, and consequent correlation, between the laser beam and the workpiece's surface, which can be observed together with the highest temperatures found for distinct levels of the focal position parameter. For instance, from Figure 5-41b it is not possible to distinguish the perimeter demarcating the melting area when considering 200 W and focal position of +3 mm. This outcome is a clear attestation that the expected outcome of the laser melting the surface of the part was not adequately fulfilled due

to the low temperature (around 900 K) revelead in the process. When contrasting it with Figure 5-41a, where the laser power was unchanged but the focal position was decreased to +1 mm, temperatures higher than 2200 K were observed in the simulation. This fact occasioned very discernible delineation for the melted and HAZ perimeters. For a better understanding of how those parameters interact and what is their consequent impact, Figure 5-41c illustrates a scenario where the focal offset is kept in +1 mm but the laser power is doubled to 400 W. In this case, the maximum temperature noticed was around 2500 K, which resulted again in an evident HAZ outline. With the higher temperature reached, the HAZ was wider and more profound, and irregular portions of the outlines were detected. Lastly, Figure 5-41d considered a focal offset of +3 mm with a laser power of 400 W. As a consequence, the wider laser diameter impacted the energy intensity, which led to to a maximum temperature around 1800 K. Therefore, besides a lower HAZ depth, this set of parameters also resulted in an apparent wider affected area in the surface of the material. All four images depicted in Figure 5-41 were acquired with a scanning speed of 1600 mm/s. With the intention of assessing new behaviors, four similar experiments were performed but this time with na scanning speed 50% lower (800 mm/s). This means that the workpieces were exposed to the laser heat source for an extended interval. Predictably, the second round of simulations with slower scanning speed resulted in more elevated temperatures when compared to the first round of simulations. Moreover, irregular perimeters were more often observed in Figure 5-42, which did not limit the acquisition of HAZ deepness values.

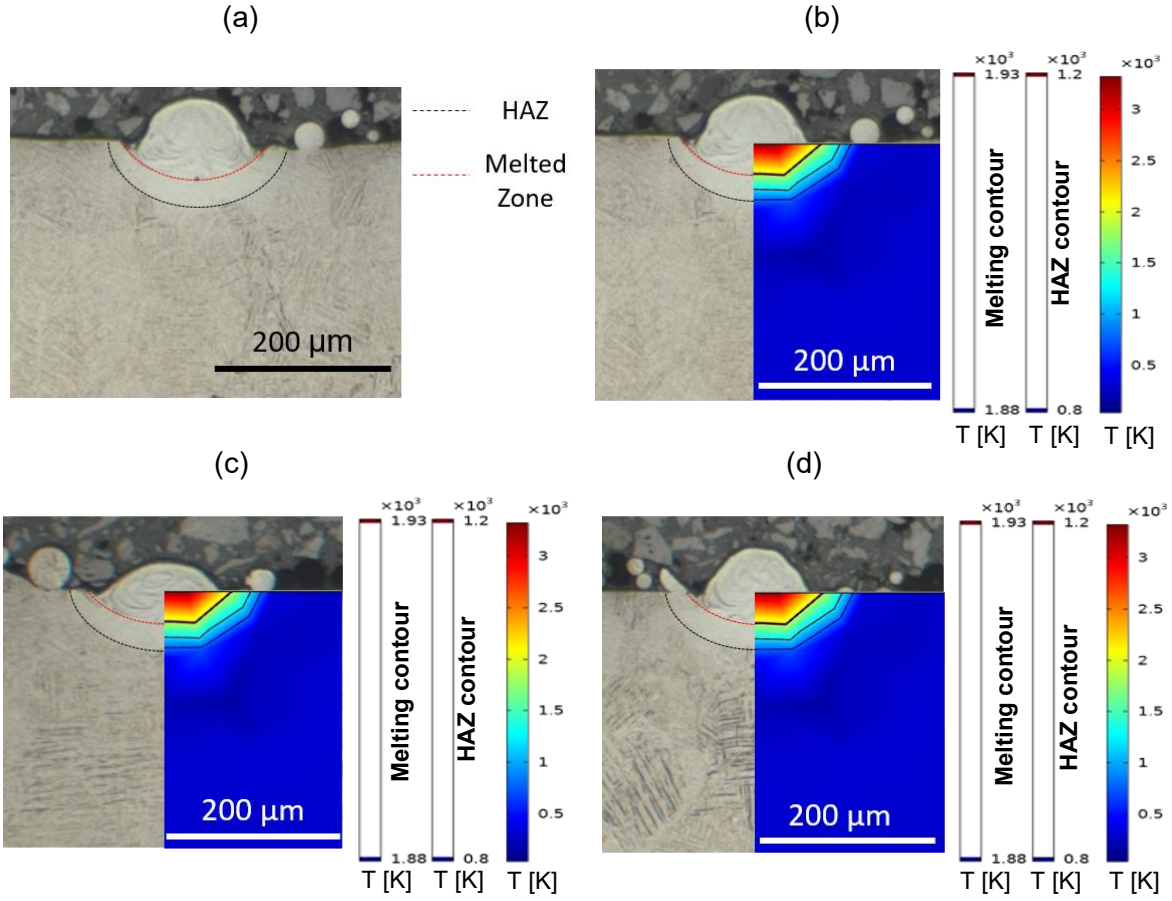

Figure 5-38. Comparison between: (a) experimental and (b,c,d) simulated depths of the melting and heat affected zones for parameter set 1. Reproduced from [122] with the permission of the Laser Institute of America.

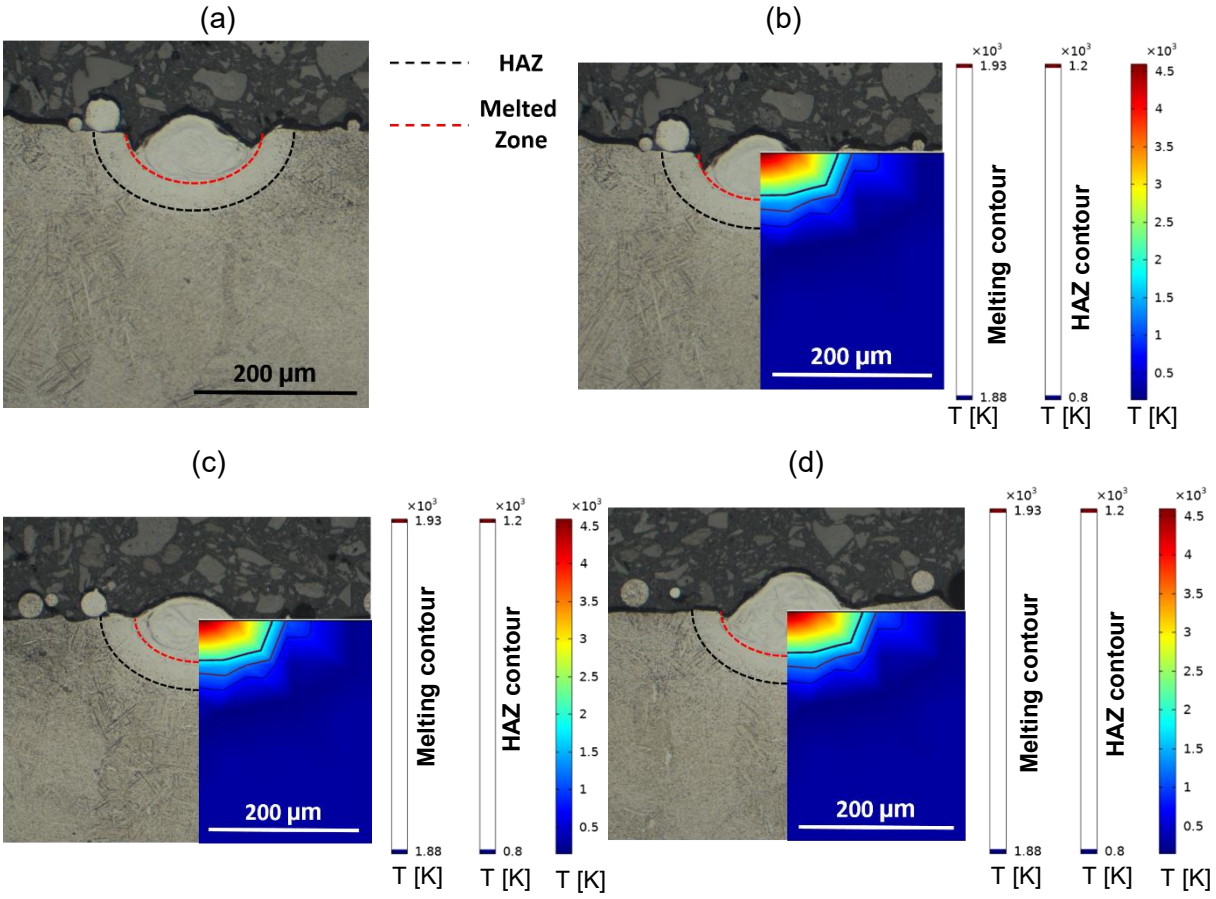

Figure 5-39. Comparison between: (a) experimental and (b,c,d) simulated depths of the melting and heat affected zones for parameter set 2.

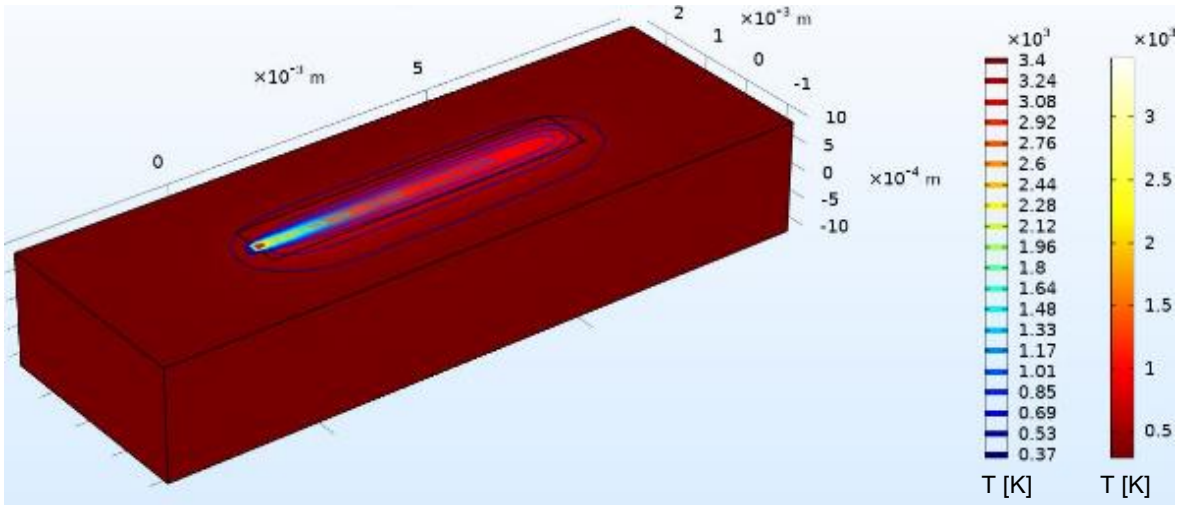

Figure 5-40. Illustration of a laser polishing process numerical simulation. Reproduced from [122] with the permission of the Laser Institute of America.

Apart from the expected differences, one can conclude that the scanning speed did not interfere in the behaviors regarding the contact zone between the laser and the workpiece's surface. Hence, the same comportment seen in Figure 5-41 is also present Figure 5-42, where defocus leads to wider contact zone but lower energy intensity and HAZ deepness.

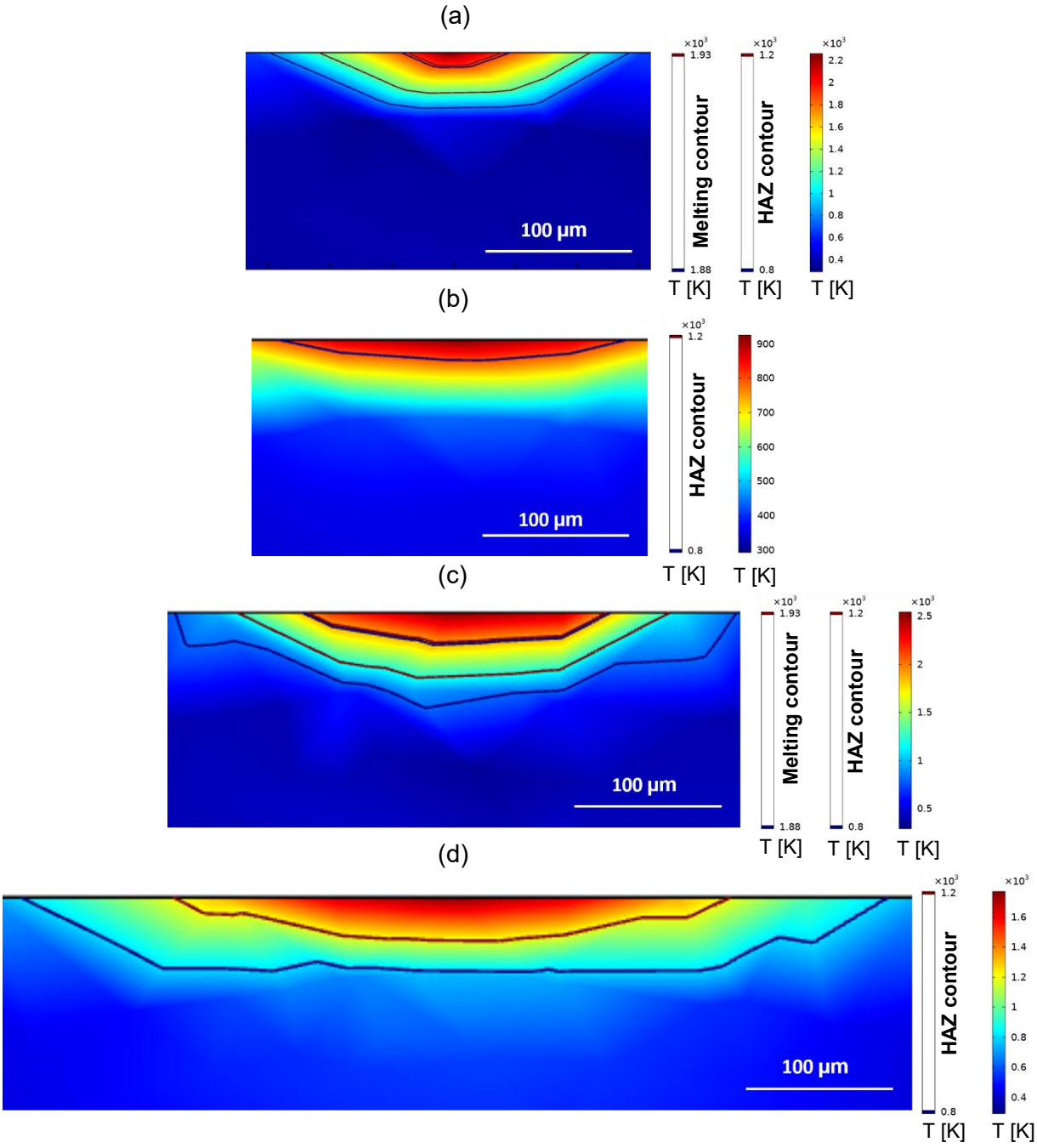

Figure 5-41. Simulated HAZ (800 K contour) and/or melted areas (1880 K contour) of single tracks laser polished with 1600 mm/s: (a) laser power: 200 W, focal position: +1 mm, (b) laser power: 200 W, focal position: +3 mm, (c) laser power: 400 W, focal position: +1 mm, (d) laser power: 400 W, focal position: +3 mm [121].

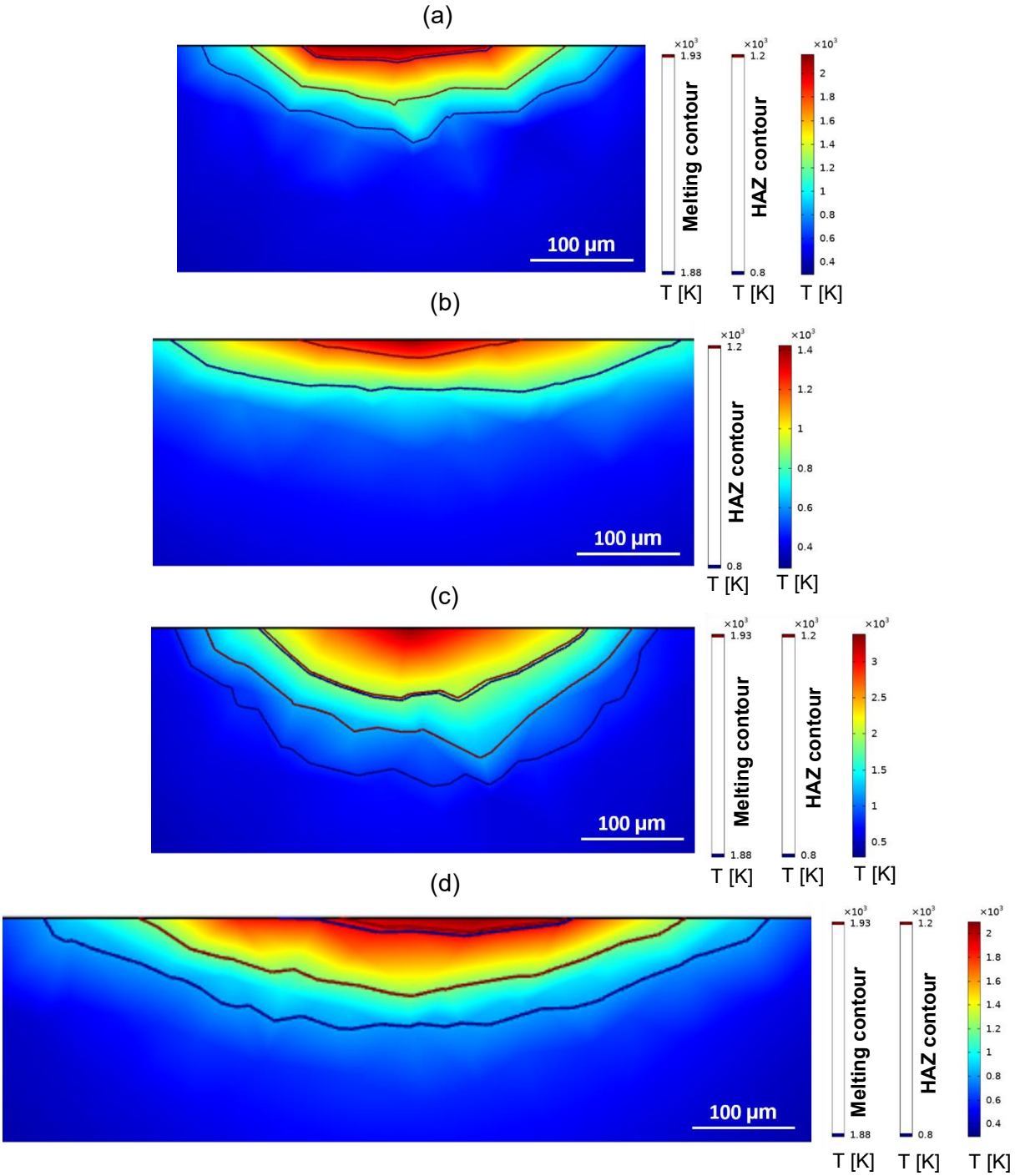

Figure 5-42. Simulated HAZ (800 K contour) and/or melted areas (1880 K contour) of single tracks laser polished with 800 mm/s: (a) laser power: 200 W, focal position: +1 mm, (b) laser power: 200 W, focal position: +3 mm, (c) laser power: 400 W, focal position: +1 mm, (d) laser power: 400 W, focal position +3 mm [121].

5.2.2. Quadratic regression model

The first modelling technique investigated in this work is the quadratic regression, whose results are further elaborated in this section. Two numerical representations were achieved through the mentioned approach, with Ra one relying on experimental data, HAZ deepness one being based on the outcomes of the FEM simulation described in section 5.2.1. Both sets

of input data were established in accordance with the DoE discussed in section 4.5. In order to give a proper overview and to allow further comparisons, this section discloses the coefficient estimation, how the governing parameters correlate with each other and their impact on the dependent variables (Ra and HAZ). Furthermore, the analysis of variance (ANOVA) is performed to support the evaluation of the model accuracy.

As formally stated in section 4.5.1, quadratic regression representations have a characteristic robustness when handling the presence of anomalies within the input data. Figure 5-43 shows the input for the creation of the Ra and HAZ deepness models. A complete list of the DoE experiment runs, with their respective combination of parameters and results are found in Appendix A. Most of the combinations of the laser polishing parameters achieved a reduction in the surface texture Ra, which had an initial value of 6.9 µm. Among the 52 sets of parameters, 50% accomplished surface roughness Ra values below 2 µm, representing a reduction of between 71% and 86%. As disclosed in Table 3-8, similar results were realized by Miller (2017) [95], Liang (2020) [98], and Marimuthu (2015) [99], with texture reductions of 83%, 79%, and 76%, respectively. Be mindful of the fact that the goal of the DoE at this stage is not to find the parameter set to achieve the lowest roughness value, but to provide a systematic approach with statistical relevance that is the basis for the numerical optimization discussed in section 5.2.5.

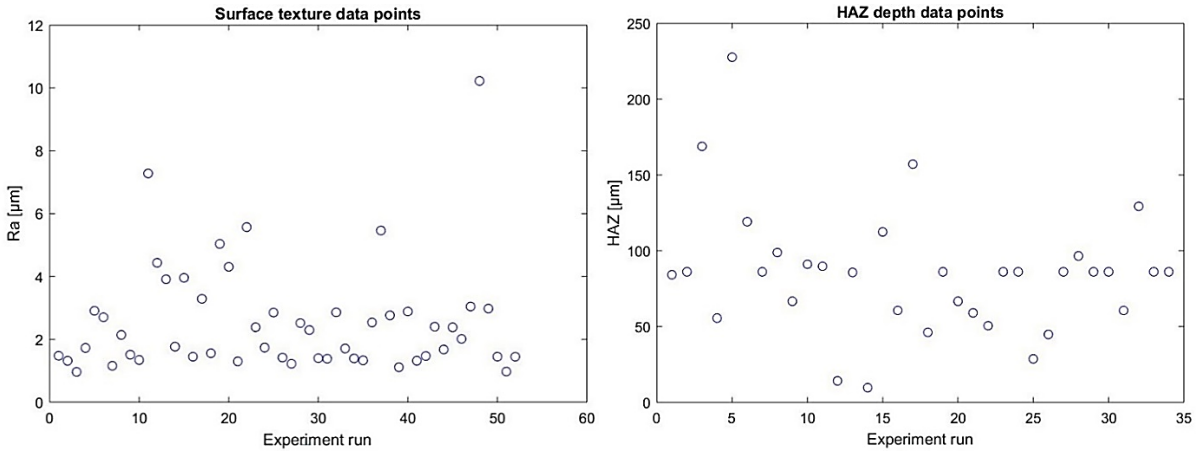

(a) (b)

Figure 5-43. Data points distribution of: (a) surface texture, and (b) HAZ depth.

The overall results aforementioned are further detailed in the sequence of this section. The quadratic regression representation is capable of generating an equation that describes the interaction of all parameters, according to the different set of information fed to the statistical tool. Therefore, the coefficients are defined in conformity with the Equation (*11*) presented in section 4.5.1. Particularly to the case of this study, the computed coefficients resulted in Equations (12) and (13), with the former describing Ra predictions with 21 terms, and the latter mathematically representing the HAZ deepness forecast with 15 terms. Table 5-7 summarizes the connotation of each variable for both models.

$$Ra = 6.4603 - 0.014571x_1 + 0.4813x_2 - 1.2822x_3 - 6.0703x_4 - 0.00022237x_5 - 0.007023x_1x_2 - 0.00026236x_1x_3 + 0.0010919x_1x_4 - 5.1816e^{-6}x_1x_5 + 0.028178x_2x_3 - 0.8623x_2x_4 + 0.00037713x_2x_5 - 0.38509x_3x_4 + 0.00020499x_3x_5 + 0.0011535x_4x_5 + 5.7231e^{-5}x_1^2 + 0.27358x_2^2 + 0.18903x_3^2 + 7.58x_4^2 + 3.8498e^{-7}x_5^2 \quad (12)$$

$$HAZ = 80.617 + 0.70384x_1 - 19.5x_2 + 7.9916x_3 - 0.15053x_4 + 0.021119x_1x_2 + 0.068898x_1x_3 - 0.0003044x_1x_4 + 2.908x_2x_3 + 0.004812x_2x_4 - 0.00061675x_3x_4 - 0.00052123x_1^2 - 3.6518x_2^2 - 3.5854x_3^2 + 6.3835e^{-5}x_4^2 \quad (13)$$

Table 5-7. List of variables representations in the regression models for Ra and HAZ depth.

Parameter\Model	Ra	HAZ depth
Laser power	x_1	x_1
Focal position	x_2	x_2
Number of repetitions	x_3	x_3
Axial feed rate	x_4	-
Scanning speed	x_5	x_4

Table 5-8 summarizes the ANOVA analysis values for each one of the statistical models achieved through quadratic regression. The error degrees of freedom (DoF) are given by the difference between the number of observations, i.e. input data points, and the number of coefficients of the respective models. The root mean squared (RMS) error is the standard deviation between the predicted and actual values, thus it is an indicator of the model's accuracy. The R^2 and adjusted R^2 values demonstrate the capability of the statistical model to fit the data, with the main difference between them being that all independent variables will impact the resultant model for the former, and only the statistically relevant independent variables are considered for the latter. Lastly, the p-value symbolizes the probability of not attaining consistent results, i.e. the statistical significance of the obtained model is increased as the p-value decreases.

Table 5-8. ANOVA analysis values for the adopted statistical model.

Measured variable	No. of observations	Error DoF	RMS error	R^2	Adjusted R^2	p-value
Ra	52	31	1.45	0.493	0.166	0.148
HAZ	34	19	13	0.949	0.911	2.66e-09

Even though the surface texture model presented a lower standard deviation of the error, it cannot represent the input data points as well as the HAZ depth model, since the latter explains 94.9% of standard and 91.1% of adjusted outputs. Additionally, the comparison between the p-value obtained for each measured variable assessed indicates that only the HAZ depth model is relevant with 95% confidence interval. Figure 5-44 displays a comparison between forecasted and experimental surface texture and HAZ deepness outputs for their respective input configuration.

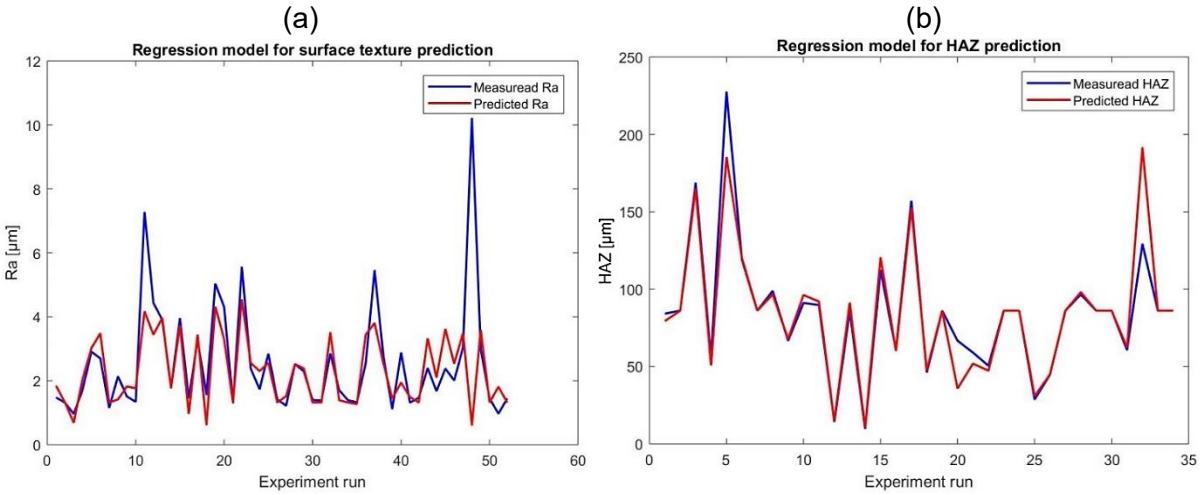

Figure 5-44. Comparison between predicted and measured values of: (a) surface texture regression, and (b) HAZ depth regression.

The unsatisfactory predictions obtained for the surface texture model is a consequence of the small pool of input data aggravated by the considerably large number of outliers within it. The same methodology already presented more accurate predictions when a superior amount of information was fed as input to the quadratic regression algorithm [127]. Conversely, the regression model for HAZ deepness exhibited a significant accuracy despite the set of input data being even smaller than the one for Ra. It is important to highlight that the HAZ depth data was acquired from simulations based on a heat transfer model, which naturally leads to very few, if not completely absent, outliers within the forecasted values.

A p-value assessment was performed and Table 5-9 summarizes the results per independent variable. Due to the inconsistency of the regression model for surface texture Ra, the only two LP parameters that exhibited statistical relevance are the focal position and the scanning speed with p-values lower than 0.05. The parameters, from most to less significant, for the HAZ depth regression model are the scanning speed, laser power, focal position, and number of repetitions, although it is worth mentioning that all parameters are within the 5% significance level. When comparing these results with the previously cited study [127], in which a larger input data set was used for the Ra regression model, equal outcomes were obtained in regard to the LP parameters significance.

Table 5-9. p-value analysis for the laser polishing parameters.

Parameter		Speed	Power	Feed rate	Focal position	Repetition
p-value	Ra	0.042512	0.78541	0.23184	0.032471	0.50122
	HAZ	2.0128×10^{-10}	3.0343×10^{-09}	-	7.9845×10^{-05}	1.9407×10^{-04}

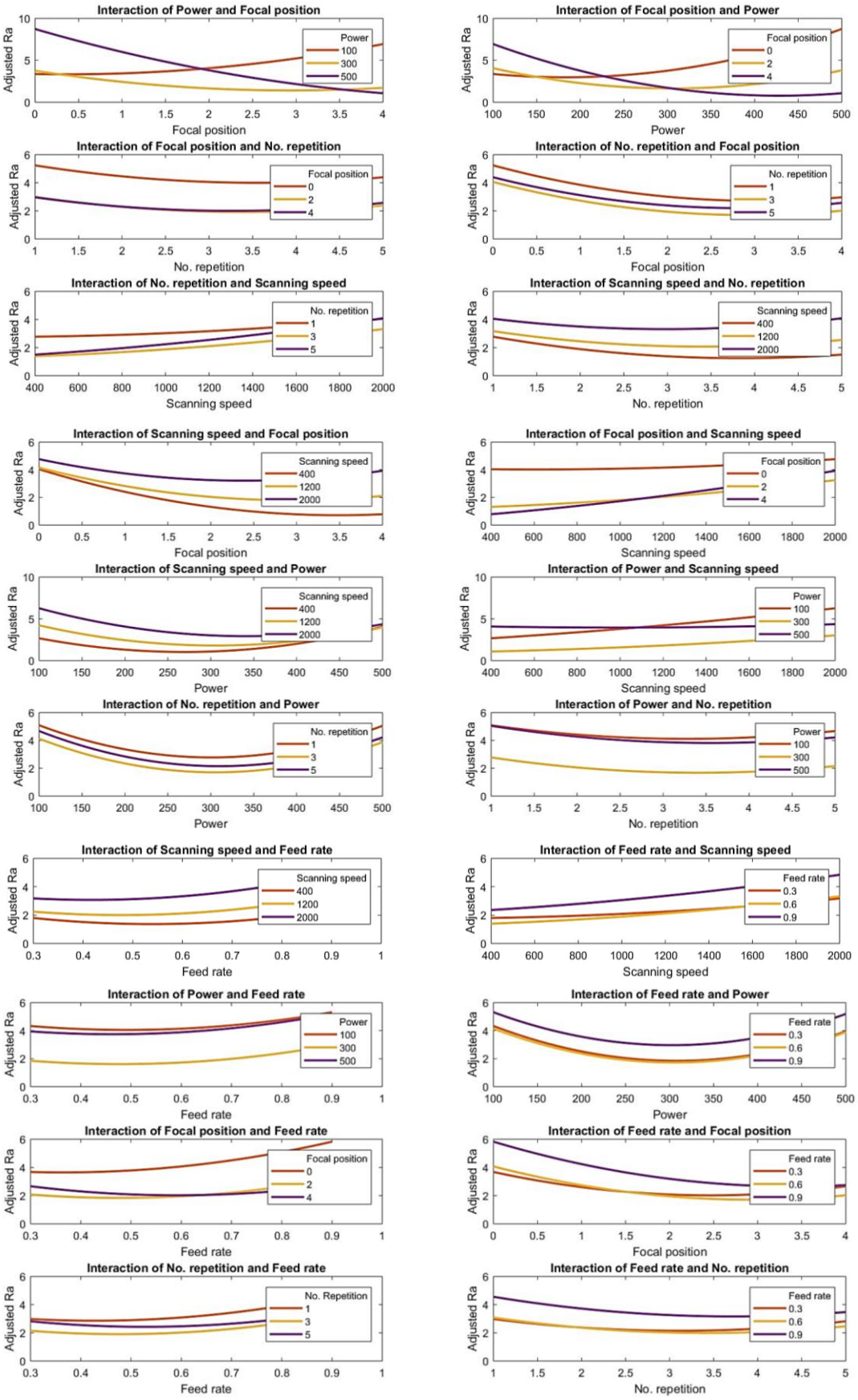

Figure 5-45. Interaction plots of the most significant laser polishing parameters based on the surface texture regression model [121].

Taking advantage of both statistical models, it is feasible to forecast the interaction between pairs of parameters along with estimated values for Ra and HAZ deepness. Those interactions are illustrated as various plots in Figure 5-45 and Figure 5-46.

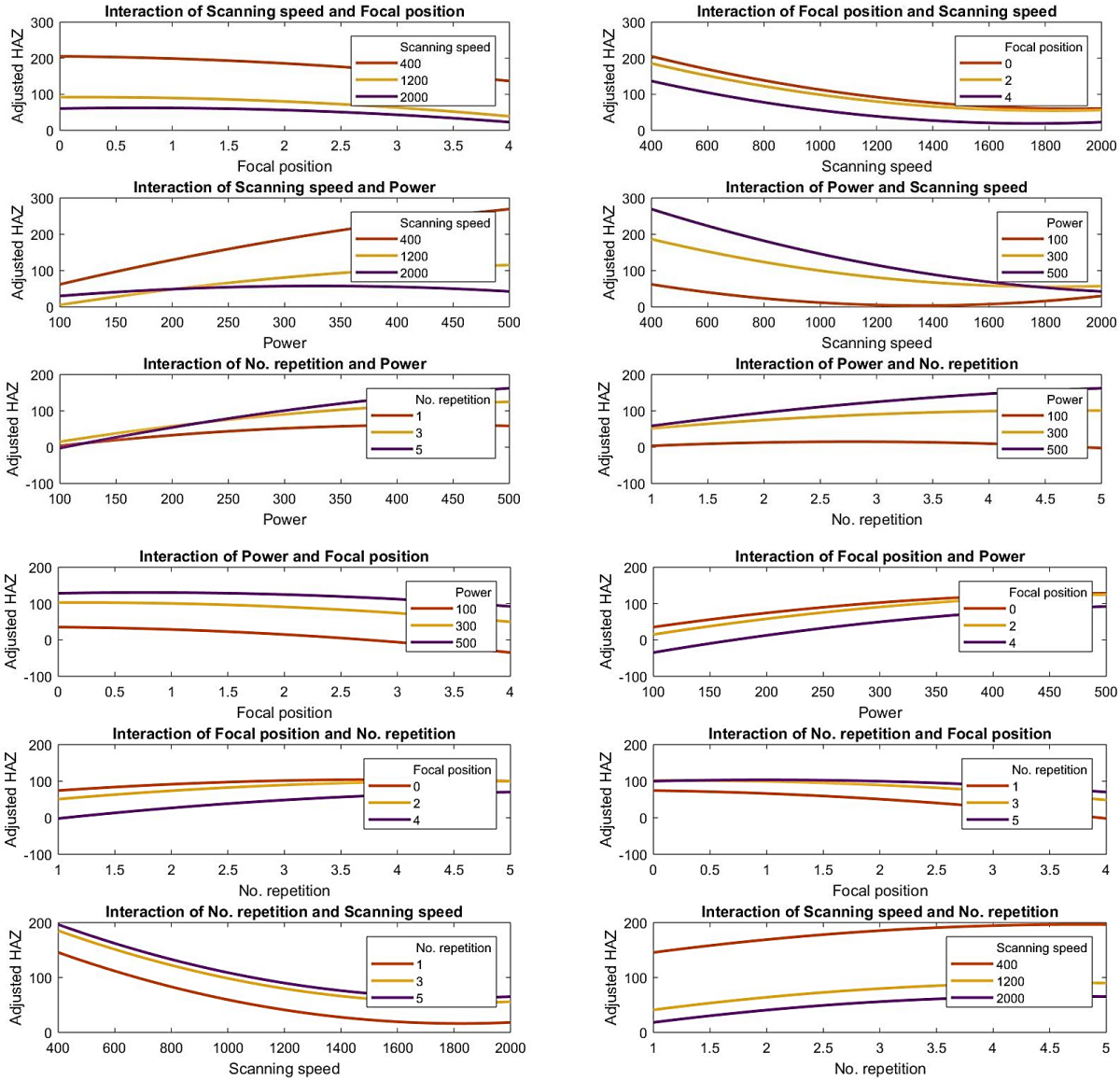

Figure 5-46. Interaction plots of the most significant laser polishing parameters based on the HAZ depth regression model [121].

In each graph, it is depicted the predicted output for the dependent variables (Ra and HAZ depth represented by the y-axis) for different values of two independent variables. The curves along the x-axis facilitate the understanding of how each parameter influences the results and if they have conflicting or harmonious comportment when paired with another LP parameter. In one plot, one parameter is kept constant in three different values, generating the three distinct curves. For every curve, the second parameter is oscillating within its specified range. Therefore, for every possible combination of parameters in pairs, a couple of interaction plots were produced. For instance, observing Figure 5-45 where the interaction graphs based on the Ra regression model is depicted, the first row contains two plots. The one on the left-hand side has the focal position in the x-axis fluctuating from 0 to 4 mm, whilst the power is maintained constant in three levels, 100 W, 300 W, and 500 W. The one on the right-hand side

has laser power in the x-axis fluctuating from 100 to 500 W, whilst the focal position is maintained constant in three levels, 0 mm, 2 mm, and 4 mm.

The same principle is valid for all rows of Figure 5-45 and Figure 5-46 with the coupling of focal position – number of repetitions, number of repetitions – focal position, number of repetitions – scanning speed, scanning speed – number of repetitions, scanning speed – focal position, focal position – scanning speed, scanning speed – laser power, laser power – scanning speed, number of repetitions – laser power, laser power – number of repetitions, scanning speed – feed rate, feed rate – scanning speed, laser power – feed rate, feed rate – laser power, focal position – feed rate, feed rate – focal position, number of repetitions - feed rate, and feed rate – number of repetitions.

From the Ra interaction plot in Figure 5-45 it is possible to observe that an average laser power of around 300 W, higher values of focal position and number of repetitions, and lower scanning speed and feed rate potentially lead to lower Ra. While this outcome is observed in the majority of the assessed cases, it does not represent an absolute rule, i.e. for focal position (+4 mm) minimum Ra occurs above 300 W. Differently, the HAZ depth interaction plots in Figure 5-46 show that the tendency for the estimated HAZ depth to decrease results from: an average laser power of around 100 W, low number of repetitions, and higher scanning speed. The only parameter that presents the same behavior for minimum Ra and HAZ is the higher values for the focal position.

Clearly, defining a combination of parameters that would concomitantly result in adequate values of Ra and HAZ deepness is not trivial. As discussed above, most independent variables exhibit opposing behaviors on the dependent variables. Considering that the minimum value of one dependent variable can only be achieved by worsening the resultant value of the other dependent variable, it is evident the benefit of optimizing both variables at the same time to obtain the most suitable set of parameters for a specific application.

5.2.3. Predictions

Using the quadratic regression models for Ra and HAZ depth discussed in the previous sections, Figure 5-47 and Figure 5-48 were created to illustrate the fitted response for Ra and HAZ, respectively, considering a specific value for each of the input variables.

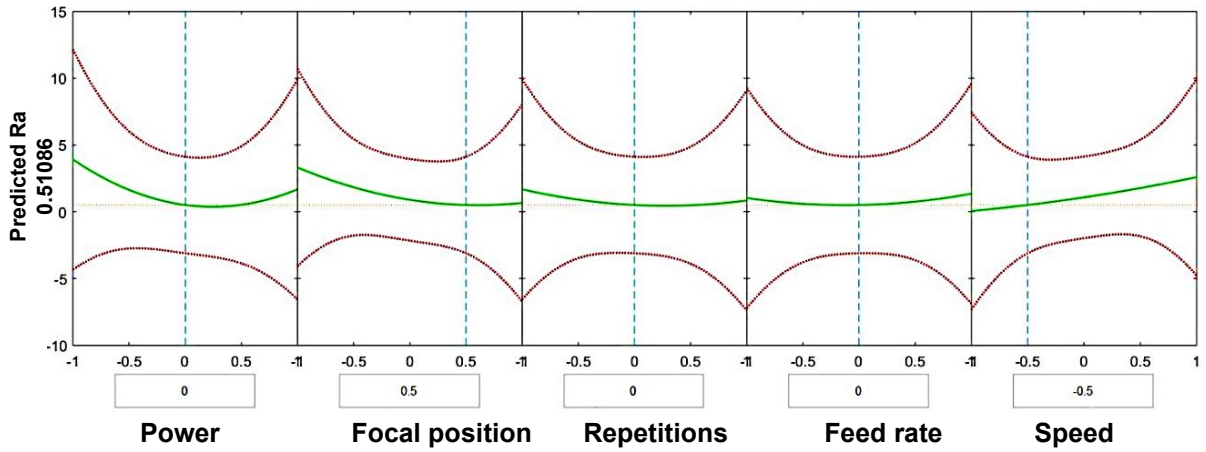

Figure 5-47. Surface texture prediction slice plot with the normalized values for each parameter [121].

The figures have one plot per parameter, each composed of the chosen level of the respective input variable, represented by the blue dashed line, the output of the dependable variable for different levels of the input variables, represented by the green curve, and the confidence interval of the forecasted Ra and HAZ, represented by the red curves. For this work, 95% of confidence was adopted and is reflected in the images aforementioned.

The graphical visualization facilitates the comprehension of the forecasted Ra and HAZ depth outcomes for different levels of each input variable. Such levels are established in the DoE described in section 4.5. Looking closely at the case displayed in Figures Figure 5-47 and Figure 5-48 it is observed that for the input levels presented in Table 5-10, Ra and HAZ depth are predicted to be in the range of 0.51 and 109.83 µm, respectively.

Table 5-10. Parameters levels and values used as input in the Ra and HAZ slice plots.

Parameter	Level	Value
Power	0	300 W
Focal position	0.5	+3 mm
Repetitions	0	3
Feed rate	0	0.6 m/min
Speed	-0.5	800 mm/s

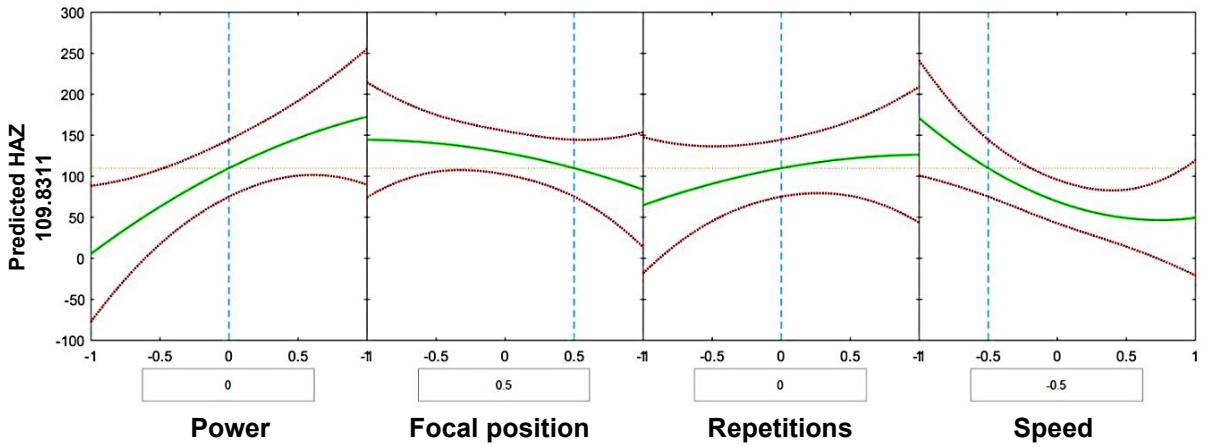

Figure 5-48. HAZ depth prediction slice plot with the normalized values for each parameter [121].

As mentioned above, the slice plots are resourceful instruments for the forecast of dependable variables. Since distinct applications will most likely have particular surface texture and HAZ specifications, this approach enables a simplified investigation of suitable outputs. Nonetheless, it is crucial to reach a model that reliably represents the experimental results. Even though the slice plots presented can be used combined as a guide for possible outputs, adopting exclusively this approach can be lengthy and potentially unreliable. For this reason, another modelling method was used in this research. Machine learning approaches can be easily enhanced as further data is acquired. Additionally, the association of machine learning and other optimization techniques can be an option for rapidly reaching a model that is more precise and reliable.

5.2.4. Artificial Neural Network model

The results discussed in section 5.2.2 for the quadratic regression models showed an insufficient performance for their further employment in this research. Instead, an approach based on machine learning was explored as a suitable alternative. This section depicts the results of the chosen predictive modelling method.

Artificial Neural Networks (ANN) was previously introduced in section 4.5.2 and was chosen due to its ability to identify complex data patterns, resulting in highly accurate models. Due to the nature of the experimental data used and the number of input data, different structures were selected for the two dependent variables studied, surface texture and HAZ depth. For the former, a cascade forward network was used with two hidden layers. As per the number of neurons, the first hidden layer has four while the second layer has only two. Differently, for the HAZ depth the architecture adopted had a simple feedforward network, which was exploited with a single hidden layer and only one neuron. As depicted in section 4.5.2, the chosen training algorithm was the Levenberg-Marquardt backpropagation as it demonstrated a great combination of performance and convergence time for the input data. Throughout the training phase, the model is continuously improved via weights and bias that are associated with the synapses amongst the neurons.

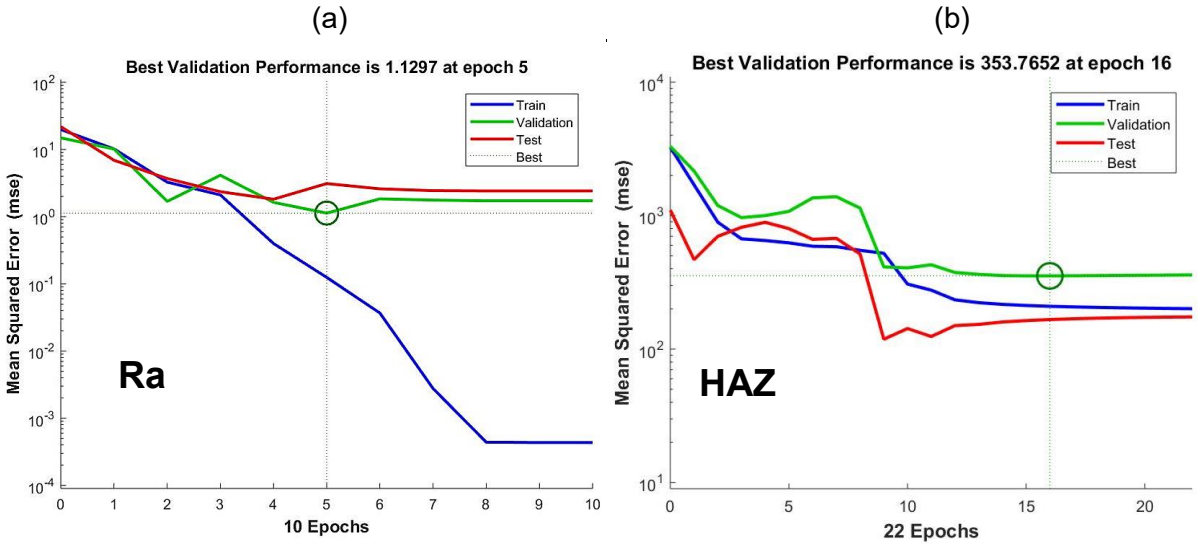

Figure 5-49. Validation performance of ANN models for: (a) surface texture Ra, and (b) HAZ depth [121].

Figure 5-49 shows the performance of the test, training, and validation data for both Ra and HAZ depth. The epoch in which the best performance was achieved is highlighted. In the y-axis, the mean squared error (mse), which is calculated for each epoch, is the parameter used to assess the performances. The mse trend should be to become smaller after each epoch, when it starts to rise, it can be an indication of overfitting. For this reason, the exit criteria of the MATLAB ANN toolbox for the training phase is the continued raise of the validation mse for a predetermined number of epochs. The results discussed in this document utilized the default number of six epochs. Another indication of overfitting is when the test mse considerably raises before the validation mse, which is not the case in any scenario exhibited in Figure 5-49. Thus, the structures demonstrated suitable results for both dependable variables while avoiding overfitting.

A further assessment can also be conducted via the regression plots. Figure 5-50 and Figure 5-51 illustrate such plots for each subset of data (test, training, and validation) and for all of them together. Each subplot has a dashed line in the diagonal going from the bottom left corner to the top right corner, which represents the perfect fit, meaning that the coefficient of correlation (R) is equal to 1. In other words, the forecasted output is exactly as the target. The graphs also have solid lines representing the factual fit of the model along with the circles representing the values that were part of each data subset.

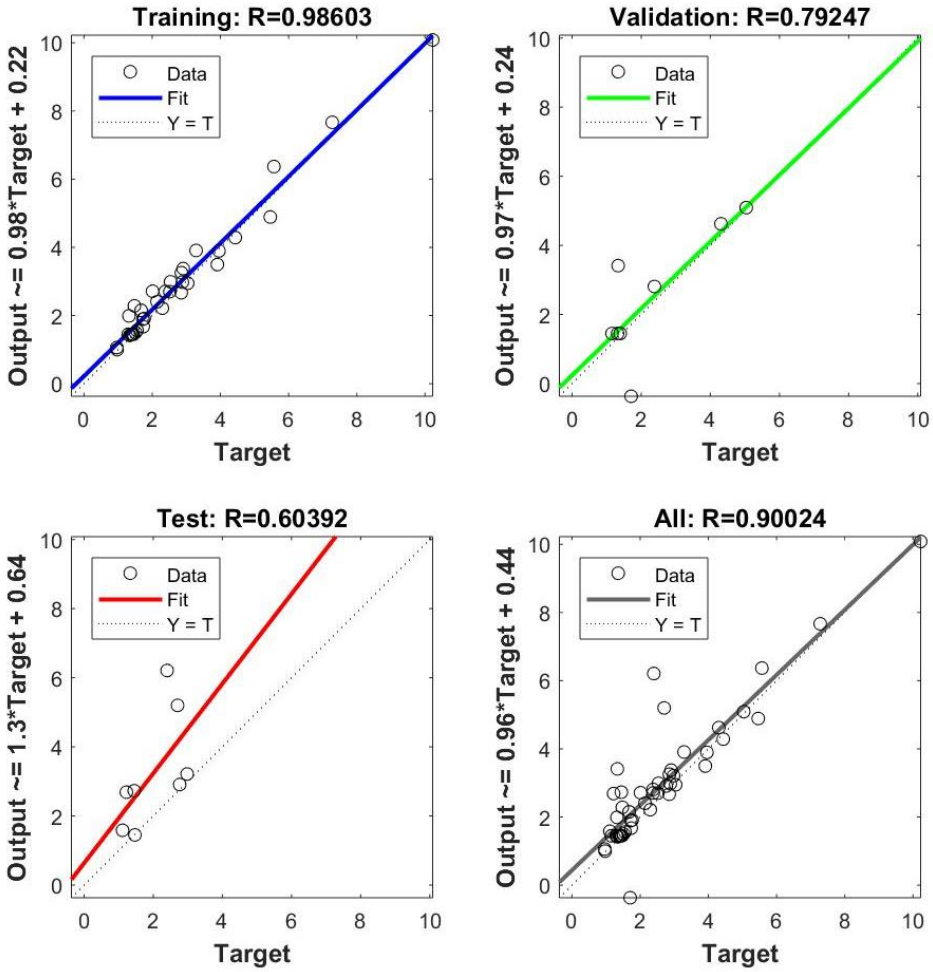

Figure 5-50. Regression plots from ANN model for surface texture Ra [121].

The tool randomly divides the whole set of input data into test data (15%), training data (70%), and validation data (15%). With respect to the surface texture (Figure 5-50), a R value of 0.604 and 0.792 were achieved for the test and validation subsets, respectively. This lower value can be justified by the presence of outliers within a smaller set of data. The outliers can be identified as circles far away from the perfect fir (R=1). The presence of the outliers shifted the fitted values to something not truly realistic. Nonetheless, for the biggest subset of data used to train the model, the fitted line is quite equivalent to the perfect fit resulting in a coefficient or correlation of 0.986. Considering all data together, a convincing overall R of 0.900 was obtained.

Following the same line of thought for the HAZ depth model acquired through ANN, a high R value was found for each subset of data. They were achieved even with a considerably smaller set of input data. This can be explained by the lack of outliers exhibited, as the values were obtained from a simulation. For the validation regression plot, despite the fact that the actual fitted line is slightly shifted from the optimal fit, as the data points are relatively close to the fitted values forecasted, a high value of R (0.980) was accomplished. The training data presented an R of 0.941 whilst the test data had an R equal to 0.896. The consistent high R values across the 3 subsets of data led to the convincing overall coefficient of correlation of 0.934 for the model.

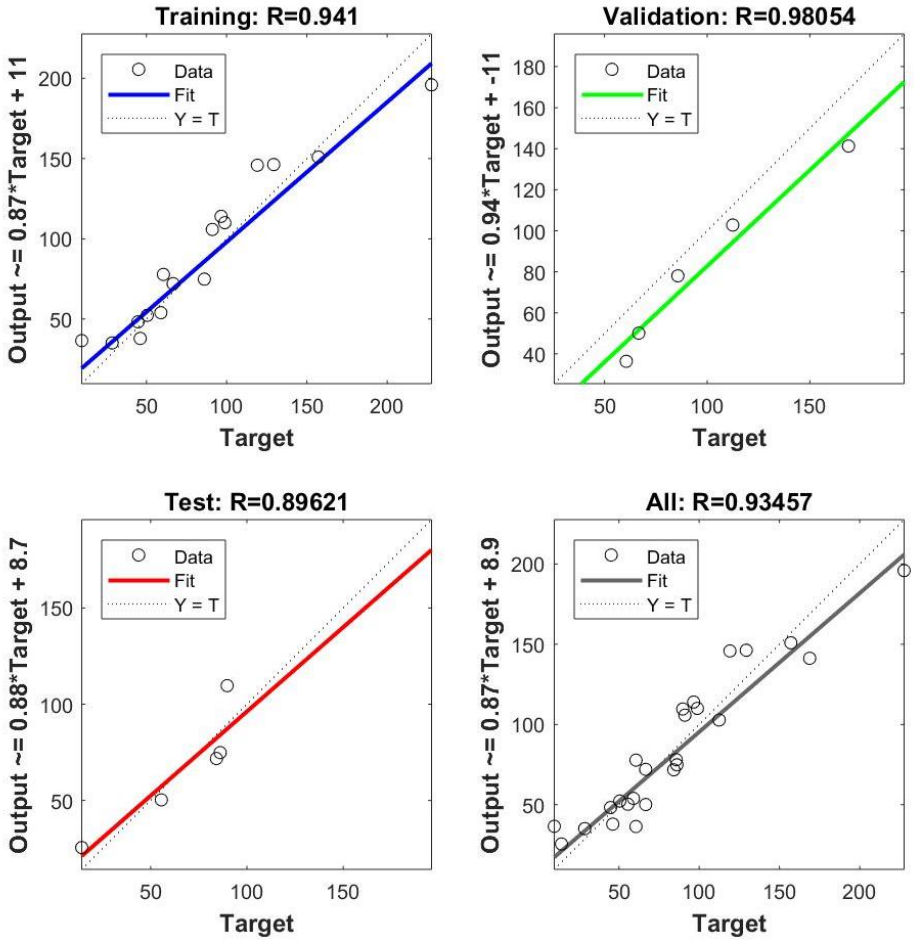

Figure 5-51. Regression plots from ANN model for HAZ depth [121].

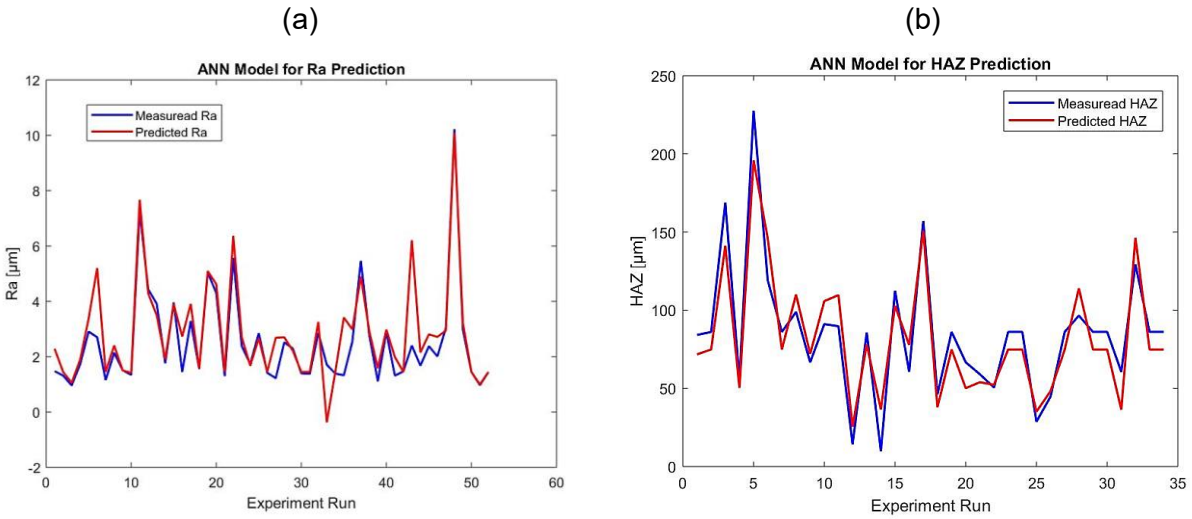

Figure 5-52. Comparison between predicted and measured values for: (a) surface texture ANN, and (b) HAZ depth ANN.

In order to give a better overview of the performance of the models acquired via ANN, the forecasted values each output data with the parameters used in the experiments were projected in a comparison graph against their respective measured values. For Ra they were the actual measurements after the experiments, while for the HAZ depth they were the values obtained through the simulation. The prediction comparison is illustrated in Figure 5-52.

Supplementary to it, relevant statistical values such as mse, the standard deviation and the mean error of each ANN model are summarized in Table 5-11. When analyzing the forementioned figure for the different models achieved using quadratic regression and ANN, the latter displays and overall better performance. Whilst both models for HAZ depth presented reasonable reliability, the ANN model for the surface texture was considerably more accurate than the quadratic regression one. As already mentioned, the ANN capability of identifying complex data pattern for several kinds of data culminated in a better prediction model. Furthermore, the ANN models are able to effortlessly incorporate new input to further improve the final model. This can be an arduous task to be performed through regression models and they can still result in a less precise model.

Table 5-11. Analysis values for the adopted ANN model [121].

ANN model	Mean Error	MSE	Std. deviation
Ra	0.473481	0.737955	0.723771
HAZ	13.125913	224.302289	7.320440

5.2.5. Multi-objective optimization

A multi-objective optimization's purpose is to obtain different combinations of results for the assessed outputs, which often present opposing behavior. This means that high values of one output happen with low values of the other output. The collection of possible results can be gathered in a Pareto front. The Pareto front for HAZ deepness and Ra, based on the quadratic regression models, is seen in Figure 5-53, while the set of parameters obtained to achieve such results are listed in Table 5-12.

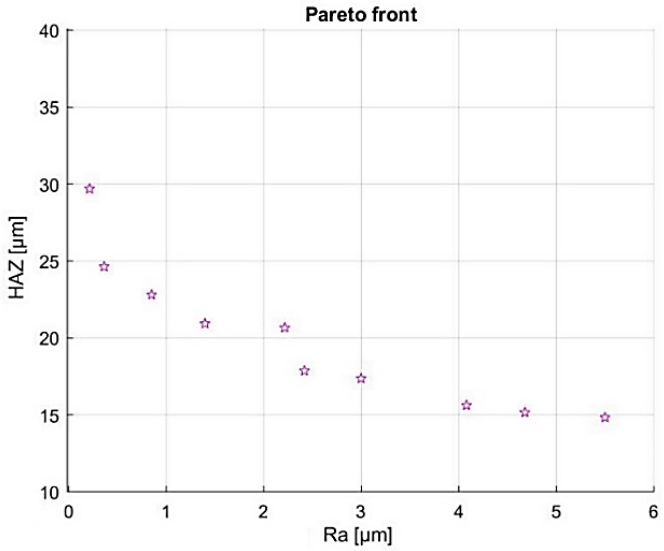

Figure 5-53. Pareto front obtained through quadratic regression models.

In the image, the described behavior is verified, as low values of Ra happen in combination with high values HAZ deepness. Oppositely, low values of the latter are reached with high values of the former. Additionally, the data derived from the mathematical optimization performed with genetic algorithm is consistent with how the inputs correlate to one another, which is discussed in section 5.2.2. A clear exemplification is that, in the mentioned section, the lowest Ra and HAZ deepness occur concomitantly when defocus value is +4 mm, which

is almost exactly the value seen in Table 5-12 (+3.99 mm) for every collection of possible results. The remaining established governing inputs presented competing comportment when the combination of low Ra and HAZ deepness are required in parallel. For these inputs, the multi-objective optimization with regression models suggests the use of the parameter sets 1, 3, 4, and 6, if the desired Ra value lies between 0.2 and 2 µm with a HAZ depth between 20 and 30 µm. A summary of the governing parameters intervals for the mentioned Ra and HAZ ranges is: Laser Power: 200 - 300 W; Focal position = +4 mm; Number of Repetitions: 1 - 2; Axial Feed Rate: 0.7 - 0.9 mm/min; Scanning Speed: 1450 – 1550 mm/s.

Table 5-12. Parameter sets for laser polishing of LPBF Ti-6Al-4V parts to obtain optimal values of surface texture and HAZ depth combined, derived from quadratic regression models.

Solution	Ra (µm)	HAZ (µm)	Laser Power (W)	Focal Position (mm)	No. of Repetitions	Axial Feed Rate (m/min)	Scanning Speed (mm/s)
1	0.21	29.69	295.12	3.99	1.63	0.75	1472.31
2	5.49	14.83	116.43	3.99	1.01	0.73	1720.08
3	0.36	24.63	258.96	3.99	1.11	0.85	1465.85
4	0.85	22.80	236.18	3.99	1.22	0.85	1503.46
5	2.99	17.36	159.69	3.99	1.16	0.87	1614.12
6	1.39	20.93	213.34	3.99	1.11	0.85	1513.39
7	4.08	15.62	128.84	3.99	1.11	0.86	1681.37
8	2.21	20.65	210.16	3.99	1.46	0.81	1590.49
9	4.68	15.15	122.62	3.99	1.10	0.81	1717.11
10	2.42	17.86	142.51	3.99	1.11	0.88	1486.30

The Pareto front for HAZ deepness and Ra, based on the ANN models, is seen in Figure 5-54, while the set of parameters obtained to achieve such results are listed in Table 5-13.

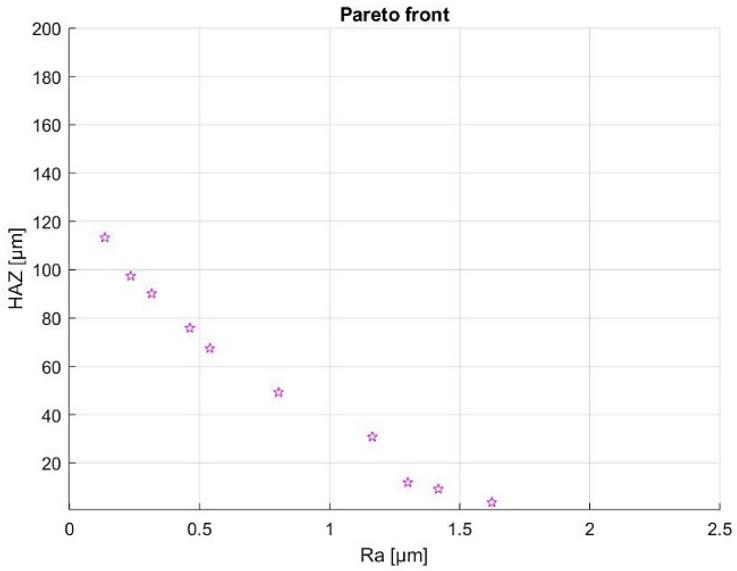

Figure 5-54. Pareto front obtained through the ANN models [121].

The focal position values obtained though the multi-objective GA with both quadratic regression and ANN models are in the same range of ~4 mm. Nevertheless, higher values of laser power and number of repetitions were found for the ANN model when compared to the quadratic regression. In contrast, the suggested values for axial feed rate and scanning speed,

obtained via the ANN model are lower. In this case, all parameter combinations are within a suitable range of Ra values for the ANN models, which caused the HAZ depth values to be on average higher than the obtained via regression models but still acceptable. A summary of the governing parameters intervals for the ANN models is: Laser Power: 400 - 460 W; Focal position = +4 mm; Number of Repetitions: 1 - 3; Axial Feed Rate: 0.6 - 0.7 m/min; Scanning Speed: 795 - 1380 mm/s.

Table 5-13. Parameter sets for laser polishing of LPBF Ti-6Al-4V parts for optimal values of surface texture and HAZ depth combined, derived from ANN models [121].

Solution	Ra (µm)	HAZ (µm)	Laser Power (W)	Focal Position (mm)	No. of Repetitions	Axial Feed Rate (m/min)	Scanning Speed (mm/s)
1	1.62	3.68	437.22	3.99	1.08	0.68	1286.11
2	0.54	67.41	407.55	3.99	2.71	0.65	1180.17
3	0.46	75.82	407.15	3.99	2.36	0.66	1022.65
4	1.16	30.78	407.68	3.99	1.49	0.68	1159.97
5	0.13	113.31	410.16	3.99	2.52	0.65	795.14
6	1.30	11.92	459.39	3.98	1.47	0.58	1366.02
7	1.42	9.18	422.03	3.99	1.36	0.66	1343.78
8	0.23	97.35	410.84	3.99	2.59	0.64	916.60
9	0.31	90.15	413.47	3.98	2.66	0.66	993.97
10	0.80	49.22	436.31	3.99	2.61	0.64	1379.07

The maximum potential surface roughness reduction with the parameter sets obtained through the multi-objective optimization with the regression and ANN models are 97% and 98%, respectively. As summarized in Table 3-8, these values are comparable to those presented by Wang (2018) [26], Ma (2017) [27], Yung (2018) [97], Zhihao (2018) [101], and Li (2020) [102], which achieved reductions of 91%, 93%, 92%, 98,7%, and 99%, respectively. It is worth noting that the multi-objective optimization was designed to simultaneously minimize the Ra and HAZ depths, which tend to present opposing behaviors, meaning that the results don't represent the global minimum value for each variable individually and the resulting surface roughness reduction is subjective to HAZ depth requirements.

5.3. Characterization after laser functionalization

In this section, the evaluation of the resultant characteristics of LPBF Ti-6Al-4V submitted to laser functionalization is presented. For this analysis, both the cw and the pulsed lasers are adopted. For the laser polishing, one set of parameters that presented promising results regarding surface quality was chosen from the ones presented in the previous sections, while the laser functionalization was performed with the two sets of parameters described in the material and methods section (4.2.2). The two post-processes were also applied in combination as a novel two-step laser post-processing for functionalization and improvement of surface quality of LPBF parts. Most of the content in this section is published in *Materials* (MDPI), referenced as [123].

5.3.1. Resulting surface structures

In this step of the presented research, different sets of ultrafast laser parameters were used to create two types of structures, pores, and nano-ripples.

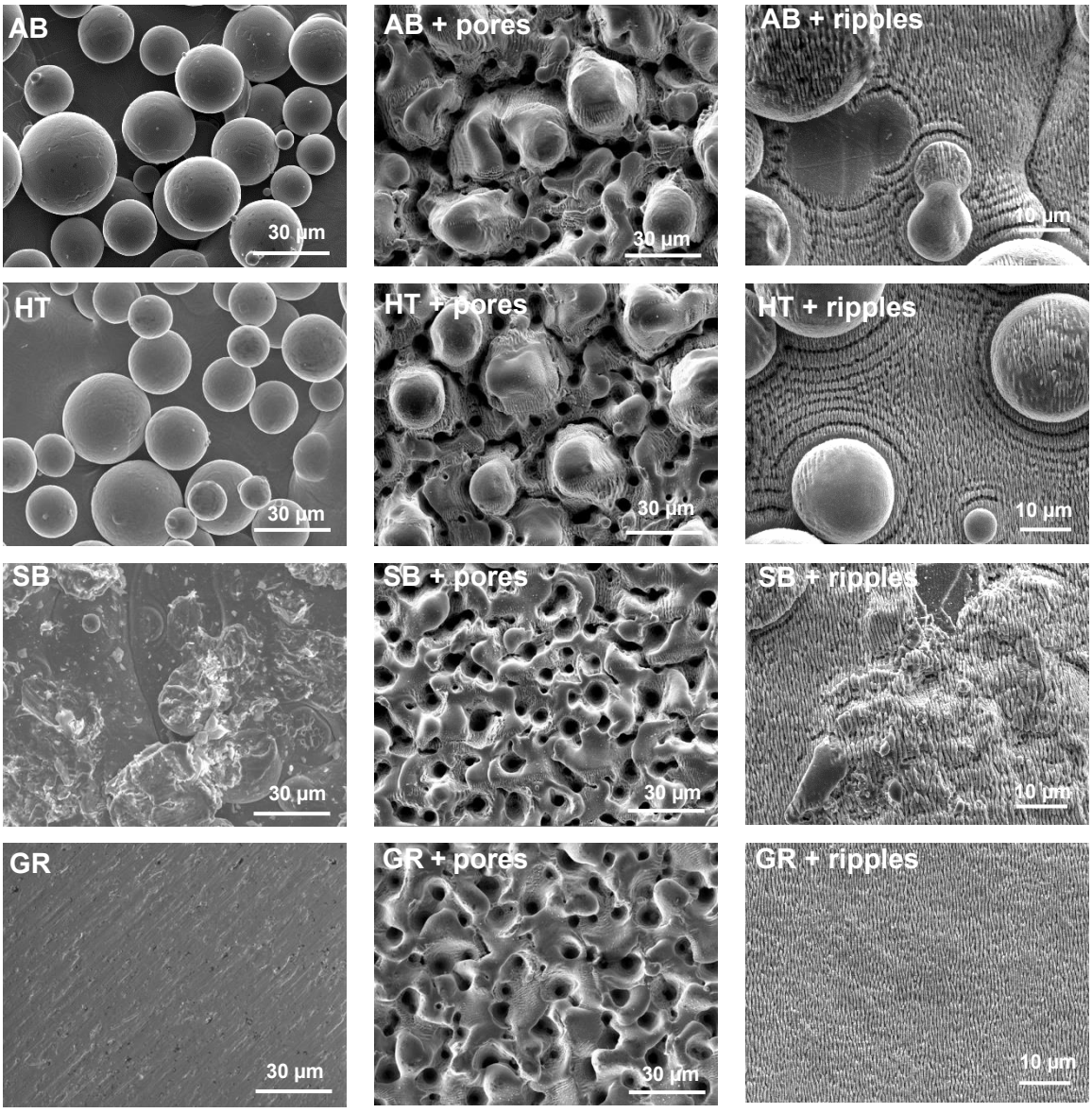

Figure 5-55. SEM image of the surfaces: (a) without laser treatment; (b) with ultrafast laser treatment for pore formation; (c) with ultrafast laser treatment for nano-ripples formation [123].

Initially, parts that had not yet been exposed to laser treatment were put through the structuring. In terms of powder attachment, the workpieces' initial topographies can be divided into three states, with powder still completely adhered to the surface following the additive manufacturing (AB) and heat treatment (HT), partially detached after sandblasting (SB) and fully removed with grinding (GR).

The interaction between the laser and material was dictated by the surface's starting condition, thus when identical set of parameters are adopted, workpieces with different initial topographies present diversified outcomes (Figure 5-55). The surface unevenness could not be eliminated exclusively by the ultrafast laser. Rather, with powder still fully adhered to the parts' surface, i.e., AB and HT, not only the workpieces' but also the particles' surfaces observed the establishment of nano-ripples (Figure 5-55c, AB + ripples and HT + ripples). Differently, porous structures were formed on the surface of the parts with powder adhesion still remnant amongst it (Figure 5-55b, AB + pores and HT + pores). Reducing or eliminating

sintered powder on the surface of the parts before applying laser structuring approaches can result in the creation of more uniform structures (Figure 5-55c, SB + ripples and GR + ripples). While the pores created by the laser structuring approach following sandblasting and grinding are comparable in size and distribution (Figure 5-55b, SB + pores and GR + pores), the formation of nano-ripples makes it noticeable that the starting surface topography could not be evened out by the sandblasting (Figure 5-55c, SB + ripples).

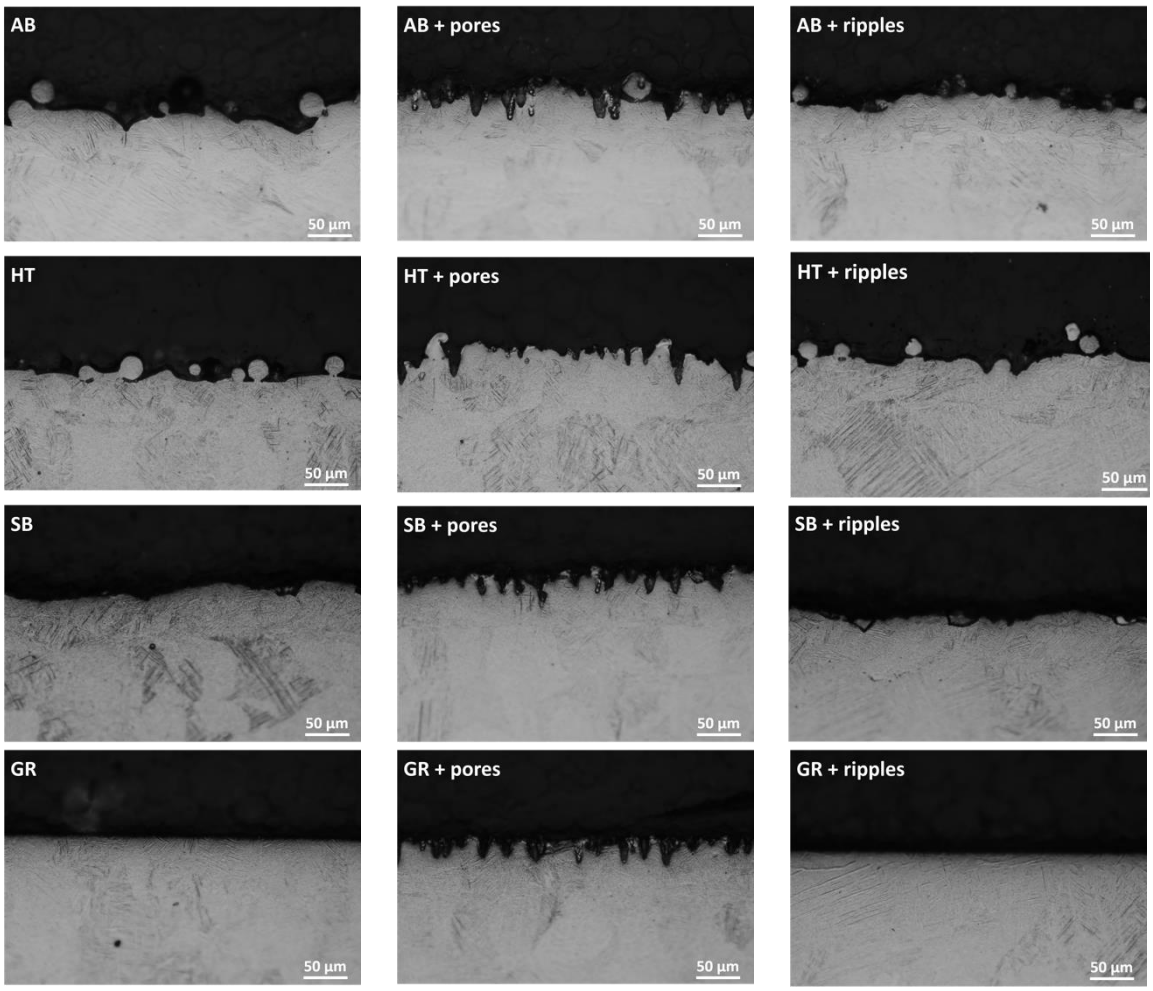

Figure 5-56. Cross-section images of the surfaces: (a) without laser treatment; (b) with ultrafast laser treatment for pore formation; (c) with ultrafast laser treatment for nano-ripples formation.

By means of cross-sectional analysis, it is observed that the nano-scaled dimensions of the ripples structures results in parts with the same profiles when compared to their initial states (Figure 5-56a and Figure 5-56c). Differently, the porous structures affect the resulting topographies by forming valleys on the surface of the parts (Figure 5-56).

The same structuring approach was applied to the parts after laser polishing. The laser polishing smoothened the workpieces' surface by effectively eliminating the powder adhered to their surfaces, which is an effect achieved in earlier works [27, 21, 99, 28, 26]. The outcome was comparable amongst all assessed parts, which also resulted in consistent surface structures following the adoption of the combination of laser polishing and ultrafast laser functionalization (Figure 5-57a), as the former procedure ensured that entirely different topographic conditions reached the same starting point.

When assessing the effects of the combination of different post-processes, the usage of ultrafast laser for porous structures formation proved to be reproducible when coupled with laser polishing, sandblasting, or grinding (Figure 5-57b). Although very comparable amongst the laser polished parts, the resulting nano-ripples structures differ from the ground surfaces even with both conditions being considered smoothened topographies, since the images indicate that higher ablation was achieved when comparing the former to the latter (Figure 5-57c). With the stated observation, it can be concluded that the interaction between the laser and material is not only dictated by the surface's starting condition but additionally by the type of processes the workpieces were subjected to in order to achieve such initial topographies.

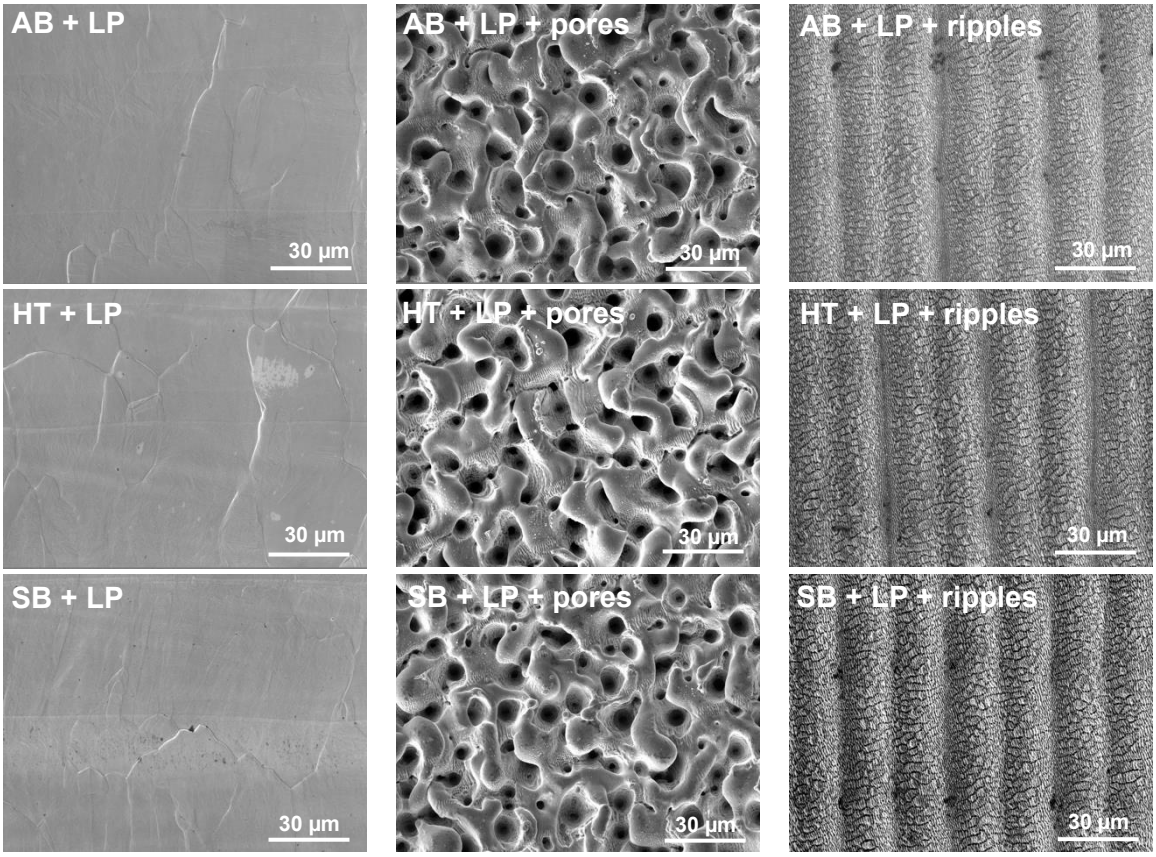

Figure 5-57. SEM image of the surfaces: (a) after laser polishing; (b) with ultrafast laser treatment for pore formation; (c) with ultrafast laser treatment for nano-ripples formation [123].

As presented previously, cross-sectional analysis was performed, in this case to evaluate the effects of combining both laser post-processes in the parts profile. The same observation is possible regarding the influence of the nano-ripples structures, which is that the resulting parts possess the same profiles when compared to their initial states (Figure 5-58a and Figure 5-58c). Although in this case, the evidence of the depressions caused due to the mentioned material removal can be observed in Figure 5-58c. As the porous structures obtained after laser polishing presented similar topography when compared to the initial states without any laser treatment, so did their cross-section analysis. The same types of valleys were formed on the surface of the parts (Figure 5-58b). The repeatability of, not only the laser polishing, but also the ultrafast laser processing is confirmed with the cross-section images, where surfaces with similar initial conditions presented similar results.

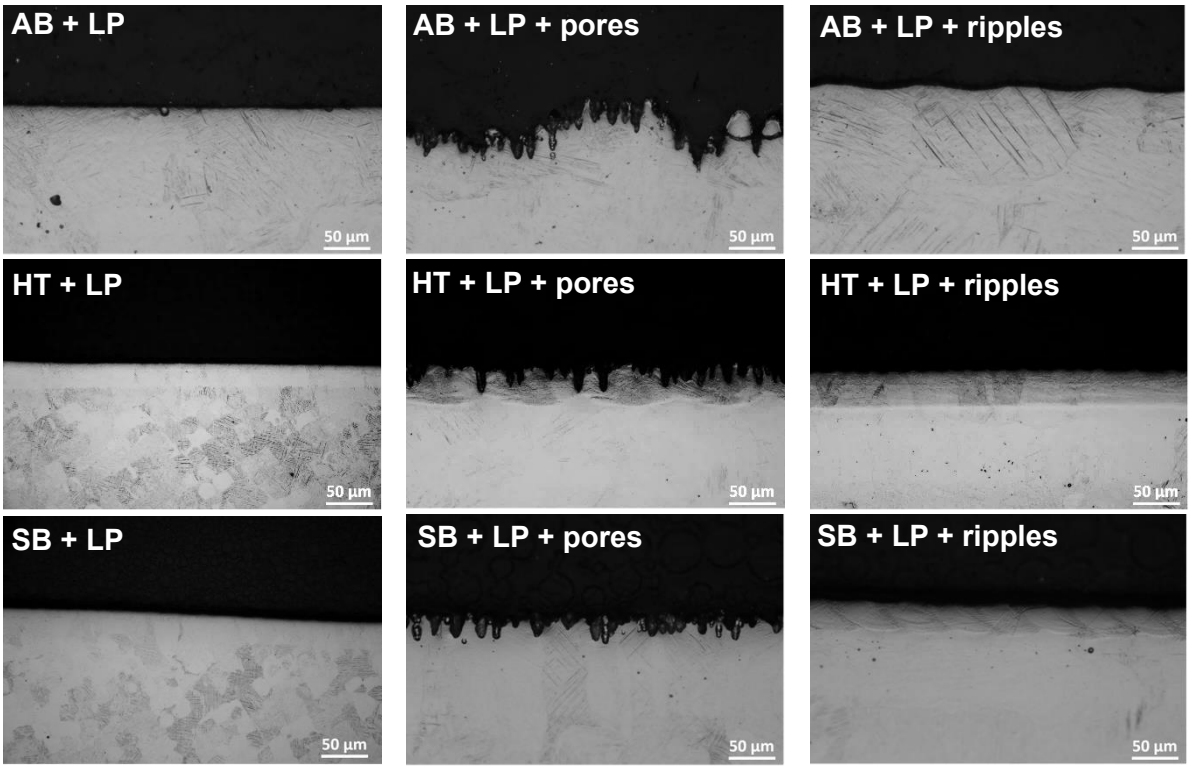

(a) (b) (c)

Figure 5-58. Cross-section images of the surfaces: (a) after laser polishing; (b) with ultrafast laser treatment for pore formation; (c) with ultrafast laser treatment for nano-ripples formation.

5.3.2. Microstructure

The potential microstructural changes of the samples subjected to the laser post-processes, combined, and separated, were assessed with an approach like the one adopted in section 5.1.3. It includes microscope images and XRD patterns of the treated samples and their initial conditions.

As already presented in the mentioned section, after additive manufacturing (AB condition) only the martensitic α'-phase occurs, while after heat treatment (HT, SB and GR conditions) the presence of α- and β-phases are observed. In Figure 5-59, overview cross-sectional images of the Ti-6Al-4V parts in the stated starting conditions are compared when the ultrafast laser processing is applied to obtain pores and nano-ripples structures. Even with contrast etching, no microstructural differentiation can be observed from the images obtained before and after the laser structuring, independently if for pores or nano-ripples.

This observation is confirmed with XRD presented in Figure 5-60, where the patterns for the AB, HT and SB starting conditions (Figure 5-60a) display the exact same patterns after the pores and nano-ripples formation (Figure 5-60b and Figure 5-60c, respectively). Smooth shifts and broadenings can be observed, which can be related to slight changes in the residual stresses' conditions of the parts after the laser treatment, even though the same microstructure is maintained.

The laser polishing eliminated the particles adhered to the workpiece's surface, but it also created heat-affected zones, as this research goes into great detail about, which, due to the similar temperature gradients of the LPBF and laser polishing process, can only be observed in samples submitted to heat treatment (Figure 5-61). When combining laser polishing and

ultrafast structuring, neither the depth nor the intensity of the visible HAZ on the HT and SB samples presented any changes (Figure 5-61b and Figure 5-61c). This is an indication that no microstructural changes occurred and the HAZ is still composed only of martensitic α'-phase, while the bulk material of the cited workpieces has the α- and β-phases mixture. A similar behavior is observed for the AB samples, with no microstructure modifications observed (Figure 5-61b and Figure 5-61c), although in this case the resulting microstructure following the combination of laser polishing and ultrafast surface structuring is exclusively the martensitic α'-phase.

The corroboration of the microstructural evolution after the combination of laser polishing and ultrafast surface functionalization is presented in Figure 5-62 with a comparison of the XRD patterns between the GR sample without laser polishing as a reference, the AB, HT, and SB samples after laser polishing. The patterns of the GR samples in its initial condition are clearly comparable to the HT patterns from Figure 5-60a, although in this case when the pores and nano-ripples are applied the different stress states are clearly evidenced by the broadening of the plotted patterns. The XRD of the AB, HT, and SB samples in their initial conditions were deeply discussed in section 5.1.3, and are illustrated again in Figure 5-60a. A clear difference in the spectra is observed when the GR sample is compared to the laser polished, which once more confirms the presence of the (α+β)-phases after heat treatment, while only the martensitic α'-phase occurs after the laser polishing.

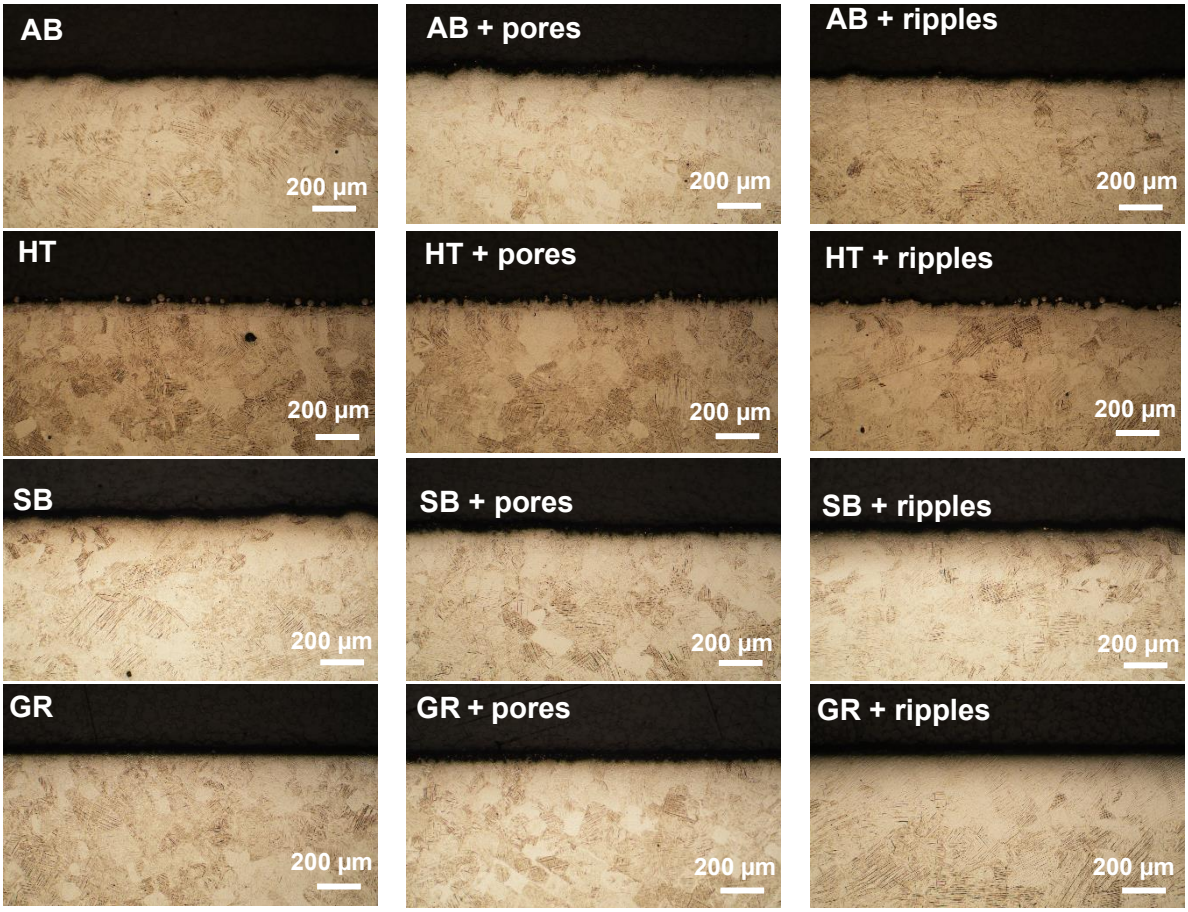

Figure 5-59. Cross-section images for microstructure evaluation of samples: (a) initial conditions; (b) with ultrafast laser treatment for pore formation; (c) with ultrafast laser treatment for nano-ripples formation. Adapted from [123].

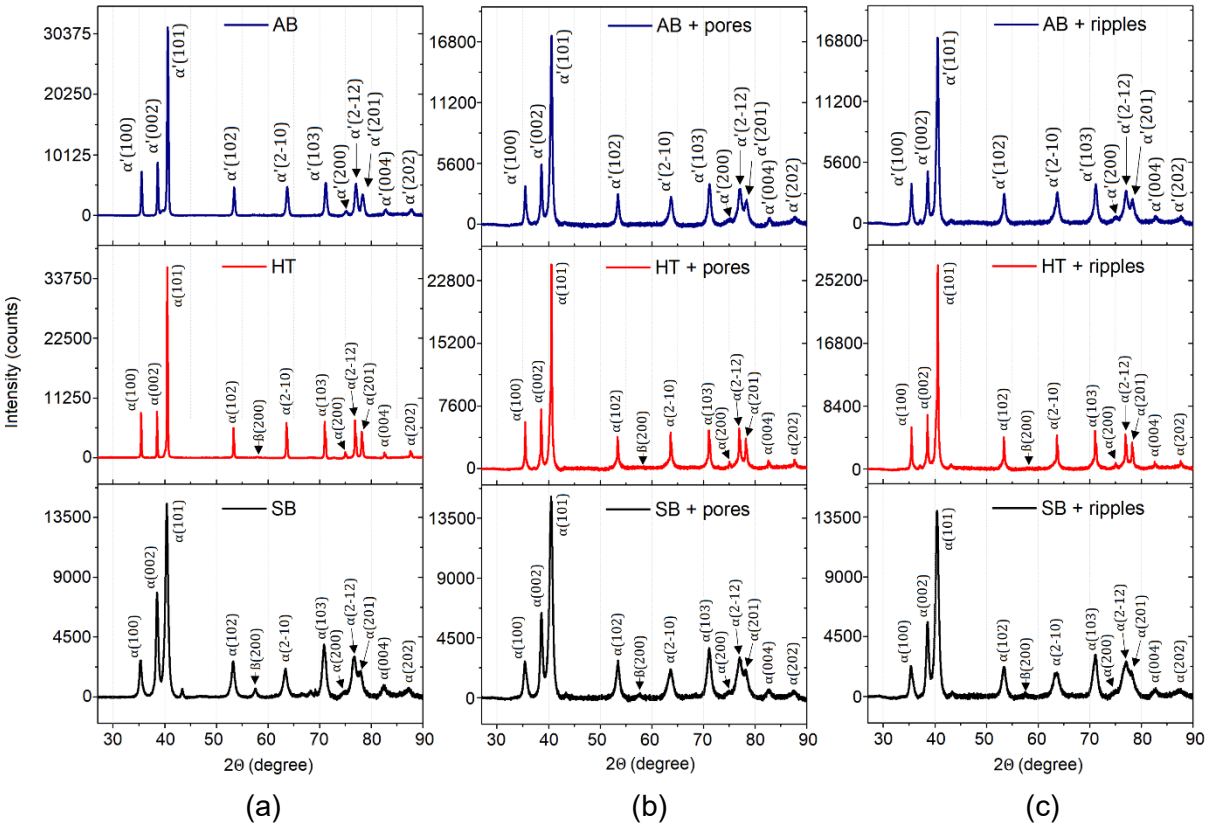

(a) (b) (c)

Figure 5-60. X-ray diffraction of the samples: (a) initial conditions; (b) with ultrafast laser treatment for pore formation; (c) with ultrafast laser treatment for nano-ripples formation.

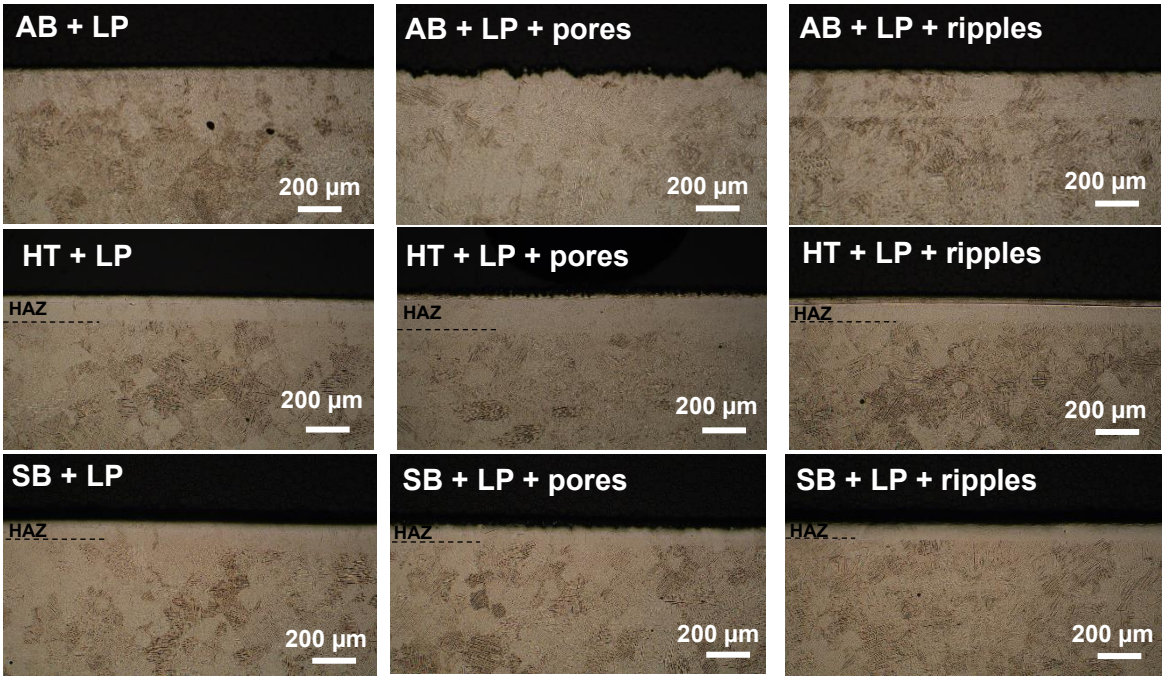

(a) (b) (c)

Figure 5-61. Cross-section for microstructure evaluation of samples after: (a) laser polishing; (b) with ultrafast laser treatment for pore formation; (c) with ultrafast laser treatment for nano-ripples formation. Adapted from [123].

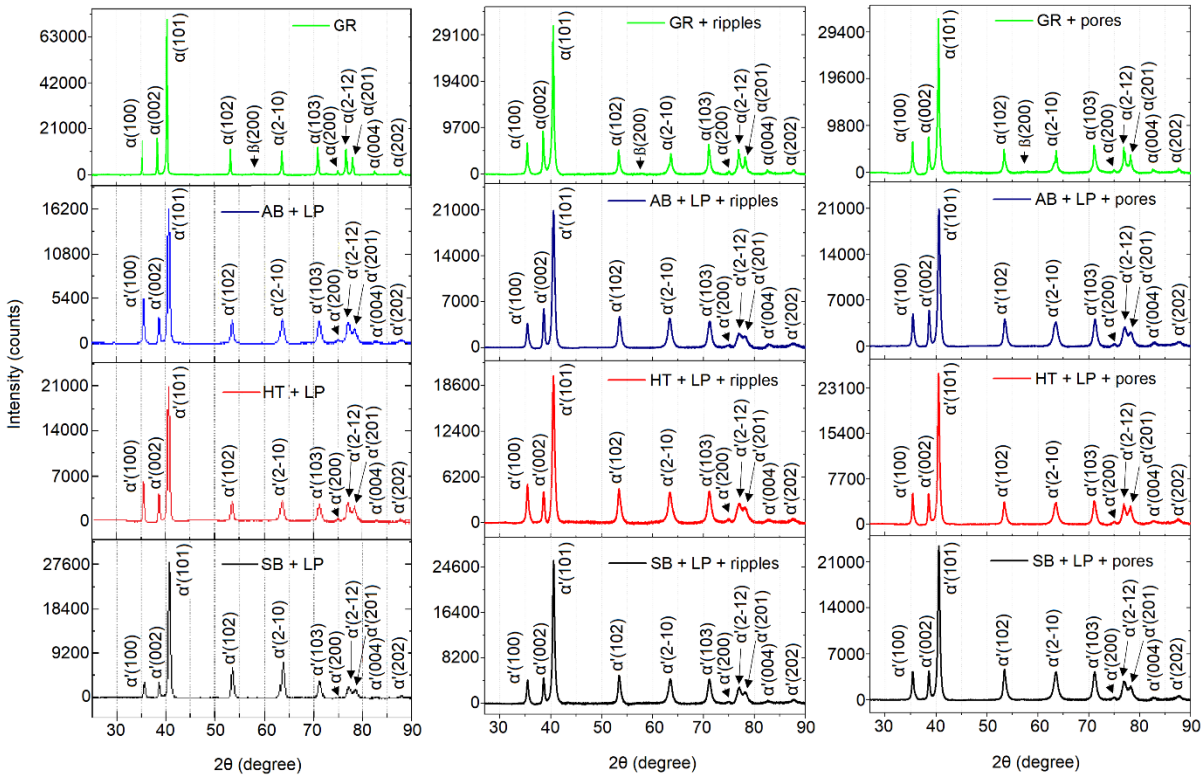

Figure 5-62. X-ray diffraction of the LP samples: (a) initial conditions; (b) with ultrafast laser treatment for nano-ripples formation; (c) with ultrafast laser treatment for pore formation.

When the pores and nano-ripples are applied to the laser polished surfaces, the said broadenings are not identified, which indicates not only similar residual stress states but supports the statement based on the optical microscope images that the ultrafast laser processing did not cause microstructural changes, which remain being the martensitic α'-phase.

The results presented in this section are of great value for the decision making regarding the LPBF process chain. The adoption of laser polishing as a post-process of these metal AM parts can result in a simplified process chain, since steps such as sand blasting, grinding or mechanical polishing can be replaced with a highly flexible and fast alternative. Although, to guarantee that the produced parts will perform according to their design, it is imperative that the microstructural evolution during process and post-process are closely followed. When the (α+β)-phases microstructure is required, the laser polishing process should be performed before the heat treatment, which limits the areas that can be processed, since in most cases the heat treatment takes place with the parts still in the building platform. The ultrafast laser processing, differently, doesn't cause microstructural changes in the parts and, therefore, doesn't cause constraints regarding its use within the LPBF process chain, since it can be performed either before or after heat treatment.

5.3.3. Hardness

The nano indentation measurements were conducted for all the samples investigated in their initial condition, after laser polishing, and after laser functionalization. As mentioned in the section 4.3.5, the nano indentation for the bulk material and laser polished were carried in lines containing nine measurement points starting from the upper surface and going down with steps

of 20 µm, while the samples submitted to the ultrafast laser surface modification had three diagonal lines containing nine measurement points with downwards increment of 6.25 µm. Examples of the measurements described are shown in Figure 5-63, where an optical microscopic cross-section image of the samples with the described indentations conducted.

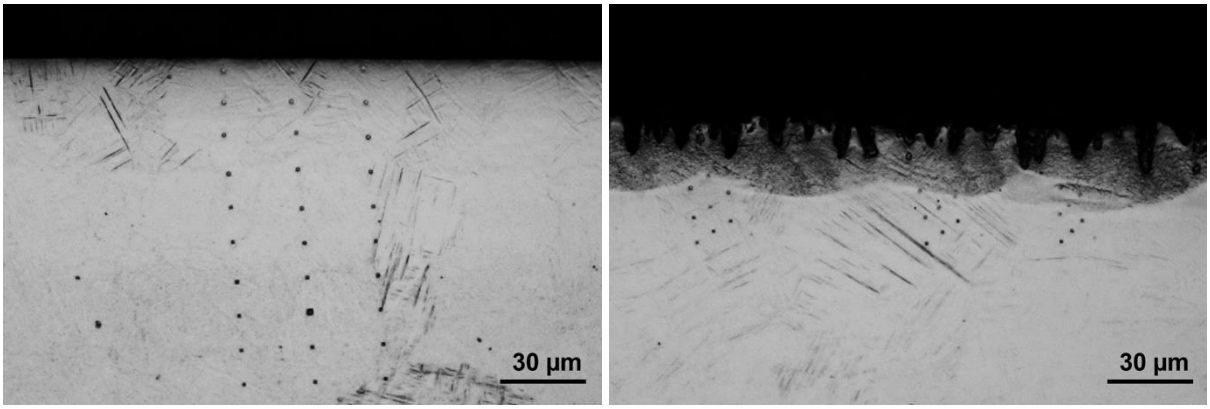

(a) (b)

Figure 5-63. Optical images of the nano indentation procedure: (a) 200 µm of depth; (b) 55 µm of depth.

Although the nano indentation values are calculated to reflect the Vickers hardness, the values for the samples in their initial conditions and after laser polishing are not comparable to those presented in the section 5.1.4, because the micro indentation is not sensitive enough to detect appropriately the hardness of the samples subjected to the ultrafast laser functionalization. For a proper comparison, the hardness of all samples was measured with the nano indentation technique. The values for the samples in their initial condition and after laser polishing are shown in Figure 5-64.

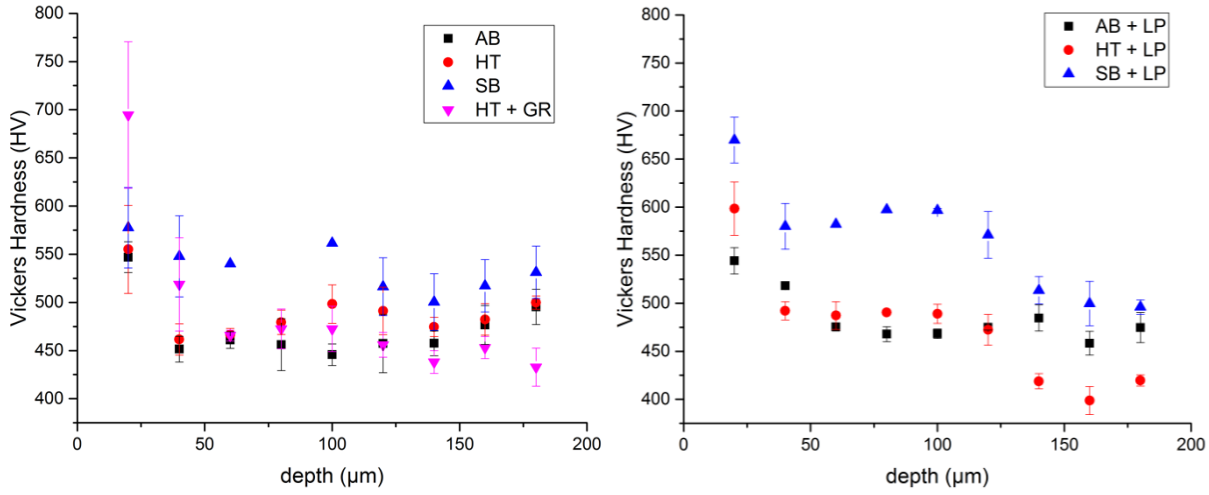

(a) (b)

Figure 5-64. Vickers hardness values from nano indentation at various depths from the surface samples: (a) initial conditions, (b) after laser polishing.

Figure 5-64(a) shows that the hardness of the Ti-6Al-4V alloy manufactured via LPBF is not changed meaningfully by the heat treatment, sandblasting, or grinding processes when

compared to the as-built condition. The initial hardness values of the workpieces AB, HT, SB and GR were between 400 HV0.01 and 500 HV0.01, despite the AB discrepant microstructure.

In Figure 5-64b, the samples submitted to laser polishing presented a slight increase, with values between 500 HV0.01 and 700 HV0.01 reached more often. A more evident hardening effect, within the HAZ of around 100 µm for the selected parameters set, occurred in the SB + LP samples, in accordance with what was presented in section 5.1.4. As in the previous analysis, different topographies can cause disparity between absorptions, which can alter the temperature and thermal gradients achieved during the laser polishing process, thus causing different values of hardness. This reinforces the implication that the same microstructure can be obtained with different thermal gradients but, when that is the case, the resultant microstructure alone cannot dictate the consequential mechanical properties of the material. Even though the micro and nano indentations result in different quantitative results, the resultant behaviors are comparable. The comparable hardness between the AB and HT samples are explained by the observation that their similar initial surface topography results in an equivalent absorption, therefore analogous thermal gradients during the laser polishing process.

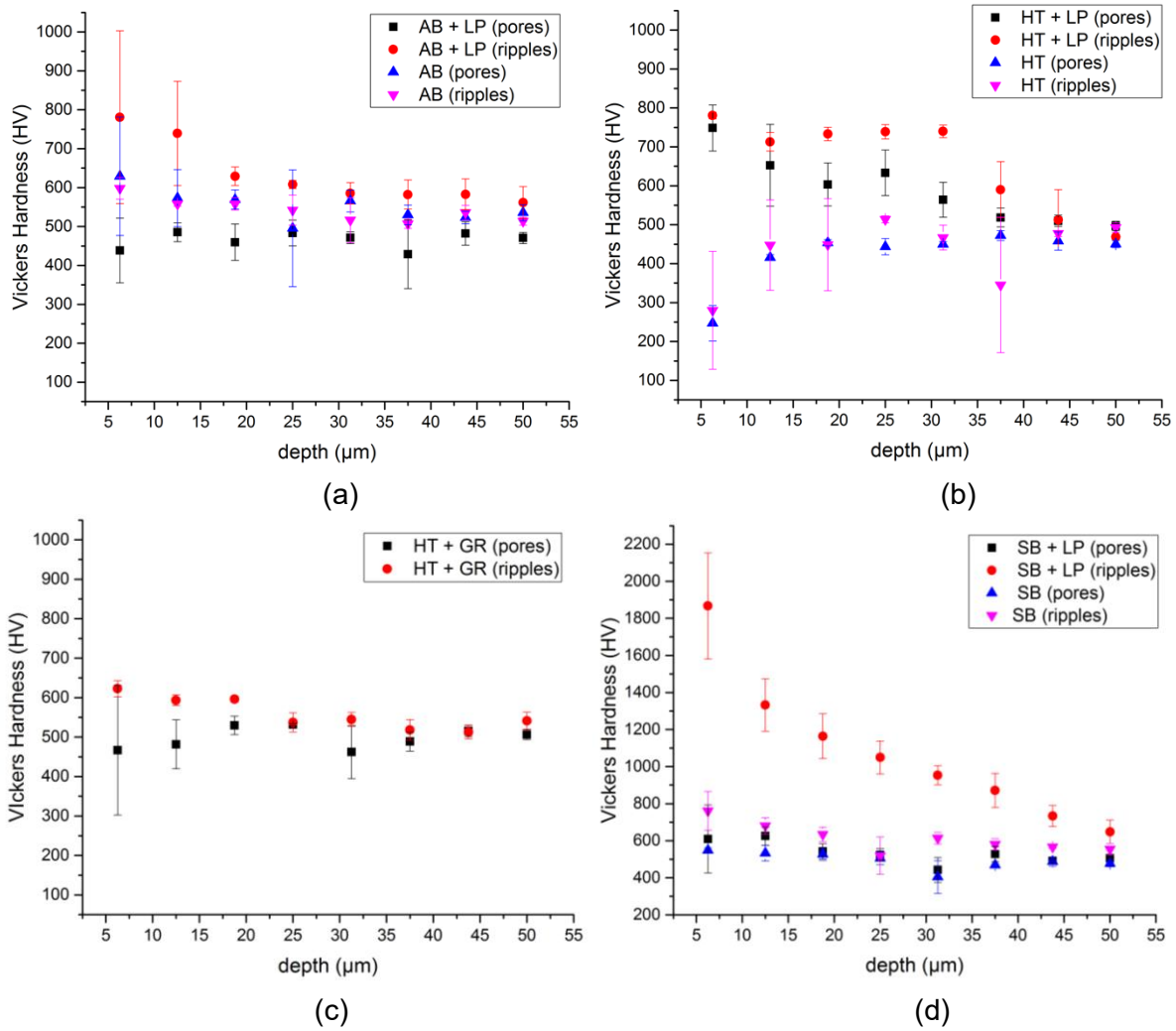

Figure 5-65. Vickers hardness values from nano indentation after pores and nano-ripples formation at various depths from the surface samples: (a) AB and AB + LP, (b) HT and HT + LP, (c) HT + GR, (d) SB and SB + LP.

As exposed in the previous section, the adoption of the ultrafast laser for the surface functionalization caused no effects in the microstructure of the parts, which implies that the influence on the mechanical properties should also be minimal. The Vickers hardness values obtained for the ultrafast laser structured samples with the nano indentation technique are presented in Figure 5-65. As established, the AB parts, before or after laser polishing, have the same martensitic α'-phase microstructure. Figure 5-65a shows that the AB and AB + LP samples after ultrafast laser treatment, independently if for nano-ripples or pore formation, the sample experienced minimal effects in the hardness when compared to their initial conditions. For the nano indentation, similarly to the micro indentation, some hardness values presented higher deviations at the certain points, which can be caused by the material defects during the LPBF process, as discussed, or by uncertainties linked to the measurement procedure. It was expected that the HT samples would display an increase in the hardness after laser polishing, although this was not the case for the initial conditions. Nevertheless, after the ultrafast laser structuring, for both nano-ripples and pores, the HT part experienced a decrease on the hardness values below 300 HV0.01 around 7 µm from the laser treated surface, while in the same depth the HT + LP samples maintained the hardness values within the same range as the initial conditions. Oppositely, an extreme increase was observed for the SB + LP sample, with hardness achieving values above 1800 HV0.01.

As already mentioned, the LPBF process faces the occurrence of defects, and the nano indentation analysis is even more sensitive to porosities associated to the LPBF process. Even though the measurements were repeated several times, the discrepancy between measurements was excessive in some cases, leading to high standard deviations, which was the case for the SB + LP sample. Finally, the GR sample presented a hardness between 450 and 650 HV0.01 for either the initial condition or after both laser structuring procedures.

5.3.4. Water wettability

Regarding particular applications, one of the main considerations is how manufacturing and/or post-processing techniques affect the parts' functionalities. Therefore, following each of the steps outlined in the preceding section, the examined samples were evaluated for their H_2O wettability properties. Here, the topographies resulting from manufacturing approaches with and without any laser post-treatment led to distinct H_2O wetting behaviors (Figure 5-66 and Figure 5-67).

The assessment conducted was carried out under four initial conditions following AM but previous to laser post-processes. The AB and HT samples displayed contact angle (CA) average values of 121° and 85°, respectively, although their topographies were similar (Figure 5-68). Distinct CA average values were seen when conventional smoothing approaches were used, with 97° for SB and 67° for GR samples.

Regardless of their original or modified topographies, the surfaces displayed hydrophobic properties following the ultrafast laser treatment. The GR + HT with formation of nano-ripples had CA average values that were consistently higher than 100°, going as high as 135°. Even though the two kinds of structures created using ultrafast laser share the hydrophobicity characteristic, the presence of nano-ripples led to a trend of higher average CA values when compared to the porous structures, with the only inconsistency for this observation being the results for the structured parts from AB initial condition (Figure 5-68a). As summarized in Table 3-9, Jiao (2018) [120], achieved comparable results after ultrafast laser treatment of AM titanium parts without previous surface altering actions, with contact angles between 91° and 150°. Overall, workpieces treated with ultrafast laser radiation exhibit comparable values for

contact angles and hydrophobicity comportment. This statement is endorsed by works that analyzed this post-process on non-AM Ti-6Al-4V [31, 32] and on samples composed by alternative metallic materials [116, 117, 118].

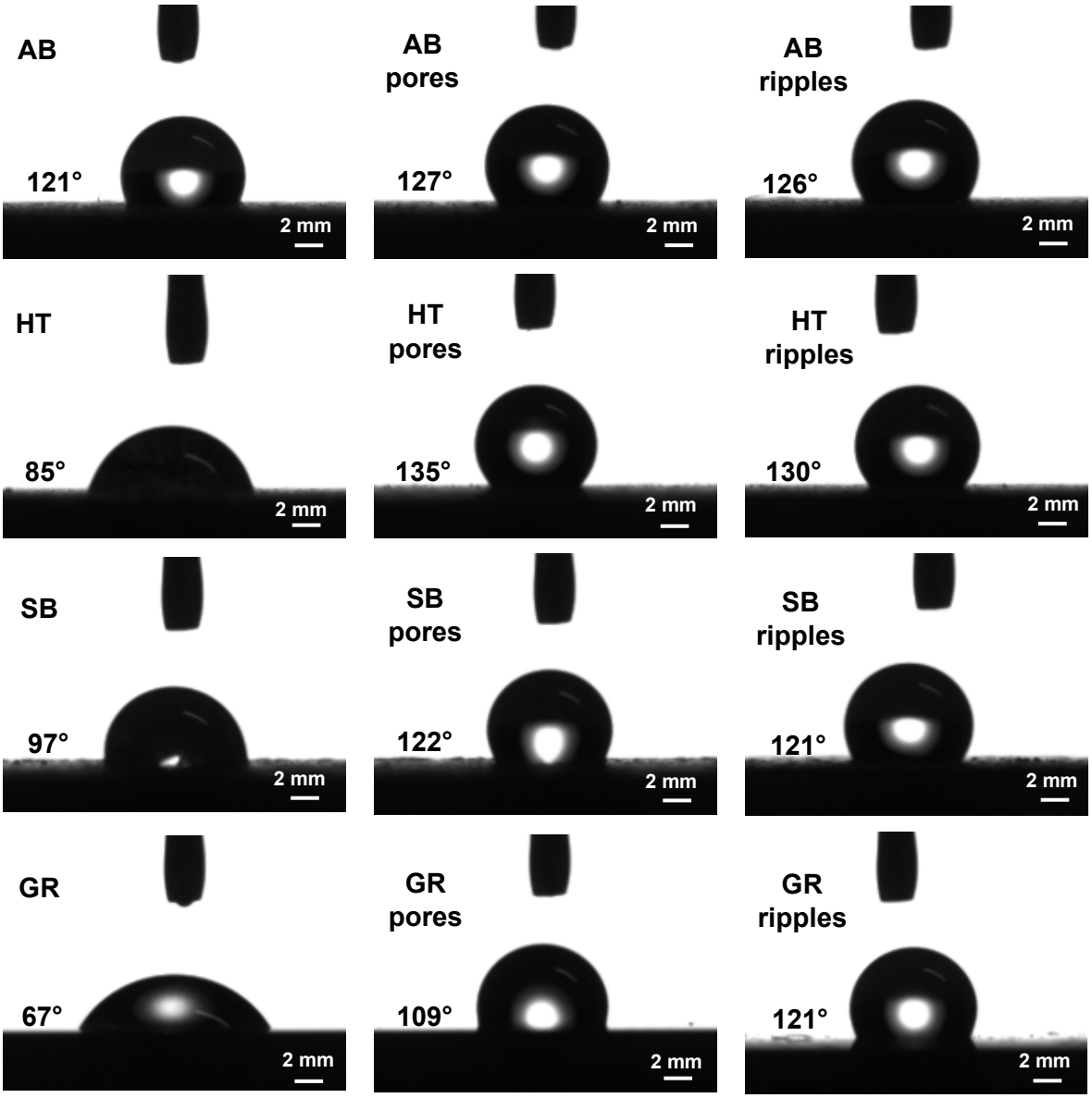

Figure 5-66. Images of water drops from wettability analysis of AB, HT, SB, and GR surfaces: (a) without laser treatment; (b) with ultrafast laser treatment for pore formation; (c) with ultrafast laser treatment for nano-ripples formation [123].

A third method considered in this study for smoothening surfaces and consequently enhancing their quality, was laser polishing. From previous discussions, it is noticeable that after LP the final surfaces were brought to an almost identical state despite their distinct initial topographies. Correspondingly behavior was found for the wettability outcomes (Figure 5-67). As depicted in Figure 5-68b, AB, HT, and SB workpieces presented a contact angle of 65° when submitted to LP. By coupling two post-processes such as LP and laser functionalization, all surface structures (nano-ripples and pores) achieved hydrophobic qualities. Analogously to samples that were subjected only to laser functionalization and not LP, which also exhibited hydrophobic characteristics and high CA values, the combination of both post-processes resulted in CA

ranging from 99° and up to 121° AB + LP (nano-ripples) sample. In this analysis, no fundamental deviation was detected for contact angle values when comparing samples with nano-ripples or porous structures.

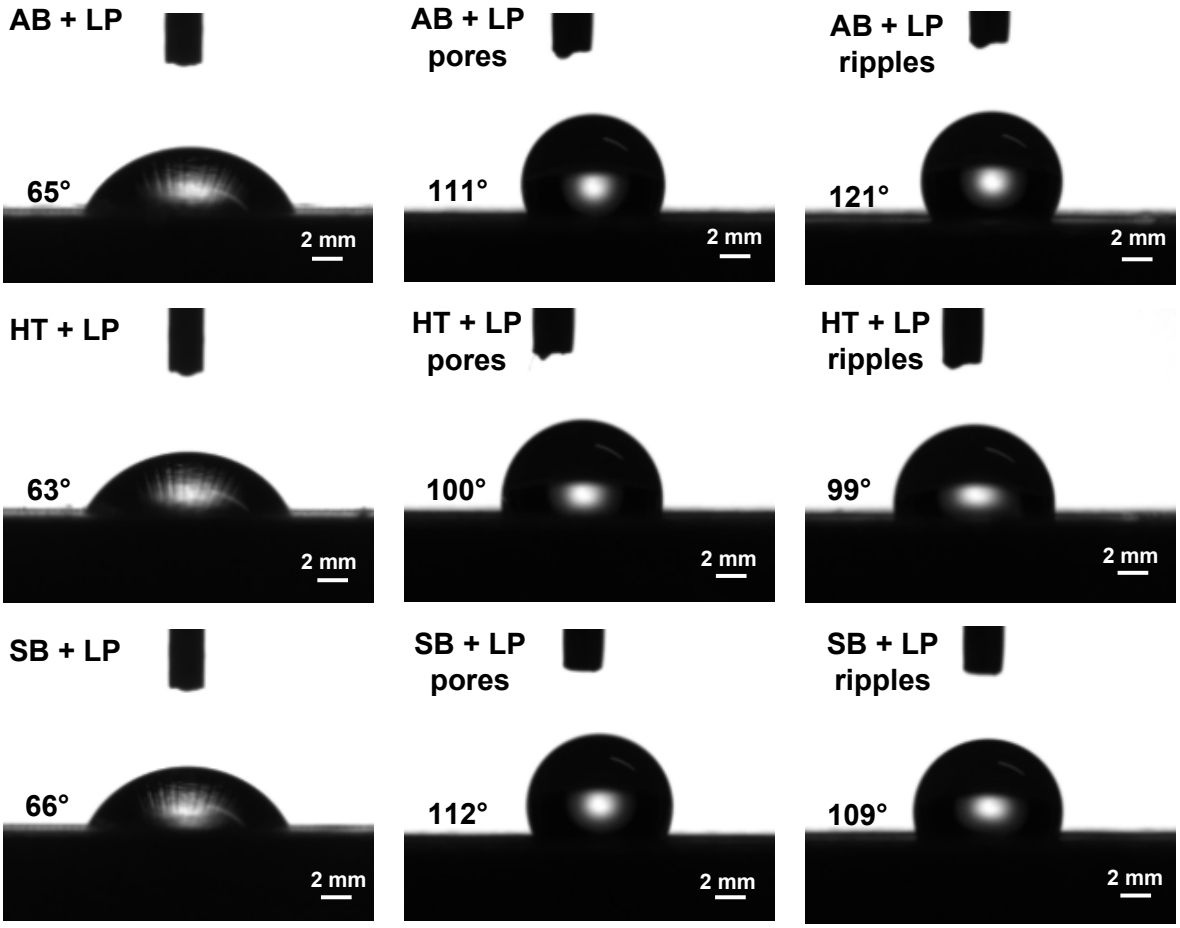

Figure 5-67. Images of water drops from wettability analysis of AB, HT, and SB surfaces: (a) after laser polishing; (b) with ultrafast laser treatment for pore formation; (c) with ultrafast laser treatment for nano-ripples formation [123].

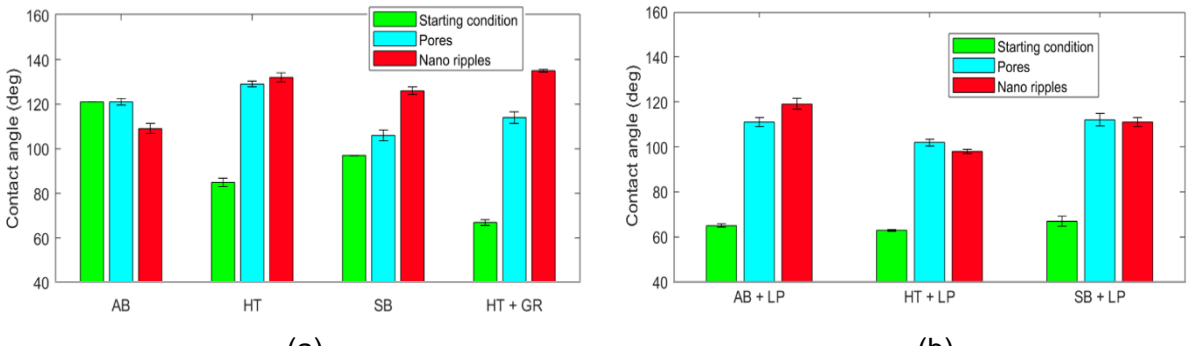

Figure 5-68. Water contact angle measurement values for AM Ti-6Al-4V samples in different steps of the post-process chain [123].

5.3.5. Surface chemical composition

The topography cannot be solely attributed to the parts' wetting behavior. XPS analysis was therefore used to determine the surface chemistry after each process that was discussed. The passivation that is frequently seen in titanium was confirmed with the occurrence of doublets credited to TiO_2 (Figure 5-69 and Figure 5-70, Ti $2p_{3/2}$ at 459.0 eV) and TiO_x (Figure 5-69 and Figure 5-70, ~ 456.5 eV) [169] because the processed workpieces were kept in standard atmosphere in the days prior to the surface chemistry analysis. Al_2O_3 and V_2O_5 are two additional metal oxides that were found on the surfaces of several samples but are not shown in the images. All workpieces, regardless of their manufacturing approach, had a layer of combined metal oxides in varied percentage.

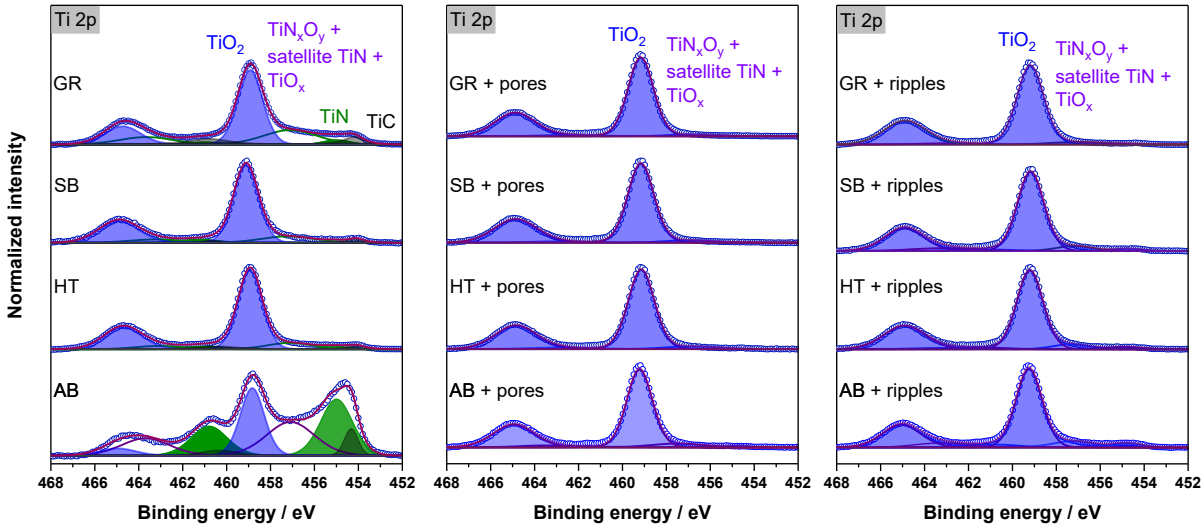

Figure 5-69. Ti 2p XPS spectra for different processing steps: (a) starting conditions, (b) after pore formation, (c) after ripples formation. Adapted from [123].

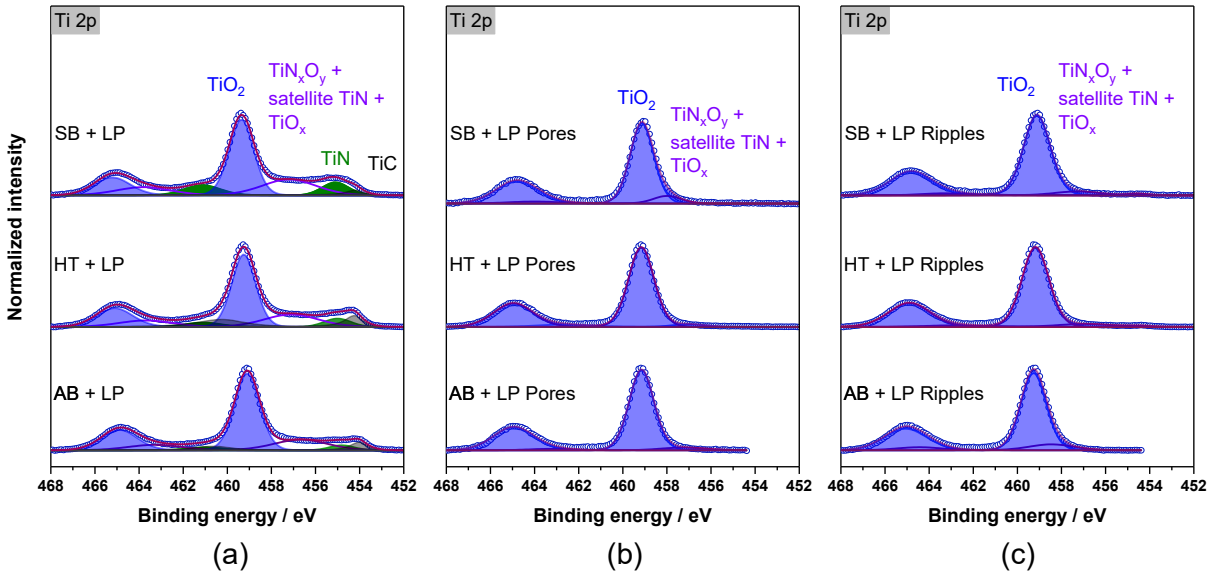

Figure 5-70. Ti 2p XPS spectra for different processing steps followed by laser polishing: (a) starting conditions, (b) after pore formation, (c) after ripples formation. Adapted from [123].

Additional doublets are observed with Ti $2p_{3/2}$ at 454.2 eV, 455.0 eV and 457.0 eV representing TiC, TiN with its satellite [170], and TiN_xO_y, respectively, for workpieces before and after laser

polishing. While the peaks corresponding to N1s of TiN can be seen at 396.4 eV (not shown here), C1s peaks of TiC are observed at 282.3 eV. Following AM, which is carried out in an argon-filled inert atmosphere, the highest concentration of TiN and TiC was found on the AB parts, with GR workpieces presenting the second highest concentration, and less evident presence on HT and SB samples. Inert atmospheres were not used for the manufacturing processes of HT, SB, and GR parts, with the HT being produced with one additional high temperature manufacturing step from AB parts, while SB and GR are produced with one additional low temperature post-processing step each from HT parts. In contrast to the HT parts, the non-thermal nature of the post-processes used to finish the SB and GR workpieces avoided additional reactions between the titanium alloy and the nitrogen, which is why all three parts present comparable TiN, TiC and metal oxides concentrations. Additionally, their comparable H_2O wettability results support the notion that such characteristic is heavily influenced by the surface chemical composition. Furthermore, the occurrence of nitrogen on the surface of the mentioned parts may have been caused by an interaction between such element and the printed samples following their manufacturing via LPBF and before heat-treatment.

In order to prevent surface oxidation, argon was blasted on the sample throughout the LP process, as explained in section 4.2.1, and the outcome was a larger proportion of TiN and TiC than the ones observed for HT, SB, and GR samples before LP. An argument to justify this observation is that the material keeps reacting with the surrounding atmosphere while still heated even after the process is concluded and argon is no longer being blasted. Nonetheless, if contrasted with the parts directly following AM in an inert environment, these values remain lower.

TiC and TiN were absent from all functionalized surfaces, while metal oxides predominated (Figure 5-69b, Figure 5-69c, Figure 5-70b, and Figure 5-70c). Given that the procedure was carried out with no inert gas environment or blasting, these were anticipated outcomes that in combination with the resultant topographies determined the hydrophobicity characteristic of the parts [171]. Because the process adopted to originate pores or nano-ripples on the workpieces were comparable between each other and were applied with the circumstances previously mentioned, their surface chemical composition was also similar, thus the equivalent H_2O wettability even with fairly different topographies. Additionally, due to material ablation, vanadium oxide peaks are seen in all structured workpieces with their principal component at 517.2 eV (V_2O_5) together with its weaker component at 515.2 eV (probably V_2O_3) [172].

Table 5-14 provides a summary of the surface chemical composition detected on the samples following the different manufacturing stages considered in this work. Before discussing the results, it is crucial to highlight the fact that the XPS analysis can only probe a few nanometers deep. Therefore, the results depicted and addressed in this section are rather associated with the surface of the samples than with their bulk. Moreover, the displayed amounts oxygen, carbon and nitrogen are not only an outcome of the chemical reactions between such elements and the material's core elements, but a composition of such reactions and surface contamination [173]. In every instance, oxygen and carbon are the elements most present on the workpieces' surfaces, since their content surpass even the core elements' (Ti, Al, V) together. The nitrogen content between 6 and 8 at% detected on some samples (AB, AB + LP, SB + LP, and HT + LP) was considerably high, which is attributed to the existence of TiN and TiN_xO_y. The analysis also revealed that nearly no nitride nor oxynitride is found following ultrafast laser processing. As a matter of fact, contamination is the only source for the nitrogen concentrations between 1 to 2 at%. The same is true for the majority of oxygen detected on

the workpieces' surfaces subjected to laser functionalization, as it most arose from metal oxidation (O1s at 530.4 eV).

Table 5-14. Main chemical components detected on the surface of different samples (at. %) [123].

Sample	Ti2p	Al2p	V2p	O1s (Metal Oxide)	N1s (TiN, TiN_xO_y)	O1s cont.	C1s	N1s cont.
AB	14.1	2.9	-	10.8	5.8	18.5	40.2	2.1
AB + LP	11.1	4.8	-	12.2	5.3	18.0	43.2	2.3
AB + LP + pores	10.9	0.8	0.6	26.3	0.2	13.9	39.6	1.2
AB + LP + ripples	9.8	4.8	0.5	23.4	-	15.4	43.0	1.2
HT	13.5	2.3	0.8	27.4	1.3	14.6	36.6	1.0
HT + LP	16.3	4.8	0.3	28.4	3.3	12.4	31.3	1.5
HT + LP + pores	11.3	4.6	0.6	26.1	0.1	14.4	39.0	1.2
HT + LP + ripples	10.5	5.4	0.6	25.1	0.2	15.3	40.1	1.0
HT + GR	15.1	3.2	0.7	25.4	3.6	14.3	34.6	1.5
SB	6.9	10.0	-	18.9	0.5	21.0	38.0	0.9
SB + LP	13.6	6.6	0.1	24.5	4.2	14.0	31.9	1.6
SB + LP + pores	8.8	6.6	0.2	21.2	0.1	17.6	40.3	1.2
SB + LP + ripples	6.0	3.3	0.3	14.2	-	18.5	51.8	1.6

A quotient analysis between the metal alloy's fundamental constituents is crucial for ignoring contamination when examining the material composition itself. This enables comprehension of the element content behavior on the parts' surface for every manufacturing step used.

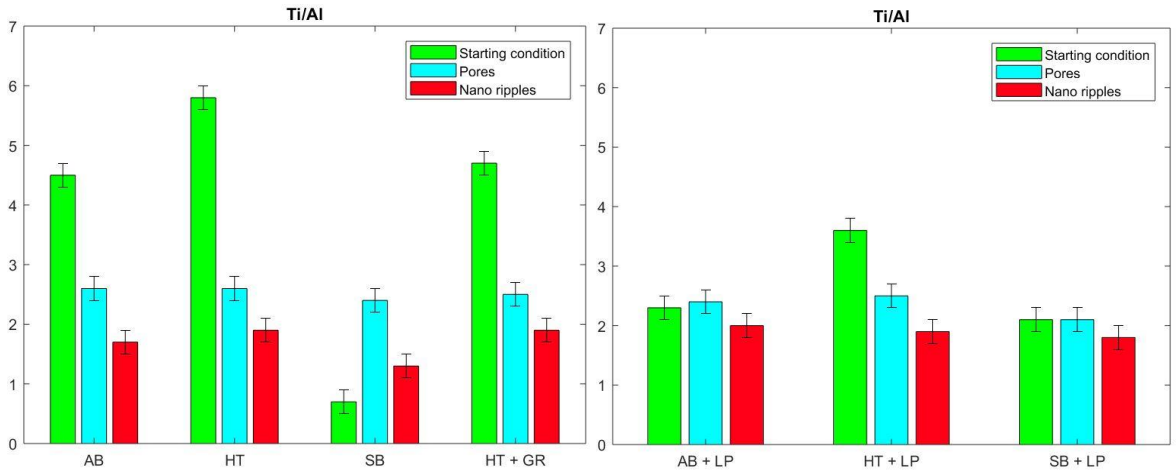

(a) (b)

Figure 5-71. Ti:Al ratio for AM Ti-6Al-4V samples in different steps of the post-process chain [123].

Figure 5-71 shows that the Ti:Al ratios for the AB, HT, SB, and GR samples are significantly different, with values of 4.5, 5.8, 0.7, and 4.7, respectively. Following the sandblasting, the aluminum concentration increased, indicating a notable change in the elemental composition. The amounts of titanium and aluminum, however, remained within the same range for the

subsequent procedures. The most significant alteration after laser polishing was on the SB parts, where a considerable increase in titanium and a decrease in aluminum resulted in the higher Ti:Al quotient of 2.1. Conversely, relevant rise in aluminum led to decreased ratios on AB and HT samples of 2.3 and 3.6, respectively, following the laser smoothing process. The workpieces whose surfaces are structured with either pores or nano-ripples presented a consistent Ti:Al proportion (2.2 ± 0.2) amongst all studied cases. The functionalized workpieces also exhibited a stable Ti:V ratio (20 ± 2), independently of their initial states. Such value is reasonably close to the theoretical ratio of 24, determined from the expected stoichiometry. No conclusions could be drawn regarding the Ti:V ratio assessment for non-functionalized parts, as no vanadium oxide could be detected in most cases (Table 5-14). The Ti:Al:V proportions were similar under all circumstances, irrespective of the kind of laser process that was applied. When laser polishing is adopted before the functionalization, samples with entirely distinct surface chemical composition are brought to the same initial state, which makes the results very repeatable and controllable. Laser polishing produced TiC and TiN in addition to the anticipated metal oxides, which differ from the results observed for the ultrafast laser processing.

The relationship between H_2O wettability, chemical composition, and topography can be better understood after assessing the results altogether. The presence of metal oxides on the surface of smooth workpieces has a propensity to be hydrophilic, whereas having the same surface chemical composition on structured parts (even in the nano scale) leads to a tendency of hydrophobicity [171]. These assumptions are aligned with the results seen during the development of this research for the samples submitted to both laser post-processes, separated or combined.

5.3.6. Biocompatibility

It is crucial to ensure that no laser post-processing adopted reduces the material's biocompatibility, as titanium and its alloys are frequently used in medical applications due to their exceptional mechanical and biocompatible qualities.

The ability of cells to adhere and proliferate on the part's surface was not negatively impacted by the laser functionalization either before or after laser polishing, according to the grown cells fluorescence images (Figure 5-72 and Figure 5-73). All cells showed a typical morphology, and the orientation of the attached cells appears to be random in each of the scenarios without laser polishing (Figure 5-72).

The laser-polished results in Figure 5-73a and Figure 5-73b, before and following the generation of porous structures, respectively, exhibit the same random cell orientation behavior described earlier. Differently, the cells displayed a slight propensity to grow in a particular direction when nano-ripples were generated following the combination of both laser post-processes (Figure 5-73c), which corresponds to the formation of depression lines covered in section 5.3.1.

Figure 5-74 and Figure 5-75 provide a summary of the toxicity analysis derived from an MTT assay. The sample's cell viability is expressed as a percentage of the negative controls. Cells grown with the extracts generally showed the same viability as the controls, suggesting that the parts under investigation maintained their high biocompatibility despite the various post-processing steps.

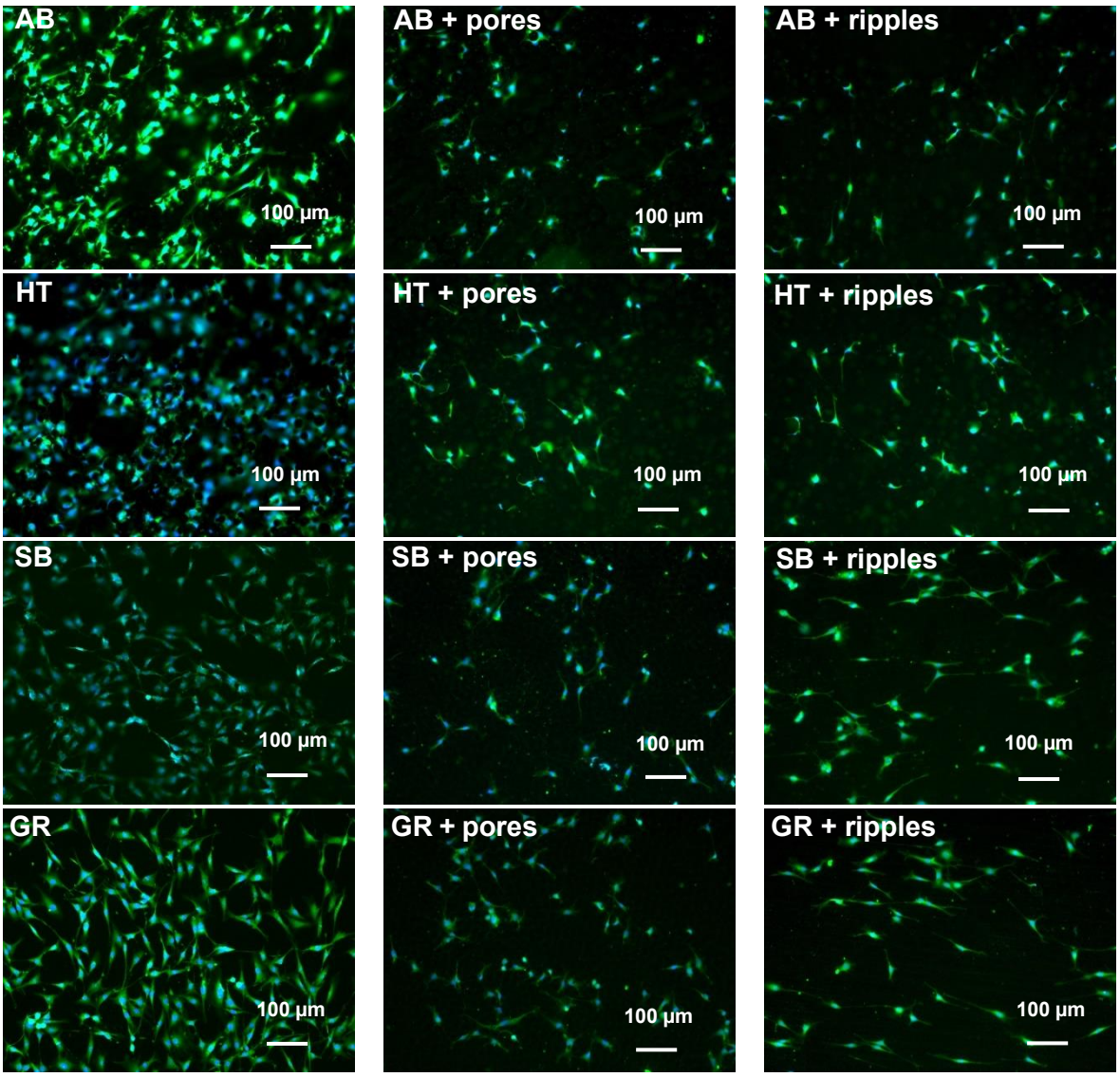

(a) (b) (c)

Figure 5-72. Fluorescence images of MC3T3-E1 cells growing on the surfaces of parts: (a) without laser treatment; (b) with ultrafast laser treatment for pore formation; (c) with ultrafast laser treatment for nano-ripples formation [123].

Topographies with patterns can serve as scaffolds and promote the cell growth [174], however such performance was not exhibited in this investigation. The cell proliferation viability suggests that any post-process applied does not adversely affect the biocompatibility of the Ti-6Al-4V samples, thus laser polishing and functionalization can be used together or separately to replace specific steps in the process chain and to achieve functionalities as hydrophilicity and hydrophobicity at certain areas of the workpiece.

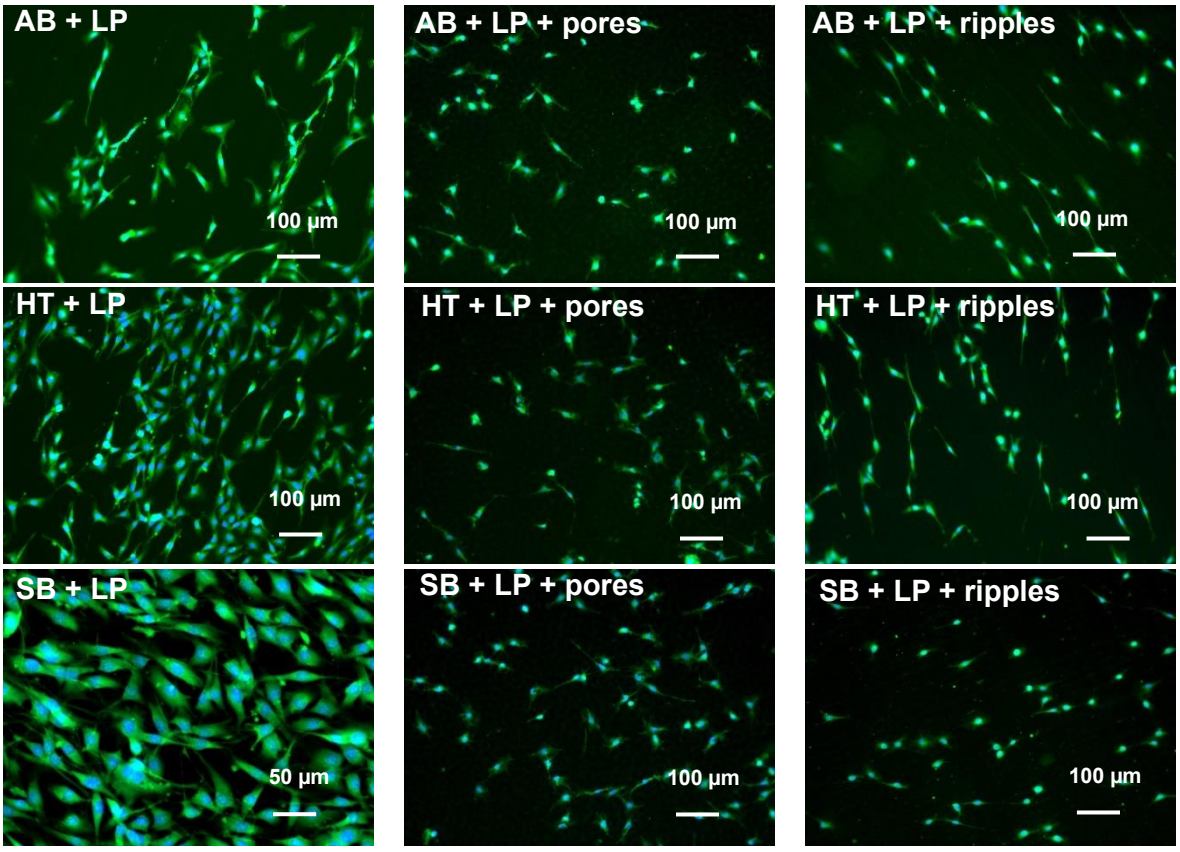

Figure 5-73. Fluorescence images of MC3T3-E1 cells growing on the surfaces of parts: (a) without laser treatment; (b) with ultrafast laser treatment for pore formation; (c) with ultrafast laser treatment for nano-ripples formation [123].

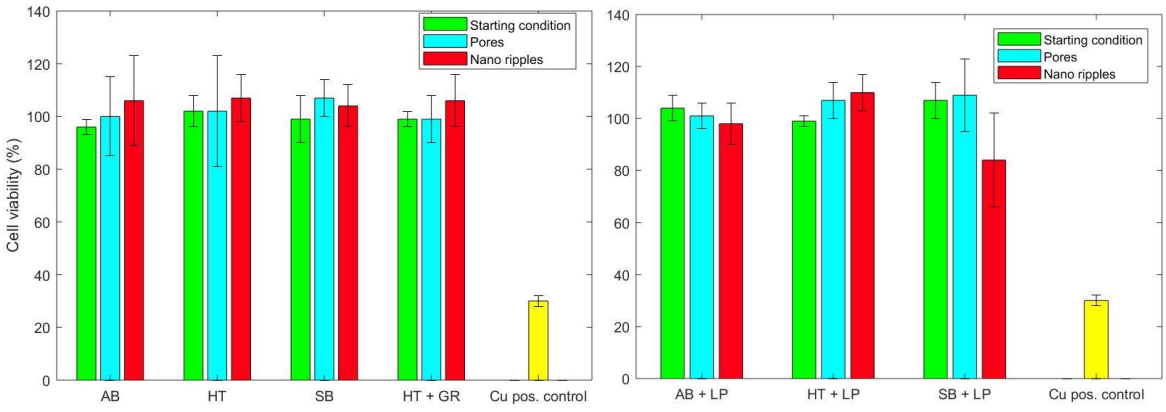

Figure 5-74. Cell viability (in percentage) of MC3T3-E1 cells cultivated with the extracts from differently treated samples compared with the negative control (100% viability) [123].

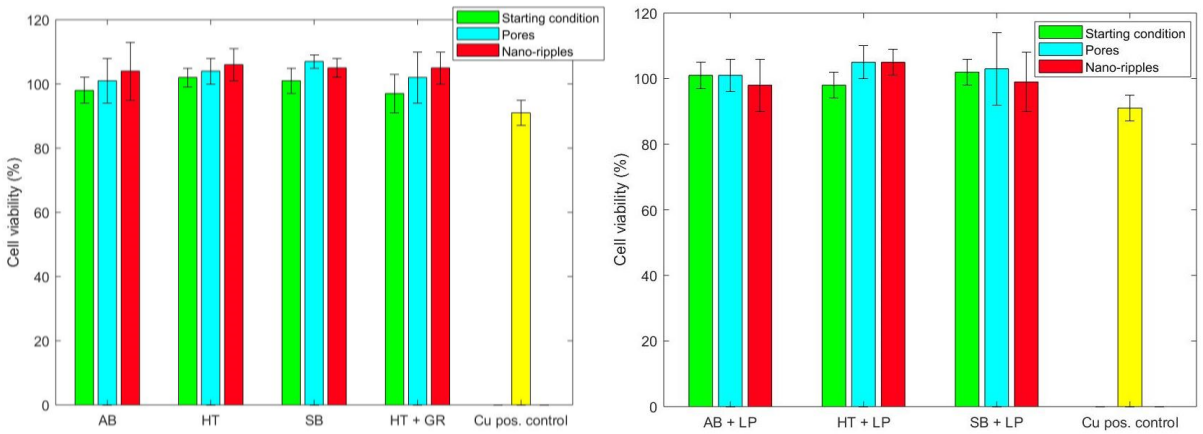

(a) (b)

Figure 5-75. Cell viability (in percentage) of MC3T3-E1 cells cultivated with the extracts from differently treated samples compared with the negative control (10% viability).

6. Summary and outlook

The aim of the current work was the investigation of laser-based post-processes for the surface quality improvement and modification of Ti-6Al-4V parts produced via the LPBF process. Laser polishing with a continuous wave (cw) laser source and laser functionalization with an ultrashort pulse laser source were used. The resulting surfaces of the parts were characterized following different steps of the metal AM process chain, before and after the application of the laser treatments, and the effects of the proposed post-processing methods on the parts microstructure and mechanical properties were evaluated. The different laser post-processes had slightly divergent sub-goals throughout the development of this work and the most relevant findings are summarized in this chapter.

6.1. Laser polishing

Ti-6Al-4V parts produced via LPBF were available in three starting conditions: as-built (AB), heat treated (HT) and sandblasted (SB), with initial surface roughness Ra of 7.1 µm, 6.9 µm and 5.6 µm, respectively. All mentioned samples were subjected to a laser polishing process, performed in a continuous wave disk laser source (λ = 1064 nm) with a pendulum scanning system (f = 100 Hz), and an argon flow (10 L/min) delivered to the surface of the parts by a nozzle. The selection of the process parameters to achieve smoothened surfaces was performed by means of a process development approach, systematically executed in accordance with the design of experiments technique selected for this study. The material was then characterized accordingly.

Three types of surface structures were obtained after laser polishing: ripples, grooves, and step structures. The ripples were more prominent when low laser power (P = 100 W) and low number of repetitions (N = 1) were applied. This type of structure, in the micro scale, did not represent a satisfactory improvement in the surface roughness of the parts assessed. Although the reduction reached up to 70% when compared to the initial states (Ra = 7 µm), the Ra values obtained were not in the range required for practical applications. With the increasing of the laser power from 100 W to 200 W, and number of repetitions from 1 to 3, the ripple form on the surface started to fade, giving space to the groove structures, due to a more efficient re-melting of the surface, hence a higher degree of homogeneity was achieved. The groove forms could also be observed on samples processed with laser power of 300 W, depending on the combination of the remaining parameters. The nano scale nature of the step structure does not affect the Ra roughness in the micro scale, which makes it the most suitable outcome to achieve a polished surface trait. The parameter combination of 300 W, 3 repetition, +3 mm focal position, and 0.4 m/min, resulted in a 91.1%, 86.1%, and 53.9% of reduction in the surface roughness Ra for the HT, AB, and SB parts, respectively. These values evidence that the laser/materials interaction is highly dependable on the surface topography of the samples. Similar conclusion can be drawn when evaluating the research work where Ra roughness reductions between 27.6% and 98.6% were achieved for different initial surface texture of 0.58 µm and 7.5 µm, respectively.

Following the surface quality assessment, the effects of the laser polishing in the materials properties were assessed in three different ways: microstructural changes, heat affected zones depths, and micro hardness measurements. By means of optical microscopy and XRD analysis, the investigation of the microstructural change on the AB, HT, and SB samples, before and after laser polishing, was conducted. The visual investigation of the AB Ti-6Al-4V

alloy manufactured using the LPBF process showed equiaxed grains, and the XRD analysis confirmed that this material presented a majority content of hexagonally close-packed (hcp) fine acicular martensitic α'-phase caused by temperatures above β-transus that are achieved during the process, which altered the microstructure from (α+β)-phase to β-phase, and the rapid cooling of the process. It is standard practice that Ti-6Al-4V samples manufactured via LPBF are submitted to heat treatment for microstructural change, as a post-process step of this manufacturing method. The microstructures of the HT and SB base material are identical since both workpieces were heat treated in accordance with the same heating method and specific thermal history. For these samples, the optical images showed basketweave structures, which are attributed to the α'-phase decomposition and forming of the mixed (α+β)-structure during the heat-treating process. The XRD analysis, in this case, confirmed the occurrence of a microstructure that is a mixture of hexagonally close-packed (hcp) α-phase and body centered cubic (bcc) β-phase. After laser polishing, fine acicular martensitic α'-phase was observed in the optical images of the re-melted areas in all the samples and confirmed via XRD. The principle of the generation of the martensite during laser polishing is analogous to the martensitic phase transformation during the LPBF, since for both processes the temperature achieved during the process exceeds the β-transus temperature and the cooling rates are in the same order of magnitude ($1.2x10^4$ K/s to $3x10^5$ K/s).

Despite having the capability of improving the surface quality of LPBF Ti-6Al-4V parts, the microstructural change caused in samples already submitted to heat treatment can become an impediment to the wide use of such technology as a post-process. The microstructural changes mentioned occur within the melted and heat-affected zones (HAZ) and could be easily observed in the HT and SB samples due to contrast etching and distinct resultant microstructures. In a similar way, the identical microstructure before and after laser polishing for the AB sample can be observed after contrast etching but the depth of the HAZ is more difficult to find due to the analogous microstructures. It was observed that the depths of the HAZ depend greatly on the laser intensity to which the part was subjected during the laser polishing, with the power of 100 W causing HAZ of up to 64.2 ± 2.5 µm, 200 W up to 94.1± 4.9 µm, and 300 W up to 124.8 ± 5.5 µm. The axial feed rate was not considered of major influence in the resulting HAZ depth, with values around the same range for 0.4 m/min and 0.6 m/min, in all cases, when the remaining parameters were kept constant. Similarly, when the number of repetitions increased from 1 to 3, while the other parameters were kept constant, the resulting HAZ depth remained in the same order. For the number of repetitions, the lack of influence in the HAZ depth was attributed to the fast solidification that occurred prior to each repetition, which did not permit energy accumulation between repetitions and could not promote the continuous expansion of the HAZ. The altered focal position from 0 to + 3 mm influenced greatly the HAZ depth, with significant reduction from 108.7 ± 3.9 µm to 75.5 ± 3.1 µm, respectively, in the most extreme case. Finally, when comparing the HAZ depth of the AB, HT, and SB samples it is observed that the SB sample clearly tends to absorb less laser energy and present distinct thermal conductivity due to the different initial topography, while the HAZ depth values for the AB and HT samples tend to be in the same range due to comparable initial topographies. For a parameter set that included 100 W, 0.6 m/min, 1 repetition, and focal position of 0 mm, the HAZ depth for the AB, HT, and SB workpieces were 57.4 ± 1.8 µm, 52.5 ± 4.3 µm, and 46.9 ± 5.1 µm, respectively.

One of the implications of the microstructural changes within the HAZ during the laser polishing is the altered mechanical properties, which can lie outside the requirements for specific applications. The initial hardness values of the workpieces AB, HT, and SB, were between around 440 HV0.01 and 480 HV0.01 for the HT and SB, and 460 HV0.01 and 500 HV0.01 for

the AB. Although there is a slight increase in the hardness when the microstructure consists of fine acicular martensitic α'-phase, which is the case of the AB samples, the hardness of the Ti-6Al-4V alloy manufactured using the LPBF is not changed significantly with the microstructural alteration after the heat treatment process. After laser polishing the hardness had a significant increasing within the melt pool zones of the SB parts (at around 15 µm for the polished surface) reaching values around 800 HV0.01. As the measurement depths approached the transition area of the HAZ and the bulk materials, no significant variations were observed. With higher laser absorptions, the AB and HT parts present deeper HAZ. A behavior similar to the SB samples was expected for the HT ones, although after laser polishing the hardness values within the HAZ remained in the range of those observed for the bulk material, even though at different depths the presence of distinct microstructures is observed. Expected for the AB material, due to the same type of microstructure being present in both melted/heat affected zones and bulk material, the results indicate that the laser polishing process, with the parameter in the range described in this study, could hardly affect the hardness results. The values remained between 400 HV0.01 and 500 HV0.01 throughout the measurement depth. Despite the continuous development of the LPBF process, AM parts from such process face the occurrence of porosity, which can make the characterization of the mechanical properties difficult. Micro indentation analysis can be overly sensitive to defects associated with the LPBF process, such as voids. These imperfections were observed in the base material during the cross-section analysis and are the cause of discrepant measurements and unexpected behaviors observed in some cases.

The use of cw laser radiation for the laser polishing of LPBF Ti-6Al-4V samples has proved a fast and flexible technique for the surface quality improvement of such parts. The results demonstrate that independently of the initial condition, the adopted post-process can eliminate surface asperities in a satisfactory way. One drawback of this approach is that the high temperatures achieved during the process, which were extensively discussed in this work, lead to undesired microstructural changes in samples previously subjected to heat treatment for stress relief. In general, this microstructure modification can alter the mechanical properties of the parts, which then become unsuitable for practical applications. For this reason, based on the results presented in this work, if laser polishing is under consideration to be adopted as a post-process for LPBF Ti-6Al-4V parts for surface quality improvement, it is recommended to perform such process prior to the heat treatment, while the sandblasting process can be eliminated altogether.

6.1.1. Numerical analysis

It is common practice in the LPBF process chain to perform the heat treatment of the Ti-6Al-4V parts while they are still attached to the build platform, making the use of laser polishing before the heat treatment difficult to be applied to certain areas of the workpieces. In this case, it is important to have the opportunity to fast assess the HAZ depth within which the microstructure change will occur. For this reason, finite element method (FEM) based simulation was built to represent the thermal conditions of the laser polishing process, with the laser beam assumed to be a focused surface heat source that scans the top surface, the top and side surfaces exchanging heat with the environment through convection and radiation, and with the bottom surface is considered adiabatic. The heat transfer model was validated for single track experiments. Even though a mesh refinement analysis was performed, the sharp effects on the simulated HAZ contours could not be further improved without the major increase of computational efforts. Nevertheless, the model predictions were within the desired level of accuracy for the HAZ depth data acquisition, while saving material and time.

The analysis of the surface characteristics allowed the selection of parameter ranges for the definition of the design of experiments adopted for the development of the laser polishing process, while the heat transfer model allowed the fast assessment of the depth of the heat affected zones for the same set of parameters, thus saving material and time. The parameter included in the process development were the laser power, focal position, number of repetitions, axial feed rate and scanning speed, which varied from, 100 W to 500 W, 0 mm to + 4 mm, 1 to 5, 0.3 m/min to 0.9 m/min, and 400 mm/s to 2000 mm/s, respectively. With the values of Ra and HAZ depth obtained, a quadratic regression method was applied, and it originated 2 equations that represent the behavior of the responses (Ra and HAZ) as a function of the variables (parameters). The R^2 and p-value of the Ra and HAZ statistical models were 0.493 and 0.148 (Ra) and 0.949 and $2.66x10^{-09}$ (HAZ), respectively. The discrepant values are explained by the random data acquisition of the surface roughness values and a heat transfer model that did not include any noise in the simulations, hence the superior performance of the latter. From the ANOVA analysis, it was established that the parameters that have greater effect in the Ra and HAZ depth outputs, from the most to less relevant, are the scanning speed, laser power, feed rate, focal position, and number of repetitions. From the statistical models the interaction of the parameters as a function of the responses was also assessed. In general, the Ra had a tendency to decrease with: an average laser power of around 300 W; with higher values of focal position and number of repetitions; and with lower scanning speed and feed rate. Oppositely, the tendency for the estimated HAZ depth to decrease results from: an average laser power of around 100 W; low number of repetitions; and with higher scanning speed. The only parameter that presents the same behavior for minimum Ra and HAZ is the higher values for the focal position. Finally, the statistical models enabled the generation of prediction slice plots, which can offer a possibility to check the Ra and HAZ depth values for specific parameter combinations at the users will.

As an alternative to the statistical models, artificial neural networks (ANN) models were developed and assessed based on the same experimental and simulated data used in the regression analysis. For this type of modelling, the full dataset is divided into training (70%), validation (15%) and test (15%) data. In the ANN model built to predict surface texture, the fit for the training data presented an R value of 0.986, which indicates an almost perfect linear relationship. When considering the validation and test data, the R values obtained are 0.792 and 0.604, respectively. The resulting fit for the entire dataset presented a satisfactory R of 0.900. As for the HAZ depth ANN model, the fit for the training data had an R value of 0.941, while the validation and test data presented R values of 0.980 and 0.896, respectively. The resulting fit for the entire dataset presented a higher R value of 0.935. In general, the ANN models display better fit than the models obtained via quadratic regression. Besides presenting a great fit for the experimental input data, the ANN can receive new data to improve the performance of the developed model, which is not possible through regression analysis.

The conflicting behaviors of the Ra and HAZ depth evidenced the complexity of trying to identify the set of parameters that would deliver suitable values of Ra and HAZ depth simultaneously. Often, it is only possible to reach the minimum Ra by degrading the HAZ depth, and vice versa. To find a set of solutions that would result in satisfactory values of Ra and HAZ depth concomitantly, a multi-objective genetic algorithm (GA) optimization was applied using both quadratic regression and ANN models as fit function, for comparison. In all optimal solutions, the focal position value is constant in the + 4 mm value, which agrees with the parameter interaction analysis from the regression model. Ra values considered suitable for practical applications lie between 0.2 µm and 1.5 µm. Four combinations of parameters provided by the GA, using the ANN as fitness function, resulted in Ra values within this range

and HAZ depth values between 20 µm and 30 µm. These values are obtained with laser polishing process parameters in the range of 200 W ≤ Laser Power ≤ 300 W; Focal Position = +4 mm; 1 ≤ Number of Repetitions ≤ 2; 0.7 m/min ≤ Axial Feed Rate ≤ 0.9 m/min; and 1450 mm/s ≤ Scanning Speed ≤ 1550 mm/s. As a comparison, the combinations of parameters provided by the GA, using the quadratic regression as fitness function, resulted in Ra values between 0.13 µm and 1.62 µm and HAZ depth values between 4 µm and 113 µm. These values are obtained with laser polishing process parameters in the range of 405 W ≤ Laser Power ≤ 460 W; Focal Position = +4 mm; 1 ≤ Number of Repetitions ≤ 3; 0.5 m/min ≤ Axial Feed Rate ≤ 0.7 m/min; and 790 mm/s ≤ Scanning Speed ≤ 1400 mm/s. When considering the validation experiments and outcomes, the parameters range resulting from the GA with ANN as fitness functions presented output values with equivalent trending behavior as the computational optimization's prediction.

The assessed numerical methods were considered appropriate options for the fast assessment of the laser polishing parameters' influence in relevant features such as surface texture and heat affected zones depths. The findings show that DoE approaches are a systematic manner of acquiring inputs for the establishment statistical output representation. The quadratic regression upheld its importance as a process parameter correlation instrument, even though the statistical representation obtained did not present a great performance. Whereas ANN models showed satisfactory results for the representation of the Ra and HAZ deepness output behaviors. Moreover, the genetic algorithm multi-objective optimization was able to grant intervals for each parameter to achieve adequate Ra and HAZ deepness results, concurrently. Additionally, considering the input data is acquired from practical trials and FEM modelling, this method shows potential to optimize laser manufacturing processes, independently of the variables to be optimized, while avoiding time and material waste.

6.2. Laser functionalization

For the laser functionalization investigation, the Ti-6Al-4V parts produced via LPBF were assessed in 7 starting conditions: as-built (AB), heat treated (HT), sandblasted (SB), ground (GR), and the first 3 surface combined with laser polishing resulting in: as-built + laser polishing (AB+LP), heat treated combined with laser polishing (HT+LP), and sandblasted combined with laser polishing (SB+LP). All mentioned samples were subjected to a laser functionalization process, performed with an ultrafast laser (450 fs; λ = 1030 nm) under ambient air atmosphere. The goal was to create two types of structures, nano-ripples and pores, in the 7 starting conditions, thus obtaining different functionalities. The process parameters to achieve the desired surfaces were laser power of 4 W, scanning speed of 400 mm/s, and repetition rate of 1 MHz. The main difference between the two proposed structures in terms of process parameters is that to obtain the nano-ripples the laser scanning needs one repetition, while to achieve the porous structure four repetitions were necessary. The material was then characterized accordingly.

The effects of the laser structuring in the materials functionalization were assessed in different ways: resulting topographies, microstructural changes, nano hardness and H_2O wettability measurements, surface chemical composition and toxicity analysis. When identical set of parameters are adopted, workpieces with different initial topographies present diversified outcomes. With powder still fully adhered to the parts' surface, not only the workpieces' but also the particles' surfaces observed the establishment of nano-ripples. Differently, porous structures were formed on the surface of the parts with powder adhesion still remnant amongst it. Reducing or eliminating sintered powder on the surface of the parts before applying laser

structuring approaches can result in the creation of more uniform structures. While the pores created by the laser structuring approach following sandblasting and grinding are comparable in size and distribution, the formation of nano-ripples makes it noticeable that the starting surface topography could not be evened out by the sandblasting. Although very comparable amongst the laser polished parts, the resulting nano-ripples structures differ from the ground surfaces even with both conditions being considered smoothened topographies, since the results indicate that higher ablation was achieved when comparing the former to the latter. With the stated observation, it can be concluded that the interaction between the laser and material is not only dictated by the surface's starting condition but additionally by the type of processes the workpieces were subjected to in order to achieve such initial topographies. Consistent surface structures following the adoption of the combination of laser polishing and ultrafast laser functionalization were achieved, as the former procedure ensured that entirely different topographic conditions reached the same starting point.

The microstructure analysis of the samples after surface functionalization with the ultrafast laser radiation was performed equally to the laser polishing study, by means of optical microscopy and XRD analysis. It is observed in optical images that no HAZ was detected whatsoever after the laser functionalization, which is aligned with the XRD analysis of each sample as being comparable to prior laser functionalization. The AB, AB + LP, HT + LP, and SB + LP majority content of hexagonally close-packed (hcp) fine acicular martensitic α'-phase, even following the ultrafast laser structuring for both nano-ripples and pore formation. The HT, SB, and GR, on the other hand, remained with the mixture of hexagonally close-packed (hcp) α-phase and body centered cubic (bcc) β-phase after the ultrafast laser structuring for both nano-ripples and pore formation.

With no major effects from the surface functionalization in the microstructure of the parts, the implications in the mechanical properties should also be minimal. To detect any alterations, the hardness of the parts submitted to laser functionalization, a nano indentation technique was used. For a suitable comparison, all samples in their initial conditions and after nano-ripples and pore formation were assessed. The initial hardness values of the workpieces AB, HT, SB and GR were between 400 HV0.01 and 500 HV0.01, despite their discrepant microstructures. A slight increase was observed after laser polishing, when values between 500 HV0.01 and 700 HV0.01 were reached more often. Although, no evident difference can be observed among the samples, even those with different microstructures. After ultrafast laser treatment, independently if for nano-ripples or pore formation, the AB, AB + LP, HT + LP, SB, and GR sample experienced minimal effects in the hardness, with the maximum values of 600 HV0.01, 800 HV0.01, 800 HV0.01, 800 HV 0.01, and 600 HV0.01 achieved, respectively. The HT sample experienced a decrease on the hardness values below 300 HV0.01 around 7 µm from the laser treated surface. Oppositely, an extreme increase was observed for the SB + LP sample, with hardness achieving values above 1800 HV0.01. As already mentioned, the LPBF process faces the occurrence of defects, and the nano indentation analysis is even more sensitive to porosities associated to the LPBF process. Even though the measurements were repeated several times, the discrepancy between measurements was excessive in some cases, leading to big error bars, which was the case for the SB + LP sample.

Regarding the H_2O wetting behavior of the parts assessed, the AB and HT samples displayed contact angle (CA) average values of 121° and 85°, respectively, although their topographies were similar. Distinct CA average values were seen when conventional smoothing approaches were used, with 97° for SB and 67° for GR samples. AB, HT, and SB workpieces presented a contact angle of 65° when submitted to LP. By coupling two post-processes such as LP and laser functionalization, all surface structures (nano-ripples and pores) achieved hydrophobic

qualities. The GR + HT with formation of nano-ripples had CA average values that were consistently higher than 100°, going as high as 135°. Even though the two kinds of structures created using ultrafast laser share the hydrophobic characteristic, the presence of nano-ripples led to a trend of higher average CA values when compared to the porous structures, with the only inconsistency for this observation being the results for the structured parts from AB initial condition.

The investigation of the wettability characteristics, after each workflow step described, showed that the topography is not solely responsible for the functionality of the sample's surfaces, thus the need for assessing the surface chemistry following each process discussed via XPS analysis. The passivation that is frequently seen in titanium was confirmed with the occurrence of doublets credited to TiO_2 and TiO_x because the processed workpieces were kept in standard atmosphere in the days prior to the surface chemistry analysis. Al_2O_3 and V_2O_5 are two additional metal oxides that were found on the surfaces of several workpieces. All samples, regardless of the process they were submitted to, had a layer of combined metal oxides in varied concentrations. TiC, TiN with its satellite, and TiN_xO_y are observed for workpieces before and after laser polishing. Following AM, which is carried out in an argon-filled inert atmosphere, the highest concentration of TiN and TiC was found on the AB parts, with GR workpieces presenting the second highest concentration, and less evident presence on HT and SB samples. The occurrence of nitrogen on the surface of the mentioned parts may have been caused by an interaction between such element and the printed samples following their manufacturing via LPBF and before heat-treatment. TiC and TiN were absent from all functionalized surfaces, while metal oxides predominated. Given that the procedure was carried out with no inert gas environment or blasting, these were anticipated outcomes.

It is crucial to ensure that no laser post-processing adopted reduces the material's biocompatibility, as titanium and its alloys are frequently used in medical applications due to their exceptional mechanical and biocompatible qualities. The ability of MC3T3-E1 cells to adhere and proliferate on the part's surface was not negatively impacted by the laser functionalization either before or after laser polishing. All cells showed a typical morphology, and cells grown with the extracts generally showed the same viability as the controls, suggesting that the parts under investigation maintained their high biocompatibility despite the various post-processing steps.

For titanium alloys particularly manufactured through LPBF, the combination of ultrafast laser functionalization and laser polishing has never been investigated before. The suggested method is regarded as an appropriate post-process choice, either for replacing specific manufacturing workflow stages, for inputting distinct functionalities at particular locations within the LPBF parts, or the two options concomitantly. The findings show that workpieces with discrepant surface characteristics can be brought to the same condition by laser polishing, which enables more precise and reproducible structures to be achieved by laser functionalization. Similarly, the H_2O wettability properties of all laser-polished workpieces show hydrophilic behavior and contact angle values in the same range, independent of their initial state, and all parts submitted to laser surface modification show hydrophobic behavior and contact angles in the same range, also independently from their initial state. From the XPS assessment it is established that wettability performances are not solely linked to surface topographies, but also to surface chemical compositions following each laser post-process that is examined. In every instance, there is no adverse impact on the biocompatibility of the material, and additional investigations are required to evaluate the adhesion of cell types based on potential bio applications.

6.3. Outlook on future work

This work has been mainly focused on surface modification and characterization of LPBF Ti64 parts subjected to different post-processes, from traditional approaches such as sand blasting to the proposed approaches of laser polishing and functionalization. For further development and application specific validation of the proposed approaches, the following ideas could be pursued:

1. Mechanical properties assessment for specific industrial and medical applications, such as tensile and fatigue behavior after all the individual steps in the AM process chain
2. Additional types of bio tests for specific medical applications, such as bacterial adhesion [175] and blood clotting tests
3. Implement the proposed approaches to other types of AM materials, such as polymers [176] and ceramics
4. Investigate the efficiency of the simulation and mathematical modelling methods proposed for specific applications and/or compare them with alternative simulation and mathematical modelling methods
5. Investigate the suitability of ultrafast laser radiation in burst mode and their outcome in terms of resulting mechanical properties, surface characteristics, and further applications specific potential requirements [177]

Appendix

A.1. Design of experiments

Table A-1. Combination of parameters and respective surface roughness results

Run	Order	Laser Power (W)	Focus position (mm)	Number of Repeptitions	Feed rate (m/min)	Scanning speed (mm/s)	Ra (µm)
1	36	400	3	4	0,75	1600	1.478
2	18	300	2	3	0,6	1200	1.317
3	2	400	3	4	0,75	800	0.962
4	3	200	3	2	0,45	800	1.726
5	4	400	1	4	0,45	800	2.908
6	19	500	2	3	0,6	1200	2.703
7	20	300	2	3	0,6	1200	1.155
8	5	200	1	4	0,45	800	2.141
9	6	200	3	4	0,75	800	1.511
10	21	300	2	5	0,6	1200	1.342
11	37	400	1	4	0,75	1600	6.287
12	38	200	3	2	0,45	1600	4.713
13	39	200	3	2	0,75	1600	3.875
14	7	200	1	2	0,45	800	1.796
15	22	100	2	3	0,6	1200	3.686
16	8	400	3	2	0,45	800	1.448
17	40	400	1	2	0,45	1600	3.593
18	9	400	3	4	0,45	800	1.556
19	10	400	1	2	0,75	800	5.038
20	41	400	1	4	0,45	1600	3.391
21	23	300	2	3	0,6	1200	1.298
22	42	400	1	2	0,75	1600	5.570
23	24	300	2	3	0,9	1200	2.384
24	11	200	3	2	0,75	800	1.737
25	43	200	1	2	0,45	1600	2.851
26	25	300	2	3	0,6	1200	1.418
27	44	400	3	2	0,45	1600	1.223
28	45	200	1	4	0,45	1600	2.519
29	26	300	2	1	0,6	1200	2.297
30	27	300	2	3	0,6	1200	1.399
31	28	300	2	3	0,6	1200	1.381
32	46	200	3	4	0,45	1600	3.082
33	29	300	4	3	0,6	1200	1.708

34	30	300	2	3	0,6	1200	1.390
35	12	400	3	2	0,75	800	1.331
36	31	300	0	3	0,6	1200	2.539
37	47	200	3	4	0,75	1600	5.463
38	13	200	1	2	0,75	800	2.764
39	32	300	2	3	0,3	1200	1.111
40	14	200	1	4	0,75	800	2.265
41	48	400	3	4	0,45	1600	1.319
42	33	300	2	3	0,6	1200	1.47
43	49	200	1	4	0,75	1600	2.400
44	50	400	3	2	0,75	1600	1.677
45	15	400	1	4	0,75	800	2.381
46	52	300	2	3	0,6	2000	2.011
47	16	400	1	2	0,45	800	3.042
48	1	300	2	3	0,6	400	10.505
49	51	200	1	2	0,75	1600	2.979
50	34	300	2	3	0,6	1200	1.449
51	17	200	3	4	0,45	800	0.972
52	35	300	2	3	0,6	1200	1.446

Table A-2. Combination of parameters and respective HAZ depth results

Run	Laser power (W)	Focus position (mm)	Number of repeptitions	Scanning speed (mm/s)	HAZ depth (µm)
1	400	3	4	1600	84,17
2	300	2	3	1200	86,12
3	400	3	4	800	168,82
4	200	3	2	800	55,56
5	400	1	4	800	227,64
6	500	2	3	1200	119,12
7	300	2	3	1200	86,12
8	200	1	4	800	98,86
9	200	3	4	800	66,67
10	300	2	5	1200	91,1
11	400	1	4	1600	89,75
12	200	3	2	1600	14,2
13	200	1	2	800	85,71
14	100	2	3	1200	9,73
15	400	3	2	800	112,43
16	400	1	2	1600	60,62
17	400	1	2	800	157,09
18	200	1	2	1600	46,15

19	300	2	3	1200	86,12
20	400	3	2	1600	66,67
21	200	1	4	1600	59,02
22	300	2	1	1200	50,53
23	300	2	3	1200	86,12
24	300	2	3	1200	86,12
25	200	3	4	1600	28,67
26	300	4	3	1200	44,78
27	300	2	3	1200	86,12
28	300	0	3	1200	96,55
29	300	2	3	1200	86,12
30	300	2	3	1200	86,12
31	300	2	3	2000	60,58
32	300	2	3	400	129,31
33	300	2	3	1200	86,12
34	300	2	3	1200	86,12

References

[1] T. Peng, K. Kellens, R. Tang, C. Chen and G. Chen, "Sustainability of additive manufacturing: An overview on its energy demand and environmental impact," *Additive Manufacturing,* vol. 21, p. 694–704, 2018.

[2] I. Gibson, D. Rosen and B. Stucker, Additive Manufacturing Technologies: 3D Printing, Rapid Prototyping, and Direct Digital Manufacturing, New York: Springer, 2015.

[3] M. Attaran, "The rise of 3-D printing: The advantages of additive manufacturing over traditional manufacturing," *Business Horizon,* vol. 60, pp. 677- 688, 2017.

[4] D. Bourell, J. P. Kruth, M. Leu, G. Levy, D. Rosen, A. Beese and A. Clare, "Materials for Additive Manufacturing," *CIRP Annals – Manufacturing Technology,* vol. 66, pp. 659-681, 2017.

[5] D. Herzog, V. Seyda, E. Wycisk and C. Emmelmann, "Additive manufacturing of metals," *Acta Materialia,* vol. 117, pp. 371-392, 2016.

[6] H. Koizumi, Y. Takeuchi, H. Imai, T. Kawai and T. Yoneyama, "Application of titanium and titanium alloys to fixed dental protheses," *Journal of Prosthodontic Research,* vol. 63, pp. 266-270, 2019.

[7] S. Gorsse, C. Hutchinson, M. Gouné and R. Banerjee, "Additive manufacturing of metals: a brief review of the characteristic microstructures and properties of steels, Ti-6Al-4V and high-entropy alloys," *Science and Technology of Advanced Materials,* vol. 18, pp. 584-610, 2017.

[8] F. Zhechao and F. Hongwei, "Study on selective laser melting and heat treatment of Ti-6Al-4V alloy," *Results in Physics,* vol. 10, pp. 660-664, 2018.

[9] L. Chen, Y. He, Y. Yang, S. Niu and H. Ren, "The research status and development trend of additive manufacturing technology," *International Journal of Advanced Manufacturing Technologies,* vol. 89, pp. 3651-3660, 2017.

[10] G. Pyka, G. Kerckhofs, I. Papantoniou, M. Speirs, J. Schrooten and M. Wevers, "Surface roughness and morphology customization of additive manufactured open porous Ti6Al4V structures," *Materials,* vol. 6, pp. 4737-4757, 2013.

[11] M. Moshiri, Integrated Process Chain for First-Time-Right Mould Components Production Using Laser Powder Bed Fusion Metal Additive Manufacturing, Kongens Lyngby: Technical Univesrity of Denmark, 2020.

[12] J. Metelkova, Y. Kinds, K. Kempen, C. de Formanoir, A. Witvrouw and B. van Hooreweder, "On the influence of laser defocusing in selective laser melting of 316L," *Additive Manufacturing,* vol. 23, p. 161–169, 2018.

[13] U. Paggi, M. Sinico, L. Thijs, W. Dewulf and B. van Hooreweder, "Improving the dimensional accuracy of downfacing surfaces of additively manufactured parts," in *Joint*

SIG Meeting between EUSPEN and ASPE Advancing in Additive Manufacturing, Nantes, 2019.

[14] U. Paggi, R. Ranjan, L. Thijs, C. Ayas, M. Langelaar, F. van Keulen and B. van Hooreweder, "New support structures for reduced overheating on downfacing regions of direct metal printed parts," in *Annual International Solid Freeform Fabrication Symposium*, Austin, 2019.

[15] D. J. Agius, K. I. Kourousis and C. Wallbrink, "A Review of the As-Built SLM Ti-6Al-4V Mechanical Properties Towards Achieving Fatigue Resistant Designs," *Metals,* vol. 8, p. 75, 2018.

[16] I. Yadroitsev, P. Krakhmalev, I. Yadroitsava and A. Du Plessis, "Qualification of Ti6Al4V ELI Alloy Produced by Laser Powder Bed Fusion for Biomedical Applications," *JOM,* vol. 70, p. 372–377, 2018.

[17] A. Charles, A. Elkaseer, L. Thijs, V. Hagenmeyer and S. Scholz, "Effect of Process Parameters on the Generated Surface Roughness of Down-Facing Surfaces in Selective Laser Melting," *Applied Sciences,* vol. 9, p. 1256, 2019.

[18] A. Townsend, N. Senin, L. Blunt, R. Leach and J. Taylor, "Surface texture metrology for metal additive manufacturing: A review," *Precision Engineering,* vol. 46, p. 34–47, 2016.

[19] Z. Baicheng, L. Xiaohua, B. Jiaming, G. Junfeng, W. Pan, S. Chen-nan, N. Muiling, Q. Guojun and W. Jun, "Study of selective laser melting (SLM) Inconel 718 part surface improvement by electrochemical polishing," *Materials & Design,* vol. 116, no. 15, pp. 531-537, 2017.

[20] K. L. Tan and S. H. Yeo, "Surface modification of additive manufactured components by ultrasonic cavitation abrasive finishing," *Wear,* Vols. 378-379, pp. 90-95, 2017.

[21] D. Bhaduri, P. Penchev, A. Batal, S. Dimov, S. L. Soo, S. Sten, U. Harrysson, Z. Zhang and H. Dong, "Laser polishing of 3D printed mesoscale components," *Applied Surface Science,* vol. 405, pp. 29-46, 2017.

[22] M. Wang, Y. Wu, S. Lu, T. Chen, Y. Zhao, H. Chen and Z. Tang, "Fabrication and characterization of selective laser melting printed Ti-6Al-4V alloys subjected to heat treatment for customized implants design," *Progress in Natural Science: Materials International,* vol. 26, no. 6, pp. 671-677, 2016.

[23] L. Giorleo, E. Ceretti and C. Giardini, "Ti surface laser polishing: effect of laser path and assist gas," *Procedia CIRP,* vol. 33, pp. 446-451, 2015.

[24] W. W. Gora, Y. Tian, A. P. Cabo, M. Ardron, R. R. J. Maier, P. Prangnell, N. J. Weston and D. P. Hand, "Enhancing surface finish of additively manufactured titanium and cobalt chrome elements using laser based finishing," *Physics Procedia,* vol. 83, pp. 258-263, 2016.

[25] A. Temmler, E. Willenborg and K. Wissenbach, "Laser polishing," in *Procedings SPIE Laser Applications in Microelectronic and Optoelectronic Manufacturing XVII*, San Francisco, 2012.

[26] W. J. Wang, K. C. Yung, H. S. Choy, T. Y. Xiao and Z. X. Cai, "Effects of laser polishing on surface microstructure and corrosion resistance of additive manufactured CoCr alloys," *Applied Surface Science,* vol. 443, pp. 167-175, 2018.

[27] C. P. Ma, Y. C. Guan and W. Zhou, "Laser polishing of additive manufactured Ti alloys," *Optics and Lasers in Engineering,* vol. 93, pp. 171-177, 2017.

[28] S. Mishra and V. Yadava, "Laser beam micromachining(LBMM) – A review," *Optics and Lasers in Engineering,* vol. 73, pp. 89-122, 2015.

[29] A. Elkaseer, J. Lambarri, I. Quintana and S. Scholz, "Laser Ablation of Cobalt-Bound Tungsten Carbide and Aluminium Oxide Ceramic: Experimental Investigation with ANN Modelling and GA Optimisation," in *Sustainable Design and Manufacturing*, vol. 130, Cham, Springer, 2018, p. 21–30.

[30] R. Kumari, T. Scharnweber, W. Pfleging, H. Besser and J. D. Majumdar, "Laser surface textured titanium alloy (Ti-6Al-4V) - Part II - Studies on bio-compatibility," *Applied Surface Science,* vol. 357, p. 750–758, 2015.

[31] O. Raimbault, S. Benayoun, K. Anselme, C. Mauclair, T. Bourgade, A.-M. Kietzig, P.-L. Girard-Lauriault, S. Valette and C. Donnet, "The effects of femtosecond laser-textured Ti-6Al-4V on wettability and cell response," *Materials Science and Engineering: C,* vol. 69, p. 311–320, 2016.

[32] A. Cunha, A. P. Serro, V. Oliveira, A. Almeida, R. Vilar and M.-C. Durrieu, "Wetting behavior of femtosecond laser texture Ti-6Al-4V surfaces," *Applied Surface Science,* vol. 265, p. 688–696, 2013.

[33] A. Cunha, V. Oliveira and R. Vilar, "Ultrafast laser surface texturing of titanium alloys," in *Laser Surface Modification of Biomaterials*, Amsterdam, Elsevier, 2016, p. 301–322.

[34] W. Liu, S. Liu and L. Wang, "Surface Modification of Biomedical Titanium Alloy: Micromorphology, Microstructure Evolution and Biomedical Applications," *Coatings,* vol. 9, p. 249, 2019.

[35] P. Krakhmalev, I. Yadroitsev, I. Yadroitsava and O. de Smidt, "Functionalization of Biomedical Ti6Al4V via In Situ Alloying by Cu during Laser Powder Bed Fusion Manufacturing," *Materials,* vol. 10, p. 1154, 2017.

[36] S. A. Yavari, M. Croes, B. Akhavan, F. Jahanmard, C. C. Eigenhuis, S. Dadbakhsh, H. C. Vogely, M. M. Bilek, A. C. Fluit, C. H. E. Boel, B. C. H. van der Wal, T. Vermonden, H. Weinans and A. A. Zadpoor, "Layer by layer coating for bio-functionalization of additively manufactured meta-biomaterials," *Additive Manufacturing,* vol. 32, p. 100991, 2020.

[37] S. C. Cox, P. Jamshidi, N. M. Eisenstein, M. A. Webber, H. Hassanin, M. M. Attallah, D. E. Shepherd, O. Addison and L. M. Grover, "Adding functionality with additive manufacturing: Fabrication of titanium-based antibiotic eluting implants," *Materials Science and Engineering: C,* vol. 64, pp. 407-415, 2016.

[38] H. Bikas, P. Stavropoulos and G. Chryssolouris, "Additive manufacturing methods and modelling approaches: a critical review," *International Journal of Advanced Manufacturing Technologies,* vol. 83, pp. 389-405, 2016.

[39] L. Zhou, J. Miller, J. Vezza, M. Mayster, M. Raffay, Q. Justice, Z. Al Tamimi, G. Hansotte, L. D. Sunkara and J. Bernat, "Additive Manufacturing: A Comprehensive Review," *Sensors,* vol. 24, no. 9, p. 2668, 2024.

[40] X. Gong, T. Anderson and K. Chou, "Review on powder-based electron beam additive manufacturing technology," *Manufacturing Review,* vol. 1, p. 2, 2014.

[41] E. De Leon, A. Riensche, B. D. Bevans, C. Billings, Z. Siddique and Y. Liu, "A Review of Modeling, Simulation, and Process Qualification of Additively Manufactured Metal Components via the Laser Powder Bed Fusion Method," *Journal of Manufacturing and Materials Processing,* vol. 9, no. 1, p. 22, 2025.

[42] C. Qiu, N. J. E. Adkins and M. M. Attallah, "Microstructure and tensile properties of selectively laser-melted and of HIPed laser-melted Ti–6Al–4V," *Materials Science and Engineering: A,* vol. 578, pp. 230-239, 2013.

[43] W. Xu, E. W. Lui, A. Pateras, M. Qian and M. Brandt, "In situ tailoring microstructure in additively manufactured Ti-6Al-4V for superior mechanical performance," *Acta Materialia,* vol. 125, p. 390–400, 2017.

[44] F. Klocke and C. Wagner, "Coalescence behaviour of two metallic particles as base mechanism of selective laser sintering," *CIRP Annals,* vol. 52, no. 1, pp. 177-180, 2003.

[45] M. Xia, D. Gu, G. Yu, D. Dai, H. Chen and Q. Shi, "Influence of hatch spacing on heat and mass transfer, thermodynamics and laser processability during additive manufacturing of Inconel 718 alloy," *International Journal of Machine Tools and Manufacture,* vol. 109, pp. 147-157, 2016.

[46] E. Malekipour and H. El-Mounayri, "Common defects and contributing parameters in powder bed fusion AM process and their classification for online monitoring and control: a review," *International Journal of Advanced Manufacturing Technology,* vol. 95, pp. 527-550, 2018.

[47] D. Guillen, S. Wahlquist and A. Ali, "Critical Review of LPBF Metal Print Defects Detection: Roles of Selective Sensing Technology," *Applied Sciences,* vol. 14, no. 15, p. 6718, 2024.

[48] B. Song, S. Dong, B. Zhang, H. Liao and C. Coddete, "Effects of processing parameters on microstructure and mechanical property of selective laser melted Ti6Al4V," *Materials & Design,* vol. 35, pp. 120-125, 2012.

[49] L. N. Carter, C. Martin, P. J. Withers and M. M. Attalah, "The influence of the laser scan strategy on grain structure and cracking behaviour in SLM powder-bed fabricated nickel superalloy," *Journal of Alloys and Compounds,* vol. 615, pp. 338-347, 2014.

[50] H. Ali, H. Ghadbeigi and K. Mumtaz, "Effect of scanning strategies on residual stress and mechanical properties of Selective Laser Melted Ti6Al4V," *Materials Science and Engineering: A,* vol. 712, pp. 175-187, 2018.

[51] Q. Shi, D. Gu, M. Xia, S. Cao and T. Rong, "Effects of laser processing parameters on thermal behavior and melting/solidification mechanism during selective laser melting of TiC/Inconel 718 composites," *Optics & Laser Technology,* vol. 84, pp. 9-22, 2016.

[52] S. Ghouse, S. Babu, R. J. van Arkel, K. Nai, P. A. Hooper and J. R. T. Jeffers, "The influence of laser parameters and scanning strategies on the mechanical properties of a stochastic porous material," *Materials & Design,* vol. 131, pp. 498-508, 2017.

[53] I. Koutiri, E. Pessard, P. Peyre, O. Amlou and T. de Terris, "Influence of SLM process parameters on the surface finish, porosity rate and fatigue behavior of as-built Inconel 625 parts," *Journal of Materials Processing Technology,* vol. 255, pp. 536-546, 2018.

[54] H. M. Khan, Y. Karabulut, O. Kitay, Y. Kaynak and I. S. Jawahir, "Influence of the post-processing operations on surface integrity of metal components produced by laser powder bed fusion additive manufacturing: a review," *Machining Science and Technology,* vol. 25, no. 1, pp. 118-176, 2021.

[55] B. Vrancken, L. Thijs, J.-P. Kruth and J. van Humbeeck, "Heat treatment of Ti6Al4V produced by Selective Laser Melting: Microstructure and mechanical properties," *Journal of Alloys and Compounds,* vol. 541, p. 177–185, 2012.

[56] G. M. Ter Haar and T. H. Becker, "Selective laser melting produced Ti-6Al-4V: post-process heat treatments to achieve superior tensile properties," *Materials,* vol. 11, p. 146, 2018.

[57] A. Boschetto, L. Bottini, L. Macera and F. Veniali, "Post-processing of complex SLM parts by barrel finishing," *Applied Sciences,* vol. 10, p. 1382, 2020.

[58] A. H. Maamoun, M. A. Elbestawi and S. C. Veldhuis, "Influence of shot peening of AlSi10Mg parts fabricated by additive manufacturing," *Manufacturing and Materials Processing,* vol. 2, p. 40, 2018.

[59] P. Jamshidi, M. Aristizabal, W. Kong, V. Villapun, S. C. Cox, L. M. Grover and M. M. Attallah, "Selective laser melting of Ti-6Al-4V: the impact of post-processing on the tensile, fatigue and biological properties for medical implant applications," *Materials,* vol. 13, p. 2813, 2020.

[60] L. Denti and A. Sola, "On the effectiveness of different surface finishing techniques on A357.0 parts produced by laser-based powder bed fusion: surface roughness and fatigue strength," *Metals,* vol. 9, p. 1284, 2019.

[61] D. Lesyk, V. Dzhemelinskyi, B. Mordyuk, S. Martinez, O. Stamann and A. Lamikiz, "Surface Polishing of Laser Powder Bed Fused Superalloy Components by Magnetic Post-treatment," in *IEEE 10th International Conference Nanomaterials: Applications & Properties (NAP)*, Sumy, 2020.

[62] D. Bhaduri, P. Penchev, S. Dimov, K. Essa, L. N. Carter, C. I. Pruncu, J. Jiang and D. Pullini, "On the surface integrity of additive manufactured and post-processed AlSi10Mg parts," *Procedia CIRP,* vol. 87, pp. 339-344, 2020.

[63] G. Lütjering and J. C. Williams, Titanium, Heidelberg: Springer Berlin, 2007.

[64] X. Li, X. Wang, K. Liu, J. Wang, X. Guo, M. Li, Z. Zhu and S. Wu, "Microstructure evolution and mechanical property of a new muilt-component ß titanium alloy with ultrahigh strength above 1350 MPa," *Journal of Materials Research and Technology,* vol. 21, pp. 4860-4875, 2022.

[65] L. Thijs, F. Verhaeghe, T. Craeghs, J. van Humbeeck and J.-P. Kruth, "A study of the microstructural evolution during selective laser melting of Ti–6Al–4V," *Acta Materialia,* vol. 58, no. 9, pp. 3303-3312, 2010.

[66] C. Veiga, J. P. Davim and A. J. R. Loureiro, "Properties and applications of titanium alloys: a brief review," *Review on Advanced Materials Science,* vol. 32, pp. 14-34, 2012.

[67] R. Wanhill and S. Barter, "Metallurgy and Microstructure," in *Fatigue of Beta Processed and Beta Heat-treated Titanium Alloys*, Dordrecht, Springer Netherlands, 2012, pp. 5-10.

[68] V. Raghavan, "Al-Ti-V (Aluminum-Titanium-Vanadium)," *Journal of Phase Equilibria & Diffusion,* vol. 26, no. 3, pp. 276-279, 2005.

[69] R. H. Buzolin, D. Weiß, A. Krumphals, M. Lasnik and M. C. Poletti, "Modelling the Competitive Growth of Primary, Allotriomorphic, and Secondary Alpha in Ti-6Al-4V," *Metallurgical and Materials Transactions A,* vol. 51, pp. 3967-3980, 2020.

[70] T. Majumdar, T. Bazin, E. M. C. Ribeiro, J. E. Frith and N. Birbilis, "Understanding the effects of PBF process parameters interplay on Ti-6Al-4V surface properties," *PLoS ONE,* vol. 14, no. 8, p. e0221198, 2019.

[71] N. P. Calta, V. Thampy, D. R. C. Lee, A. A. Martin, R. Ganeriwala, J. Wang, P. J. Depond, T. T. Roehling, A. Y. Fong, A. M. Kiss, C. J. Tassone, K. H. Stone, J. N. Weker, M. F. Toney, A. W. van Buuren and M. J. Matthews, "Cooling dynamics of two titanium alloys during laser powder bed fusion probed with in situ X-ray imaging and diffraction," *Materials and Design,* vol. 195, p. 108987, 2020.

[72] J. Li and D. Zuo, "Laser polishing of additive manufactured Ti6Al4V alloy: a review," *Optical Engineering,* vol. 60, no. 2, p. 020901, 2021.

[73] M. J. Donachie, "Titanium: A technical guide," ASM International, Materials Park OH, 2000.

[74] Z. Cao, Q. Liu, Q. Liu, X. Yu, J. J. Kruzic and X. Li, "A machine learning method to quantitatively predict alpha phase morphology in additively manufactured Ti-6Al-4V," *npj Computational Materials,* vol. 9, p. 195, 2023.

[75] T. Becker, M. van Rooyen and D. Dimitriv, "Heat treatment of Ti-6Al-4V produced by lasercusing," *South African Journal of Industrial Engineering,* vol. 26, no. 2, pp. 93-103, 2015.

[76] S. Gaiani, E. Ferrari, M. Gozzi, M. T. Di Giovanni, M. L. Gualtieri, E. Colombini and P. Veronesi, "Impact of Post-Process Heat Treatment Performed on Ti6Al4V Titanium Alloy Specimens Obtained Using LPBF Technology," *Technologies,* vol. 11, no. 4, p. 100, 2023.

[77] J. D. Majumdar and I. Manna, "Laser processing of materials," in *Sadhana - Academy Proceedings in Engineering Sciences*, vol. 28, Springer, 2003, pp. 495-562.

[78] G. L. Goswami and D. Kumar, "Laser materials processing," *Bulletin of Materials Science,* vol. 11, pp. 213-224, 1988.

[79] J. Kumstel and B. Kirsch, "Polishing Titanium- and Nickel-based Alloys using Cw-Laser Radiation," *Physics Procedia,* vol. 41, pp. 362-371, 2013.

[80] E. Ukar, A. Lamikiz, L. N. López de Lacalle, D. del Pozo and J. L. Arana, "Laser polishing of tool steel with CO2 laser and high-power diode laser," *International Journal of Machine Tools and Manufacture,* vol. 50, no. 1, pp. 115-125, 2010.

[81] M. S. Trtica, B. B. Radak, B. M. Gakovic, D. S. Milovanovic and D. D. T. Batani, "Surface modifications of Ti6Al4V by a picosecond Nd:YAG laser," *Laser and Particle Beams,* vol. 27, no. 1, pp. 85-90, 2009.

[82] M. Gharbi, P. Peyre, C. Gorny, M. Carin, S. Morville, P. Le Masson, D. Carron and R. Fabbro, "Influence of various process conditions on surface finishes induced by the direct metal deposition laser technique on a Ti–6Al–4V alloy," *Journal of Materials Processing Technology,* vol. 213, no. 5, pp. 791-800, 2013.

[83] E. V. Bordatchev, A. M. K. Hafiz and O. R. Tutunea-Fatan, "Performance of laser polishing in finishing of metallic surfaces," *The International Journal of Advanced Manufacturing Technology,* vol. 73, no. 1-4, pp. 35-52, 2014.

[84] C. Nüsser, I. Wehrmann and E. Willenborg, "Influence of Intensity Distribution and Pulse Duration on Laser Micro Polishing," *Physics Procedia,* vol. 12, pp. 462-471, 2011.

[85] A. Temmler, E. Willenborg and K. Wissenbach, "Design Surfaces by Laser Remelting," *Physics Procedia,* vol. 12, pp. 419-430, 2011.

[86] R. Poprawe, Lasertechnik für die Fertigung: Grundlagen, Perspektiven und Beispiele für den Innovativen Ingenieur, Heidelberg: Springer Berlin, 2005.

[87] F. Schneiter, D. Rätzel and D. Braun, "The gravitational field of a laser beam beyond the short wavelength approximation," *Classical and Quantum Gravity,* vol. 35, p. 195007, 2018.

[88] B. Burzic, M. Hofele, S. Mürdter and H. Riegel, "Laser polishing of ground aluminum surfaces with high energy continuous wave laser," *Journal of Laser Applications,* vol. 29, no. 1, p. 11701, 2017.

[89] J. Schanz, M. Hofele, S. Ruck, T. Schubert, L. Hitzler, G. Schneider, M. Merkel and H. Riegel, "Metallurgical investigations of laser remelted additively manufactured AlSi10Mg parts," *Materialwissenschaft und Werkstofftechnik,* vol. 48, no. 5, pp. 463-476, 2017.

[90] Q. Wang, J. D. Morrow, C. Ma, N. A. Duffie and F. E. Pfefferkorn, "Surface prediction model for thermocapillary regime pulsed laser micro polishing of metals," *Journal of Manufacturing Processes,* vol. 20, pp. 340-348, 2015.

[91] B. Rosa, P. Mognol and J.-Y. Hacoet, "Laser polishing of additive laser manufacturing surfaces," *Journal of Laser applications,* vol. 27, p. S29102, 2015.

[92] C. Weingarten, A. Schmickler, E. Willenborg and K. Wissenbach, "Laser polishing and laser shape correction of optical glass," *Journal of Laser Applications,* vol. 29, no. 1, p. 11702, 2017.

[93] T. L. Perry, D. Werschmoeller, X. Li, F. E. Pfefferkorn and N. A. Duffie, "Pulsed laser polishing of micro-milled Ti6Al4V samples," *Journal of Manufacturing Processes,* vol. 11, no. 2, pp. 74-81, 2009.

[94] A. Lamikiz, J. A. Sánchez, L. N. López de Lacalle and J. L. Arana, "Laser polishing of parts built up by selective laser sintering," *International Journal of Machine Tools and Manufacture,* vol. 47, no. 12-13, pp. 2040-2050, 2007.

[95] J. D. Miller, O. R. Tutunea-Fatan and E. V. Bordatchev, "Experimental Analysis of Laser and Scanner Control Parameters During Laser Polishing of H13 Steel," *Procedia Manufacturing,* vol. 10, pp. 720-729, 2017.

[96] C.-S. Chang, T.-H. Chen, T.-C. Li, S.-L. Lin, S.-H. Liu and J.-F. Lin, "Influence of laser beam fluence on surface quality, microstructure, mechanical properties, and tribological results for laser polishing of SKD61 tool steel," *Journal of Materials Processing Technology,* vol. 229, pp. 22-35, 2016.

[97] K. C. Yung, W. J. Wang, T. Y. Xiao, H. S. Choy, X. Y. Mo, S. S. Zhang and Z. X. Cai, "Laser polishing of additive manufactured CoCr components for controlling their wettability characteristics," *Surface and Coatings Technology,* vol. 351, pp. 89-98, 2018.

[98] C. Liang, Y. Hu, N. Liu, X. Zou, H. Wang, X. Zhang, Y. Fu and J. Hu, "Laser polishing of Ti6Al4V fabricated by selective laser melting," *Metals,* vol. 10, p. 191, 2020.

[99] S. Marimuthu, A. Triantaphyllou, M. Antar, D. Wimpenny, H. Morton and M. Beard, "Laser polishing of selective laser melted components," *International Journal of Machine Tools and Manufacture,* vol. 95, pp. 97-104, 2015.

[100] J. S. Solheid, H. J. Seifert and W. Pfleging, "Laser surface modification and polishing of additive manufactured metallic parts," *Procedia CIRP,* vol. 74, pp. 280-284, 2018.

[101] F. Zhihao, L. Libin, C. Longfei and G. Yingchun, "Laser Polishing of Additive Manufactured Superalloy," *Procedia CIRP,* vol. 71, pp. 150-154, 2018.

[102] Y. Li, Z. Zhang and Y. Guan, "Thermodynamics analysis and rapid solidification of laser polished Inconel 718 by selective laser melting," *Applied Surface Science,* vol. 511, p. 145423, 2020.

[103] S. Lee, Z. Ahmadi, J. W. Pegues, M. Mahjouri-Samani and N. Shamsaei, "Laser polishing for improving fatigue performance of additive manufactured Ti-6Al-4V parts," *Optics and Laser Technology,* vol. 134, p. 106639, 2021.

[104] G. Mourou, "The ultrahigh-peak-power laser: present and future," *Applied Physics B,* vol. 65, pp. 205-211, 1997.

[105] J. Meijer, K. Du, A. Gillner, D. Hoffman, V. S. Kovalenko, T. Masuzawa, A. Ostendorf, R. Poprawe and W. Schulz, "Laser machining by short and ultrashort pulses, state of the art and new opportunities in the age of the photons," *CIRP Annals,* vol. 51, no. 2, pp. 531-550, 2002.

[106] S. Marimuthu, J. Dunleavey and B. Smith, "High-power ultrashort pulse laser machining of tungsten carbide," *Procedia CIRP,* vol. 94, pp. 829-833, 2020.

[107] J.-H. Zhao, C.-H. Li, J.-J. Xu, Y.-W. Hao and X.-B. Li, "Surface modification of nanostructures ZnS by femtosecond laser pulsing," *Applied Surface Science,* vol. 293, pp. 332-335, 2014.

[108] I. Mirza, N. M. Bulgakova, J. Tomastik, V. MIchalek, O. Haderka, L. Fekete and T. Mocek, "Ultrashort pulse laser ablation of dieletrics: Thresholds, mechanisms, role of breakdown," *Scientific Reports,* vol. 6, p. 39133, 2016.

[109] Z. Lin and M. Hong, "Femtosecond Laser Precision Engineering: From Micron, Submicron, to Nanoscale," *Ultrafast Science,* p. 9783514, 2021.

[110] E. G. Zahrani, D. Kopp and B. Azarhoushang, "Comparison of material removal efficiency in laser ablation of polycrystalline diamond for different pulse durations," *Materials Letters,* vol. 377, p. 137474, 2024.

[111] C. Florian, R. Wonneberger, A. Undisz, S. V. Kirner, K. Wasmuth, D. Spaltmann, J. Krüger and J. Bonse, "Chemical effects during the formation of various types of femtosecond laser-fenerated structures on titanium alloy," *Applied Physics A,* vol. 126, p. 266, 2020.

[112] A. Y. Vorobyev and C. Guo, "Femtosecond laser structuring of titanium implants," *Applied surface sciences,* vol. 253, pp. 7272-7280, 2007.

[113] J.-H. Rakebrandt, Y. Zheng, H. Besser, T. Scharnweber, H. J. Seifert and W. Pfleging, "Laser-assisted surface processing for functionalization of polymers on micro- and nano-scale," *Microsystem technologies,* vol. 26, pp. 1085-1091, 2020.

[114] A. Cunha, A.-M. Elie, L. Plawinski, A. P. Serro, A. M. B. do Rego, A. Almeida, M. C. Urdaci, M.-C. Durriu and R. Vilar, "Femtosecond laser surface texturing of titanium as a method to reduce adhesion of Staphylococcus aureus and biofilm formation," *Applied Surface Science,* vol. 360, pp. 485-493, 2016.

[115] J. Bonse, S. V. Kirner, M. Griepentrog, D. Spaltmann and J. Krüger, "Femtosecond laser texturing of surfaces for tribological applications," *Materials,* vol. 11, p. 801, 2018.

[116] C. Lanara, A. Mimidis and E. Stratakis, "Femtosecond laser fabrication of stable hydrophobic and anti-corrosive steel surfaces," *Materials,* vol. 12, p. 3428, 2019.

[117] C. A. Zuhlke, T. P. Anderson, P. Li, M. J. Lucis, N. Roth, J. E. Shield, B. Terry and D. R. Alexander, "Superhydrophobic metallic surfaces functionalized via femtosecond laser surface processing for long term air film retention when submerged in liquid," in *Proceedings SPIE 9351, Laser-based Micro- and Nanoprocessing IX*, San Francisco, 2015.

[118] D. H. Kam, S. Bhattacharya and J. Mazumder, "Control of the wetting properties of an AISI 316L stainless steel surface by femtosecond laser-induced surface modification," *Journal of Micromechanics and Microengineering,* vol. 22, p. 105019, 2012.

[119] B. Raillard, L. Gouton, E. Ramos-Moore, S. Grandthyll, F. Müller and F. Mücklich, "Ablation effects of femtosecond laser functionalization on steel surfaces," *Surface & Coatings Technology,* vol. 207, pp. 102-109, 2012.

[120] L. Jiao, Z. Y. Chua, S. K. Moon, J. Song, G. Bi and H. Zheng, "Femtosecond laser produced hydrophobic hierarchical structures on additive manufacturing parts," *Nanomaterials,* vol. 8, p. 601, 2018.

[121] J. S. Solheid, A. Elkaseer, T. Wunsch, S. Scholz, H. Seifert and W. Pfleging, "Multiobjective optimization of laser polishing of additively manufactured Ti-6Al-4V parts for minimum surface roughness and heat-affected zone," *Materials,* vol. 15, no. 9, p. 3323, 2022.

[122] J. S. Solheid, S. Mohanty, M. Bayat, T. Wunsch, P. G. Weidler, H. Seifert and W. Pfleging, "Laser polishing of additively manufactured Ti-6Al-4V - microstructure evolution and material properties," *Journal of Laser Applications,* vol. 32, p. 022019, 2020.

[123] J. S. Solheid, T. Wunsch, V. Trouillet, S. Weigel, T. Scharnweber, H. J. Seifert and W. Pfleging, "Two-step laser post-processing for the surface functionalization of additively manufactured Ti-6Al-4V parts," *Materials,* vol. 13, no. 21, p. 4872, 2020.

[124] T. Gietzelt, L. Eichhorn, T. Wunsch, U. Gerhards, T. Przeorski, H. Weiss and R. Dittmeyer, "Contribution to the Laser Welding of Wrought and Spray-Compacted Aluminum Alloys and the Impact of the Alloy Composition on the Welding Microstructure," *Advanced Engineering Materials,* vol. 16, no. 8, p. 1052–1065, 2014.

[125] J. Pekkarinen, V. Kujanpää and A. Salminen, "Laser cladding with scanning optics: Effect of power adjustment," *Journal of Laser Applications,* vol. 24, no. 3, p. 32003, 2012.

[126] M. Mangang, Ultrakurzpulslaserstrukturierung von LiFePO4- und LiMn2O4-Dickschichtelektroden fuer Lithium-Ionen-Zellen, Karlsruhe: Karlsruher Institut für Technologie (KIT), 2019.

[127] J. S. Solheid, A. Elkaseer, T. Wunsch, A. P. Charles, H. J. Seifert and W. Pfleging, "Effect of process parameters on surface texture generated by laser polishing of additively manufactured Ti-6Al-4V," in *Proceedings SPIE Micro- and Nanoprocessing XIV*, San Francisco, 2020.

[128] M. Yuan, A. Dai, L. Liao, Y. Chen and X. Ji, "Numerical study on Surface Roughness Measurement Based on Nonlinear Ultrasonics in Through-Transmission and Pulse-Echo Modes," *Materials,* vol. 14, no. 17, p. 4855, 2021.

[129] J. Scofield, "Hartree-Slater subshell photoionization cross-sections at 1254 and 1487 eV," *Journal of Electron Spectroscopy and Related Phenoma,* vol. 8, no. 2, p. 129–137, 1976.

[130] A. Comba, N. Scotti, T. Maravic, A. Mazzoni, M. Carossa, L. Breschi and M. Cadenaro, "Vickers Hardness and Shrinkage Stress Evaluation of Low and High Viscosity Bulk-fill Resin Composite," *Polymers,* vol. 12, no. 7, p. 1477, 2020.

[131] M. Sardela, Practical Materials Characterization, New York: Springer, 2014.

[132] Z. Qiu, P. Le, P. Li, C. Qin, W. Jiang, P. Zheng, T. Zhang and C. Li, "The role of contact angle in the thermal conductivity of microencapsulated phase change material suspension," *Advances in Mechanical Engineering,* vol. 9, no. 9, pp. 1 - 7, 2017.

[133] R. D. Frank, H. Dresbach, H. Thelen and H.-G. Sieberth, "Glutardialdehyde induced fluorescence technique (GIFT): A new method for the imaging of platelet adhesion on biomaterials," *Journal of Biomedical Materials Research,* vol. 52, no. 2, p. 374–381, 2000.

[134] V. Jagota, A. P. S. Sethi and K. Kumar, "Finite element method: an overview," *Walailak Journal of Science & Technology,* vol. 10, pp. 1-8, 2013.

[135] G. P. Nikishkov, Introduction to the finite element method, Aizu-Wakamatsu: University of Aizu, 2009.

[136] T. M. Shao, M. Hua, H. Y. Tam and E. H. M. Cheung, "An approach to modelling of laser polishing of metals," *Surface & Coatings Technology,* vol. 197, pp. 77-84, 2005.

[137] M. Bayat, S. Mohanty and J. H. Hattel, "Multiphysics modelling of lack-of-fusion voids formation and evolution in IN718 made by multi-track/multi-layer L-PBF," *International Journal of Heat and Mass Transfer,* vol. 139, pp. 95-114, 2019.

[138] P. Jiang, C. Wang, Q. Zhou, X. Shao, L. Shu and X. Li, "Optimization of laser welding process parameters of stainless steel 316L using FEM Kriging and NSGA-II," *Advances in Engineering Software,* vol. 99, pp. 147-160, 2016.

[139] W. Yan, Y. Qian, G. Wenjun, S. Lin, W. K. Liu, F. Lin and G. J. Wagner, "Meso-scale modeling of multiple-layer fabrication process in Selective Electro Beam Melting: inter-layer/track voids formation," *Materials and Design,* vol. 141, pp. 210-219, 2018.

[140] L. Parry, I. A. Ashcroft and R. D. Wildman, "Understanding the effect of laser scan strategy on residual stress in selective laser melting through thermo-mechanical simulation," *Additive Manufacturing,* vol. 12, pp. 1-15, 2016.

[141] Y. Huang, L. J. Yang, X. Z. Du and Y. P. Yang, "Finite element analysis of thermal behaviour of metal powder during selective laser melting," *International Journal of Thermal Sciences,* vol. 104, pp. 146-157, 2016.

[142] M. Bayat, S. Mohanty and J. H. Hattel, "A systematic investigation of the effects of process parameters on heat and fluid flow and metallurgical conditions during laser-based powder bed fusion of Ti6Al4V alloy," *International Journal of Heat and Mass Transfer,* vol. 139, pp. 213-230, 2019.

[143] K. F. Muhammad and W. A. W. Yusoff, "Optimization of laser cutting parameters using variable weight Grey-Taguchi method," *Australian Journal of Basic and Applied Sciences,* vol. 8, no. 15, pp. 361-365, 2014.

[144] Y. Sun and M. Hao, "Statistical analysis and optimization of the process parameters in Ti6Al4V laser cladding using Nd:YAG laser," *Optics and Lasers in Engineering,* vol. 50, pp. 985-995, 2012.

[145] K. Y. Benyounis and A. G. Olabi, "Optimization of different welding processes using statistical and numerical approaches – A reference guide," *Advances in Engineering Software,* vol. 39, pp. 483-496, 2008.

[146] A. R. Hamad, J. H. Abboud, F. M. Shuaeib and K. Y. Benyounis, "Surface hardening of commercially pure titanium by laser nitriding: Response surface analysis," *Advances in Engineering Software,* vol. 41, no. 4, pp. 674-679, 2010.

[147] G. Casalino, F. Facchini, M. Mortello and G. Mummolo, "ANN modelling to optimize manufacturing processes: the case of laser welding," *IFAC-PapersOnLine,* vol. 49, no. 12, pp. 378-383, 2016.

[148] E. Boillat, S. Kolossov, R. Glardon, M. Loher, D. Saladin and G. Levy, "Finite element and neural network models for process optimization in selective laser sintering," *The proceedings of the Institution of Mechanical Engineers, Part B: Journal of Engineering Manufacture,* vol. 218, no. 6, pp. 607-614, 2004.

[149] L. A. C. Filippis, L. M. Serio, F. Facchini and G. Mummolo, "ANN modelling to optimize manufacturing processes," in *Advanced Applications for Artificial Neural Networks*, InTech, 2018.

[150] J. A. Stendal, M. Bambach, M. Eisentraut, I. Sizova and S. Weiß, "Applying machine learning to the phenomenological flow stress modeling of TNM-B1," *Metals,* vol. 9, p. 220, 2019.

[151] S. Agatonovic-Kustrin and R. Beresford, "Basic concepts of artificial neural network (ANN) modeling and its application in pharmaceutical research," *Journal of Pharmaceutical and Biomedical Analysis,* vol. 22, pp. 717-727, 2000.

[152] M. T. Hagan and M. B. Menhaj, "Training feedforward networks with the Marquardt algorithm," *IEEE Transactions on Neural Networks,* vol. 5, no. 6, pp. 989-993, 1994.

[153] M. Rokonuzzaman, S. Rahman, M. A. Hannan, M. K. Mishu, W.-S. Tan, K. S. Rahman, J. Pasupuleti and N. Amin, "Levenberg-Marquadt algorithm-based solar PV energy integrated internet of home energy management system," *Applied Energy,* vol. 378, no. Part A, p. 124407, 2025.

[154] A. Konak, D. W. Coit and A. E. Smith, "Multi-objective optimization using genetic algorithms: a tutorial," *Reliability Engineering and System Safety,* vol. 91, pp. 992-1007, 2006.

[155] K. Deb, S. Agrawal, A. Pratap and T. A. Meyarivan, "Fast Elitist Non-dominated Sorting Genetic Algorithm for Multi-objective Optimization: NSGA-II," in *Parallel Problem Solving from Nature*, Heidelberg, Springer, 2000, pp. 849-858.

[156] K. Deb and T. Goel, "Controlled Elitist Non-dominated Sorting Genetic Algorithms for Better Convergence," in *Evolutionary Multi-Criterion Optimization*, Heidelberg, Springer, 2001, pp. 67-81.

[157] A. M. Schweidtmann, A. D. Clayton, N. Holmes, E. Bradford, R. A. Bourne and A. A. Lapkin, "Machine learning meets continuous flow chemistry: Automated optimization towards the Pareto front of multiple objectives," *Chemical Engineering Journal,* vol. 352, pp. 277-282, 2018.

[158] N. L. Lukic, M. Bozin-Dakic, J. A. Grahovac, J. M. Dodic and A. I. Jokic, "Multi-objective optimization of microfiltration of baker's yeast using genetic algorithm," *Acta Periodica Technologica (APTEFF),* no. 48, pp. 211-220, 2017.

[159] T. Kiedrowski, Oberflaechenstrukturbildung beim Laserstrahlpolieren von Stahlwerkstoffen, Düren: Shaker, 2010.

[160] C. Nüsser, Lasermikropolieren von Metallen, Aachen: Apprimus, 2018.

[161] H. Taheri, M. Shoaib, L. Koester, T. Bigelow, P. Collins and L. Bond, "Powder-based additive manufacturing - a review of types of defects, generation mechanisms, detection, property evaluation and metrology," *International Journal of Additive and Subtractive Materials Manufacturing,* vol. 1, no. 2, p. 172–209, 2017.

[162] D. Gu, Laser Additive Manufacturing of High-Performance Materials, Heidelberg: Springer Berlin, 2015.

[163] S. Pal, G. Lojan, R. Hudak, V. Ratjtukova, T. Brajlih, V. Kokol and I. Drstvensek, "As-fabricated surface morphologies of Ti-6Al-4V samples fabricated by different laser processing parameters in selective laser melting," *Additive Manufacturing,* vol. 33, p. 101147, 2020.

[164] J. Yang, H. Yu, J. Yin, M. Gao, Z. Wang and X. Zeng, "Formation and control of martensite in Ti-6Al-4V alloy produced by selective laser melting," *Materials & Design,* vol. 108, p. 308–318, 2016.

[165] S. Zhang, Q. Wei, L. Cheng, S. Li and Y. Shi, "Effects of scan line spacing on pore characteristics and mechanical properties of porous Ti6Al4V implants fabricated by selective laser melting," *Materials & Design,* vol. 63, p. 185–193, 2014.

[166] Z.-Y. Zhao, L. Li, P.-K. Bai, L. Jin, R.-g. Guan and H.-Q. Qu, "The Heat Treatment Influence on the Microstructure and Hardness of TC4 Titanium Alloy Manufactured via Selective Laser Melting," *Materials,* vol. 11, no. 8, 2018.

[167] R. Li, L. Riester, T. R. Watkins, P. J. Blau and A. Shih, "Metallurgical analysis and nanoindentation characterization of Ti–6Al–4V workpiece and chips in high-throughput drilling," *Materials Science and Engineering: A,* vol. 472, p. 115–124, 2008.

[168] H. Wu, J. Ma, Q. Meng, M. P. Jahan and F. Alavi, "Numerical modeling of electrical discharge machining of Ti-6Al-4V," *Procedia Manufacturing,* vol. 26, pp. 359-371, 2018.

[169] F. Sedona, G. A. Rizzi, S. Agnoli, F. X. Llabrés i Xamena, A. Papageorgiou, D. Ostermann, M. Sambi, P. Finetti, K. Schierbaum and G. Granozzi, "Ultrathin TiOx films on Pt(111): A LEED, XPS, and STM investigation," *The Journal of Physical Chemistry B,* vol. 109, no. 51, p. 24411–24426, 2005.

[170] D. Jaeger and J. Patscheider, "A complete and self-consistent evaluation of XPS spectra of TiN," *Journal of Electron Spectroscopy and Related Phenomena,* vol. 185, no. 11, p. 523– 534, 2012.

[171] J.-Y. Zheng, S.-H. Bao, Y. Guo and P. Jin, "Natural Hydrophobicity and Reversible Wettability Conversion of Flat Anatase TiO2 Thin Film," *ACS Applied Materials & Interfaces,* vol. 6, no. 3, pp. 1351-1355, 2014.

[172] E. Hryha, E. Rutqvist and L. Nyborg, "Stoichiometric vanadium oxides studied by XPS," *Surface and Interface Analysis,* vol. 44, no. 8, p. 1022–1025, 2012.

[173] J. Vaithilingam, R. D. Goodridge, R. J. M. Hague, S. D. R. Christie and S. Edmondson, "The effect of laser remelting on the surface chemistry of Ti6Al4V components fabricated by selective laser melting," *Journal of Materials Processing Technology,* vol. 232, pp. 1-8, 2016.

[174] B. J. Papenburg, E. D. Rodrigues, M. Wessling and D. Stamatialis, "Insigths into the role of material surface topography and wettability on cell-material interactions," *Soft Matter,* vol. 6, no. 18, pp. 4377-4388, 2010.

[175] S. R. Jang, I. W. Suh and L. Heng, "Nanoscale Polishing Technique of Biomedical Grade NiTi Wire by Advanced MAF Process: Relationship between Surface Roughness and Bacterial Adhesion," *Journal of Functional Biomaterials,* vol. 14, no. 4, p. 177, 2023.

[176] N. S. Kasalkova, V. Juricova, S. Rimpelova, D. Fajstavr, B. Frydlova, Z. Kolska, V. Svorcik and P. Slepicka, "LIPSS pattern induced by polymer surface instability for myoblast cell guidance," *Polymer Degradation and Stability,* vol. 221, p. 110667, 2024.

[177] A. Zemaitis, P. Gecys and M. Gedvilas, "Efficient Ablation, further GHz Burst Polishing, and Surface Texturing by Ultrafast Laser," *Advanced Engineering Materials,* vol. 26, no. 21, p. 2302262, 2024.

List of publications

Journal publications

- Solheid, J.S., Elkaseer, A., Wunsch, T., Scholz, S.G., Seifert, H.J., Pfleging, W. Multiobjective Optimization of Laser Polishing of Additively Manufactured Ti6Al-4V Parts for Minimum Surface Roughness and Heat-Affected Zone. Materials. 2022; 15(9):3323.
- Solheid, J.S., Wunsch, T., Trouillet, V., Weigel, S., Scharnweber, T., Seifert, H.J., Pfleging, W. Two-Step Laser Post-Processing for the Surface Functionalization of Additively Manufactured Ti-6Al-4V Parts. Materials. 2020; 13(21):4872.
- Solheid, J.S., Mohanty, S., Bayat M., Wunsch T., Weidler, P.G., Seifert, H.J., Pfleging, W. Laser polishing of additively manufactured Ti-6Al-4V - Microstructure evolution and material properties. 2020 Journal of Laser Applications 32 022019.
- Solheid, J.S., Seifert, H.J., Pfleging, W. Laser surface modification and polishing of additive manufactured metallic parts. 2018 Procedia CIRP 74 280-284.

Conference proceedings

- Solheid, J.S., Elkaseer, A., Wunsch, T., Charles, A.P., Seifert, H.J., Pfleging, W. Effect of process parameters on surface texture generated by laser polishing of additively manufactured Ti-6Al-4V. Paper presented at the SPIE Photonics West LASE Conference - February 2020, San Francisco - USA.
- Solheid, J.S., Mohanty, S., Bayat, M., Wunsch, T., Weidler, P.G., Seifert, H.J., Pfleging, W. Laser polishing of additively manufactured Ti-6Al-4V - Microstructure evolution and material properties. Paper presented at the 38th International Congress on Applications of Lasers & Electro-Optics (ICALEO) - October 2019, Orlando - USA.
- Solheid, J.S., Seifert, H.J., Pfleging, W. Experimental analysis of laser postprocessing of additive manufactured metallic parts. Abstract presented at the Materials Science and Engineering Congress (MSE) - September 2018, Darmstadt - Germany.
- Solheid, J.S., Seifert, H.J., Pfleging, W. Laser surface modification and polishing of additive manufactured metallic parts. Paper presented at the 10th CIRP Conference on Photonic Technologies (LANE) - September 2018, Fürth - Germany.
- Solheid, J.S., Seifert, H.J., Pfleging, W. Laser-assisted post-processing of additive manufactured metallic parts. Paper presented at the 18th European Society for Precision Engineering & Nanotechnology (EUSPEN) International Conference & Exhibition - June 2018, Venice - Italy.

Book Chapter

- Pfleging, W., Solheid, J.S. (2021). Laser Additive Manufacturing for the Realization of New Material Concepts. In Bock, E.G.P. (Ed.), Bioengineering and Biomaterials in Ventricular Assist Devices (1st ed.). CRC Press.